Numerical and Experimental Study of a Boosted Uniflow 2-Stroke Engine

A thesis submitted for the degree of Doctor of Philosophy

by

Jun Ma

Department of Mechanical, Aerospace and Civil Engineering
College of Engineering, Design and Physical Sciences
Brunel University London

September 2014

Abstract

Engine downsizing is one of the most effective ways to reduce vehicle fuel consumption. Highly downsized (>50%) 4-stroke gasoline engines are constrained by knocking combustion, thermal and mechanical limits as well as high boost. Therefore a research work for a highly downsized uniflow 2-stroke engine has been proposed and carried out to unveil its potential.

In this study, one-dimensional (1D) engine simulation and three-dimensional (3D) computational fluid dynamic analysis were used to predict the performance of a boosted uniflow 2-stroke DI gasoline engine. This was experimentally complemented by the in-cylinder flow and mixture formation measurements in a newly commissioned single cylinder uniflow 2-stroke DI gasoline engine.

The 3D simulation was used to assess the effects of engine configurations for engine breathing performance and in order that the design of the intake ports could be optimised. The boundary conditions for 1D engine simulation were configured by the 3D simulation output parameters, was employed to predict the engine performance with different boost systems. The fuel consumption and full load performance data from the 1D engine simulation were then included in the vehicle driving cycle analysis so that the vehicle performance and fuel consumption over the NEDC could be obtained.

Based on the modelling results, a single cylinder uniflow 2-stroke engine was commissioned by incorporating a newly designed intake block and modified intake and exhaust systems. In-cylinder flow and fuel distribution were then measured by means of Particle Image Velocimetry (PIV) and Planar Laser Induced Fluorescence (PLIF) in the single cylinder engine.

The numerical analysis results suggested that a 0.6 litre two-cylinder boosted uniflow 2-stroke engine with an optimised boosting system was capable of delivering comparable performance to a NA 1.6 litre four-cylinder 4-stroke engine yet with a maximum 23.5% improvement potential on fuel economy. Furthermore, simulation

results on in-cylinder flow structure and fuel distribution were then verified experimentally.

Acknowledgments

First of all, I would like to express my sincere gratitude to my supervisor, Professor Hua Zhao and Professor Alasdair Cairns for their unlimited support and guidance throughout the work.

Also, I would like to give my deepest thanks to Mr Quan Liu, Mr Kangwoo Seo, Dr Yan Zhang and Dr Cho-Yu Li for their help throughout my time at Brunel University.

And I would like to thank the technicians Mr Andrew Selway, Mr Kenneth Anistiss and Mr Clive Barratt for the guidance and support in the laboratory.

Last but not least, I would like to thank my parents and my wife Lei Wang for their unconditional support.

Nomenclature

Abbreviations

ATDC	After Top Dead Centre
BDC	Bottom Dead Centre
BDD	Blow-Down Duration
BR	Burnt Rate
BSFC	Brake Specific Fuel Consumption
BTDC	Before Top Dead Centre
BUSDIG	Boosted Uniflow Scavenged Direct Injection Gasoline
CA	Crank Angle
CAI	Controlled Auto Ignition
CCD	Charge Coupled Device
CE	Charging Efficiency
CFD	Computational Fluid Dynamics
DAQ	Data Acquisition
DCA	Degree Crank Angle
DEV	Duration of Exhaust Valves Opening
DI	Direct Injection
DIATA	Direct Injection Aluminium Through-Bolt Assembly
DISI	Direct Injection Spark Ignition
DPM	Discrete Phase Model

DR	Delivery ratio
EGR	Exhaust Gas Recirculation
EVC	Exhaust Valve Closing
EVO	Exhaust Valve Opening
FMEP	Friction Mean Effective Pressure
FTP	Federal Test Procedure
GDI	Gasoline Direct Injection
HWA	Hot Wire Anemometry
IA	Interrogation Area
IMEP	Indicated Mean Effective Pressure
IPC	Intake Port Closing
IPO	Intake Port Opening
LDA/LDV	Doppler Anemometry/Velocimetry
LES	Large-eddy Simulation
LIEF	Laser Induced Exciplex Fluorescence
LIF	Laser-Induced Fluorescence
LRS	Laser Rayleigh Scattering
MBF	Mass of Burned Fraction
NA	Natural Aspirated
NEDC	New European Drive Cycle
PFI	Port fuel injection
PIV	Particle image velocimetry

PLIF	Planar Laser-Induced Fluorescence
PTV	Particle Tracking Velocimetry
RANS	Reynolds-Averaged Navier-Stokes
SE	Scavenging Efficiency
SI	Spark Ignition
SMD	Sauter Mean Diameter
SOI	Start of Injection
SRS	Spontaneous Raman Scattering
TDC	Top Dead Centre
TE	Trapping Efficiency
TTL	Transistor–Transistor Logic
VCT	Variable Cam Timing
VVT	Variable Valve Timing
WOT	Wide Opening Throttle

Symbols in Roman

A	engine stroke
A_E	effective area of intake port
A_{eff}	effective area of the valve
A_{front}	vehicle frontal area
A_i	axis inclination angle
A_j	area at the cell centre
A_p	intake port area along the cylinder wall
BSR*	blade speed ratio
C_{drag}	aerodynamic drag coefficient
C_f	flow coefficient
C_{ht}	heat transfer multiplier constant
CoV_{cyc}	deviation of the mean light intensity to the ensemble average value
CoV_f	deviation of the light intensity at each pixel from the mean light intensity
C_p	specific heat of the gas
C_{pb}	port width ratio
C_{roll}	tyre rolling resistance factor
C_{wb}	exponent in Wiebe function
D	valve reference diameter
D_{ref}	reference diameter

d	feature diameter of pipe wall
E	total energy
E_v	spectral fluence of the laser
$\vec{F}$	force vector
F_{drag}	drag force
F_{roll}	tyre rolling resistance force
f	lens focal length
H	angular momentum
h	enthalpy
h_e	elevation of the point above a reference plane
G_b	generation of turbulence kinetic energy due to buoyancy
G_k	generation of turbulence kinetic energy due to the mean velocity gradients
$\vec{g}$	gravitational acceleration
I	momentum inertia
I_i	light intensity of each pixel
I_{mean}	mean light intensity of all pixels in the region of interest of each frame
$I_{mean,cyc}$	mean light intensity of all frames taken with same condition
I_v	laser spectral intensity
$\vec{J_J}$	diffusion flux
k	turbulence kinetic energy
k_e	conductivity of the wall

k_{eff}	effective conductivity
L	valve lift
m	mass flow
m_{load}	passenger and cargo mass
m_{veh}	vehicle mass
$\dot{m}*$	dimensionless mass flow
N	number of ports
N*	dimensionless speed
N_r	rotational speed
PR	pressure Ratio
P_r	prandtl number
Δp	pressure drop along the pipe
p	pressure
p_{cyl}	peak in-cylinder pressure
p_s	piston location from TDC at specified crank angle
Q	heat transfer between pipe wall and inner gas
R	resistivity of the absorptive material
R_E	effective ratio of area
Re	Reynolds number
R_g	gas constant
$\vec{r}$	location vector
r_{cy}	engine bore

r_p	radius of swirl circle
S	swirl ratio
S_h	heat of chemical reaction, and any other volumetric heat sources
S_m	mass added to the continuous phase from the dispersed second phase
SA_{wall}	wall surface area
T	temperature
T_{cb}	combustion duration
T_{gas}	inner gas temperature
T_t	engine Torque
T_{wall}	wall temperature
t	time
Δt	time interval
U_j	velocity at the cell centre
u_i	fluid velocity
v	fluid kinematic viscosity
$\vec{v}$	velocity vector
W_c	power consumed by the compressor
W_t	power generated by the turbine
Δx	length of the cell
$\Delta\vec{x}$	element displacement
x_b	effective port shoulder width

x_p	effective port width
Y_M	contribution of the fluctuating dilatation in compressible turbulence to the overall dissipation rate

Symbols in Greek

Γ^*	dimensionless torque coefficient
Ψ	state of the particle ensemble
Ω	collection solid angle
γ	special heat capacity ratio
ε	turbulence dissipation rate
θ	degrees past start of combustion
θ_b	port shoulder width angle
θ_c	crank angle
θ_p	port width angle
η	transmission efficiency of the collection optics
ρ	density
τ	Shaft torque
$\bar{\bar{\tau}}$	stress tensor
φ_p	swirl orientation angle
ω_0	crank shaft angular velocity

Contents

List of Figures

List of Tables

Chapter 1 Introduction

1.1 Introduction

Since their introduction over a century ago, internal combustion (IC) engines have played a key role in shaping the modern world. It is currently widely realised throughout the automotive industry that the IC engine will continue to remain the dominant powerplant for decades, albeit operating in refined form and in some cases as part of a hybrid powertrain. However, in recent decades, serious concerns have been raised with regard to the environmental impact of the gaseous and particulate emissions arising from operating such engines. As a result, ever stringent legislations of pollutants emitted from the vehicles have been introduced by governments globally. In addition, concerns in world's finite oil reserves, and more recently, climate change due to CO_2 emissions has led to increased taxation on road transport. These two factors have forced vehicle manufacturers to continue researching and developing ever cleaner and more fuel efficient vehicles. Nonetheless, there are technologies that could theoretically provide many environmentally sound alternatives to IC engines, such as fuel cells and battery powered electric motors; practicality, cost, efficiency and power density issues will prevent them from replacing IC engine in any significant volume in the near future.

Engine downsizing achieved by reducing the total capacity has drawn more and more interest in engine studies in recent years. By downsizing the engine, the CO_2 emission can be reduced by shifting the engine operating conditions to the more efficient regions. At same engine speed and load, the downsized engine operation points are moved to higher IMEP or torque region, within such region, the engine efficiency and fuel economy is normally better. And to avoid penalizing the output power, boosting system is required to supply same air flow rate on a downsized engine as on its larger counterparts. Besides, the downsizing strategy allows engines to be operated at higher torque, which lets the engine cruise at lower rpm with less frictional and pumping losses.

However, further downsizing beyond 50% in the 4-stroke gasoline engines is limited by knocking combustion, thermal and mechanical limits, potential turbo lag as well as

reliability and durability of the engine components. For diesel engines, the main limitation of applying such technology is thermal loads and consequently the right type of cooling as well as the emission of particulate matter and nitrogen oxides, which would become drawbacks within the idea of reducing CO_2.

The 2-stroke engine has double the firing frequency of the 4-stroke engine, and for the same output torque its IMEP and peak in-cylinder pressure are approximately halved. Thus the 2-stroke engine has much greater potential over the 4-stroke engine for aggressive downsizing without having to increase the boost to a degree that 4-stroke engine requires. This may meet the existing challenges that are with 4-stroke engine downsizing.

However, the conventional 2-stroke engines suffer from uneven thermal and mechanical loads, poor gas-exchange efficiency which result in poor durability, fuel economy and emission issues. In comparison, the uniflow 2-stroke engine can avoid the uneven thermal and mechanical loads due to its simple piston design, it provides better scavenging efficiency and it has great potential to deliver better performance by thorough optimisation. Therefore, it was decided that a feasibility study would be needed to explore the potential of a boosted uniflow 2-stroke DI gasoline engine via combination of engine modelling and testing.

1.2 Objectives

The aim of this work is to study the feasibility and potential of a boosted uniflow 2-stroke DI gasoline engine, as a highly downsized engine to achieve significant reduction in fuel consumption by replacing a large NA 4-stroke gasoline engine. The specific objectives are as follows:

- Development and application of 3D CFD simulation for the study of in-cylinder flow structure, mixture formation and the optimisation of intake ports design in a uniflow 2-stroke engine;
- Development and application of 1D engine simulation for the prediction of engine performance and boosting system optimisation;

- Development and application of a vehicle driving cycle simulation program to predict the fuel savings potential of a boosted uniflow 2-stroke DI gasoline engine over a larger 4-stroke NA counterpart;
- Commissioning a single cylinder uniflow 2-stroke engine via designing and implementing of a new engine intake block, with modifications to the intake and exhaust systems;
- Characterisation of in-cylinder flow and fuel distributions via laser diagnostics and combustion visualisations.

1.3 Outline of thesis

Following the introduction and summary of the objectives presented in Chapter 1, Chapter 2 is a review of relevant literature relating to this project. It starts with a brief introduction to vehicle CO_2 emission legislation. Advanced high efficiency engines and engine downsizing techniques are then discussed. In addition, relevant research and development works in 2-stroke engines are reviewed. The applications of PIV and LIF for in-cylinder flow and fuel distributions are also discussed.

Chapter 3 focuses on the CFD simulation for engine breathing and fuel injection processes. A 2D based model was initially set up to investigate the axis inclination angle of intake port. Then a 3D model was developed and applied to the optimisation of intake port swirl orientation as well as their geometries and numbers. Direct fuel injection was then added to the model. Finally the optimum fuel injection strategy was investigated and the split injections were shown to improve the fuel evaporation and mixture quality.

In Chapter 4, the 3D CFD simulation used for the optimisation of the engine breathing process through the intake port design is described. In addition, the 3D CFD flow results used to provide the intake flow data for the subsequent 1D calculation is discussed. The calibration of Flynn-Chen model was introduced for the estimation of the engine friction FMEP. The effects of engine configurations on the engine breathing process are then discussed.

Chapter 5 covers the discussion of the 1D simulation of the uniflow 2-stroke engine. First, the modelling work of the boosted uniflow 2-stroke engine and vehicle fuel

consumption calculation based on NEDC is introduced. Then the simulation results that cover the engine breathing, output and fuel consumption are presented. The engine boost system optimisation is discussed according to 1D simulation results. The fuel consumption calculation based on NEDC is presented and discussed.

Chapter 6 details the general set-up of the test facility as well as the newly commissioned single cylinder uniflow 2-stroke engine. Specifications of the engine and test bed are presented, along with details of the modifications applied to achieve the uniflow 2-stroke operation and optical access. Also, the intake system, exhaust system, equipment control unit and data acquisition system are presented.

Chapter 7 describes the engine and PIV experiments. The laser, flow seeding device and imaging setup of the PIV system are introduced. The in-cylinder flow structure obtained from the experiment under different engine operating conditions and the comparison with previous simulation results are presented and discussed.

Chapter 8 explains the engine configuration and experimental facilities for PLIF measurements and the flame propagation study on the uniflow 2-stroke engine. Several parameters are introduced to describe the fuel distribution characteristics. For the flame propagation study, two image capturing strategies were employed for both continuous frame sequence and cyclic high resolution images. The results from two systems and their compatibility are discussed.

Chapter 9 begins by briefing the general conclusions drawn as a result of knowledge gained from this project. The conclusions are summarised from Chapter 3, 4, 5, 7 and 8. This chapter also includes recommendations for further work.

Chapter 2 Literature Review

2.1 Introduction

In the last few years, significant efforts have been made to research and develop more efficient IC engines and to reduce the CO_2 emission from passenger vehicles due to increased fuel cost and the concerns over greenhouse gases.

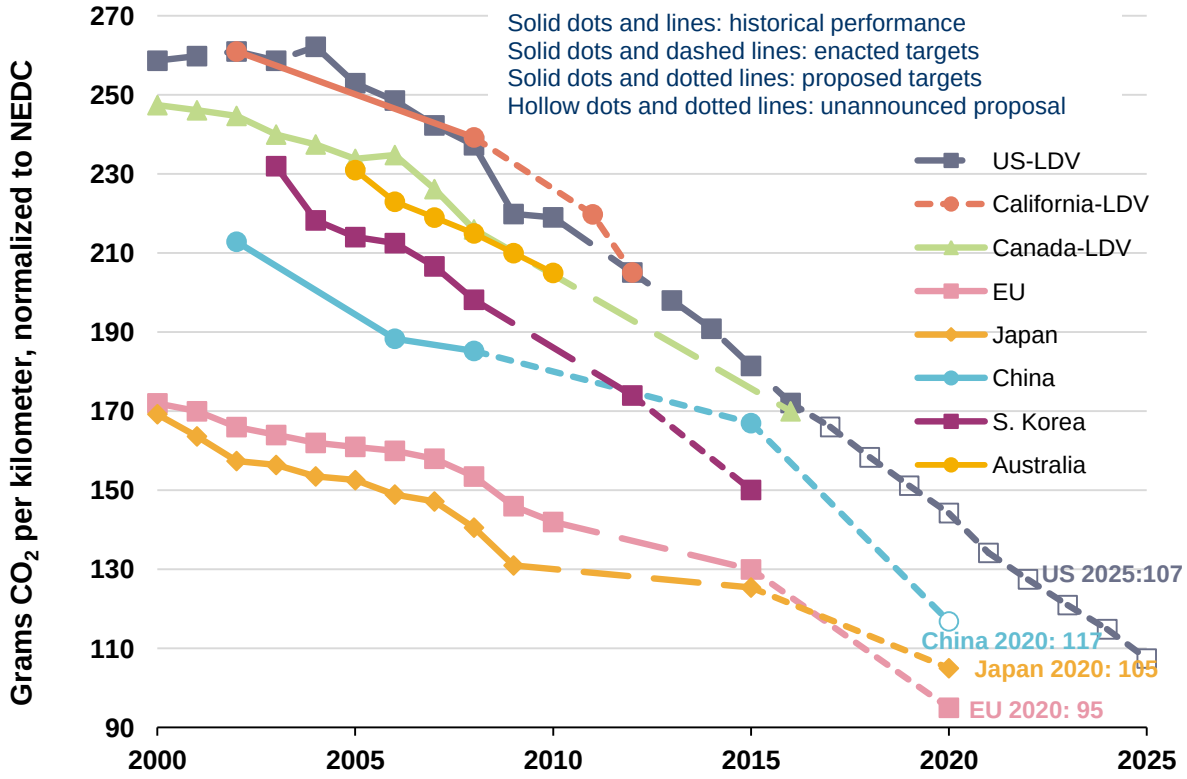

Figure 2.1 Comparison of global regulations for passenger cars [1]

Figure 2.1 provides the legislation trends of vehicle CO_2 emissions around the world. The data has been converted to be consistent with EU standards applied. It can be concluded that the CO_2 emission regulation is becoming more and more rigorous globally.

The EU legislation sets the CO_2 emission target of the sales-weighted averaged new car to 130g/km by 2015, and 95g/km by 2020. In the case that the target cannot be satisfied, a penalty up to €95 for each gram of CO_2 emission exceeding the limit multiplied by the EU-wide registration will be applied [2].

2.2 Advanced engine technologies

In order to improve the engine performance and comply with the legislations, various technologies have emerged to optimise IC engines.

The fuel delivery system affects the IC engine fuel economy directly. Research works have indicated that fuel Direct Injection (DI) shows great potential in improving engine performance. For the conventional engine fuel delivery system, known as Port Fuel Injection (PFI), fuel is injected onto the back of intake valves via the intake ports. This method requires the amount of fuel delivered to greatly exceed the ideal stoichiometric ratio and causes a lag of fuel delivery. This is mainly attributed to the partial vaporisation of the fuel film on the back of the intake valves. With a direct fuel injection system, while the fuel is injected directly into the combustion chamber, the issues of over fuelling with PFI can be reduced and also offers a potential for lean combustion [3]. The research work of Kume et al. has proved that with fuel direct injection, especially at part load, the engine can reach very lean combustion, an air/fuel ratio exceeded 40 could be achieved and significant fuel economy improvement was found [4]. Also, Toyota [5] has revealed that a stratified in-cylinder mixture was achieved via Gasoline Direct Injection (GDI) with concaved pistons, and a 22% fuel consumption reduction was obtained. Another study focused on the in-cylinder mixture formation and suggested general requirements of combining fuel direct injection and stratified mixture, such as the air fuel ratio around spark plug should be 10 to 20, and the spray with 15μm Sauter Mean Diameter (SMD) is achievable for the in-cylinder swirl flow [6].

The Controlled Auto-Ignition (CAI) combustion, also known as Homogeneous Charge Compression Ignition (HCCI) is another technique combining the advantages of both Spark Ignition (SI) and Compression Ignition (CI) methodologies. It is receiving more and more attention in engine development study and research [7]. CAI/HCCI combustion is achieved by controlling the temperature, pressure, and composition of the fuel and air mixture, so that it spontaneously ignites the air/fuel mixture in the engine. This unique characteristic of CAI/HCCI allows the combustion to occur within very lean or diluted mixtures, resulting in low temperatures that dramatically reduce engine NOx emissions. Similar to an SI engine the charge is well mixed which minimises the particulate emissions, also inheriting the advantages of a

CI engine being no throttling losses, therefore an overall higher efficiency can be achieved [8]. Oakley, Zhao and Ladommatos presented an experimental study of CAI/HCCI combustion in a 4-stroke engine, and the results suggested that with EGR dilution, the CAI/HCCI improves the fuel economy by 20% at moderate engine load [9]. In addition, Christens et al. presented that with supercharged CAI/HCCI favourable 59% net indicated efficiency can be achieved [10].

2.3 Engine downsizing and boosting technologies

Engine downsizing via reducing the total engine capacity is now reasonably understood as one of the most effective means to reduce the fuel consumption of IC engines. The idea of engine downsizing concept is to move the engine operation point towards the higher load region; within such region, the engine normally performs with higher efficiency. This can be achieved by reducing the engine displacement, which is known as downsizing, this technique can also be combined with downspeeding, achieved by adopting higher transmission ratios while used on vehicle applications. Meanwhile, engine downsizing also reduces the relative mechanical losses and the engine manufacturing costs.

For example, one research work of Nobuhiro et al. [11] claimed a 12% BSFC reduction at its maximum torque with a 2.3L boosted gasoline engine delivered comparative driving performance to 3.0 to 3.5L Natural Aspirated (NA) engine. The study carried out by Han et al. [12] showed a fuel consumption decrease of 17% based on Federal Test Procedure (FTP) city mode when replacing a V6 3.3L gasoline engine with a 2.0L turbocharged Direct Injection Spark Ignition (DISI) unit. Also, a 0.66L downsized gasoline engine delivered a 5.7% fuel economy improvement based on the Japanese 10-15 mode [13].

The FORD downsized 1.2L Direct Injection Aluminium Through-Bolt Assembly (DIATA) diesel engine showed a good compromise between emissions, noise, and fuel consumption [14]. A downsized 1.5L diesel engine designed by FEV also shows that by downsizing a 4-cylinder to 3-cylinder benefits the engine performance in many ways such as fuel economy and et al [15].

Engine downsizing is possible with boosting techniques for the reason of avoiding the output power and torque penalty due to the reduction of displacement. The

boosting systems applied on IC engines normally consist of supercharging and/or turbocharging. A supercharger usually utilises an air compressor arranged on the upstream of intake manifold driven by the crankshaft directly. The turbocharger consists of a turbine, normally propelled by the exhaust gas and a compressor coupled to the turbine via a common shaft and driven by the turbine. Both systems have advantages and disadvantages. For supercharger, since the compressor is driven directly by the crankshaft, response time lag is therefore eliminated, but it suffers from parasitic losses. Compared to supercharging, turbocharging shows better performance from its thermodynamic prospective. This is mainly because no power drained from the engine crankshaft directly to drive the compressor. However the downside is its poor performance which occurs due to insufficient exhaust gas energy at low load conditions, where the sufficient power for exhaust gas to drive the turbine is not yet reached, so the turbocharger cannot operate at its high efficient region. Furthermore, a response delay which called turbo lag is also associated. This response delay is mainly due to the acceleration of the rotor of the turbine and the pressure increase delay because of the flow fluid dynamic characteristic. And at high engine speed, the turbocharger may elevate the exhaust back pressure, resulting in pumping losses. This is mainly because of the pressure difference across the turbine, which created by the turbine itself to drive the compressor.

Turner et al. carried out study on a downsized engine with an ultra-boost system [16]. The boost system in this case was a combination of a supercharger and a turbocharger, capable of providing 4.5bar or above to its 5L V8 test engine. The results suggested that a 23% fuel economy improvement can be achieved with a 60% downsizing factor. The study of Lake et al. demonstrated another example of boosted downsized engine [17]. In this work, a substantial fuel economy benefit of more than 20% has been analysed in comparison with the base NA vehicle whilst being capable of maintaining half of Euro IV emissions over the NEDC cycle. The feasibility of replacing larger engines found in compactly sized regular passenger vehicles with smaller engines has also been investigated by William P. Attard, Steven Konidaris, Elisa Toulson and Harry C. Watson [18], the study presented that the performance of a 1.25L NA engine found in the 2007 Ford Fiesta can be matched by a 0.43L turbocharged engine, meanwhile, the fuel economy improvement can reach 20%.

Although the engine performance can be benefit by downsizing and boosting, there are numerous limitations of such a technology awaiting advanced solutions to overcome.

As revealed by the research work of Maria Thirouard and Pierre Pacaud [19], with a 0.5L single cylinder engine, to reach a power density of 80kW/L or above, a boost pressure of at least 3bar was required, and at 90kW/L the boost pressure level was found to be 3.4bar, the in-cylinder peak pressure was measured ~200bar.

A research work presented by University of Melbourne revealed the limits of boost system applications with a supercharger and a turbocharger [20]. The PL was defined by the author as the Performance Limit, corresponding to the Wide Opening Throttle (WOT) condition, and the MAP was defined as the Manifold Absolute Pressure. As shown in Figure 2.2, the engine performance at high speed, high load area was restricted by the compressor flow limit of the supercharger. Meanwhile, the high load area suffered from the knocking combustion although it was still below the failure limit. Turbocharger boosting system in this case was capable of delivering higher boost pressure. However, at medium speed high load, the engine performance was limited by the turbocharger flow, and at high speed high load, it was restricted by the flow limit due to the intake and exhaust system. Meanwhile, the rest of the high load area can be reached but knocking combustion frequently occurred. The results also suggested that supercharging are not restricted by the intake and exhaust system whereas turbocharging suffers from back pressure elevation.

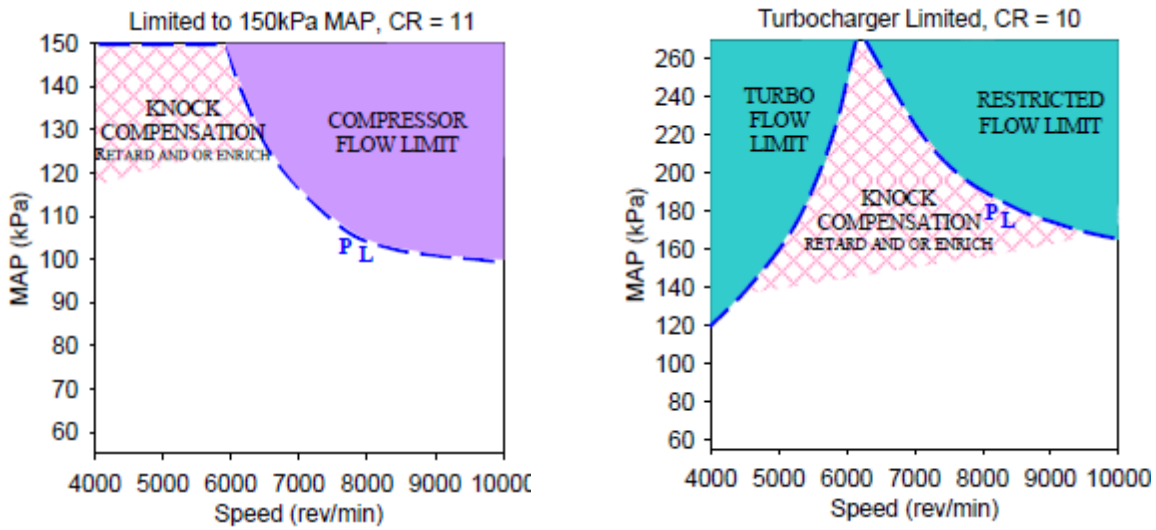

Supercharged **Turbocharged**

Figure 2.2 Limits of engine boosted by supercharger and turbocharger [20]

In general, the main technical barriers of downsizing strategy for conventional 4-stroke engines are as follows [21]:

- Combustion limitations – Increased propensity to knock leads to reduced compression ratio and retarded spark timing, hence lower efficiency
- Steady state low speed torque – With increased downsizing, low speed BMEP requirement increases to maintain acceptable performance
- Transient performance – Transient response needs to be maintained with increased low speed torque requirement
- Engine geometry/layout – As engine capacity falls below 1 litre, bore size and/or cylinder number will require re-optimisation
- Part load fuel economy – As downsizing continues the fuel economy gains inherently reduce due to the limitation of boosting system, measures will need to be taken to mitigate this

Besides, for gasoline engines, the major technique barriers are also knocking, thermal and mechanical loads of the engine components, response time of turbocharging as well as reliability and durability of the engine parts. And for diesel engines, the main limitation of applying such technology is thermal loads and consequently the right type of cooling as well as the emission of particulate matter and nitrogen oxides would become drawbacks within the idea of reducing CO_2. And

to extend the engine working range, the boost system design can be greatly complicated.

By comparison, the 2-stroke engine has double firing frequency of the 4-stroke, and for the same output torque its IMEP and the peak pressure are approximately halved. Thus the 2-stroke engine has much greater potential over the 4-stroke for aggressive downsizing without having to increase the boost to a degree that 4-stroke engine demands. These advantages promise to address existing challenges associated with 4-stroke engine downsizing.

2.4 2-stroke engines

2.4.1 Scavenging methods of the 2-stroke engine

The 2-stroke engines rely on the scavenging of burned gases by fresh charge during the overlap period of intake and exhaust processes. The scavenging can be achieved by cross-flow, loop-flow and uniflow methods, as shown in Figure 2.3. In early 2-stroke configurations, the cross-flow is applied by arranging the scavenge ports virtually opposite to the exhaust ports. During the scavenging process, some of the incoming charge passes directly across the cylinder and exits the exhaust ports, which is known as charge short circuiting. The piston is therefore shaped with a deflector on the crown to direct the fresh charge upwards towards the cylinder head. In the case of loop-flow, the exhaust ports are positioned on the same side as the air intake ports so that the intake charge is directed towards the other side of cylinder and then reflected off the cylinder wall before they flow back to the exhaust ports. In comparison, the uniflow scavenging method is achieved by combining intake ports at the lower part of the cylinder volume and poppet valves on the cylinder head. The intake ports are designed typically to generate an upward swirling flow structure. The positive pressure difference across the intake and exhaust as well as ascending piston forces the in-cylinder charge towards the exhaust valves. Alternatively, the reversed uniflow can be arranged by supplying the intake charge through the valves on the cylinder head.

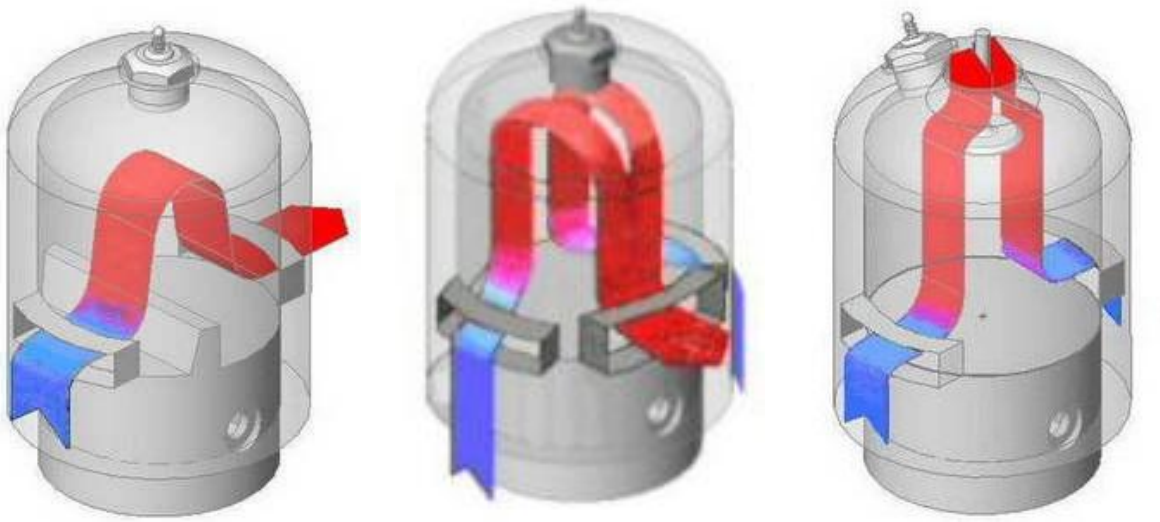

Cross-flow **Loop-flow** **Uniflow**

Figure 2.3 Typical 2-stroke engine scavenging methods

Among all these scavenging methods, a uniflow 2-stroke engine produces better scavenging [22] and minimum short circuiting. The short circuiting will deliver fresh charge directly into exhaust system, wasting the boosted energy, creating a error measurement of the lambda sensor, and combustion could happen in the exhaust system. In addition, the uniflow 2-stroke engine can be boosted at higher intake pressure by closing the exhaust valves earlier and may operate with proven wet sump and poppet valve technology. The uniflow 2-stroke engine avoids bore distortion caused by uneven thermal loads in the conventional ported design with its cold intake port on one side and hot exhaust port on the other. Furthermore, the uniflow 2-stroke engine is by nature very suitable for CAI combustion operation which gives stable and fuel efficient part-load operation by adjusting the scavenging efficiency and hot residual gases through phasing of the poppet exhaust valves using variable cam timing (VCT) devices. Using CAI addresses the unstable part load combustion often experienced by the 2-stroke gasoline engine resulting in further reduced uHC and CO emissions, better fuel economy and significantly lower NOx emissions. Finally, a centrally mounted injector can be installed in such engines of smaller bore size due to the absence of intake valves. By combining direct injection and a uniflow layout, the air and fuel short circuiting associated with conventional 2-stroke SI engines can be avoided.

2.4.2 Previous research on uniflow 2-stroke engines

Uniflow 2-stroke engines are widely used in large marine diesel engines (eg. MAN, Wärtsilä-Sulzer) and in some diesel locomotives (Electro-Motive Diesel). Detroit Diesel had been manufacturing uniflow 2-stroke direct injection diesel engines for heavy duty vehicles until late 1990s as well as for military vehicles requiring very high power density engines. The most recent and relevant example for passenger applications is Daihatsu E202 engine shown at the 1999 Frankfurt Motor show [23]. It is a prototype 3-cylinder 987cc, uniflow 2-stroke direct injection diesel engine with a hybrid scavenging system that combines a supercharger and a turbocharger. Variable Valve Timing (VVT) was used to control the timing of exhaust valves in the cylinder head, in order to ensure startability at start-up and best possible fuel consumption and output. A high pressure common rail fuel injection system was used to feed centrally located injectors for optimum mixture formation and engine performance. A 1.0 litre 3-cylinder uniflow 2-stroke direct injection diesel engine designed for automotive applications was also demonstrated by AVL with a similar design in the mid 90s [24]. Daimler-Benz conducted an experimental evaluation of a single cylinder uniflow 2-stroke DI diesel engine and demonstrated that it had similar performance to the 4-stroke DI diesel engine [25].

However, there have been very few works carried out on the uniflow 2-stroke direct injection gasoline engine. Chiba University and Fuji Heavy Industry did some preliminary research on a reverse uniflow 2-stroke direct injection gasoline engine [26]. In this work, the scavenging processes and in-cylinder flow patterns at various load and speed conditions were studied using 3D CFD simulation. Universidade do Minoho presented the design of a single cylinder crankcase boosted semi-direct injection gasoline uniflow 2-stroke engine of 43.3cm^3 displacement volume [27]. The engine was predicted to produce a rated BMEP of 8bar and was intended for a student marathon fuel economy competition.

As discussed above, for 2-stroke engines, the scavenging process plays significant role to the engine performance. And among all scavenging methods, the uniflow shows best scavenging efficiency. Daimler-Benz AG presented a study of 2-stroke engines with common rail fuel supply systems [25]. The study compared the performance of 2-stroke loop-flow and uniflow configurations. As shown in Figure 2.4,

the uniflow method shows better performance than the loop-flow under similar engine conditions.

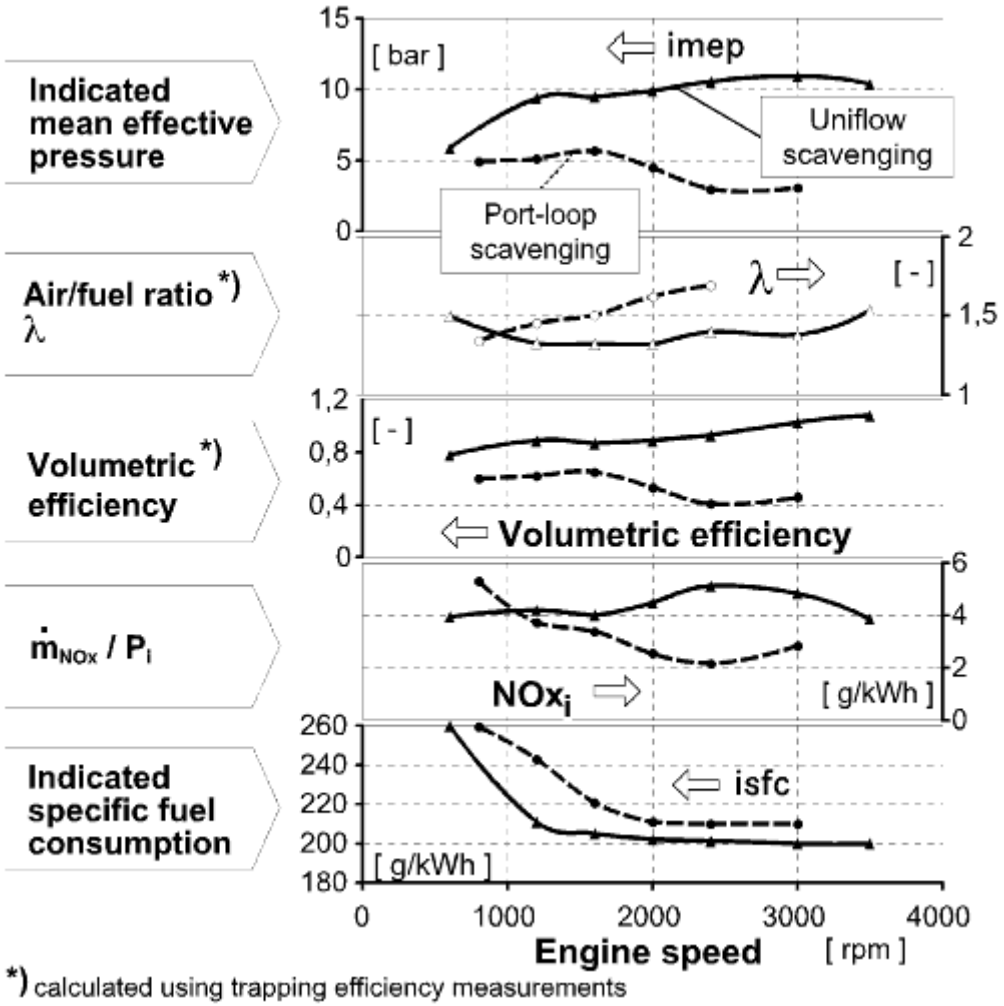

Figure 2.4 Full-load performance of loop-flow and uniflow 2-stroke engine [25]

Although the uniflow scavenging shows superior performance, the uniflow scavenging method has a disadvantage. It is the significantly greater cylinder spacing and the unfavourable overall engine lengths. When the engine bore/stroke ratio is extremely high of low, it is very hard for the intake port design to optimize and generate a proper flow to blow the residual gas due to the spatial narrow shape. AVL carried out research work on the intake port to optimise the scavenging process of the uniflow 2-stroke engine [24]. As shown in Figure 2.5, a), the conventional intake port arrangement and b) illustrated the optimised intake port arrangement. With careful design of the size and orientation of the intake ports, the lack of scavenging ability around the centre of the engine can be overcome.

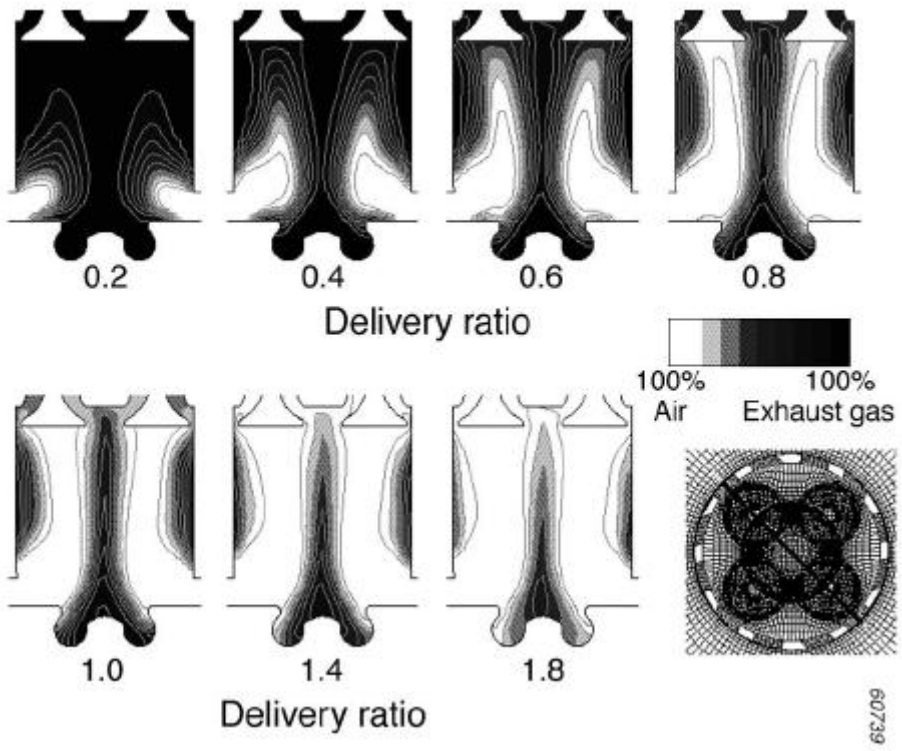

a)

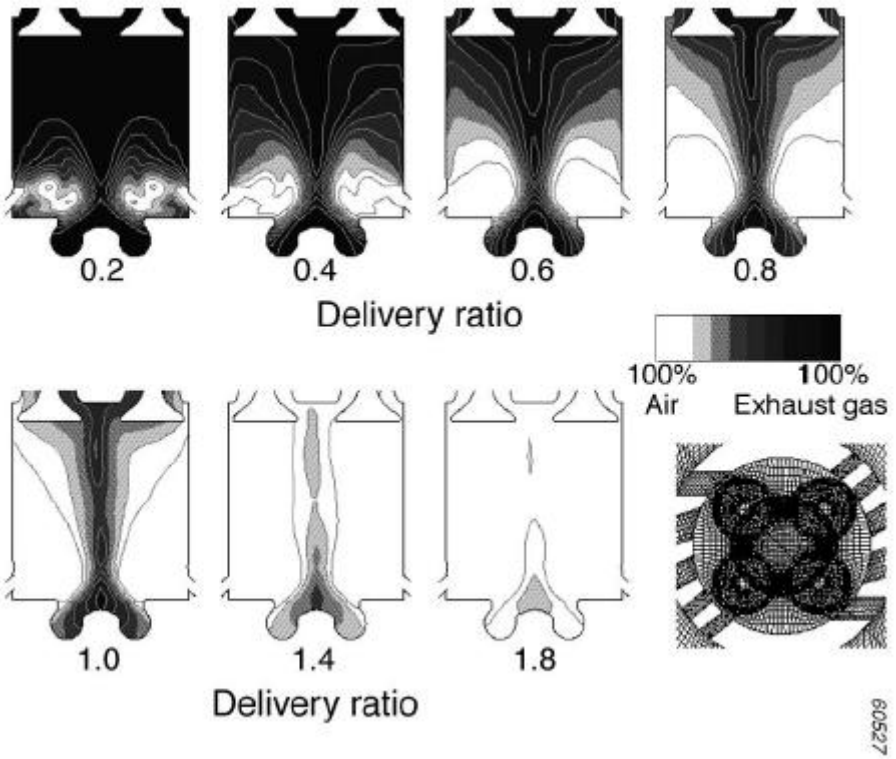

b)

Figure 2.5 In-cylinder flow structure (a) (b) [24]

Being different from the conventional 4-stroke engine, the boost system for 2-stroke engines is indispensable. It is due to the scavenging method for 2-stroke engine

breathing, that the intake and exhaust processes have much greater overlap than 4-stroke engines. The boost system of a 2-stroke engine requires careful optimisation. Mattarelli et al. published their study on a 2-stroke GDI engine [28]. The study revealed the strategy of boost system optimisation on 2-stroke engines. For a supercharger, it is relatively easy to increase the engine power & torque, unfortunately, the fuel consumption also increases due to the mechanical losses. The strategy is to keep the boost pressure as low as possible while the engine power target is satisfied. For a turbocharger, the conflict is that while the requirement of boost pressure is higher, the turbine nozzle size has to be smaller. However, the exhaust pressure will increase and therefore the fuel consumption increases too. The strategy of turbocharger optimisation is to compromise the nozzle size and the required boost pressure.

2.5 In-cylinder flow measurements

The in-cylinder flow structure has a great effect on the engine gas-exchange, air/fuel mixing, combustion and output performance [22]. For conventional engines, large scale flow structures, such as swirl or tumble are often used to maintain the flow's kinetic energy until the end of the compression stroke, where they break down into micro scale turbulence, promoting early flame kernel growth and increased flame speed [29], which increases the engines knock limit, allowing the use of increased compression ratios that result in increase fuel efficiency and reduced CO2 emissions. In addition, higher flame speed allows leaner air/fuel mixture to be burned for better fuel economy. For uniflow 2-stroke engine, the effect of in-cylinder flow organisation is even more significant on the engine performance. In order to provide information to optimise the in-cylinder flow structure, the in-cylinder flow investigation is required. Despite the development of ever more powerful CFD modelling tools that are of great value to designers of such combustion systems, their limitations mean that experimental validation of models will still be required for the foreseeable future.

The Hot Wire Anemometry (HWA) and Laser Doppler Anemometry/Velocimetry (LDA/LDV) methods have been developed to provide single point flow data [30] [31][32][33][34][35]. The complex flow structure in the cylinder is better measured by the spatially resolved flow field measurement techniques. In early stage of the in-cylinder flow structure studies, smoke, metaldehyde crystals and white goose down

cut into short pieces after the heavier pieces had been removed were all used as the mediums to trace the in-cylinder air flow [36]. The quantitative whole field measurement began with the development of Particle Tracking Velocimetry (PTV) [37][38][39] and Particle Image Velocimetry (PIV) [40][41][42]. Such techniques have been developed and enabled to provide instantaneous, cycle resolved, two-dimensional velocity maps across extended measurement planes within the cylinder. With these in-cylinder flow measurement methods, small seeding particles are required to indicate the flow movement, the seeding particles are normally planted at the upstream of the intake ports, and then illuminated by a certain light source, such as lasers in most of the cases, so two frames recorded within a very short time interval can be obtained.

With the PTV technique, the particles are identified individually and correlated between two exposures taken in a narrow time window, the particles velocity vectors can be determined by their displacements. The PTV method has been used to conduct an extensive in-cylinder flow visualisation study. For example, the research of the intake-generated fluid motion produced different intake configurations [43], the cyclic variability of the pre-combustion flow field in a motored engine [44], and the effects of intake port configurations on in-cylinder flow organisation [45]. These previous research works have proved that the PTV method is able to provide useful data for in-cylinder flow study. However, there are several technique barriers that restrict the application within engine research. Firstly, the light source for the PTV method is required to be with long pulses, this requirement leads to a low power density of the illumination of seeding particles. To provide images with adequate quality, the seeding particles have to be large size so they can scatter sufficient light to be captured by cameras. Furthermore, because of the combination of low light power density and large size seeding particles, the planting density of the particles has to be low in order to avoid confusion of seed pairs during analysis, the lean flow will increase the load of post-processing works.

The development of the PIV technique and its application to IC engines has allowed in-cylinder flow field measurement to be obtained with high spatial resolution. For PIV measurements, the seeding particles are illuminated by high energy, thin laser sheet pulses, and two frames are captured in a very short duration. The whole region of interest is divided into small interrogation areas, the mean flow velocity vectors are

calculated within these interrogation areas, typically with a cross-correlation method. By doing so, the identification of distinct, individual particles is no longer required. The illumination light source for PIV with short pulse and high power density allows the use of micron sized particles that can track high frequency flows. The high density seeding particles is allowed to be used, so a more comprehensive velocity map can be obtained than with PTV. The PIV method is suitable for the measurement of both large scale and small scale flow structures.

General Motors R&D Centre has carried out a study applying PIV technique to take measurements of in-cylinder flow velocity in order to calculate the swirl and tumble. The results were also compared with numerical calculation results [46]. The experiments were carried out on a motored 4-stroke engine, and the measured and computed turbulence distributions at TDC compression both show a maximum near the cylinder centre that agreed to within 25% of each other. Apart from running PIV on combustion investigation, David L. Reuss has also carried out a study using PIV technique to a motored engine [47], this study proved that not only a steady in-cylinder flow structure can be created, but also a flow structure with different scale can be achieved within the same cycle. The research of Haider et al. applied the PIV technique to a large 2-stroke marine engine [48], the study focused on the effect of the piston position to the in-cylinder flow structure while the intake ports were partially and fully opened.

2.6 In-cylinder fuel distribution

The effort of the engine in-cylinder fuel distribution and the air/fuel mixing process affects the engine performance to a great extend. In the case of a 2-stroke direct injection engine, the fuel atomisation and mixture formation are even more important due to the reduced time for the mixing process.

Several non-intrusive laser based diagnostic techniques have been developed to allow in-cylinder fuel concentration measurement. The major techniques are based on Rayleigh scattering, Raman scattering and laser induced fluorescence.

The Laser Rayleigh Scattering (LRS) is a simple and user friendly method for measuring gaseous species concentration. The Rayleigh scattering signal is the strongest among the three techniques mentioned above. However, the LRS method

suffers from the interference of the Rayleigh signal by Mie scattered light from both solid and liquid particles and the cylinder walls and it is not species specific. LRS was used in some early studies of in-cylinder fuel vapour distribution. For example, the concentration of Freon-12 vapour from diesel injector was measured by LRS to study the simulated diesel injection process in [49]. The in-cylinder gasoline fuel vapour concentration in a motored engine was measured by LRS through careful optical arrangement and calibration. A research work focused on a steady flow rig was presented in a series of studies [50]. A more substantial case of LRS application was presented for the fuel vapour concentration measurement in an evaporating and combusting spray in an optical DI diesel engine under fired and motored conditions [51].

The Spontaneous Raman Scattering (SRS) technique is capable of providing simultaneous multiple-species measurements of major species such as N_2, O_2 and CO_2 and etc. With the appropriate laser and multi-channel detector developed, multi-point, multi-species SRS measurements have been demonstrated [52]. But the SRS suffers from very weak signal-to-noise ratio due to the small Raman scattering cross section.

Among all three techniques, the Laser-Induced Fluorescence (LIF) is probably the most successful and the most widely used for engine fuel distribution studies. The main reason of its success is the ability of providing fuel distribution data with a good signal to noise ratio. With proper calibration, this method can be used to obtain quantitative air/fuel ratio measurements.

According to the work of Christof Schulz and Volker Sick [53], the ideal tracer for LIF should behave like the base fuel used, and should yield LIF signal intensities that are directly proportional to the desired quantity and should not be influenced by the ambient conditions. Toluene has been used as LIF tracer in research work carried out by Sandia National Laboratories [54], while an Nd:YAG laser (266 nm) was used as the excitation source, and iso-octane was used as the fuel because of their similar boiling points. The inert gas in this case was N_2, because the tracer toluene experienced fluorescence quenching problems due to oxygen. Another research applied PLIF technique to a DISI engine using same laser light source, the tracer in this study was 3-pentanone, and to compensate the early depletion of the 3-

pentanone, 3- hexanone was also used. The advantages of 3-pentanone for fuel distribution measurements is that its boiling point (102ºC) closely matches the iso-octane (99ºC) at ambient temperature and pressure. However, evidences also indicated that Rapid depletion of 3-pentanone in the liquid mixture shows significant uncertainties in iso-octane distribution measurements, especially in a GDI engine when the fuel is evaporated in the combustion chamber [55]. A very recent publication of LIF technique applied on a GDI engine was carried out by Changan Automobile Company [56]. In this research work, a KrF excimer laser with the wavelength of 248nm is used as the excited laser source. The tracer was 3-pentanone and it was mixed up with iso-octane with a 1:9 ratio in volume. The properties of iso-octane and 3-pentanone are shown in Table 2.1.

Table 2.1 Key properties of the experimental fuels and dopant

	Iso-Octane	3-Pentanone
Lower Heating Value (MJ/kg)	44.31	33.4
RON	100	-
MON	100	-
(R+M)/2	100	-
Density at 15ºC (kg/dm^3)	0.69	0.81
H/C Ratio	2.25	2
O2 (% weight)	0	18.6

2.7 Summary

This chapter presents the related research literature dedicated to reducing the engine fuel consumption, and also many related techniques applied to IC engines.

Studies suggest that engine downsizing is a very effective way to reduce the engine CO_2 emission. However, some technical barriers restrict the further downsizing of 4-stroke gasoline engines, such as knocking, thermal and mechanical loads of the engine components, response time of turbocharging as well as reliability and durability of the engine.

On the other hand, the 2-stroke engine has double firing frequency of the 4-stroke, Thus the 2-stroke engine has much greater potential over the 4-stroke for aggressive downsizing without having to increase the boost to a degree that 4-stroke engine demands.

One big issue of 2-stroke engine optimisation is the scavenging process. Several scavenging methods are available for 2-stroke operation, such as cross-flow, loop-flow and uniflow. In comparison, uniflow has the best scavenging performance. By combining uniflow and direct injection in a 2-stroke operation, the fuel consumption can be improved through aggressive engine downsizing with the absence of typical ported 2-stroke engines.

Optical diagnostic techniques are very helpful for providing engine in-cylinder information. Various types of optical diagnostic and their applications on IC engine studies have been discussed. The PIV technique is identified as the most suitable technique for the in-cylinder flow measurements of the uniflow 2-stroke engine. The PLIF technique is selected for the in-cylinder fuel distribution due to its suitability, strong signal and relatively simple setup.

Chapter 3 Analytical studies of flow and mixing in a uniflow 2-stroke engine

3.1 Introduction

Over the past decade, the numerical analysis has been extensively used for engineering design and optimisation. In the research and development of the IC engine, the Computational Fluid Dynamics (CFD) is increasingly used for the analysis of in-cylinder flow, mixture formation and combustion.

In the current study, the CFD method was used to investigate the in-cylinder flow pattern, the fuel injection process and the air/fuel mixing process in the direct injection gasoline uniflow 2-stroke engine. The results were also used to provide the initial and boundary conditions in the 1-D engine simulation for optimising the intake ports, the exhaust valve timing, and the prediction of the engine's performance.

As the computational hardware and techniques develop, the numerical analysis on IC engines play a more and more important role to research and hardware optimisation. The traditional methods of engine research and development is following the procedure as:

- Building prototype engines
- Running tests on the test bed to gain relevant information
- Modifying the prototype according to the test results to optimise the engine

The traditional way of engine research is a costly and highly time consuming process due to the large number of variables that have an effect on the design. Numerical engine study and analysis plays a very important role in the development of engines. It helps in analyzing the various engine configurations without actually building the engine. Thus, Engine Simulation helps in reducing the cost and time involved in developing a new engine [57].

The state-of-the-art of computational simulation has advanced on many fronts. Nowadays, computer hardware itself has improved dramatically over the last half century. As we close the 20th century, computers are 109 times faster and more cost

effective than they were in the days of World War II. The computational expense reduces by a factor 2 every 1.5–2 years, which fits well with this remarkable performance achievement. Furthermore, while state-of-the-art electronic chip manufacturing today uses 0.25μm feature size technology, the path to 0.05μm or smaller technology now seems apparent, thereby ensuring same speedup rate for the next 15 years or so [58]. The development of computational technology secures the numerical analysis method plays a role as important and experimental studies on IC engines.

3.1.1 Introduction to CFD simulation

CFD is the abbreviation of Computational Fluid Dynamics. It is computational method that uses numerical methods and algorithms to solve and analyze problems that involve fluid flows. Numerical simulations of CFD are normally used for two purposes. First, the applications of CFD are associated with fundamental research. This kind of studies requires very high accuracy of the numerical data; the physical models used to present the fluid behaviour must be pertinent and so are the algorithms used. Second, the CFD simulation is used to predict the flow characteristic. The goal here is to predict physical characteristic of the flow structure and its efforts on certain objects rather than providing data for flow dynamics itself. In this case, the introduction of CFD simulation is on purpose of reducing the cost and time required to develop a study subject [59]. This technique has been widely used for the studies of flow structure, fuel spray and distribution and combustion organisation on IC engines. The applications of CFD simulation on engine research is used mostly for the second purposed. Many commercial types of software have been developed for the purpose of CFD simulation, the software used for the study related to the work described in this article is the Ansys Fluent.

3.1.2 Turbulence model

It is an unfortunate fact that no single turbulence model is universally accepted as being superior for all classes of problems. The choice of turbulence model will depend on considerations such as the physics encompassed in the flow, the established practice for a specific class of problem, the level of accuracy required, the available computational resources, and the amount of time available for the simulation.

For the turbulent simulation, also there are many models can be used to calculate the flow structure. The Reynolds-averaged Navier-Stokes (RANS) and Large-eddy simulation (LES) are two most popular modelling methods of IC engine applications. Both methods use similar equations and are based on same principle ground. However, in terms of physical meanings of parameters in the equations, the difference is identified.

3.1.2.1 Reynolds-Averaged Approach

Time-dependent solutions of the Navier-Stokes equations for high Reynolds-number turbulent flows in complex geometries which set out to resolve all the way down to the smallest scales of the motions are unlikely to be attainable for some time to come. One of the methods can be employed to render the Navier-Stokes equations tractable so that the small-scale turbulent fluctuations do not have to be directly simulated. It is the Reynolds-averaging approach.

The Reynolds-Averaged Navier-Stokes (RANS) equations govern the transport of the averaged flow quantities, with the whole range of the scales of turbulence being modeled. The RANS-based modelling approach therefore greatly reduces the required computational effort and resources, and is widely adopted for practical engineering applications.

The flow of a viscous incompressible fluid with constant properties is governed by the Navier–Stokes equations (Einstein summation convention applies to repeated indices) [60].

$$\frac{\partial u_i}{\partial t} + \frac{\partial}{\partial x_j}\left(u_i u_j\right) = -\frac{\partial p}{\partial i} + v\frac{\partial^2 u_i}{\partial x_j \partial x_j} \qquad \text{[E-3.1]}$$

$$\frac{\partial u_i}{\partial x_i} = 0 \qquad \text{[E-3.2]}$$

u_i – The fluid velocity

p – The pressure

v – The fluid kinematic viscosity

The dependent variables of Equation 3.1 and 3.2 can be decomposed into mean and fluctuating parts as follow,

$$u_i = \bar{u}_i + u_i', \;\; p_i = \bar{p}_i + p_i' \qquad \text{[E-3.3]}$$

By substituting Equation 3.3 into Equation 3.1 and 3.2, taking an ensemble average, the system of partial differential equations that governs the mean-velocity and pressure fields of incompressible turbulent flow can be derived as follows,

$$\frac{\partial \bar{u}_i}{\partial t} + \frac{\partial}{\partial x_j}\left(\overline{u_\iota u_\jmath}\right) = -\frac{\partial \bar{p}}{\partial x_i} + \nu \frac{\partial^2 \bar{u}_i}{\partial x_j \partial x_j} \qquad \text{[E-3.4]}$$

$$\frac{\partial \bar{u}_i}{\partial x_i} = 0 \qquad \text{[E-3.5]}$$

With reference to the nonlinear term shown below,

$$\overline{u_\iota u_\jmath} = \bar{u}_i \bar{u}_j + \overline{u'_\iota u'_\jmath} \qquad \text{[E-3.6]}$$

The RANS can be derived as follow,

$$\frac{\partial \bar{u}_i}{\partial t} + \bar{u}_j \frac{\partial \bar{u}_i}{\partial x_j} = -\frac{\partial \bar{p}}{\partial x_i} + \nu \frac{\partial^2 \bar{u}_i}{\partial x_j \partial x_j} - \frac{\partial \tau_{ij}}{\partial x_i} \qquad \text{[E-3.7]}$$

$$\tau_{ij} = \overline{u'_\iota u'_\jmath} \qquad \text{[E-3.8]}$$

τ_{ij} – The Reynolds-stress term that incorporates the effects of turbulent motions on the mean stresses

3.1.2.2 Large-Eddy Simulation

LES provides an alternative approach in which large eddies are explicitly computed in a time-dependent simulation using the filtered Navier-Stokes equations. The rationale behind LES is that by modelling less of turbulence, the error introduced by turbulence modelling can be reduced. It is also believed to be easier to find a universal model for the small scales, since they tend to be more isotropic and less affected by the macroscopic features like boundary conditions, than the large eddies. Filtering is essentially a mathematical manipulation of the exact Navier-Stokes equations to remove eddies that are smaller than the size of the filter, which is usually taken as the mesh size when spatial filtering is employed. Like Reynolds-averaging, the filtering process creates additional unknown terms that must be modeled to achieve closure. Statistics of the time-varying flow-fields such as time-averages values of the solution variables, which are generally of most engineering interest, can be collected during the time-dependent simulation. LES for high

Reynolds number industrial flows requires a significant amount of computational resources. This is mainly because of the need to accurately resolve the energy containing turbulent eddies in both space and time domains, which becomes most acute in near-wall regions where the scales to be resolved become much smaller. Wall functions in combination with a coarse near wall mesh can be employed, often with some success, to reduce the cost of LES for wall-bounded flows. However, one needs to carefully consider the ramification of using wall functions for the flow in question. For the same reason (to accurately resolve eddies), LES also requires highly accurate spatial and temporal discretizations.

In general, the LES model shows advantages in details of flow structure, such as eddies and vortices. Furthermore, LES model has the potential to be more predictive. However, the assumption of potential of prediction is based on the solver calculation methods, but this assumption is hard to be validated, and the settings of boundary conditions will contribute to the result variations of LES to further extend than RANS.

In contrast, the RANS shows advantages in resulting a time based average data, which is more compatible with experimental results, and the computational time expense is lower than LES with same grid conditions.

Research Institute of Automotive Engineering and Vehicle Engines Stuttgart has carried out 3D CFD simulations in order to provide information for the intake system design on an 8-cylinder engine with external exhaust gas recirculation [61]. CFD simulation also has been used to investigate the evaluation of the effects of cycle by cycle variation on knock tendency of a high performance spark ignition engine [62], the simulation data provided qualitative information for the identification of best park plug location. The study of Cornolti et al [63] presents different methodologies of CFD analysis applied to the intake plenum of a turbocharged HSDI Diesel engine. The discharge and pressure loss coefficients representing the flow losses within the plenum have been calculated. The comparison with the steady flow bench experimental results confirmed the accuracy of the 3D model.

3.2 CFD Model Set-Up

ANSYS FLUENT was chosen for the simulation. Fluent has a powerful pre-processor to import geometry files from CAD and provides high quality mesh creating ability

with flexibility. It has advanced physical models for the description of turbulence, heat and energy transfer, multi-phase/species and etc. Two solver types of solver are available for both steady and transient flow calculations. They are pressure-based and density-based.

3.2.1 Principle of calculations

ANSYS FLUENT uses the conservation equations of mass and momentum for all flow calculation, when heat transfer is involved, an additional energy conservation equation is introduced. The equations are shown below

$$\frac{\partial \rho}{\partial t} + \nabla \cdot (\rho \vec{v}) = S_m \qquad \text{[E-3.9]}$$

$$\frac{\partial}{\partial t}(\rho \vec{v}) + \nabla \cdot (\rho \vec{v} \vec{v}) = -\nabla \mathrm{p} + \nabla \cdot (\bar{\bar{\tau}}) + \rho \vec{\mathrm{g}} + \vec{\mathrm{F}} \qquad \text{[E-3.10]}$$

$$\frac{\partial}{\partial t}(\rho E) + \nabla \cdot (\vec{v}(\rho E + p)) = \nabla \cdot \left(\mathrm{k}_{\mathrm{eff}} \nabla \mathrm{T} - \sum_{\mathrm{j}} \mathrm{h}_{\mathrm{j}} \vec{\mathrm{J}}_{\mathrm{j}} + (\bar{\bar{\tau}}_{\mathrm{eff}} \cdot \vec{v})\right) + \mathrm{S}_{\mathrm{h}} \qquad \text{[E-3.11]}$$

ρ – Density

t – Time

$\vec{v}$ – Overall velocity vector

S_m – Mass added to the continuous phase from the dispersed second phase (e.g., due to vaporization of liquid droplets) and any user-defined sources

p – Pressure

$\bar{\bar{\tau}}$ – Stress tensor

$\vec{\mathrm{g}}$ – Gravitational acceleration

$\vec{\mathrm{F}}$ – Force vector

E – Total energy

$\mathrm{k}_{\mathrm{eff}}$ – The effective conductivity

T – Temperature

h – Enthalpy

$\vec{J}_j$ – The diffusion flux of species j

S_h – The heat of chemical reaction, and any other volumetric heat sources defined by user

Equation 3.9 and Equation 3.10 describe the conservation of mass and momentum respectively. The equation of energy conservation shows as Equation 3.11 [64].

One of the main targets for the study is to investigate and predict the in-cylinder turbulent flows and the swirl generating ability with corresponding intake port designs. There are different fluid flow-modelling techniques.

The RANS calculation method was applied for the flow structure simulation in this study and the turbulence model used was Re-Normalisation Group (RNG) $k-\varepsilon$ model. The RNG $k-\varepsilon$ model is derived using a rigorous statistical technique with following features:

- The RNG model has an additional term in its ε equation that significantly improves the accuracy for rapidly strained flows.
- The effect of swirl on turbulence is included in the RNG model, enhancing accuracy for swirling flows.
- The RNG theory provides an analytical formula for turbulent Prandtl numbers, while the standard $k-\varepsilon$ model uses user-specified, constant values.

While the standard $k-\varepsilon$ model is a high-Reynolds-number model, the RNG theory provides an analytically-derived differential formula for effective viscosity that accounts for low-Reynolds-number effects. Effective use of this feature does, however, depend on an appropriate treatment of the near-wall region.

These features make the RNG $k-\varepsilon$ model more accurate and reliable for a wider class of flows than the standard $k-\varepsilon$ model [64].

Transport Equations for the RNG $k-\varepsilon$ Model are shown below:

$$\frac{\partial}{\partial t}(\rho k)+\frac{\partial}{\partial x_i}(\rho k u_i)=\frac{\partial}{\partial x_j}\left(\alpha_k \mu_{eff}\frac{\partial k}{\partial x_j}\right)+G_k+G_b-\rho\epsilon-Y_M+S_k \qquad \text{[E-3.12]}$$

$$\frac{\partial}{\partial t}(\rho \epsilon)+\frac{\partial}{\partial x_i}(\rho \epsilon u_i)=\frac{\partial}{\partial x_j}\left(\alpha_k \mu_{eff}\frac{\partial \epsilon}{\partial x_j}\right)+C_{1\epsilon}(G_k+C_{3\epsilon}G_b)-C_{2\epsilon}\rho\frac{\epsilon^2}{k}-R_\epsilon+S_\epsilon \qquad \text{[E-3.13]}$$

k – Turbulence kinetic energy

ϵ – Turbulence dissipation rate

G_k – Generation of turbulence kinetic energy due to the mean velocity gradients

G_b – Generation of turbulence kinetic energy due to buoyancy

Y_M – Contribution of the fluctuating dilatation in compressible turbulence to the overall dissipation rate

$C_{1\epsilon}, C_{2\epsilon}, C_{3\epsilon}$ – Constants

$\alpha_k, \alpha_\epsilon$ – Inverse effective Prandtl numbers for k andϵ, respectively

S_k, S_ϵ – User-define boundary

By solving equation set combined by equation 3.12 and 3.13, the value of k and ϵ can be derived.

3.2.2 Boundary Conditions

To define the calculation, the boundary conditions are as important as the physical equations. The boundary conditions include mechanical structure codes, engine breathing inlet/outlet pressure and temperature, piston movement profile, valve lift profiles and etc.

For the mechanical structure, the basic engine parameters are the bore and stroke, the intake port geometry configuration, exhaust valves dimensions and etc. The engine mechanical structure is defined by Pro Engineering, and then imported into the CFD tools. All engine mechanical structures were defined prior to the CFD calculations.

The other boundary conditions can be generated after the mechanical code is imported into CFD tools and meshed. For the engine modelling system, in terms of mass flow transfer, inlet/outlet boundary conditions are required to describe the intake/exhaust conditions on the interface between the engine model and the global environment, including:

- Pressure on the environment side of the inlet/outlet interface.

- Flow direction on the inlet/outlet interface.
- Turbulent kinetic energy and dissipation rate.
- Temperature of the flow at the boundary interface.
- The components of the inlet species and exhaust species if backflow occurs at the exhaust outlet boundary

The dynamic mesh boundaries for the engine structure are piston and exhaust valves. The piston movement is defined by the engine geometry configurations, including:

- Crank shaft speed
- Piston stroke
- Connecting rod length

In FLUENT, the piston location is calculated by

$$p_s = L + \frac{A}{2}(1 - \cos(\theta_c)) - (L^2 - (\frac{A}{2}\sin(\theta_c))^2)^{\frac{1}{2}} \quad \text{[E-3.14]}$$

p_s – Piston location from TDC at specified crank angle

L – Length of connecting rod

A – Engine stroke

θ_c – Crank angle

The exhaust valve lift profile is defined by a code contains the crank angle and corresponding valve lift, which is created separately and then imported into the CFD tool. During the simulation, the valve moving axis is defined and the valve position at a given crank angle is then governed by the valve lift profile.

3.2.3 Grid and Mesh Types

CFD calculations are based on the finite element method by discretizing the geometry into grids. By doing this, the formula to solve the problem related to the geometry is also discretized and integrated into a matrix which describes the physical problems.

The grids will have great impact on the convergence rate of calculation, the accuracy of the calculation and the calculation time consumption.

The typical grid types of 2D and 3D are shown in Figure 3.1.

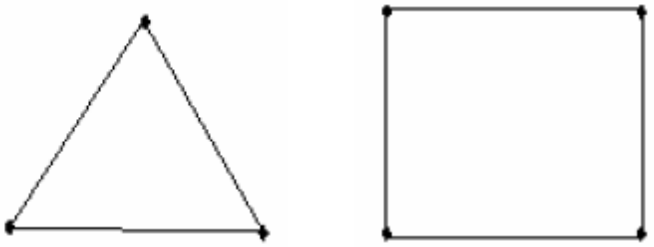

Triangle **Quadrilateral**

2D Grid Types

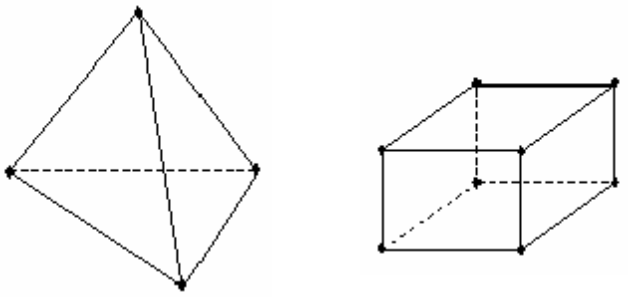

Tetrahedron **Hexahedron**

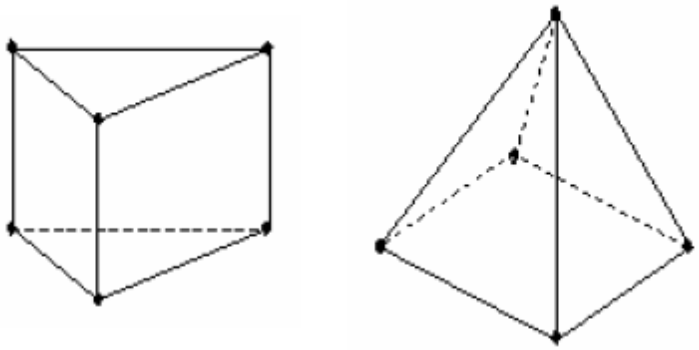

Wedge **Pyramid**

3D Grid Types

Figure 3.1 Typical Grid Shapes

The grid details of the CFD calculation in this study will be discussed in following chapters.

3.3 CFD Calculation with 2D Model

The performance of the uniflow 2-stroke engine is largely determined by the scavenging process during the overlap period of intake and exhaust opening. In a uniflow 2-stroke engine, intake ports geometry and opening time determine the intake fresh charge mass flow rate, the scavenging performance, and the swirl generation of in-cylinder flow.

At the start of the project, a single cylinder 2-dimensional uniflow 2-stroke engine base model was set up for the study of scavenging process and the optimisation of the intake ports. The engine model features intake ports at the bottom of the cylinder liner. Exhaust valves are included in the cylinder head and actuated by a camshaft. A set of parameters are introduced [22] to define the intake port configuration settings of the uniflow 2-stroke engine, as shown in Figure 3.2 and Table 3.1.

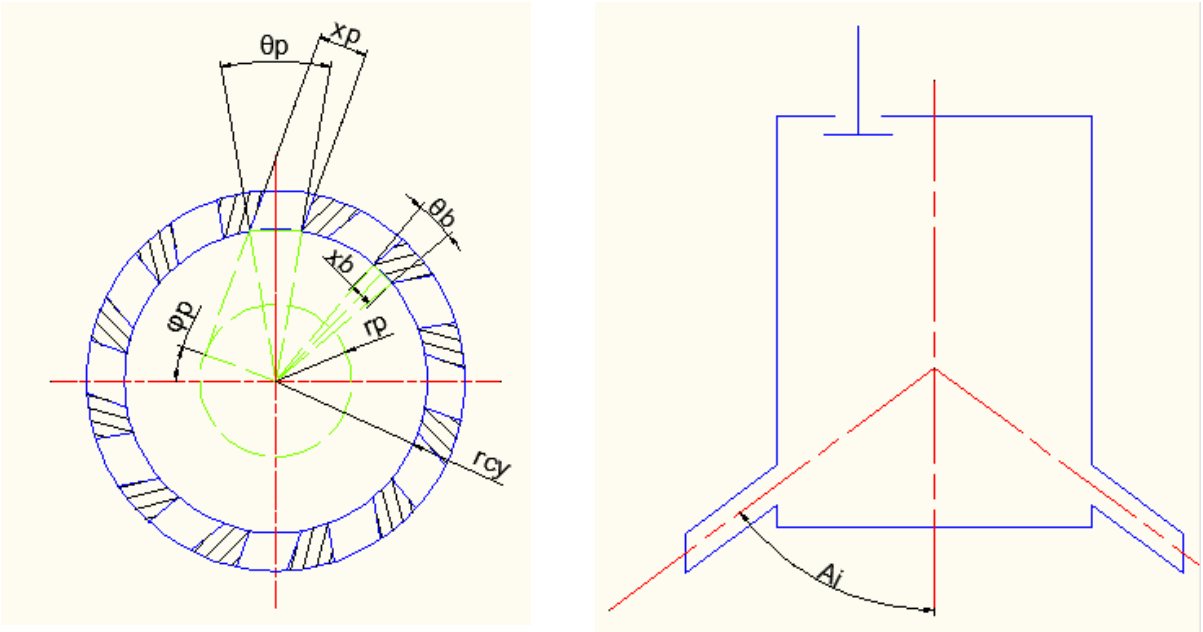

(a) **(b)**

Figure 3.2 The intake port geometry parameter

Table 3.1 The intake port geometry parameter

Parameter	Definition
r_{cy}	engine bore
r_p	radius of swirl circle
θ_p	port width angle
N	Number of ports
A_i	Axis inclination angle
φ_p	Swirl orientation angle $= 90° - \cos^{-1}(r_{cy}/r_p) - \theta_p/2$
x_p	Effective port width $= r_{cy} \times sin(\theta_p/2) \times cos\,\varphi_p$
θ_b	Port shoulder width angle $= 360/N - \theta_p$
x_b	Effective port shoulder width $= 2 \times r_{cy} \times sin\,\theta_b/2$

3.3.1 2D Model Design

In order to determine a baseline configuration of the uniflow 2-stroke engine, a 2D CFD model was first used to predict the effect of axis inclination angle, Ai, on in-cylinder flow and the scavenging process during the overlap period of intake port opening and exhaust valve opening. The 2D model is shown in Figure 3.3.

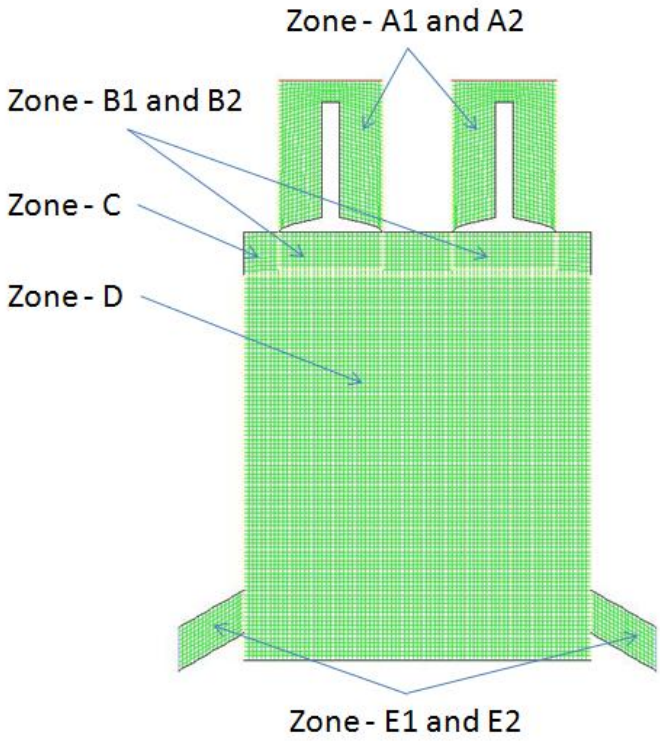

Figure 3.3 The 2D CFD model

At this stage, the engine bore is set to 80mm and stroke is set to 89mm, which will be used for the single cylinder engine experiments later.

As shown in Figure 3.3, the engine geometry structure has been simplified and divided into 5 groups, which are shown below,

- A1 and A2 – Exhaust valves
- B1 and B2 – Valve dynamic zones
- C – Clearance volume
- D – Swept Volume
- E1 and E2 – Intake port channels

The reason of simplification and the divisions of the geometry structure is that two moving groups were involved, exhaust valves and piston. So the dynamic mesh has to be assigned. To secure the transient calculation process, a structured grid is chosen. In this case, the quadrilateral grid type is chosen. The structured grid requires less time and achieves best transient calculation performance when dynamic mesh is applied. In addition, the performance of mesh regeneration and calculation convergence performance are better.

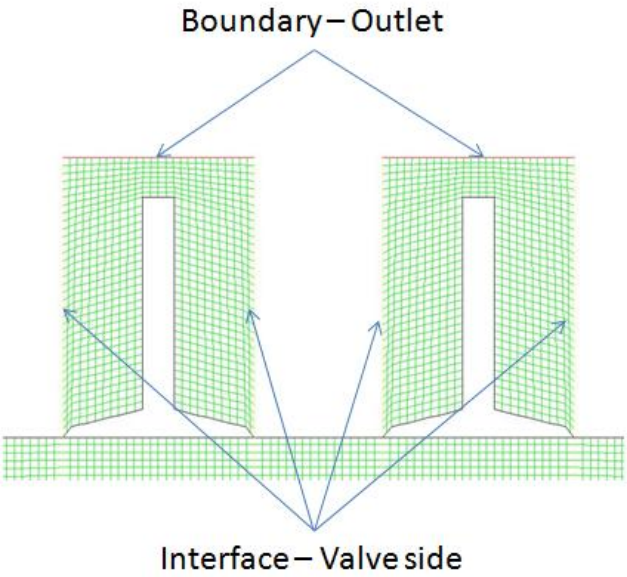

Figure 3.4 Boundary of exhaust valves

Figure 3.4 shows the mesh structure and boundary setup of the exhaust valves. The top edge of exhaust valve meshes is set to be an outlet boundary which is the outlet of the entire system. The back-pressure is set to the ambient pressure. The backflow component can be also defined and are set to be burnt gas. The side walls of the exhaust valves meshes are set to as interfaces. The interface allows mass and energy transfer across and is mainly used with dynamic mesh and moving components. Because of the valves movement, the interface here is set to couple with the corresponding interface on the valve dynamic zones. When the valves move down, the couple of interface sets overlaps and the in-cylinder components and the energy are allowed to travel from one side to the other freely. As a result, when the exhaust valves are opened, the in-cylinder components are allowed to follow the flow towards the outlet boundary. All other edges are set to solid walls including those in the interior. The entire valve zone moves as a rigid body so the mesh and boundary edges posses exactly the same relative positions during the simulation. The valve movement is controlled by a user defined lift profile.

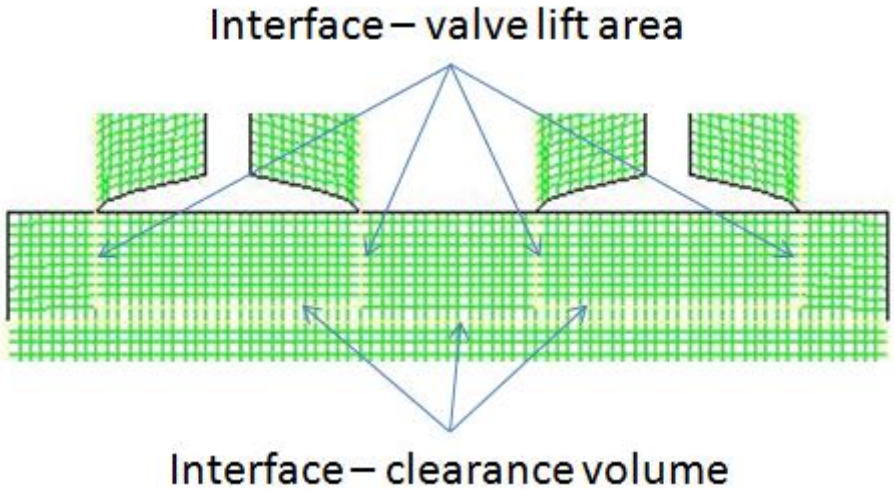

Figure 3.5 Boundary of valve dynamic zones and clearance volume zone

The clearance volume zone and valve dynamic zones are shown in Figure 3.5. The grid type for these two zones is also structured quadrilateral. The clearance volume zone has two sets of interfaces and the other edges are walls. Two interface sets are coupled with the swept volume and the valve dynamic zones respectively, both allows the in-cylinder components to travel freely in the cylinder chamber.

The top edge of valve dynamic zone adjacent to the exhaust valve is set to wall and the other edges are set to interface. When the exhaust valve is moving, the vertical length of valve dynamic zone changes. The interior mesh is squeezed when valves move down and expanded when valves move up. The quadrilateral grid is applied to the valve dynamic zone. When valves move during the simulation, the layers of mesh are recalculated and regenerated. The layers adjacent the moving side are removed when mesh is squeezed and added when mesh expands. The grids on the rest of zones remain the same. Different types of grid of mesh has been applied to the model, a set of preliminary simulation has been carried out under same boundary conditions. The results suggested this meshing method gives the best convergence ability and requires less computing time.

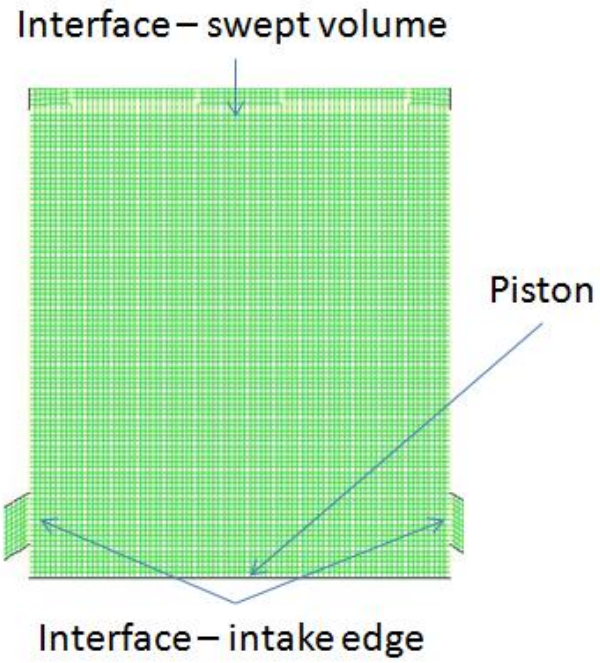

Figure 3.6 Boundary of swept volume

The swept volume zone is shown in Figure 3.6. The dynamic mesh design is the same as the valve dynamic zone. The bottom edge of the swept volume zone is set to be the piston. The movement is defined by the pre-defined engine speed, piston stroke and connecting rod length. The interior mesh is also regenerated by removing and adding layers. Two sets of interfaces are defined, one set couples with the corresponding interface on clearance volume, the other couples with the intake port channels.

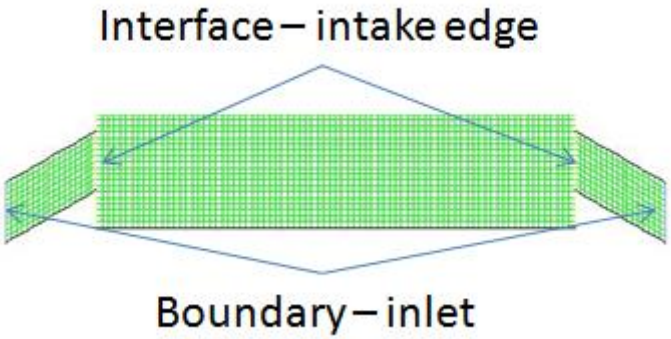

Figure 3.7 Boundary of intake port channel

As shown in Figure 3.7, the far side of the intake port channel is set to the inlet boundary. The inlet pressure, temperature, species and initial flow direction is defined and assigned to the inlet boundary. On the edge adjacent to the swept volume zone, the edge is defined as interface coupling with the swept volume zone.

3.3.2 2D Model simulation and results

The intake ports opening time is governed by their relative location to the piston at BDC. When the piston position is higher than the port top edge, the ports are fully covered by the piston, and the intake ports are closed. When the piston location is lower than the top edge of intake ports, the intake ports are opened. The exhaust valves timing is governed by their lift profile.

The calculation started from 120°ATDC, at which exhaust valves start to open, to 250°ATDC, when the intake ports are fully covered by the piston and the exhaust valves are closed. Thus, simulation covers the range from the beginning to the end of the scavenging process of the 2-stroke operation.

A 1.5bar absolute boost pressure was applied to the intake flow. The initial in-cylinder pressure was set to 1.2bar @120°ATDC, and in-cylinder temperature was set to 500K. The initial in-cylinder charge was assumed to be stationary. The exhaust backpressure was set at the ambient pressure.

The following parameters are used to characterise the quality of scavenging process [66]:

- Delivery Ratio (DR): defined as the ratio of delivered fresh charge mass to reference mass. The reference mass is calculated by the displaced volume multiplied by ambient air density.
- Trapping Efficiency (TE): defined as the ratio of mass of delivered fresh charge retained in the in-cylinder to the total mass of delivered fresh charge.
- Scavenging Efficiency (SE): defined as the ratio of mass of delivered fresh charge retained in the cylinder to the total trapped cylinder charge.
- Charging Efficiency (CE): defined as the ratio of mass of delivered air retained in the cylinder to the reference mass.
- Calculations were carried out for 5 intake port's axis inclination angles, Ai, which are 30º, 45 º, 60 º, 90 º and 135 º as shown in Figure 3.8.

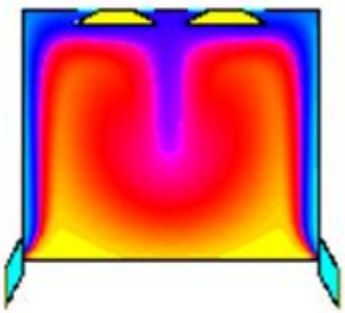

Ai - 30º

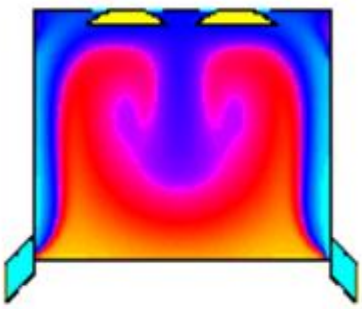

Ai - 45º

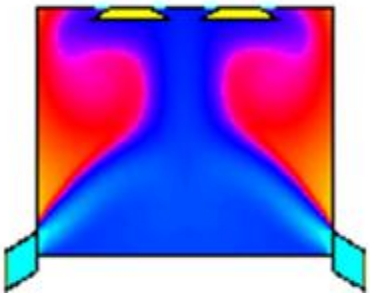

Ai - 60º

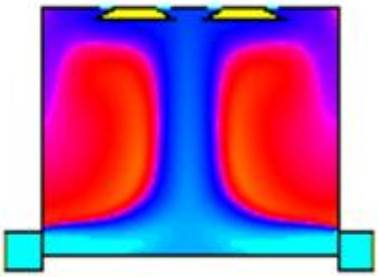

Ai - 90º

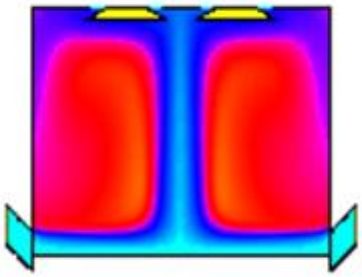

Ai - 135º

Figure 3.8 In-cylinder components distribution contour

The red area in Figure 3.8 represents the residual gas and the cyan area the fresh charge. With 30º axis inclination angle, the fresh charge flows into the cylinder chamber and then moves up along the cylinder wall. After reaching the top of chamber, flow on each side turns towards the exhaust valves and collides at the centre of the cylinder before flowing down towards the bottom of the cylinder along the central line of the cylinder. When the axis inclination angle increases to 45 º, the flow structure and pattern remains the similar to the one with 30 axis inclination

angle intake ports. However, the fresh charge occupies more area and flows further down at central line of the cylinder in a reversed vortex shape. With 60 º axis inclination angle, the flow structure of fresh charge is distributed in an area of the shape of an upside-down wine cup. The sides of fresh charge area are formed at the same angle as intake ports and converge towards each other before diverging upwards to the exhaust valves. With 90 º and 135 º intake port inclination angle, the fresh charge moves along the piston top and collides to form a vertical flow along the central line towards the top of the cylinder chamber.

The cumulative results of delivery ratio, charging efficiency, scavenging efficiency and trapping efficiency over the scavenging period are shown in Figure 3.9.

Figure 3.9 Engine scavenging performance as a function of axis inclination angle based on 2D models

The delivery ratio reaches its peak at 90º intake port inclination angle. Either increase or decrease in the axis inclination angle will cause a drop of the delivery ratio. This is better explained by the effective area ratio of intake port, which is defined as

$$R_E = {}^{A_E}/_{A_P} = \sin A_i \qquad \text{[E-3.15]}$$

R_E – Effective ratio of area

A_E – Effective area of intake port

A_P – Intake port area along the cylinder wall

A_i – Axis inclination angle

And the definition of R_E, A_E, and A_P is shown in Figure 3.10.

When the intake port inclination angle is 90º, the effective area ratio of intake port reaches 1.

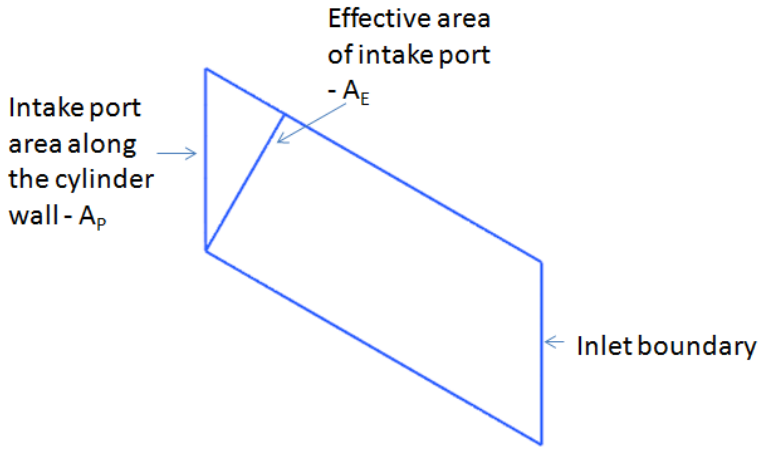

Figure 3.10 Effective area ratio of intake port

But 90º axis inclination angle intake ports resulted in the lowest trapping efficiency, because of the “short-circuiting” phenomenon [22], which involves the fresh charge going directly out of the cylinder through the exhaust valves during the scavenging period. As shown in Figure 3.8, with 90º axis inclination angle intake port, some of the fresh charge can flow to the exhaust valves and escape the cylinder chamber. The 30º axis inclination angle intake port has the highest trapping efficiency but the lowest delivery ratio.

The charging efficiency, indicating the charging ability of the intake system, reaches its maximum value with 60º axis inclination angle intake port. The scavenging

efficiency shows the same trend as the charging efficiency and indicates the ability of fresh charge blowing the residual gas out of the cylinder chamber. Because the charging efficiency has most direct impact on the engine power output, the 2D calculation suggests that the 60 º axis inclination angle intake ports can be adopted for maximum engine output.

3.4 3D CFD Calculations

3.4.1 3D CFD engine model

In order to carry on more realistic simulations, a 3D engine CFD model is set up as shown in Figure 3.11. The base engine is based on the engine geometry of the single cylinder engine to be used for experimental studies and it has an 80mm bore and 89mm stroke. The cylinder head includes a pent roof combustion chamber and four valves.

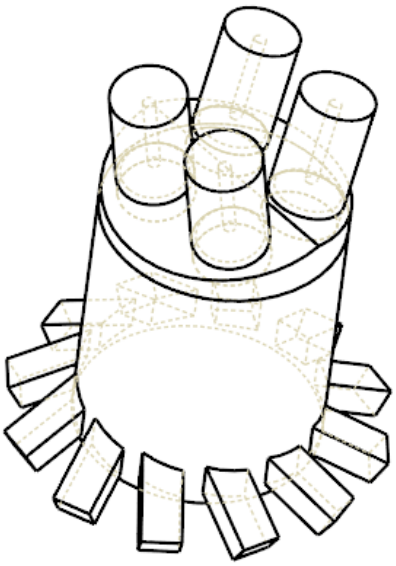

Figure 3.11 3-D CFD base model

Similar to the 2D model, the entire engine geometry is divided into 5 groups, exhaust valves, valve dynamic zones, clearance volume, swept volume and intake port channel.

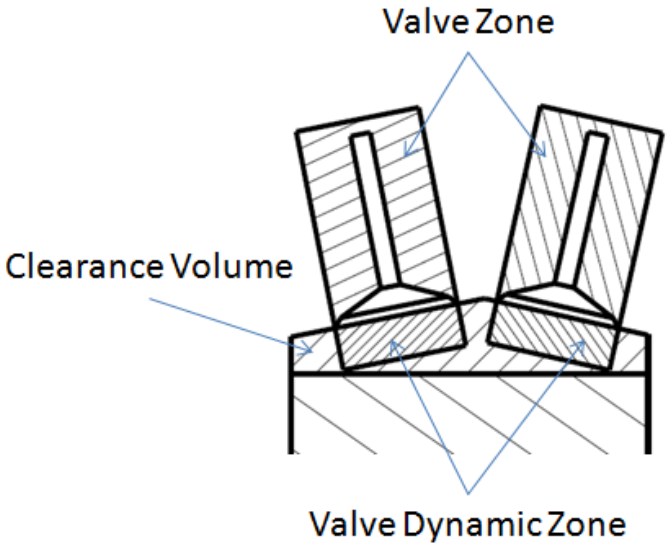

Figure 3.12 Valve zone, valve dynamic zone and clearance volume

As shown in Figure 3.12, valve zones with solid valve features are generated as rigid body and located on top of the valve dynamic zones. The top surface of valve body is assigned as outlet. The valve dynamic zones are seating in the clearance volume zone. When valves are closed, the real engine clearance volume is made up by valve dynamic zones and clearance volume zone. When valves open, the valve zone moves down along the valve zone central axis as a rigid body, squeezing the valve dynamic zone in the process. The side walls of valve zones, valve dynamic zones and corresponding surfaces on clearance volume are set to interfaces to allow the mass and energy transfer across the boundary freely. The dynamic mesh regeneration method is layering and the mesh type is structured quadrilateral grid to secure the calculation process and reduce the required time.

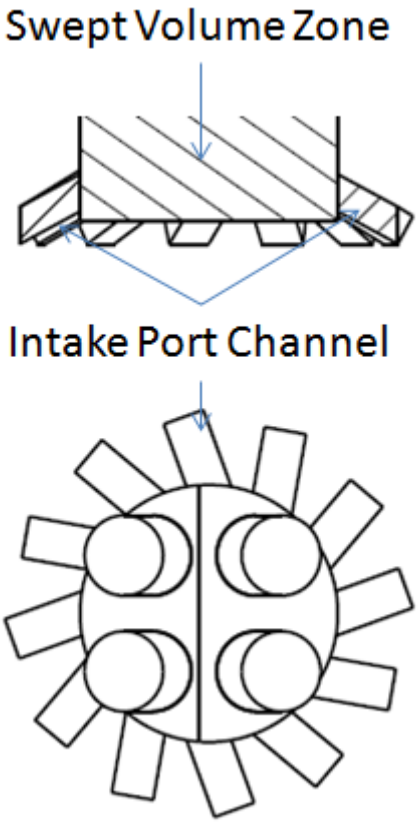

Figure 3.13 Intake port channel layout

The outside boundary of each intake port channel is assigned to be the inlet, the inside surface is assigned to be the interface coupled with the interface of the swept volume. The bottom surface of the swept volume body is assigned as piston. The same set of parameters is used to describe the intake port geometry as mentioned at the beginning of this chapter and set to be adjustable. For the 3D CFD simulation, the baseline single cylinder engine model intake ports are set all around the cylinder liner. For the engine performance calculation of the multiple-cylinder configuration, ports between cylinders will be removed.

3.4.2 3D CFD simulation results

The 1st simulation carried out is investigation of the intake port axis inclination angle effect on the scavenging process. The chosen axis inclination angles are 30º, 45º, 60º, 75º and 90º.

The simulation boundary conditions are set the same as the 2D simulation. The calculations started from 120°ATDC, and end at 250°ATDC. A 1.5bar absolute boost

pressure was applied to the intake flow. The initial in-cylinder pressure was set to 1.2bar @120°ATDC, and in-cylinder temperature was set to 500K. The initial in-cylinder charge was assumed to be stationary. The exhaust backpressure was set at the ambient pressure. The boundary conditions were imported from a 1D simulation model discussed later in Chapter 4, the engine model was operated at 4000rpm at full load.

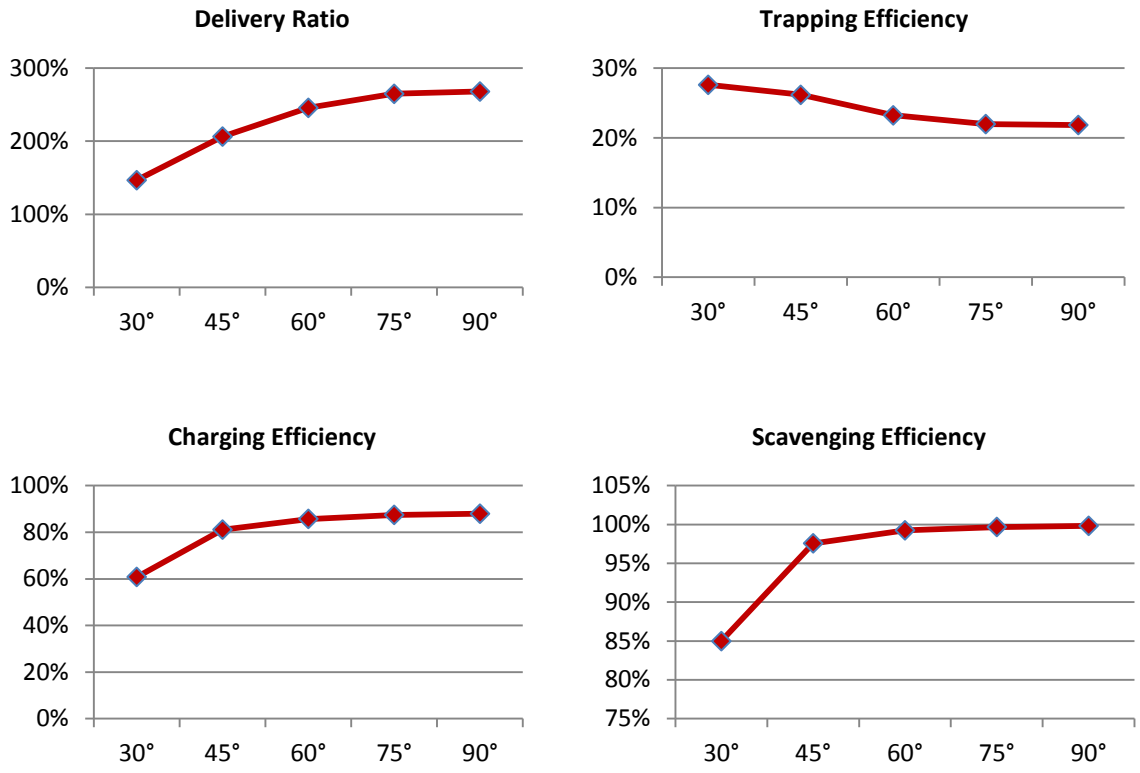

Figure 3.14 Engine breathing performance as a function of axis inclination angle based on 3D models

As shown in Figure 3.14, the same effect of the axis inclination angle of intake port on the delivery ratio level is predicted by the 3D CFD as the 2D simulation result. When axis inclination angle increasing from 30º to 90º, the effective area of the intake port increases, resulting in a decreasing delivery ratio. But the absolute values of delivery ratio are much lower than those predicted by the 2-D because of the 3D effect of the port geometry.

The trapping efficiency drops as the axis inclination angle decrease, due to the "short-circuiting" effect. The charging efficiency and scavenging efficiency of 3D simulation exhibit different trends from the 2D calculation. The 90º axis inclination

angle intake port shows the best charging and scavenging performance. However, the results of 60º and 75º axis inclination angle are very close to the maximum value. Considering the negative effect of “short-circuiting” on engine emissions, 60º axis inclination angles is chosen for the subsequent simulations.

In order to maximize intake flow through the intake ports, the number of intake ports and their geometry need to be designed to give the highest flow efficiency. For a given number of intake ports, N, the port width ratio C_{pb} can be used to describe the port’s geometry effect on flow as defined below,

$$C_{pb} = {(N \cdot x_p)}/{2r_{cy}} \qquad \text{[E-3.16]}$$

C_{pb} – Port width ratio

N – Port number

x_P – Effective port width

r_{cy} – Engine bore

For a given engine bore diameter of r_{cy} and fixed value of C_{pb}, intake ports can be arranged with wider port width and less number of ports or narrower port width and more number of ports.

Different combinations of N and x_p were evaluated as given in Table 3.2 and the definition of each parameter can be found in Table 3.1.

Table 3.2 The setting of combination of N and x_p

Setting	SET1	SET 2	SET 3	SET 4	SET 5
r_{cy} [mm]	80	80	80	80	80
r_p [mm]	40	45.7	51.4	55.5	61.2
φ_p [°]	20	20	20	20	20
θ_p [°]	20	30	40	48	60
θ_b [°]	10	15	20	24	30
x_b [mm]	13.94	20.88	27.78	33.27	41.41
x_p [mm]	26.12	38.96	51.44	61.20	75.24
N	12	8	6	5	4
A_i [°]	60	60	60	60	60
C_{pb}	1.9	1.9	1.9	1.9	1.9

For all calculations, the swirl orientation angle was set to 20° according to the swirl orientation angle optimization simulation discussed later in this section. The port width ratio was fixed to 1.9. The number of ports decreased whilst the width of individual ports was enlarged from Set 1 to Set 5 design. The boundary condition is kept the same as before.

To evaluate the results, the swirl ratio was introduced [67]. Assuming at one location in the cylinder, PNT4, with the velocity vector points from PNT4 to PNT5, as shown in Figure 3.15, the location vector can be represented as

$$\vec{r} = x\hat{\imath} + y\hat{\jmath} + z\hat{k} \qquad \text{[E-3.17]}$$

and the velocity vector can be represented as

$$\vec{v} = u\hat{\imath} + v\hat{\jmath} + w\hat{k} \qquad \text{[E-3.18]}$$

then the angular momentum to axis z at this point is

$$H_z = xv - yu \quad \text{[E-3.19]}$$

the momentum inertia of axis z is

$$I_{zz} = x^2 + y^2 \quad \text{[E-3.20]}$$

the swirl ratio can be calculated as follow

$$S = \frac{\sum_i^N (H_z)_i}{\sum_i^N (I_{yy})_i \omega_0} \quad \text{[E-3.21]}$$

where $\omega_0$is the corresponding crank shaft angular velocity

$$\omega_0 = \frac{2\pi n}{60} \quad \text{[E-3.22]}$$

n – Engine speed in rpm

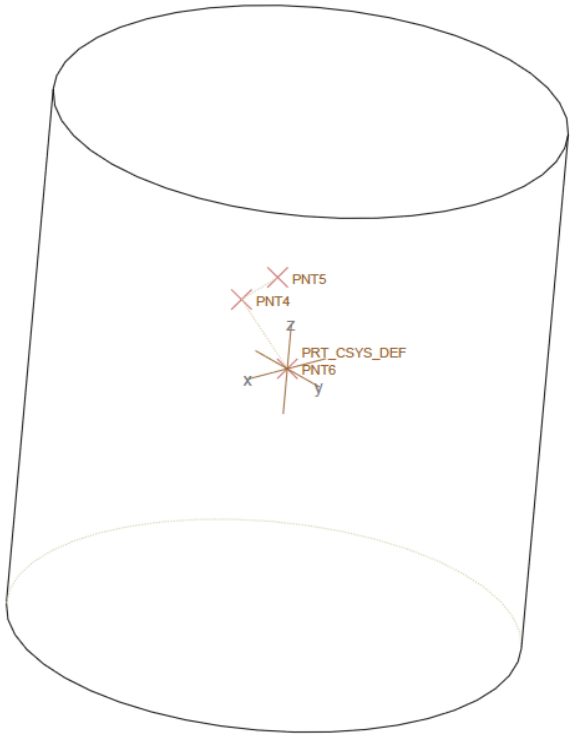

Figure 3.15 In-cylinder velocity vector

As shown in Figure 3.16, the air mass flow rate through the intake ports is independent of the number of intake ports when the port width ratio is kept constant. For a given swirl orientation angle, the swirl ratio decreases slightly as the number of

ports is reduced. That is, a higher swirl ratio can be obtained with a larger number of narrower ports due to high flow velocity and better swirl quality as shown in Figure 3.17.

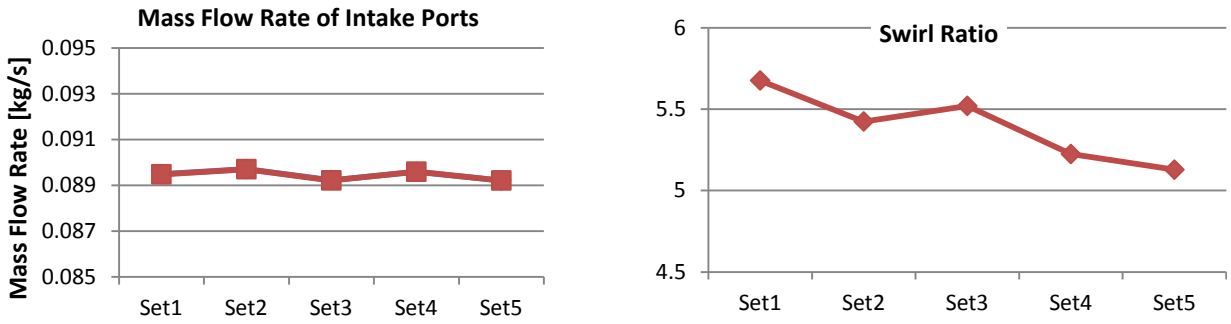

Figure 3.16 Mass flow rate of intake ports and swirl ratio

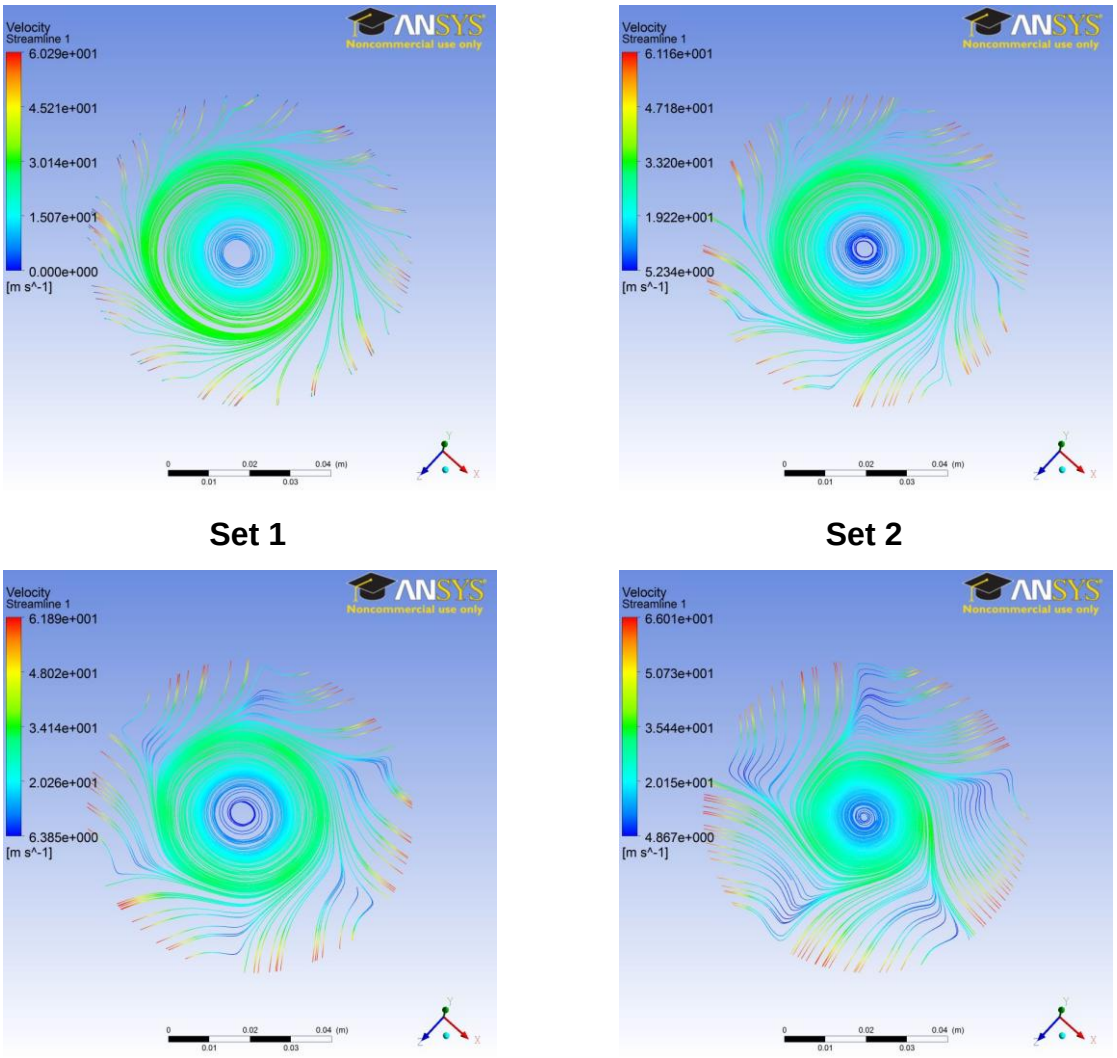

Figure 3.17 In-cylinder flow field

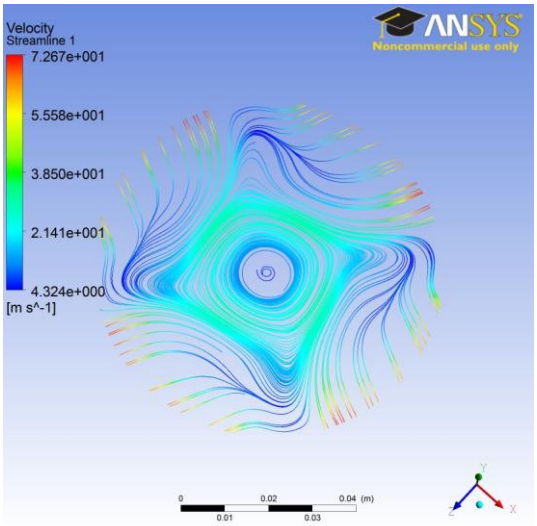

Set 5

Figure 3.17 (cont.) In-cylinder flow field

One of the advantages of uniflow scavenging method is its ability to generate strong swirling flow in the cylinder by optimising the intake ports swirl orientation angle φ_p. Table 3.3 shows the 6 different sets of intake configurations used to investigate the effect of intake ports swirl orientation angle φ_p.

Table 3.3 Swirl orientation angles φ_p

Setting	SET 1	SET 2	SET 3	SET 4	SET 5	SET 6
r_{cy} [mm]	80	80	80	80	80	80
r_p [mm]	20	30	40	50	60	70
φ_p [°]	4.43	11.98	19.95	28.64	38.54	51.00
θ_p [°]	20	20	20	20	20	20
θ_b [°]	10	10	10	10	10	10
x_b [mm]	13.94	13.94	13.94	13.94	13.94	13.94
x_p [mm]	27.70	27.18	26.12	24.39	21.73	17.49
N	12	12	12	12	12	12
A_i [°]	60	60	60	60	60	60
C_{pb}	1.73	1.70	1.63	1.52	1.36	1.09

As shown in Figure 3.18, when the swirl orientation angle is increased from 4.43º in Set 1 to 51 º in Set 6, the delivery ratio drops gradually from 2.4 to 1.9 whilst the port width ratio has to be reduced to achieve the increased swirl orientation angle. Figure 3.19 shows that a larger swirl orientation angle produces a greater swirl ratio.

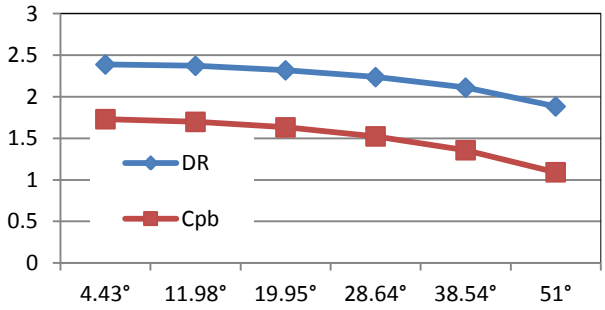

Figure 3.18 Delivery ratio and port width ratio

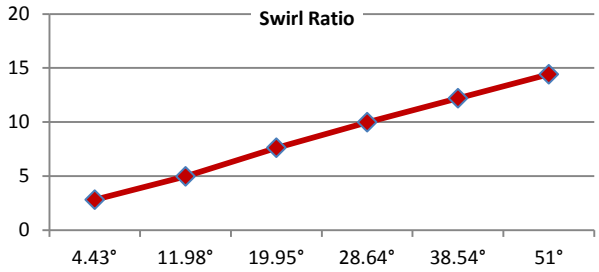

Figure 3.19 Swirl ratio vs. swirl orientation angle

As shown in Figure 3.20, the best scavenging performance is obtained with a swirl orientation angle of 20°. Scavenging and trapping efficiency decreased when the swirl orientation angle being less than 20°. Although delivery ratio increases, however, due to the air short circuiting effect, the trapping efficiency still decreased. When the swirl orientation angle becomes greater than 20°, the scavenging performance also decline because of the reduction in the delivery ratio.

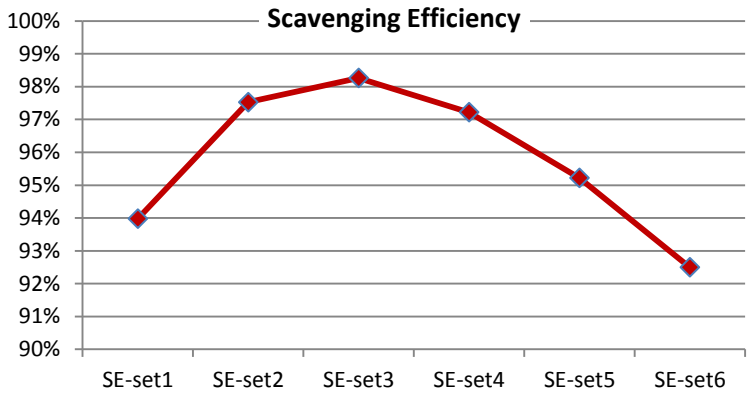

Figure 3.20 Scavenging performance vs. swirl orientation angle

Therefore, the 60° axis inclination angle and 20° swirl orientation angle design has been adopted as the optimised angle for the subsequent 3D flow analysis.

3.5 Fuel injection and in-cylinder mixing

A series of 3D CFD simulations has been carried out to investigate the fuel injection and its effect on in-cylinder air/fuel mixture formation. The initial conditions of the in-cylinder flow field are the same as the condition in previous gas-exchanging process simulations. The location of the injector is based on the setup in the experimental engine. A Siemens outward open piezo DI gasoline injector with a 90º spray cone angle was adopted and its details are shown in Figure 3.21.

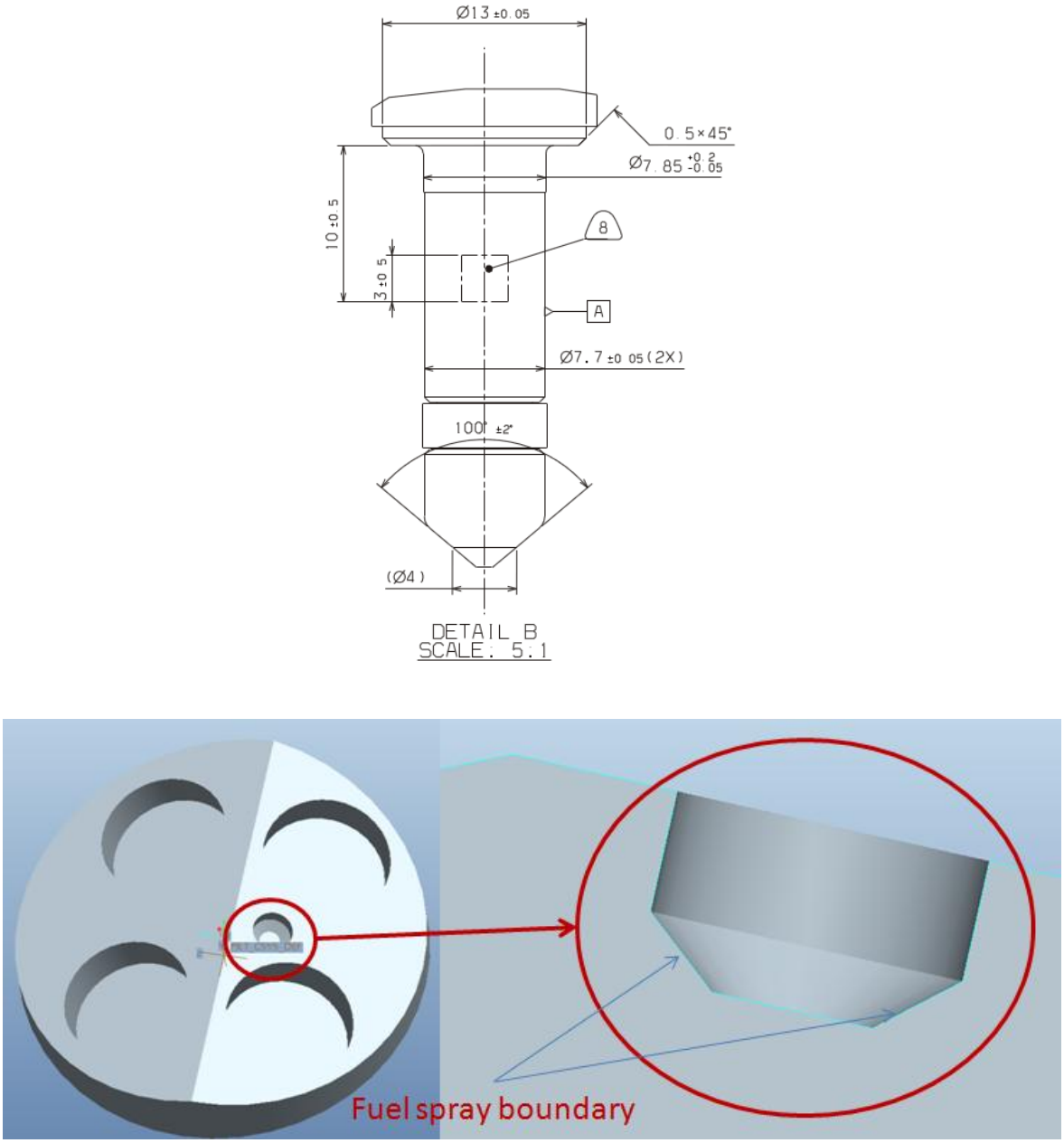

Figure 3.21 DI injector geometry

The injection simulation starts after the gas-exchange process when all ports and valves are closed. An initial in-cylinder swirl is generated during the gas-exchanging process with a swirl ratio of 17.93.

The Discrete Phase Model (DPM) is used to simulate the fuel injection process. The injected fuel is treated as particles and droplet breakup calculation is included to model the atomisation process. The injector tip has a 4.0mm protrusion. The fuel delivery mass flow rate is set to 0.035kg/s and initial injection velocity is 200m/s.

In order to consider the movement of the piston and exhaust valves, a layering dynamic mesh is applied. The hex/wedge type grid with 1~2mm internal grid size is used in the CFD calculations.

3.5.1 Single injection

For single injection cases, the injection duration is set to 30° CA at 4000rpm. The in-cylinder evaporated fuel mass is also recorded, as shown in Figure 3.22.

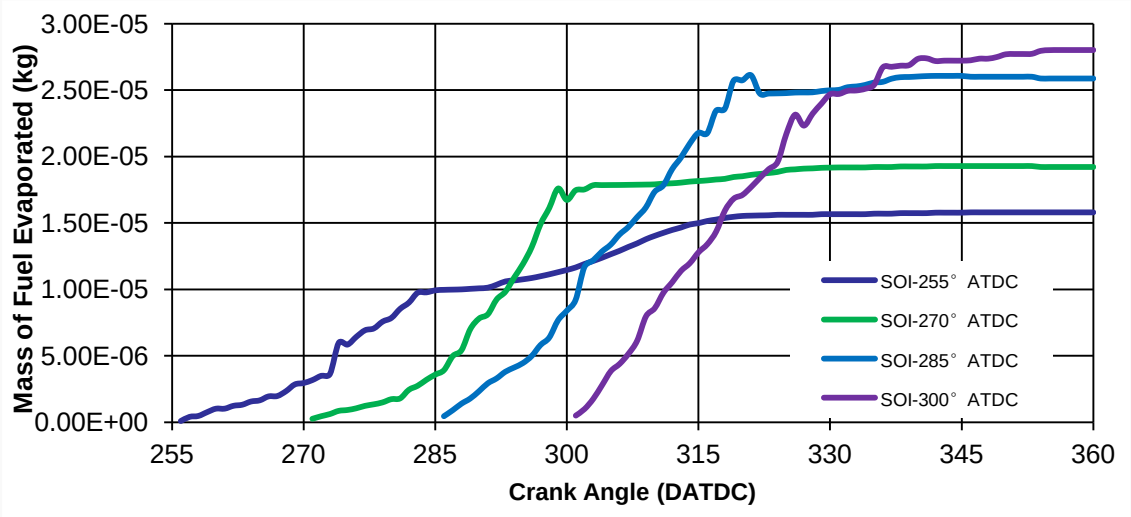

Figure 3.22 Mass of Evaporated Fuel

In all cases, the speed of fuel evaporation increases during the injection process. After the end of injection, the liquid fuel evaporating speed slows down. Faster fuel evaporation takes place at retarded injection due to higher charge temperature.

The main cause for the less total fuel vapour from the early injection cases is the fuel film effect. Because of the in-cylinder swirl and lower charge density during the earlier injection, the fuel spray has more chance to reach the cylinder wall and form a liquid fuel film there, as shown in Figures 3.23 and 3.24.

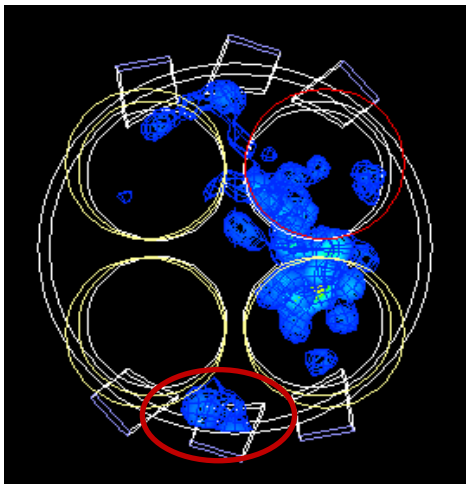

Figure 3.23 The liquid fuel distribution

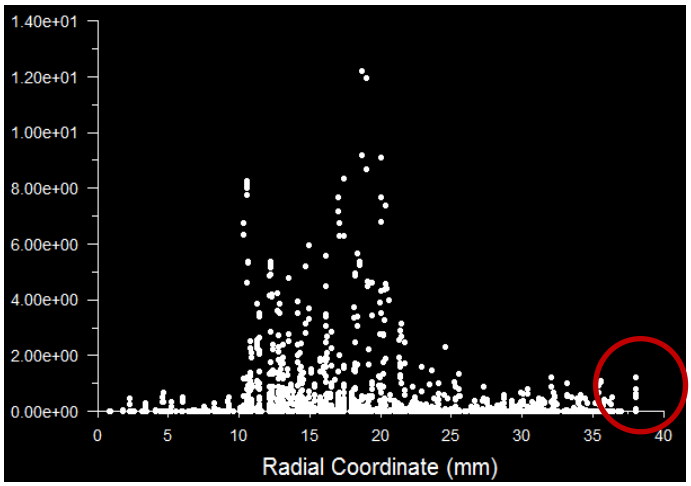

Figure 3.24 Liquid fuel location against radial coordination of CFD model

3.5.2 Split Injections

To improve the fuel injection and mixing quality, split injection simulation was then carried out.

First, a simulation was performed to investigate the difference in performance between single injection and split injection. The injection timing is shown in Figure 3.25. When a single injection is used, the injection starts from 240°ATDC and lasts for 30°CA. During the split injection operation, fuel is delivered in two injections of 15°CA duration each. The dwell angle between the two injections is set to 10°CA. The initial in-cylinder condition is the same as the single injection operation with an initial swirl ratio of 17.93.

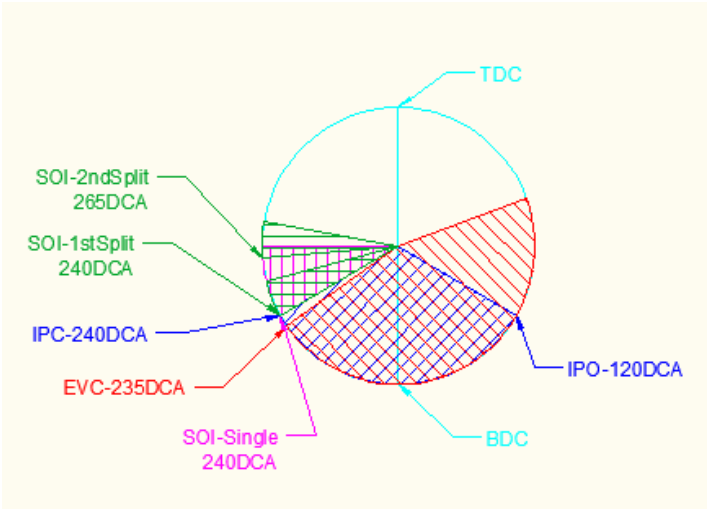

Figure 3.25 Injection Timing Sequence

As shown in Figure 3.26, the overall fuel evaporation is improved by the split injection. Due to reduced momentum of each injection of shorter duration, there is less chance for the liquid fuel to reach the piston, resulting in a more homogeneous mixture.

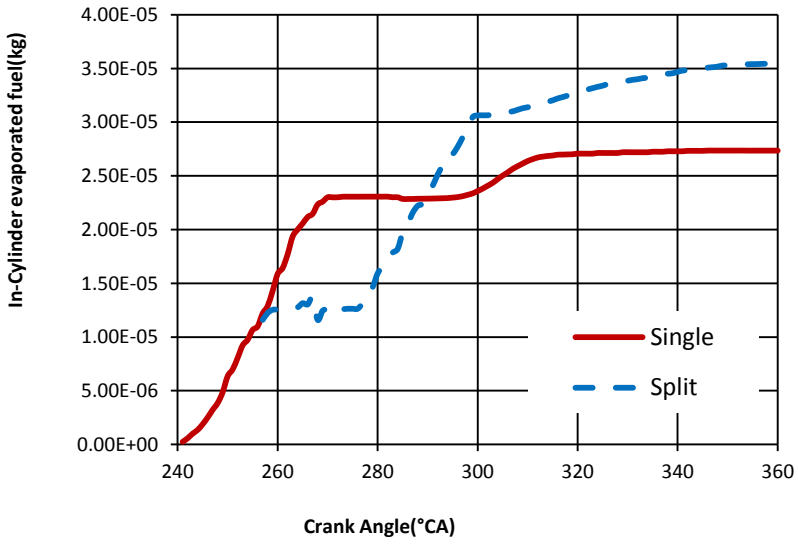

Figure 3.26 Injection Timing Sequence

Since early injection has more chance to produce the fuel film, the effect of first injection quantity has also been studied. As Figure 3.27 shows, the total fuel evaporation is improved as the percentage of the first injection is reduced from 50% to 20% despite the drop in fuel evaporation rate in the first injection.

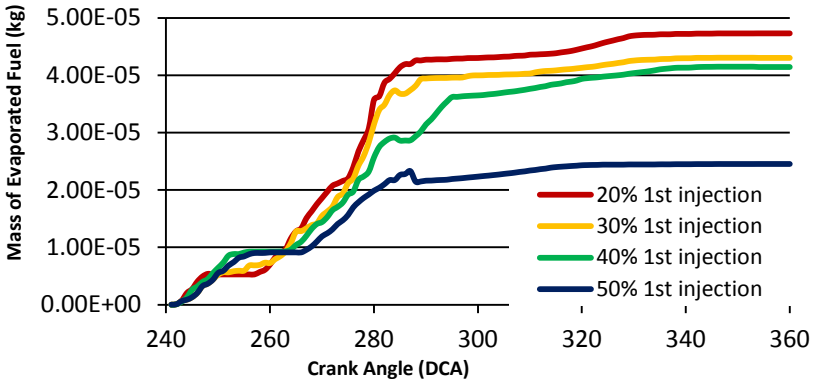

Figure 3.27 Mass of Evaporated Fuel

Figures 3.28 and 3.29 show that both the liquid fuel volume and droplet number increase as the 1st injection rate increases from 20% to 40%. As the first injection is increased to 50%, the liquid fuel volume is still increasing but the droplet number decreases sharply due to the presence of bigger droplets.

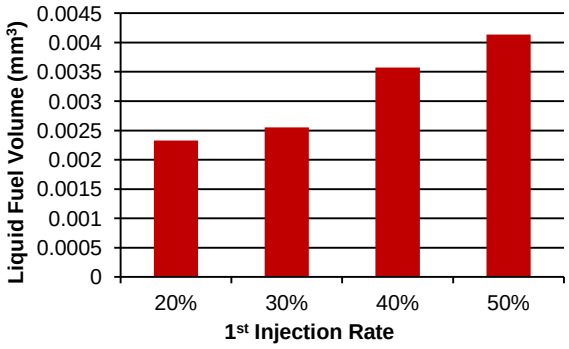

Figure 3.28 Liquid Fuel Volume

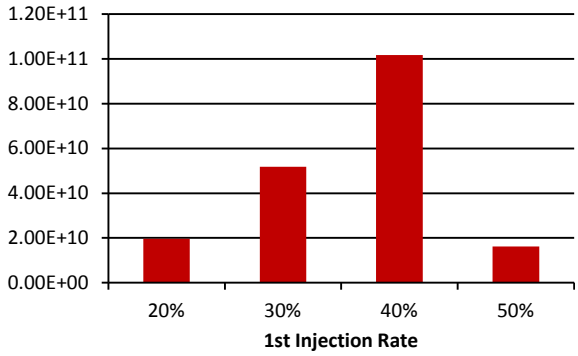

Figure 3.29 Liquid Droplet Number

In conclusion, split fuel injection improves the air/fuel mixing performance by increasing the evaporated fuel quantity. However, the higher ratio of fuel delivered by the 1st injection may cause less fuel evaporated, when the ratio goes up to 50%, big size droplets may appear in the cylinder chamber, and there is higher chance to cause higher emission.

3.6 Summary

This chapter focuses the CFD simulation of the engine breathing and fuel injection process. A 2D base model was initially used to investigate the axis inclination angle of intake port. Then a 3D base model is set up and applied to the optimisation of

intake port swirl orientation angle and the port number. The injector feature was then applied to the model. Finally the fuel injection strategy was investigated and the split injection was shown to improve the fuel evaporation and mixture quality.

Chapter 4 Prediction of the Uniflow 2-Stroke Engine Performance

4.1 Introduction

Although 3D CFD simulation is able to provide a wide range of information on engine performance on a three-dimensional basis, 1D simulation is still used for engine performance prediction because of its advantages of fast computation, high flexibility, and adaptability of the model for the complete range of engine operation points.

For most of the cases in engine research, the 1D simulation code is developed precisely for engine performance prediction. The code must be able to provide a fully integrated treatment of time-dependent fluid dynamics and thermodynamics by means of a one-dimensional formulation which enables performance simulations on dynamics of pressure waves, mass flows, and energy losses in ducts, plenums, and the manifolds of various systems.

A 1D thermo-fluid dynamic numerical code has been applied to the modelling of a modern four-cylinder, turbocharged Diesel engine [63]. The results of average quantities and the pressure pulsations along the ducts, the transient response of the engine and the EGR system performance has been analyzed and resulted in satisfactory agreement with measured data for every operating point considered, showing the good quality of the 1D modelling. Research work has also been dedicated to the development and validation of an advanced 1D thermo-fluid dynamic model for the simulation of a single cylinder hydrogen SI engine [68]. The comparison between measurements and computations of this research work has pointed out a satisfactory agreement for most of the operating points considered, with a good reliability of the adopted models in the studied range of operating conditions and engine configurations.

The comparison between measurements and computations of this research work has pointed out a satisfactory agreement for most of the operating points considered, with a good reliability of the adopted models in the studied range of operating conditions and engine configurations.

The model and simulation environment for the work described in this article is RICARDO WaveBuild 8.3.2. WAVE is the 1D gas dynamics and engine simulation software package. It is a computer-aided engineering code developed to carry out simulations based on virtually any intake, combustion and exhaust system configuration.

4.2 1D Engine Model Setup

WAVE is a 1D gas dynamics and engine simulation software package and is capable of analyzing the dynamics of pressure waves, mass flows, and energy losses in ducts, plenums, and the manifolds of various systems and machines. It provides a fully integrated treatment of time-dependent fluid dynamics and thermodynamics by means of a one-dimensional formulation which enables performance simulations to be carried out based on virtually any intake, combustion and exhaust system configuration [68].

Three baseline engine models were created, including a 1.6L naturally aspirated 4-stroke engine, a 2-stroke 3-cylinder model and a 2-stroke 2-cylinder model respectively shown in Figure 4.1. The 4-stroke engine was chosen as the bench mark for the other uniflow 2-stroke engines.

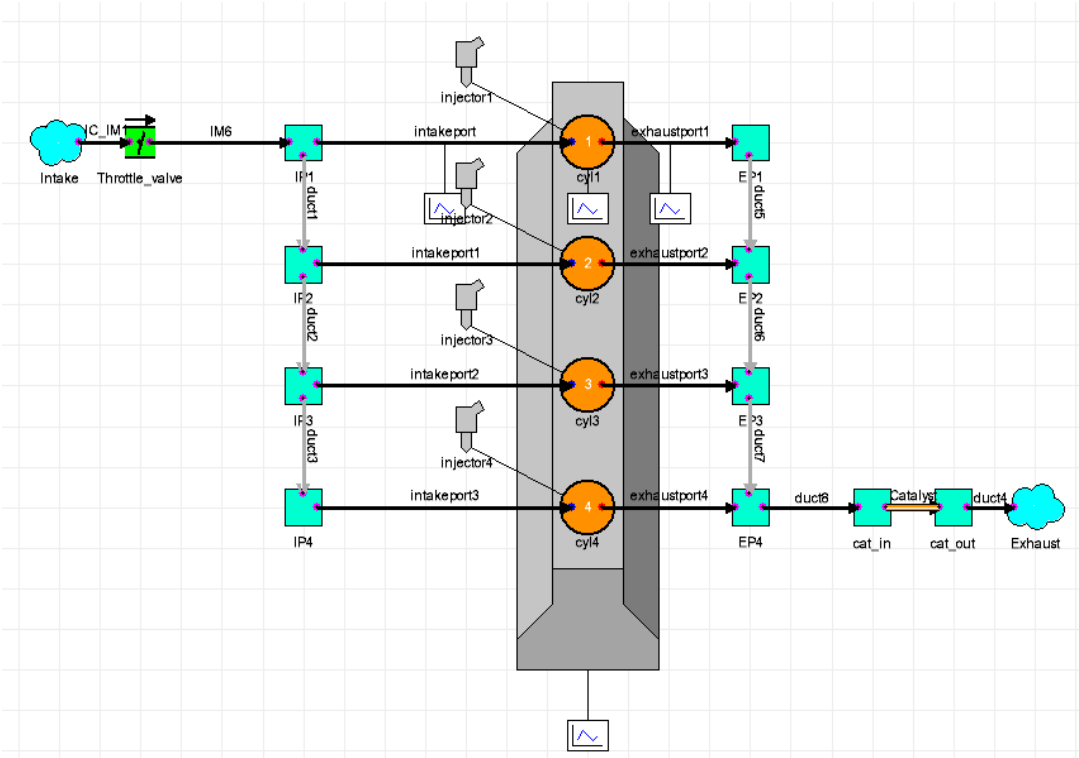

1.6L 4 –stroke NA engine model

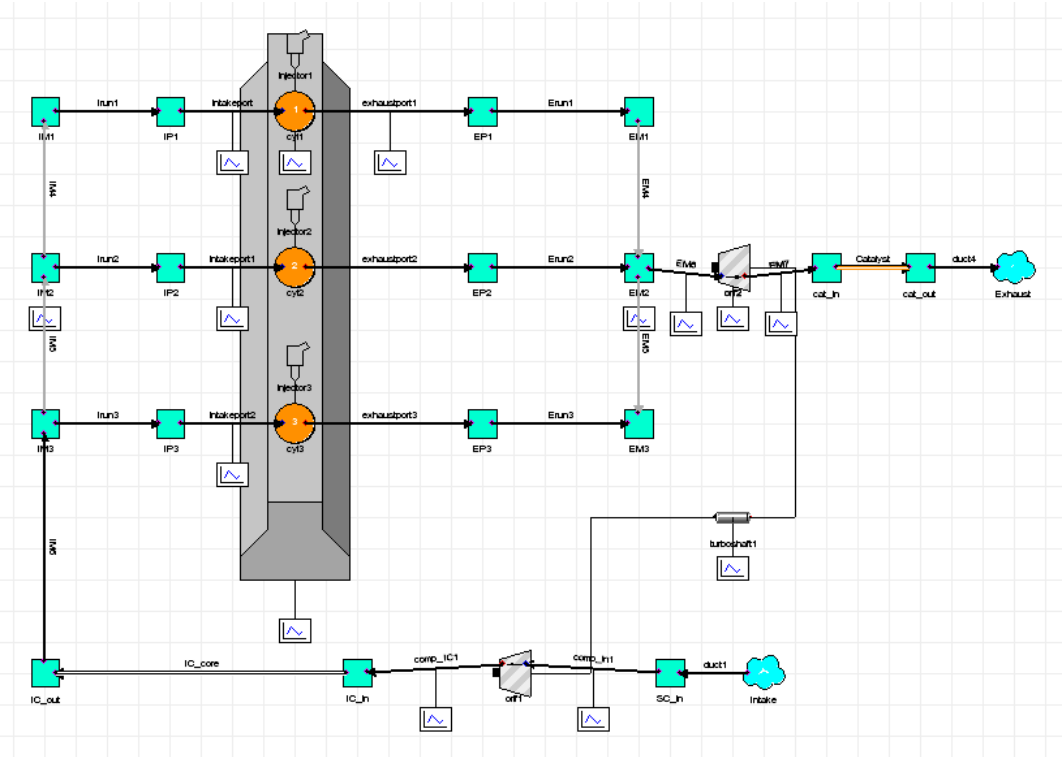

2-stroke 3-cylinder engine model

Figure 4.1 Baseline 1D engine models

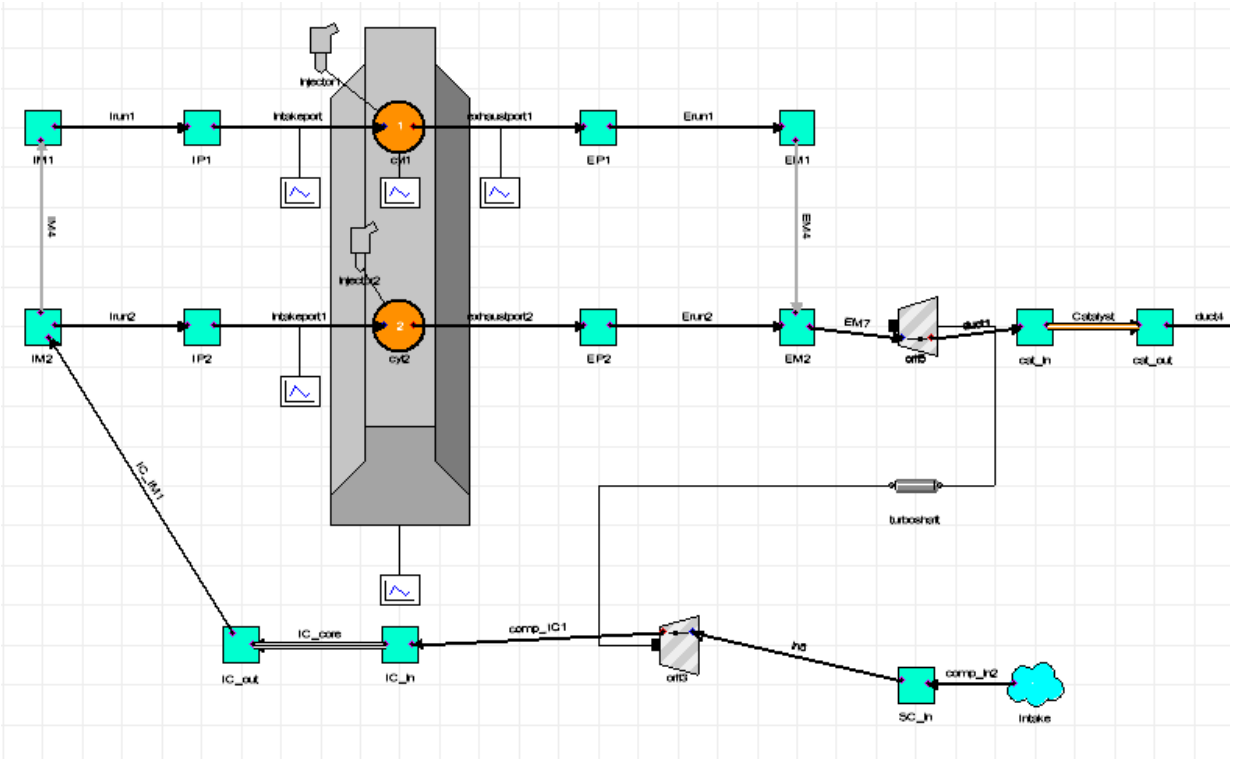

2-stroke 2-cylinder engine model

Figure 4.1 (cont.) Baseline 1D engine models

Each engine model comprises

- Inlet environment boundary
- Intake system
- Engine body
- Boost system
- Exhaust system
- Outlet environment boundary

In this case, both inlet and outlet environment is set to be ambient at 1bar pressure and temperature of 300K. The initial fluid composition is defined as fresh air. The solution type is set to fixed boundary pressure, temperature and composition during the simulation.

For the intake system, a butterfly plate in an orifice is used to represent the throttle as shown in Figure 4.2. The orifice bore diameter is 50mm.Butterfly plate shaft diameter is 6mm.

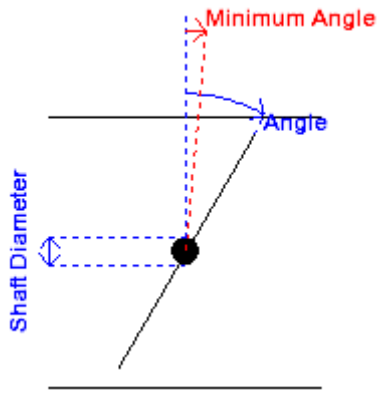

Figure 4.2 Throttle element structure

The intercooler system in the intake system is represented by a long pipe work at the upstream side of intake manifold. The pressure drop along the pipe work is calculated by Equation 4.1

$$\Delta P = U_j * A_j * \Delta x * R \qquad \text{[E-4.1]}$$

Where

ΔP – Pressure drop along the pipe

U_j – Velocity at the cell centre

A_j – Area at the cell centre

Δx – Length of the cell

R – Resistivity of the absorptive material

And the heat transfer between the pipe wall and the inner gas is calculated by Equation 4.2.

$$\mathrm{Q} = C_{ht} * h * SA_{wall} * (T_{wall} - T_{gas}) \qquad \text{[E-4.2]}$$

Where

Q – Heat transfer between pipe wall and inner gas

C_{ht} – Heat transfer multiplier constant

h – Heat transfer coefficient

SA_{wall} – Wall surface area

T_{wall} – Wall temperature

T_{gas} – Inner gas temperature

The heat transfer coefficient is calculated by

$$h = \frac{k_c}{d} * 0.647 {R_e}^{0.574} * {P_r}^{1/3} \quad \text{[E-4.3]}$$

Where

k_c – Conductivity of the wall

d – Feature diameter of pipe wall

R_e – Reynolds number

P_r – Prandtl number

Engine body element defines the main engine configurations, such as engine bore, stroke, cylinder number, firing sequence etc., and governs main calculations on performance, such as friction losses calculation, scavenge governing profile combustion model and etc. Also the valve lift profile and flow coefficient are defined in the engine body element.

In the 4-stroke engine, the engine breathing model is defined and calculated by the flow through the valves. In the case of the uniflow 2-stroke model, the gas exchange and scavenging processes are defined by the flow coefficient of exhaust valves and a pseudo intake valve, and a scavenge profile model.

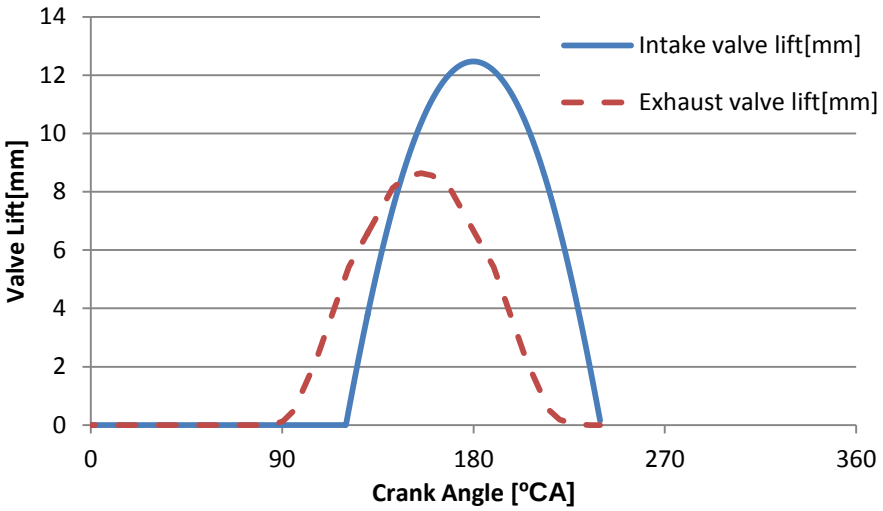

Figure 4.3 Base valve lift profile of uniflow 2-stroke engine model

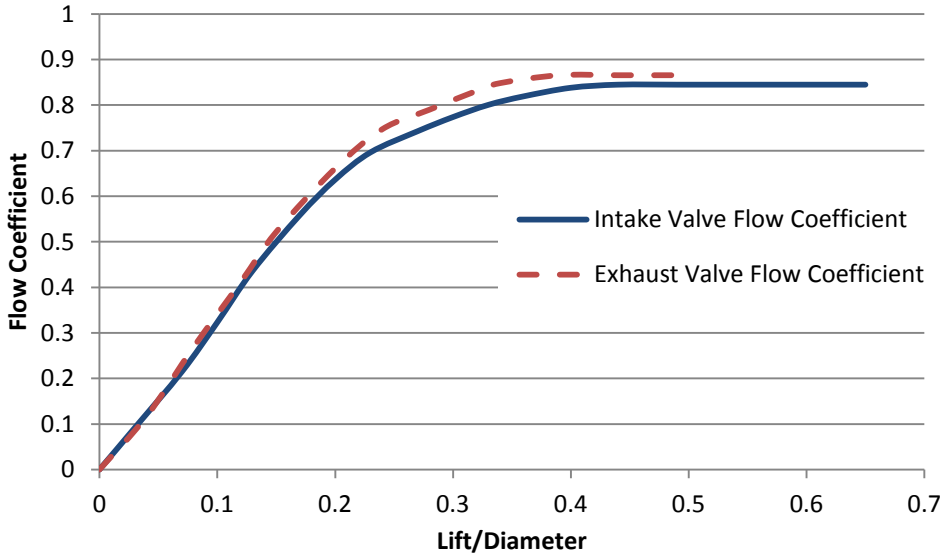

Figure 4.4 Valve flow coefficient of uniflow 2-stroke model

As shown in Figure 4.3, the lift profile and timing of the pseudo intake valve is specified according to the port geometry and its relative location to the piston. The flow coefficient of the gas flow through the valves is calculated as follows,

$$C_f = {A_{eff}}\Big/{(\pi DL)} \qquad \text{[E-4.4]}$$

Where

C_f – Flow coefficient

A_{eff} – The effective area of the valve

D – Valve reference diameter

L – Valve lift

By setting the engine and valve configuration to the same as the 3D CFD calculation model, the flow coefficient can be calibrated. The flow coefficient calibrated and applied in the uniflow 2-stroke engine model is shown in Figure 4.4.

The scavenge model is based on tracking of residual and fresh mass in the cylinder. At EVO, the entire contents are initialized to residual mass, and as fresh charge enters, the incoming mixture is counted as the fresh mass. The scavenge model contains a thermal mixing model that assumes that the fresh gas will gradually mix with the exhaust gas during the scavenging event. It is set to heat up the fresh gas to the cylinder-average gas temperature as the mass in the fresh zone reaches 100% of the cylinder contents. The scavenging curve represents the instantaneous composition flowing through the exhaust valve as a function of instantaneous in-cylinder composition. The scavenge curve is shown below in Figure 4.5. BR (COMBUSTION CHAMBER) represents the burned mass fraction of the cylinder contents, it will be 1.0 after combustion (100% combustion products) and decreases toward zero as fresh air enters during the intake process. BR (EXHAUST STREAM) is the instantaneous composition of the flow through the exhaust valve. When the composition of the cylinder is 100% combustion products, the exhaust stream must also be 100% products. Likewise, if the cylinder contains 100% fresh air, the exhaust stream must also be 100% fresh air. Therefore, any scavenging curve must move from the top right corner (1.0, 1.0) to the lower left corner (0.0, 0.0) of the profile. Between these points, the curve can take any shape. When BR (EXHAUST STREAM) is 1.0 according to the scavenging curve, perfect displacement scavenging is occurring, fresh air entering the cylinder pushes out exhaust gases, while no fresh air leaks out of the cylinder. When BR (EXHAUST STREAM) is 0.0, complete short-circuiting is occurring, any exhaust gas in the cylinder is trapped while fresh air blows out the exhaust valve. When BR (EXHAUST STREAM) equals BR (COMBUSTION CHAMBER), a perfectly mixed scavenging is occurring: the exhaust stream has the same composition as the combustion chamber's average contents [68].

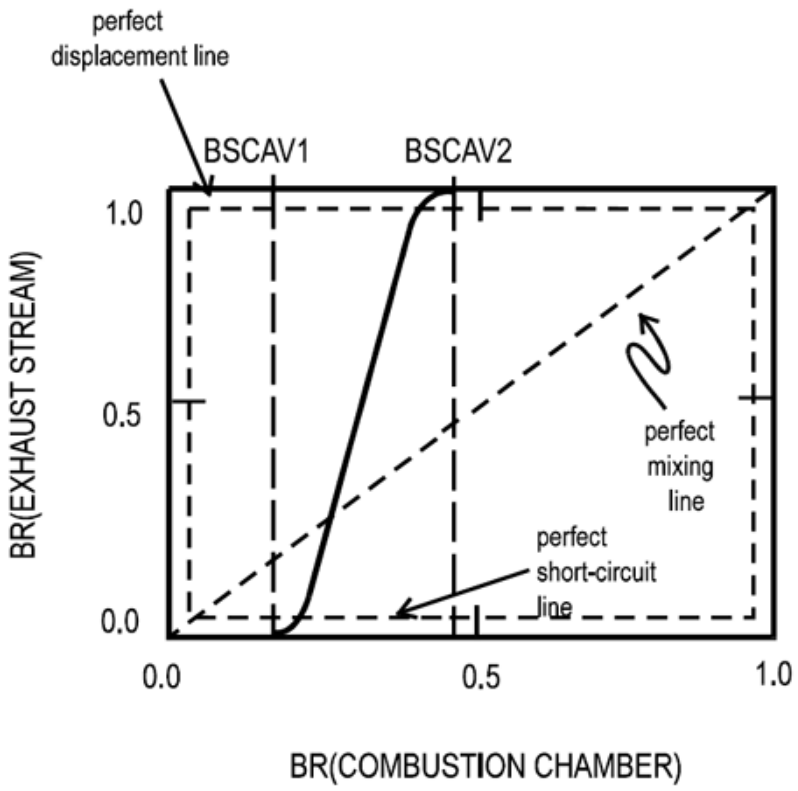

Figure 4.5 Scavenge profile

After the flow coefficient applied, a single cylinder model has been used for a simulation with same engine configuration as the 3D CFD model. The gas-exchange performance has been compared and validated between 1D and 3D mode. As shown in Figure 4.6, there is good agreement between 1D and 3D models. In most cases, the differences are less than 5%. The maximum difference of 8.93% appears with the trapping efficiency at 2000rpm but the absolute difference is rather small. Thus, 1D calculations of gas-exchange and scavenging performance are considered to be acceptable.

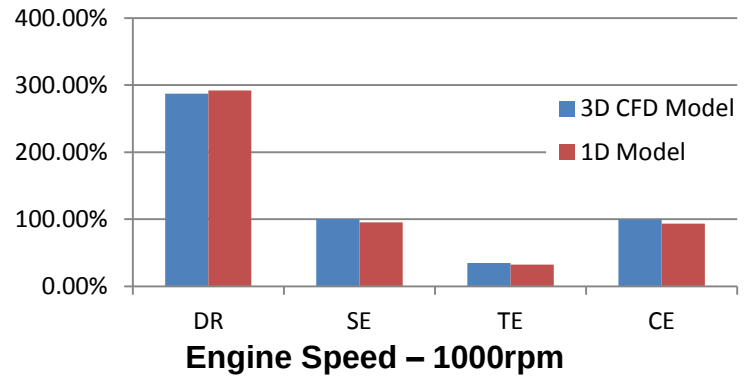

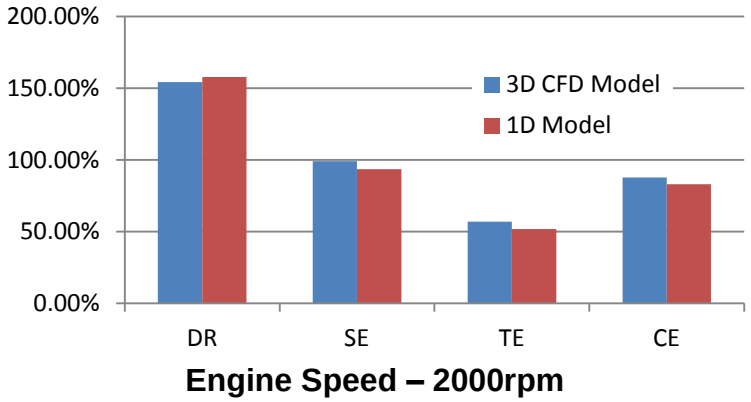

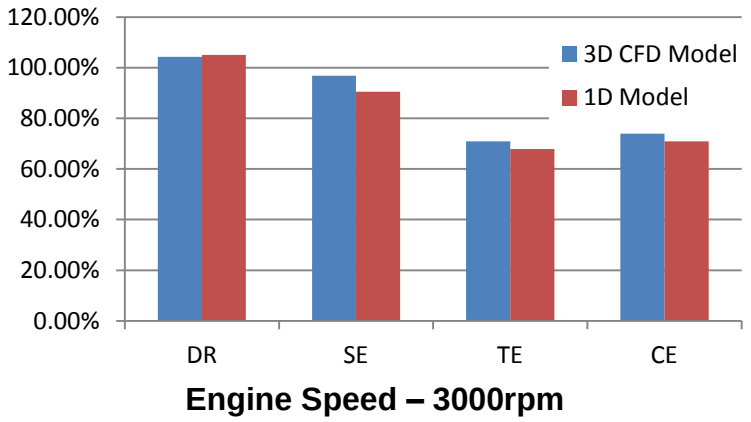

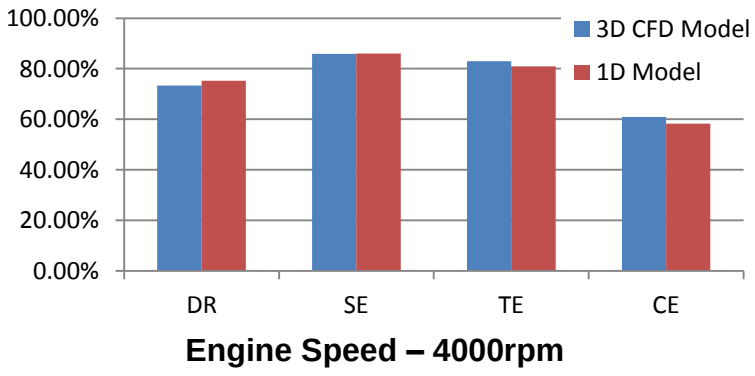

Figure 4.6 Gas-exchange performance of 3D and 1D models

The Wiebe function is used to describe the heat release process of combustion. This relationship allows the independent input of function shape parameters and of burn duration. It is based on calculation of the cumulative mass of burned fraction [68]

$$MBF = 1 - \exp\left(-C_{cb}\left({}^{\theta}/_{T_{cb}}\right)^{(C_{wb}+1)}\right) \qquad \text{[E-4.5]}$$

Where

C_{cb} – Internally calculated parameter to allow $\mathrm{T_{cb}}$ covering the range of 10%-90%

T_{cb} – Combustion duration (10%-90%)

θ – Degrees past start of combustion

C_{wb} – The exponent in Wiebe function

Since the calculation of the brake engine output needs to take into account of frictional losses, the engine friction model in the 1-D engine simulation model was set up and calibrated. Calculation of the frictional losses is based on Flynn-Chen model [70],

$$FMEP = A_{cf} + \frac{1}{ncyl}\sum_{i=1}^{ncyl}\left[B_{cf}\left(P_{cyl}\right)_i + C_{cf}\left(S_{fact}\right)_i + Q_{cf}\left(S_{fact}\right)_i^2\right] \qquad \text{[E-4.6]}$$

Where $S_{fact} = RPM * stroke/2$

P_{cyl} – Peak in-cylinder pressure

$A_{cf}, B_{cf}, C_{cf}, Q_{cf}$ – Constant used to replicate the FMEP values determined by engine experiments and then used to calculate FMEP at different load and speeds

The constants, $A_{cf}, B_{cf}, C_{cf}, Q_{cf}$ in Equation 4.6 were determined based on the engine friction data of Mahle I3 DI gasoline engine, which represents one of the most advanced boosted DI gasoline engines, because this engine has similar configurations with the 2-stroke engine model. In order to determine the constants in Flynn-Chen model, a quadratic curve was created according to Equation 4.6, the experimental data of the Mahle I3 DI gasoline engine such as engine speed, peak in-cylinder pressure and etc. were imported, by solving the quadratic functions with

experimental data, the constants in Flynn-Chen model were determined. The calibration results are shown in Figure 4.7 with values of $A_{cf}, B_{cf}, C_{cf}, Q_{cf}$ is given in 0.35bar, 0.005, 10pa.min/m and 6pa.min^2/m^2 respectively.

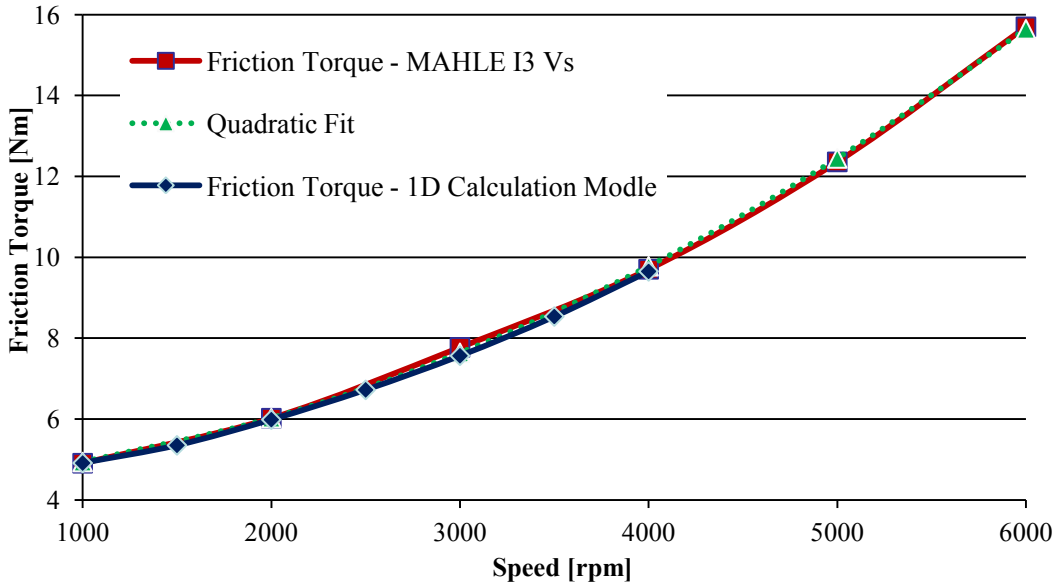

Figure 4.7 FMEP calibration of 2-stroke engine model

4.3 1D Engine Simulation Results

The fuel mass flow rate of the 1D model was calculated according to the stoichiometric air to fuel ratio of 14.7:1. In the spark ignition Wiebe heat release model, the combustion duration (10% to 90% mass fraction burned) was set to 31°CA according to previous simulations. The 50% mass fraction burned angle, CA50º, was varied to control the combustion phase. Figure 4.8 shows the timing sequence of the 2-stroke cycle operation. The intake port opening and closing are represented by IPO and IPC respectively and DIP is the duration of intake ports opening. The exhaust valves open at EVO and closes at EVC. DEV is the duration of exhaust valves opening period. The period between EVO and IPO defines the blow-down duration, BDD. Fuel was injected directly into the cylinder after both the intake ports and exhaust valves were closed to avoid the fuel short-circuiting.

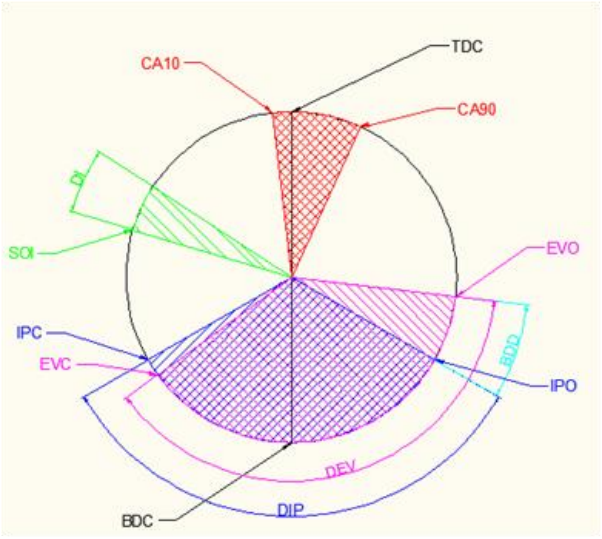

Figure 4.8 The timing sequence of 2-stroke operation

4.3.1 Effect of Engine Geometry on Performance

The previous 3D CFD simulation was focused on the engine breathing performance optimisation and in-cylinder charge flow structure generation in the single cylinder uniflow 2-stroke engine and to be compared with the experimental results. In order to carry out a systematic evaluation of the boosted uniflow 2-stroke engine, 1D simulation has been used to optimise the bore and stroke ratio for maximum engine performance.

The first series of 1D engine performance simulation studies were carried out on a 3-cylinder uniflow 2-stroke engine. The absolute boost pressure was set to 2bar, engine speed at 4000rpm and CA50 at 15°ATDC. The intake port opening (IPO) was set at 90°ATDC and blow-down duration of 60°CA.

The engine delivery ratio, trapping efficiency, and charging efficiency is shown in Figures 4.9 to 4.11. The long engine stroke results in reduced engine delivery ability but higher trapping efficiency because of the longer path of the fresh charge. The charging efficiency is a combination of delivery ratio and trapping efficiency. The higher the charging efficiency, the more power can be produced from the combustion of a larger amount of air/fuel mixture. Thus, according to the charging efficiency results in Fig.4.11, the best performance can be obtained in the engine of a shorter stroke and bigger bore.

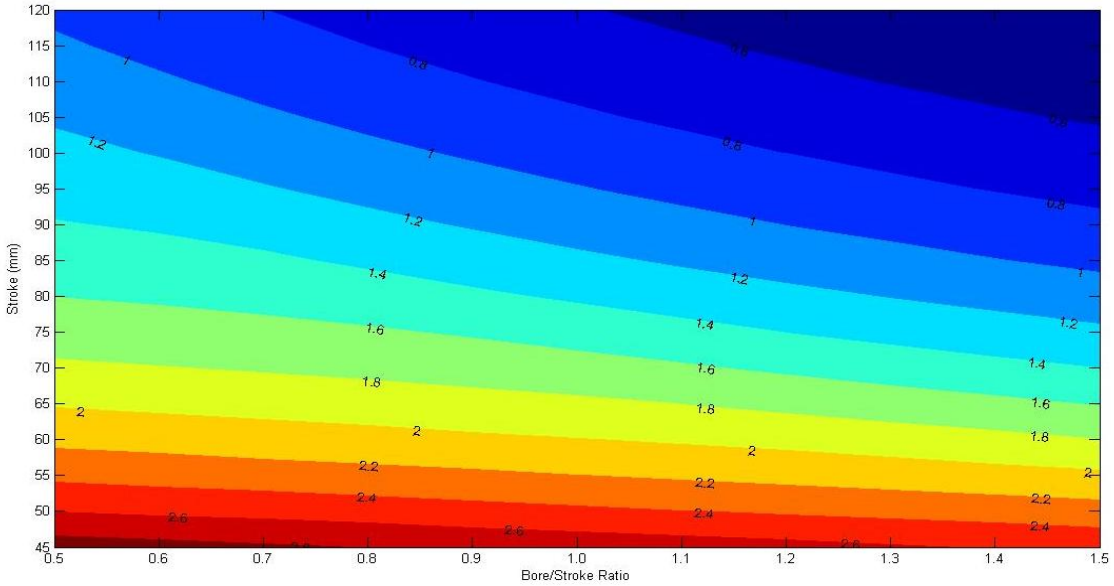

Figure 4.9 Delivery ratio at IPO – 90°ATDC , BDD – 60°CA

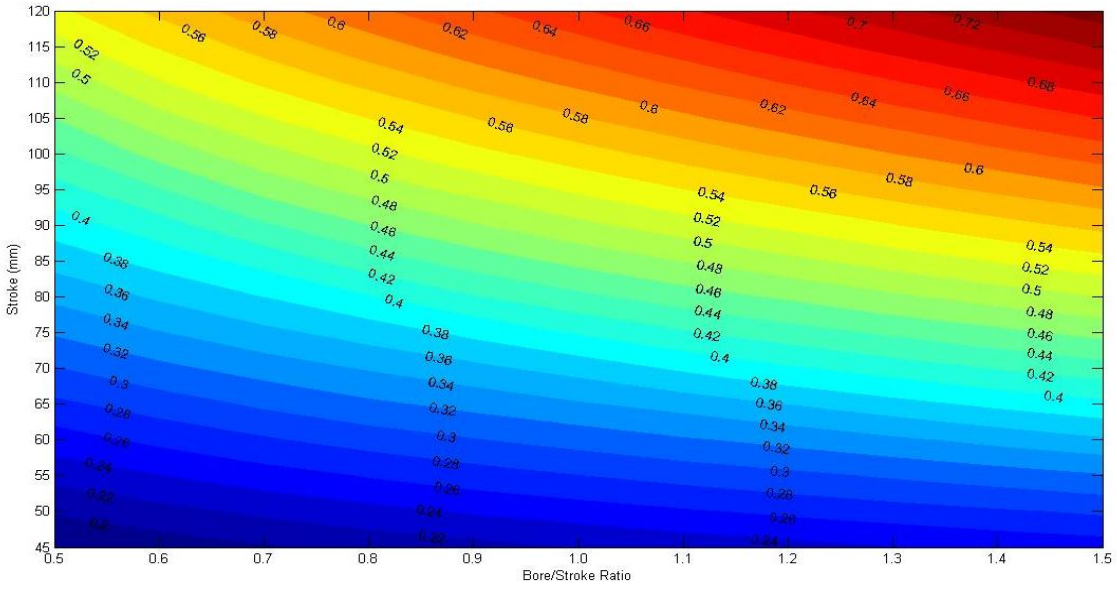

Figure 4.10 Trapping efficiency at IPO – 90°ATDC , BDD – 60°CA

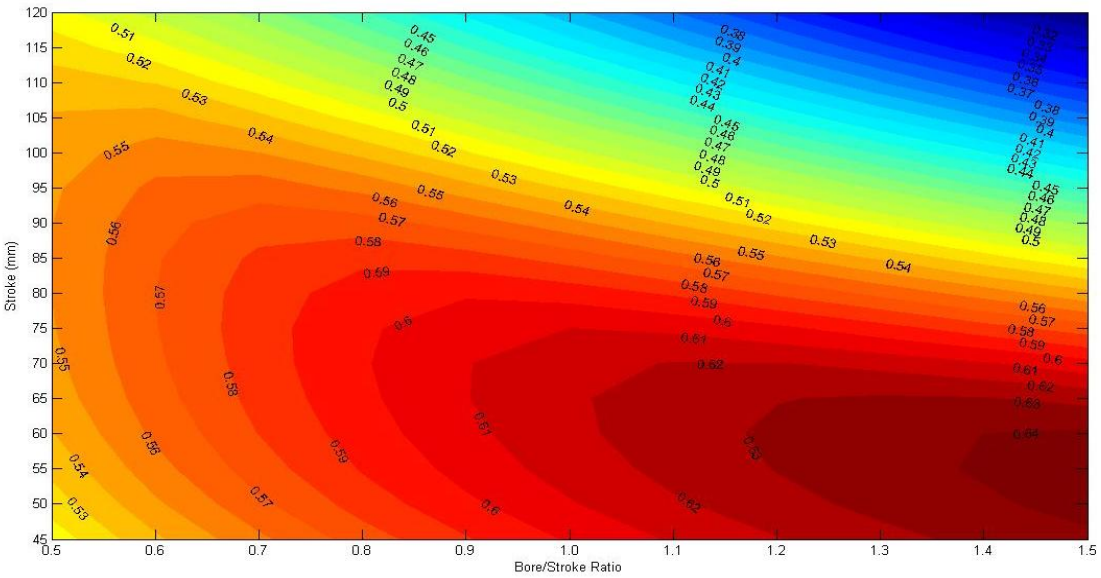

Figure 4.11 Charging efficiency at IPO – 90°ATDC , BDD – 60°CA

As shown in Figure 4.12, at a given stroke of 80mm the highest specific indicated power of the 3-cylinder uniflow 2-stroke engine can reach 78kW/L for larger bore/stroke ratios.

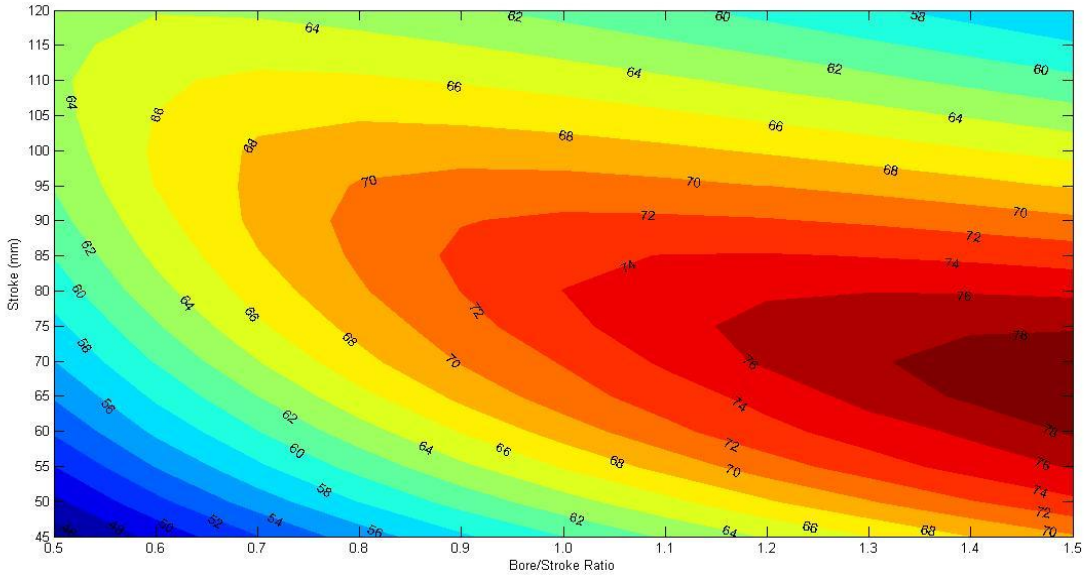

Figure 4.12 Specific indicated power at IPO – 90°ATDC , BDD – 60°CA, CA50 - 15º ATDC

The results in Figure 4.12 can be explained by the trade-off between the scavenging performance and expansion work. For a given bore/stroke ratio and IPO, the shorter stroke results in a reduced intake port opening period and the fresh charge mass

flow rate is insufficient to scavenge the residual gas out of the cylinder, which leads to a relatively low charging efficiency and hence lower power. Conversely, a longer stroke extends the intake opening period and improves the gas-exchange performance. However, with a long intake port opening duration and blow-down duration, the effective expansion stroke is reduced, thus the output power is limited with longer stroke. Therefore, the highest power output is achieved at an intermediate stroke of 80mm.

The combustion phase also has an effect on engine output power. The results shown in Fig.4.12 were obtained with CA50 set to 15º ATDC. When the CA50 was advanced to 5º ATDC (Fig.4.13), the best performance zone was shifted up to an area of longer stroke around 80mm and the bore/stroke ratio of the best performance zone was extended. But the engine peak specific indicated power remained the same.

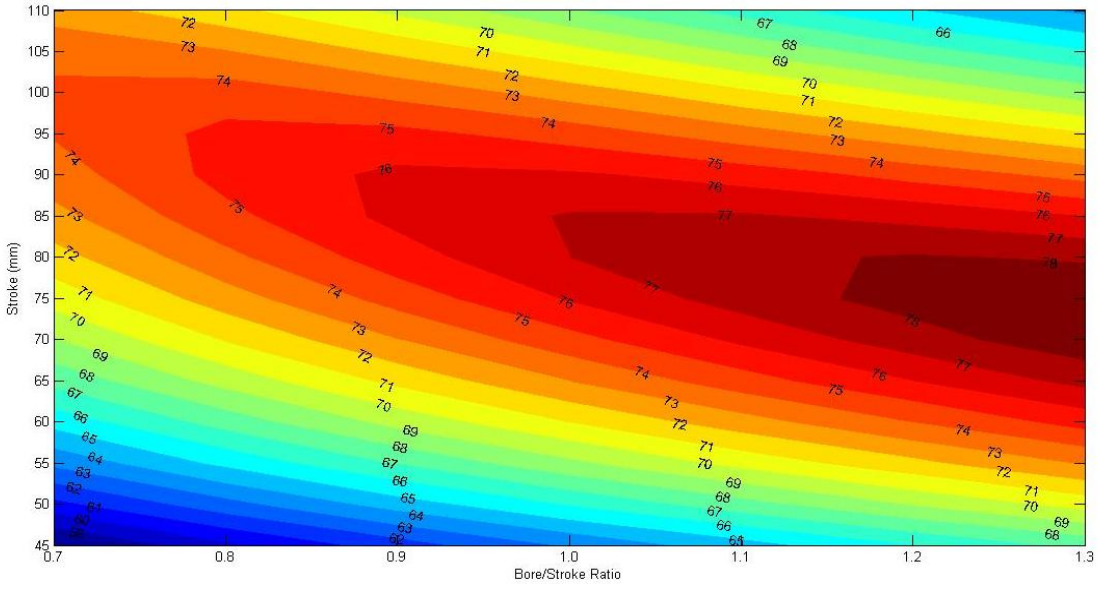

Figure 4.13 Specific indicated power at IPO – 90°ATDC , BDD – 60°CA, CA50 - 5º ATDC

In order to reach the same power output as the 1.6L 4-stroke baseline engine, a higher boost pressure than 2bar would be required. As shown in Fig.4.14, when the boost pressure was increased to 3bar, the peak specific indicated power could reach 121kW/L.

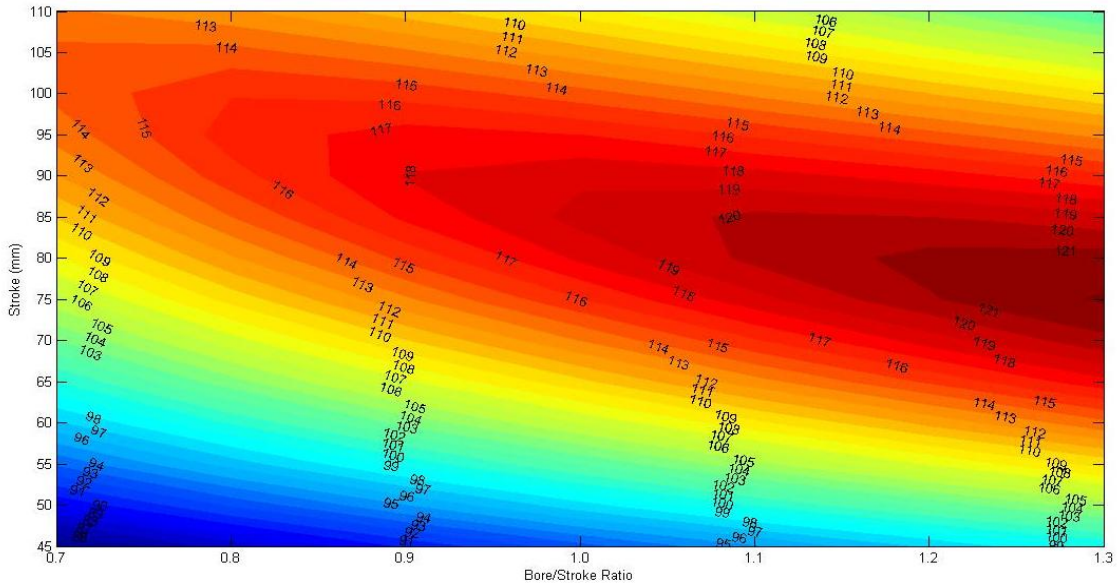

Figure 4.14 Specific indicated power at IPO – 90°ATDC , BDD – 60°CA, CA50 - 5º ATDC

4.3.2 Effect of the Blow-down Duration

The intake port timing is determined by the intake port location in a uniflow 2-stroke engine. For a given intake port design, the intake port timing is fixed. The exhaust valves are driven by a camshaft and can be altered through a variable valve timing device. The optimised exhaust valve timing is a compromise between the gas-exchanging performance and output power. With a longer blow-down duration and hence less air short-circuiting, a higher trapping efficiency can be achieved. However, for a fixed IPO timing, longer blowdown duration means the exhaust valves need to be opened earlier, resulting in less expansion work and output power.

Figures 4.15 to 4.17 show the specific indicated power maps with intake port openings at 110°ATDC, 120° ATDC, and 130° ATDC, respectively. The CA50 was set to 5º ATDC and the intake pressure at 3bar. In light of the higher boost pressure applied, the blow-down duration was reduced from 60°CA to 40°CA for greater expansion work.

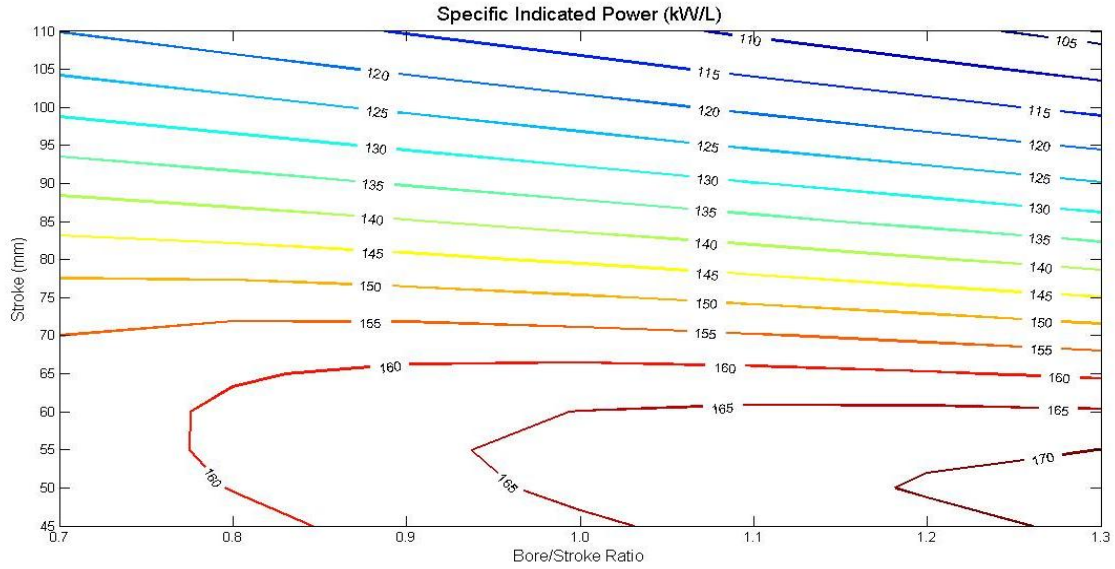

Figure 4.15 Intake port opening - 110°ATDC

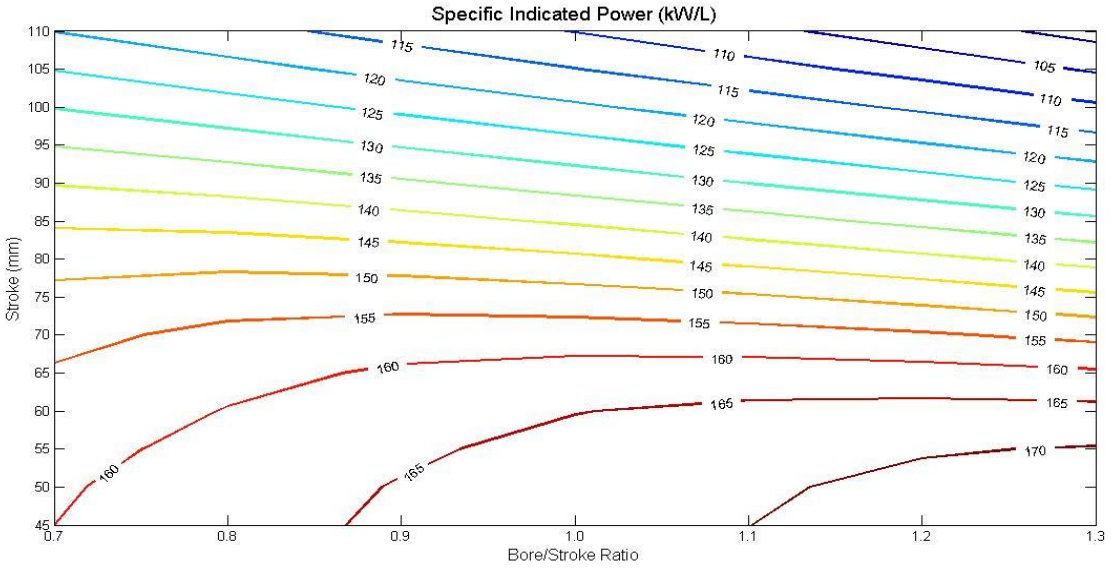

Figure 4.16 Intake port opening – 120°ATDC

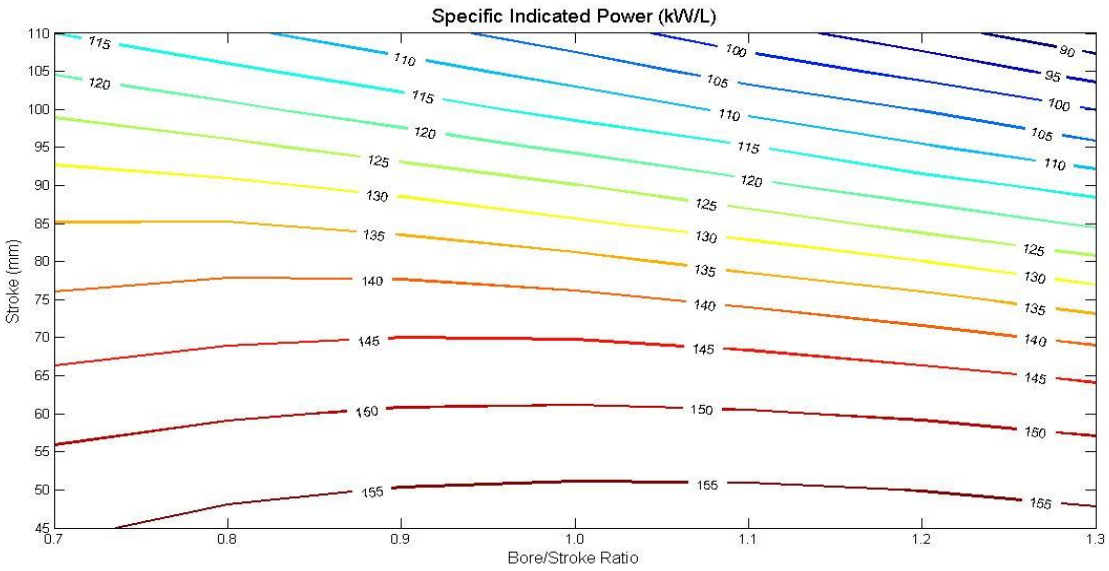

Figure 4.17 Intake port opening - 130°ATDC

It can be seen that the maximum specific indicated power can reach 170kW/L. In the case of IPO at 110°ATDC, the best output performance was achieved with a higher bore/stroke ratio and shorter stroke. As the IPO was retarded to 120°ATDC, the high performance range was extended further, because of the increased effective expansion stroke. When the IPO timing was retarded further to 130°ATDC, the specific indicated power became lower because of the shorter intake port opening duration and hence reduced intake charge mass flow rate.

As the specific indicated power was increased, the corresponding in-cylinder peak pressure became very high. To reduce the peak pressure, the combustion phase was retarded by changing CA50 from 5°ATDC to 15°ATDC. IPO timing was kept at 120°ATDC and blow-down duration of 40°CA. As shown in Figure 4.18, the peak pressure was reduced by 25% with the retarded combustion phasing. As shown in Figure 4.19, the peak cylinder pressure was below 120bar when the specific indicated power was over 160kW/L.

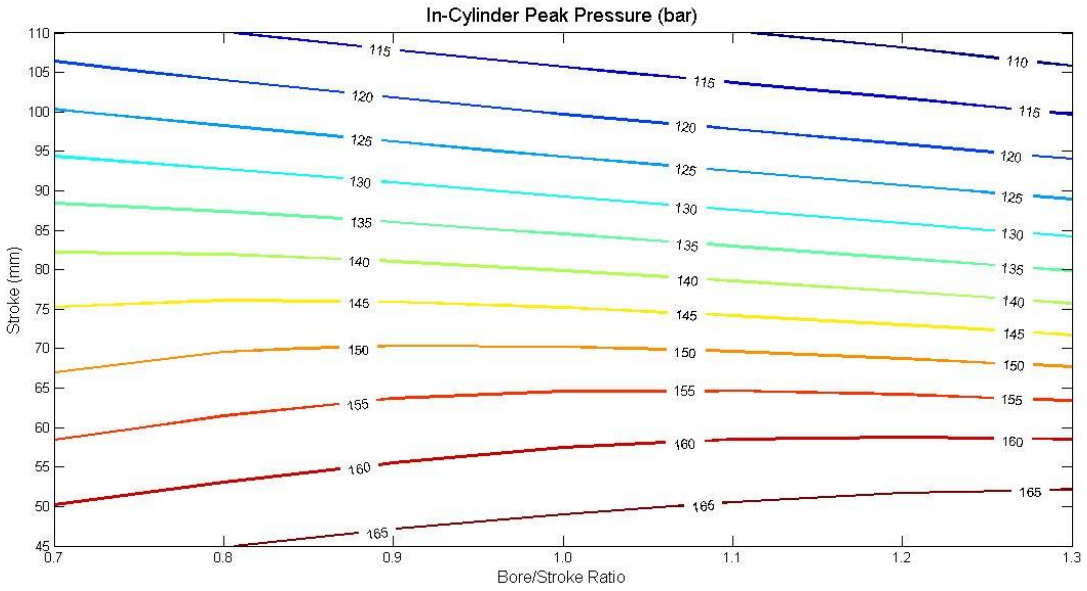

CA50 at 5°CA

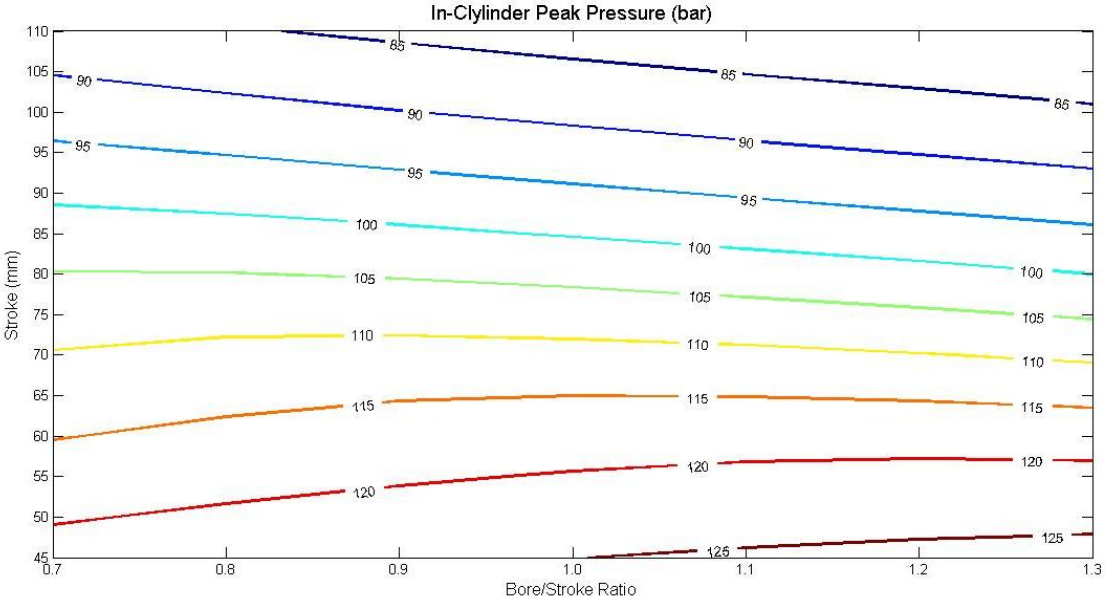

CA50 at 15°CA

Figure 4.18 In-Cylinder Peak Pressure

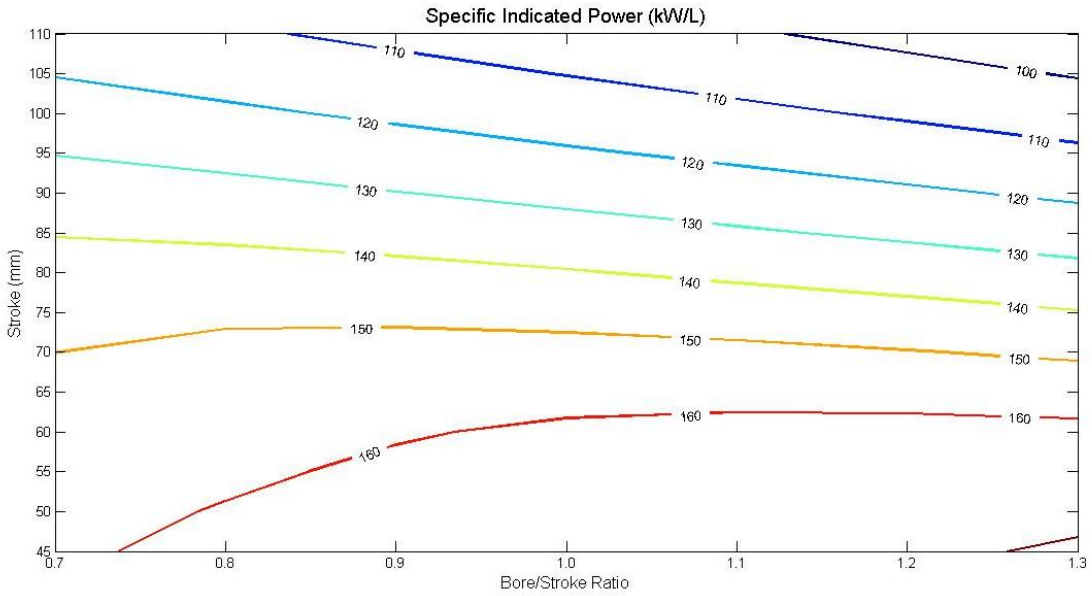

Figure 4.19 Specific indicated power output at 4000rpm, 3 bar boost, and CA50 at 15 CA ATDC

Figure 4.20 shows the effect of the blow-down duration on the brake specific power output at different engine speeds.

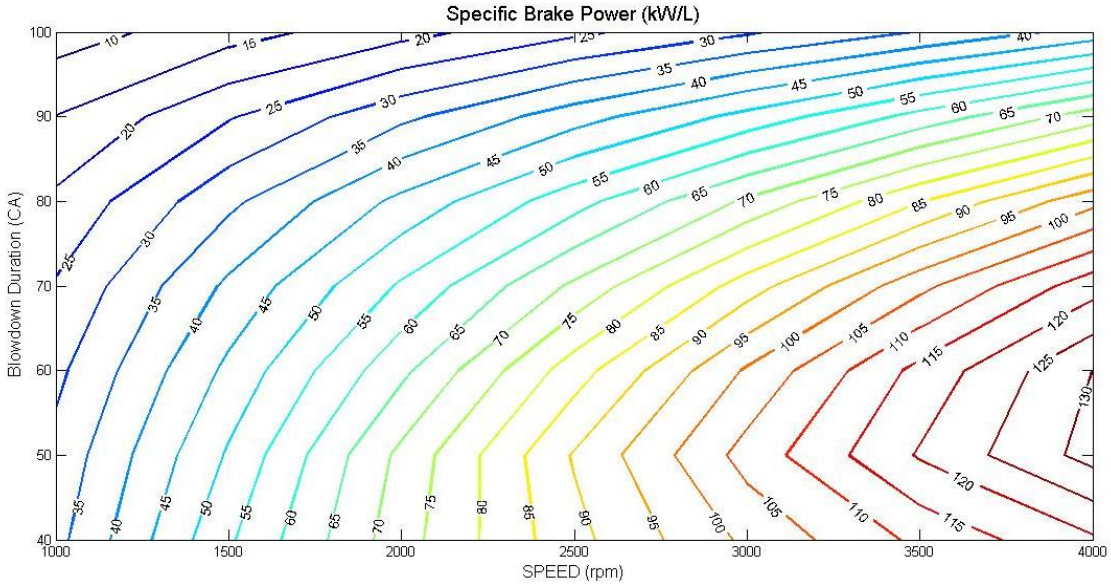

Figure 4.20 Effect of blowdown duration on specific brake power output with 3 bar boost

At lower engine speeds, as the blowdown duration decreased, the brake specific power increased. However, for engine speeds above 3000rpm, the brake specific

power increased initially with shorter blowdown duration and then decreased as the blowdown duration became less than 50º CAs. Maximum power output was reached when a balance between the trapping efficiency and charge efficiency was reached. Therefore, it would be desirable that a variable valve timing device can be used to alter the exhaust valve timing for different engine operating conditions.

4.3.3 Engine Packaging

The target of this research work is to evaluate the potential of the uniflow 2-stroke engine to replace a bigger 4-stroke engine in a passenger car. Therefore it is necessary to consider the dimension of the uniflow 2-stroke engine in the context of the vehicle packaging requirement.

A typical practical engine packaging restriction in a VW Golf sized vehicle is shown in Figure 4.21. As shown in figure 4.21, another vertical length will be added to engine block, because of the valve driven system. And the above simulation shows the best engine output performance can be achieved with 80mm engine stroke. However, with 80mm engine stroke, the overall engine height including the valve driven system (198mm) will be 438mm, which will exceed the restriction by 36mm. By reducing the engine stroke down to 67mm, the engine overall height will be brought down to 406mm, which is only 4mm more than the engine restriction and is deemed acceptable.

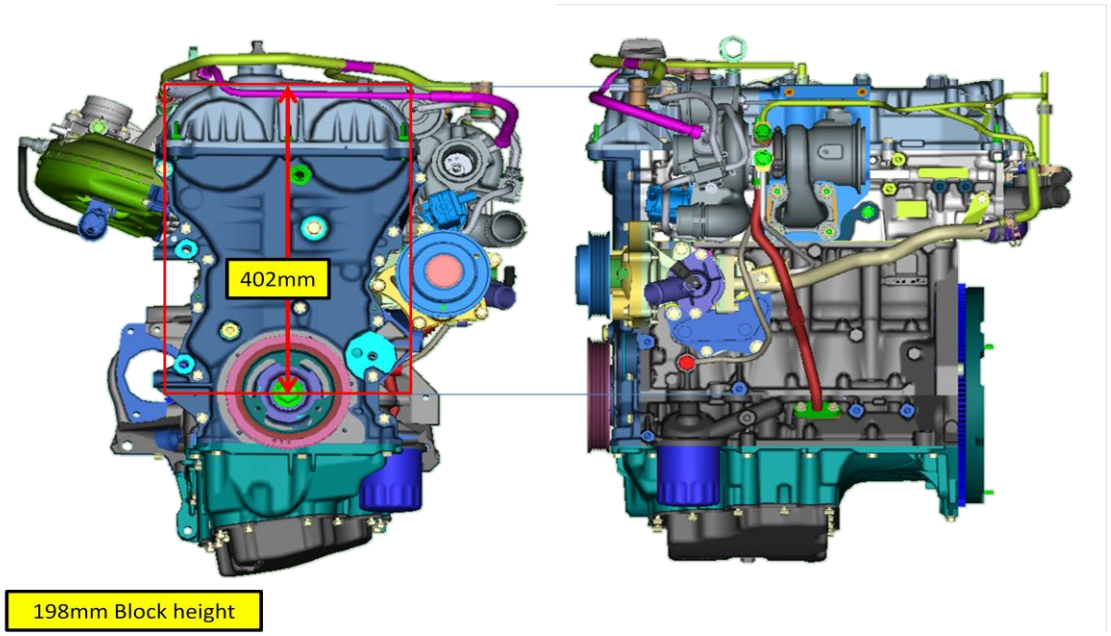

Figure 4.21 Vehicle application packaging restrictions

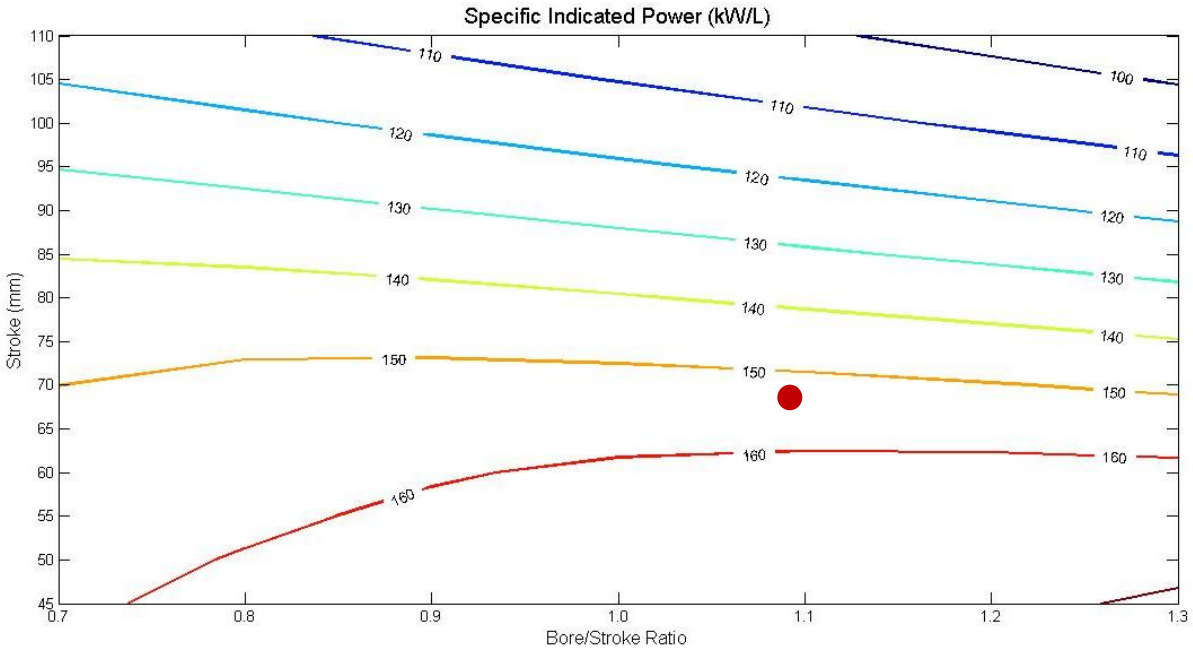

Figure 4.22 Engine size determination

Taking into account of the engine packaging requirement and the cylinder head space required for centrally mounted injector and spark with 4 exhaust valves, it is decided that each cylinder will have a bore and stroke of 76mm x 67mm, giving a displacement volume of 0.3L, as indicated by the red dot. Therefore, a 3-cylinder uniflow 2-stroke engine of 0.9 litre capacity will be able to produce more than 150kW

indicated power at 4000rpm with the intake port opening set to 120°ATDC, much greater than the 1.6 litre 4-stroke engine.

4.4 Summary

3D CFD simulation has been used for the optimisation of the engine breathing process through the intake port design. In addition, the 3D CFD flow results were used to provide the intake flow data for the subsequent 1D calculations. In order to determine the frictional losses, the Flynn-Chen model was adopted to calculate the engine FMEP and the coefficients in the model were determined from a state-of-art gasoline engine.

Based on the 1D simulation result and engine packaging requirements, a 3-cylinder uniflow 2-stroke engine of 0.9 litre capacity and a 2-cylinder version of 0.6L capacity were selected for the subsequent vehicle simulations. The engine has a bore of 76mm and stroke of 67mm. The intake port opening time is set to 120ºATDC and the intake port closing time is set to 240ºATDC. The exhaust valve opening and closing time are 80ºATDC and 240ºATDC respectively.

Chapter 5 Optimisation of the Boost System for the Uniflow 2-Stroke Engine

5.1 Introduction

In Chapter 4, potential performance of the boosted uniflow scavenged direct injection gasoline (BUSDIG) 2-stroke engine was predicted for different stroke and bore combinations. The intake air was boosted to achieve the target torque and power output, limited by the maximum in-cylinder pressure of 120bar. In this chapter, the boost system and engine interactions were examined to determine the appropriate boosting arrangement for maximum performance and minimum fuel consumption. Then, the vehicle driving cycle analysis is carried out to determine the fuel economy benefit of the optimised BUSDIG engine system.

5.2 Modelling of the Boosted Engine and Vehicle Simulation Model

The boost system comprises a turbocharger and/or a supercharger. The supercharger is defined by a single performance map whilst the turbocharger performance is determined by both the turbine and compressor performance maps, which are characterised by the mass flow, pressure ratio, rotational speed and efficiency. The physic model assumes that the flow in the boost system elements behave in a quasi-steady manner and calculates the mass flow and enthalpy rise across the elements as well as the torque produced by the elements or used to driven the elements by interpolating a lookup map of steady state performance behaviour.

Four basic parameters are required to define the maps: dimensionless speed, dimensionless mass flow, dimensionless torque coefficient and blade speed ratio. The parameters are defined as follow [71],

$$N^* = \frac{\pi N_r D_{ref}}{30\sqrt{R_g T_i}} \quad \text{[E-5.1]}$$

$$\dot{m}^* = \frac{\dot{m}\sqrt{R_g T_i}}{P_i {D_{ref}}^2} \quad \text{[E-5.2]}$$

$$\Gamma^* = \frac{\tau}{P_i {D_{ref}}^3} \quad \text{[E-5.3]}$$

$$BSR^* = \frac{\pi N_r D_{ref}}{60\sqrt{2C_\rho T_i\left(1-\left({P_i}/{P_0}\right)^{{1-\gamma}/{\gamma}}\right)}} \quad \text{[E-5.4]}$$

Where

N^* – Dimensionless speed

$\dot{m}^*$ – Dimensionless mass flow

Γ^* – Dimensionless torque coefficient

BSR^* – Blade speed ratio

N_r – Rotational speed

D_{ref} – Reference diameter

R_g – Gas constant

m – Mass flow

T_i – Inlet temperature

P_i – Inlet pressure

τ – Shaft torque

C_ρ – Specific heat of the gas

γ – Special heat capacity ratio

During the calculation, the pressure ratio, dimensionless speed and blade speed ratio are calculated first and then used to interpolate the dimensionless mass flow and torque coefficients and efficiency from the maps. The dimensionless mass flow and torque coefficients can then be used to calculate the instantaneous mass flow,

torque, and the enthalpy rise of the compressor. The turbine power generated or compressor work consumed is calculated as follows,

$$W_t = C_\rho T_i \eta (1 - PR^{1-\gamma/\gamma}) \dot{m} \quad \text{[E-5.5]}$$

$$W_c = \frac{C_\rho T_i}{\eta} (PR^{1-\gamma/\gamma} - 1) \dot{m} \quad \text{[E-5.6]}$$

Where

W_t – Power generated by the turbine

W_c – Power consumed by the compressor

η – Isentropic efficiency of an element

PR – Pressure Ratio

When the operating point of the elements is beyond the boundaries of the map, extrapolation is applied, as shown in Figure 5.1.

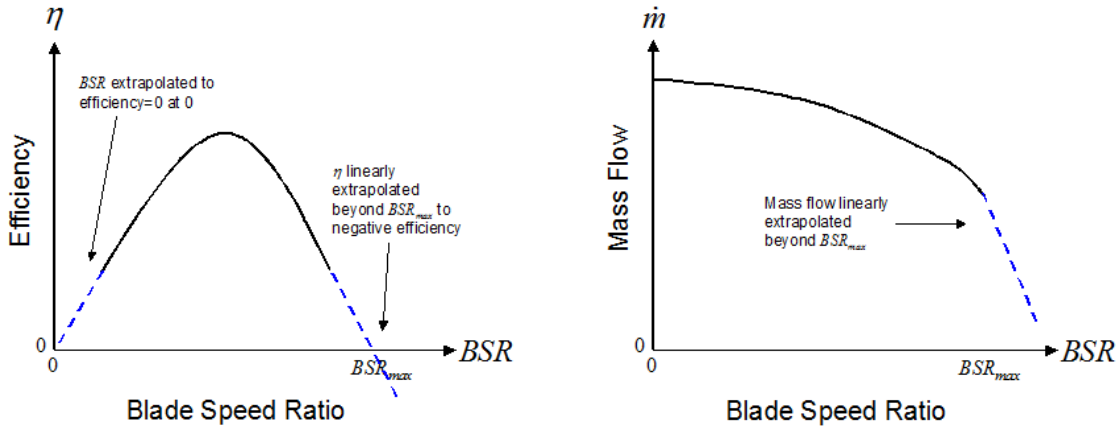

Figure 5.1 Boost elements map extrapolation

The calculation results of boosted engine models were then exported to a vehicle model to carry out calculations based on new European driving cycle (NEDC). The baseline vehicle model parameters are shown in Table 5.1 based on a VW Golf.

The vehicle drag force F_{drag} in the vehicle model can be calculated as follows,

$$F_{drag} = \frac{1}{2} C_{drag} \rho V^2 A_{frontal} \quad \text{[E-5.7]}$$

Where

C_{drag} – Aerodynamic drag coefficient

ρ – Air density

V – Vehicle speed relative to air

$A_{frontal}$ – Vehicle frontal area

Table 5.1 Baseline vehicle parameters

Vehicle data		
	Units	Value
Vehicle mass	kg	1157
Passenger and cargo mass	kg	100
Frontal area	m^2	2.3
Aerodynamic drag coefficient		0.3
Tyre data		
	Units	Value
Tyre rolling resistance		0.015
Tyre rolling radius	m	0.3

The tyre rolling resistance force is calculated as follows,

$$F_{roll} = C_{roll} * (m_{veh} + m_{load}) * g \quad \text{[E-5.8]}$$

Where

C_{roll} – Tyre rolling resistance factor

m_{veh} – Vehicle mass

m_{load} – Passenger and cargo mass

g – Gravitational

The rotation inertia of the elements set up is shown in Table 5.2.

Table 5.2 Rotation elements inertia

Tyre axle	0.13 kg•m^2
Differential input side	0.01 kg•m^2
Differential output side	0.01 kg•m^2
Drive shaft	0.01 kg•m^2
Gearbox input inertia	0.05 kg•m^2
Gearbox output inertia	0.05 kg•m^2

The results of power, torque and fuel consumption of the engine model then were transferred to the vehicle calculation model, the fuel consumption calculation based on the new Europe drive-cycle was carried out to investigate the in-vehicle engine fuel economy performance. The imposed vehicle speed and corresponding gear engaged is shown in Figure 5.2.

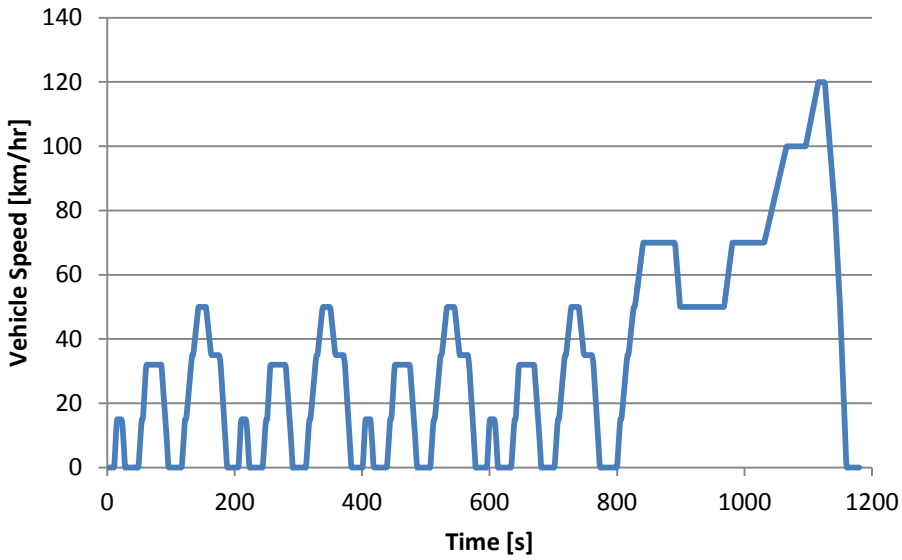

Imposed vehicle speed

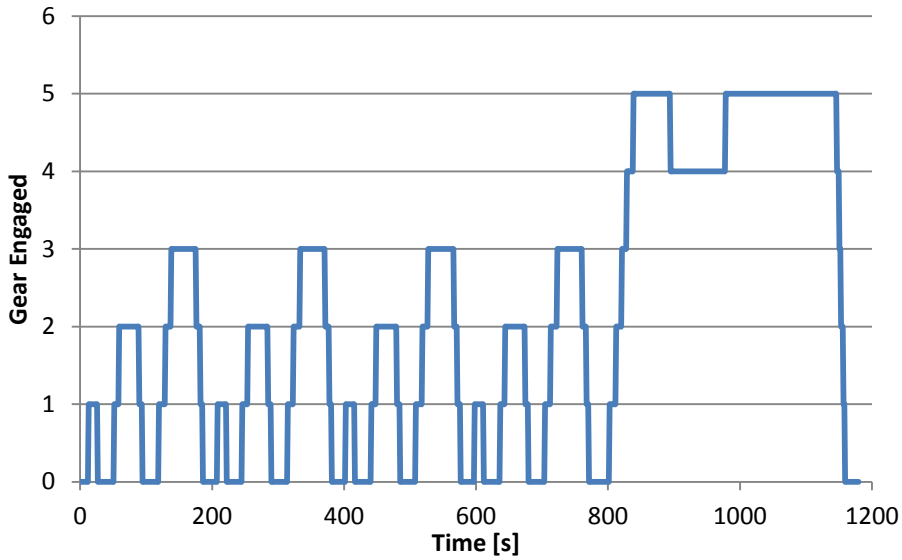

Imposed gear engaged

Figure 5.2 The new Europe drive-cycle (NEDC) conditions

5.3 Analysis of Boosted uniflow 2-stroke engine operations

In order to set a reference to the optimisation calculation of boosted engine model, a baseline 4-stroke engine of 1.6L capacity was set up. The valve lift and timing are as shown in Figure 5.3. As shown in Figure 5.4, the CA50 was set to 5ºCA ATDC at this stage and the combustion duration was 30ºCA.

Figure 5.5 shows the predicted full load performance curves of the baseline 4-stroke engine model. The baseline 4-stroke engine delivers its maximum brake power of 79kW at 6000rpm and maximum brake torque of 140Nm at 5000rpm engine speed.

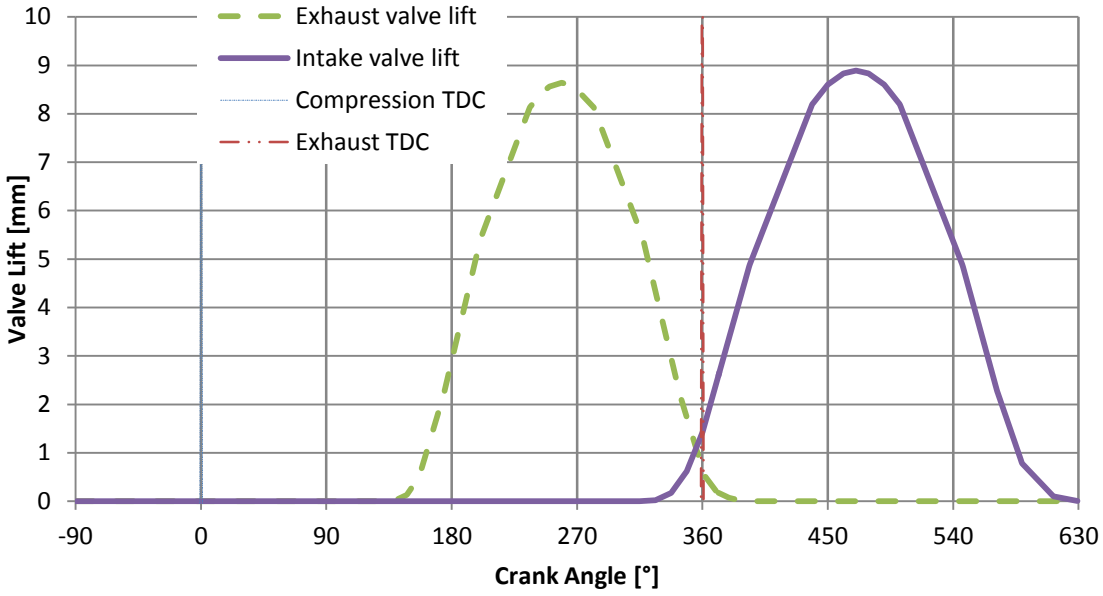

Figure 5.3 Valve timing and lift of 4-stroke baseline model

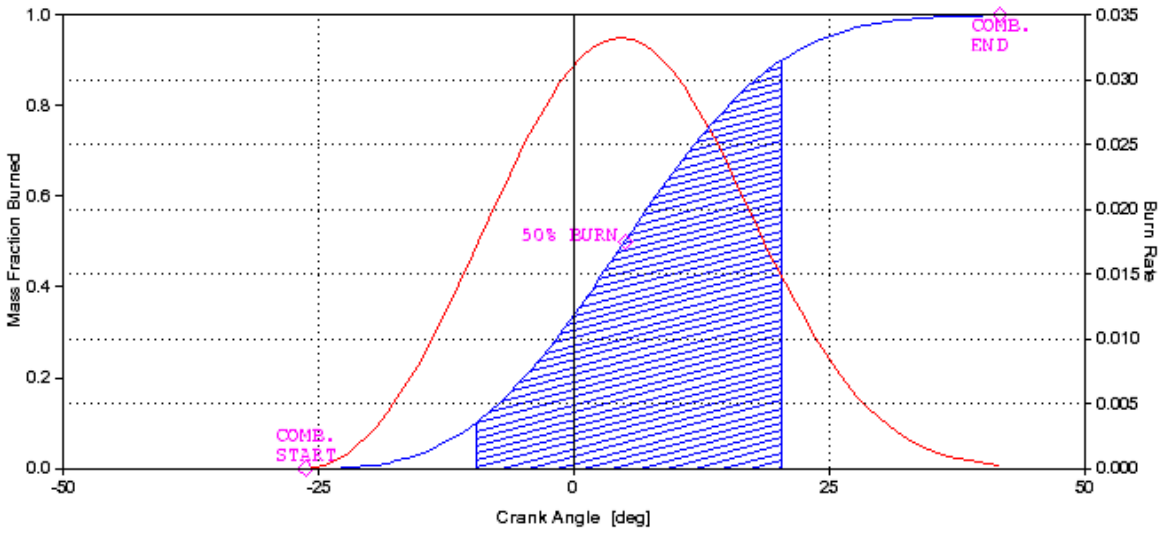

Figure 5.4 Combustion phase of the 4-stroke engine model

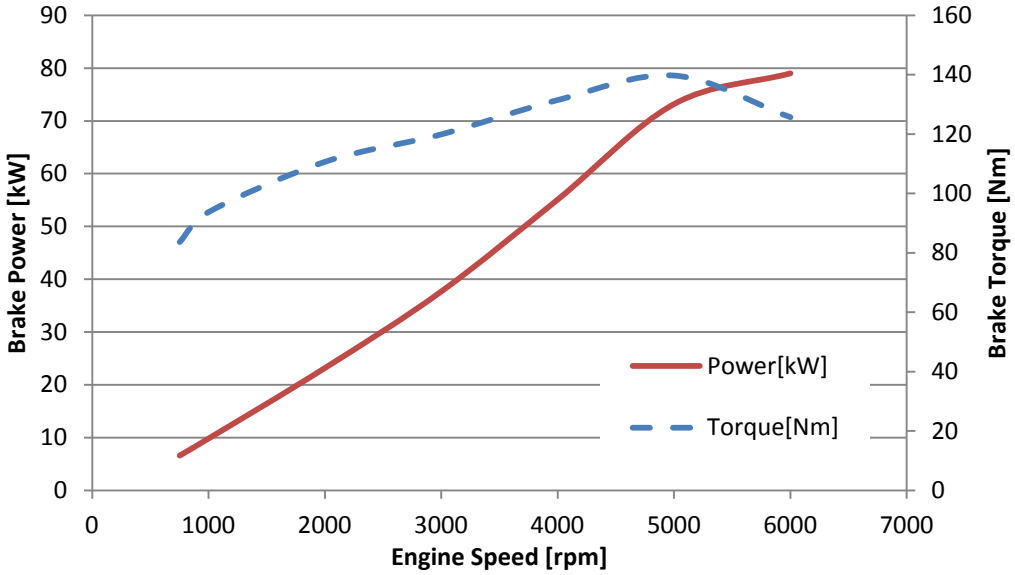

Figure 5.5 Baseline engine model performance curve

5.3.1 2-stroke engine model set up

The first boosted 2-stroke engine modelled is a 0.9L 3-cylinder engine with a single supercharger. Subsequently, a turbocharged version of the 2-stroke engine is modelled. Figure 5.6 shows the 1D calculation base model layout with supercharger and turbocharger. Compared to the 4-stroke NA model, the engine's capacity is downsized by 44%. The engine has a bore of 76mm and a stroke of 67mm as determined before. The air/fuel ratio was regulated by the injector element in the model and was set to 14.7/1 of mass for the trapped air/fuel ratio. The restriction of 120bar peak in-cylinder pressure was applied. The ambient boundary was set at pressure of 1bar and temperature of 300K.

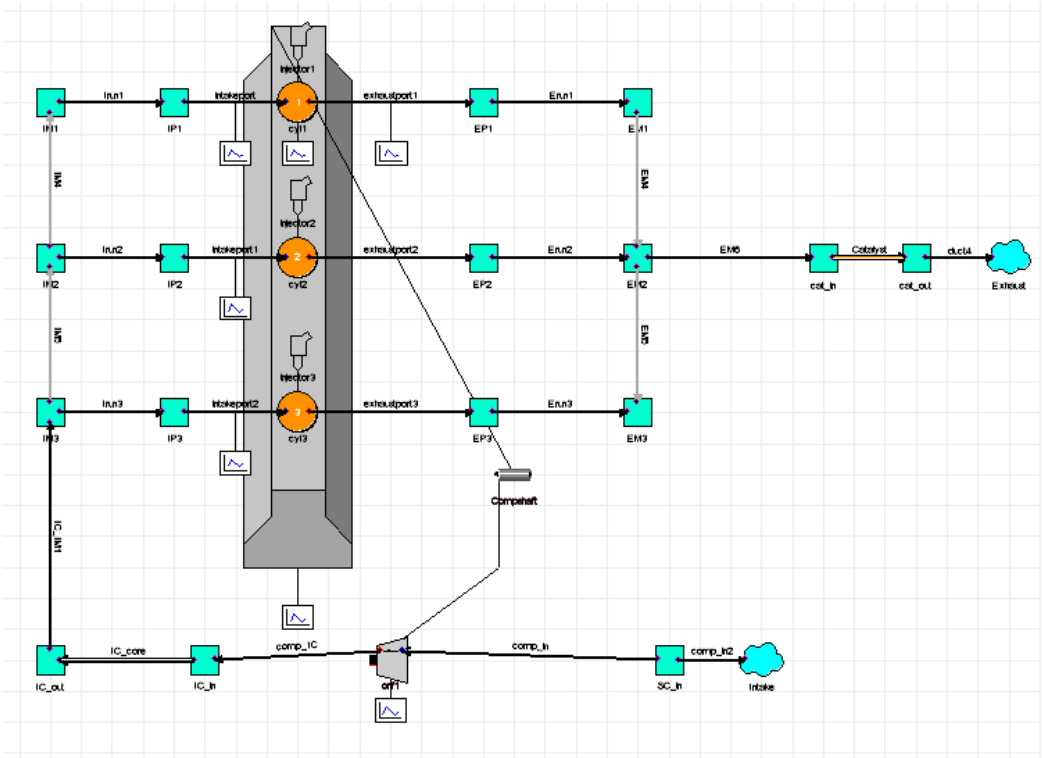

Model with supercharger

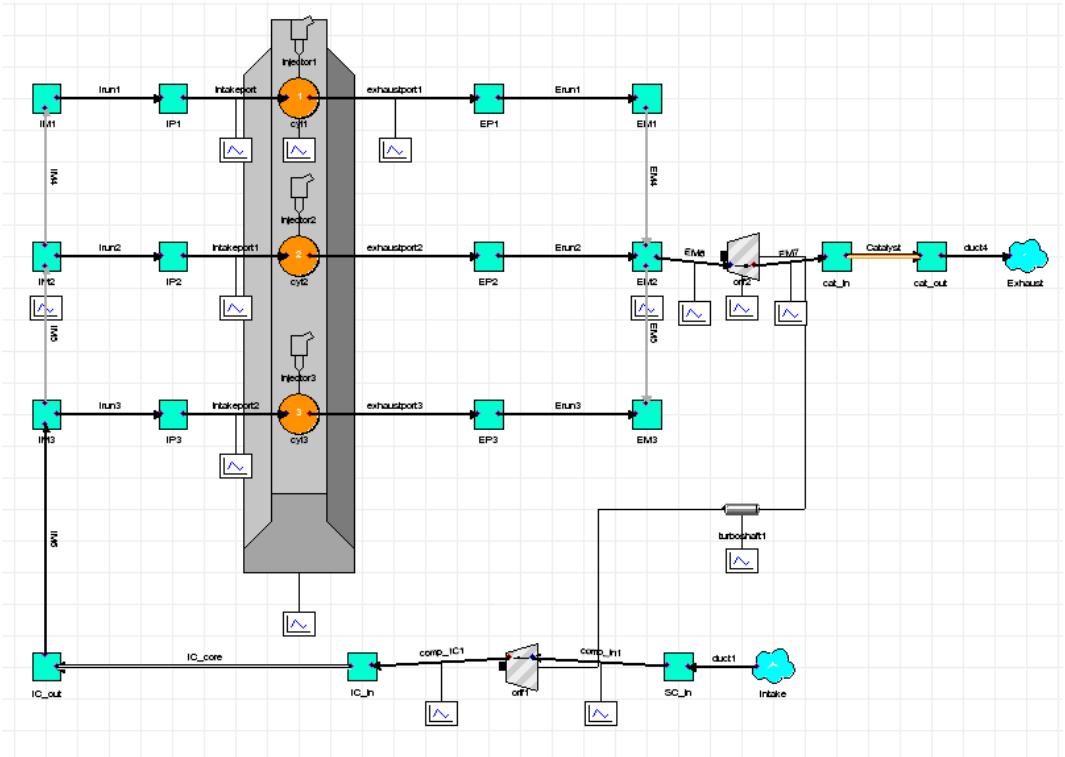

Model with turbocharger

Figure 5.6 2-stroke 1D calculation base model layout

The supercharger, Eaton R200GT or R410GT, and the turbocharger used to boost the Mahle I3 engine was chosen as the boost elements for engine models, it is because Mahle I3 engine has similar engine configuration and capacity to the 2-stroke engine model. To fit the mass flow through the 2-stroke engine model, the performance maps of the turbocharger have been rescaled. The mass flow rate of the turbine TD04L4-F5 is expanded by 125% and the mass flow rate of the compressor TF035-13TK3S shrunk by 65%. The performance maps of those boost elements are shown in Figure 5.7 to Figure 5.10.

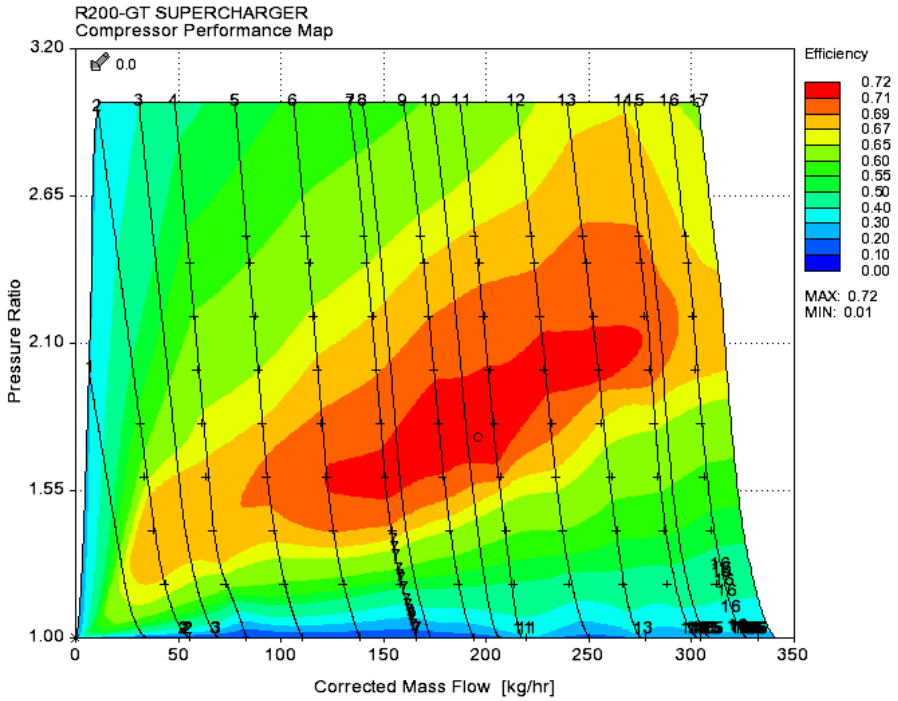

Figure 5.7 Eaton R200GT performance map

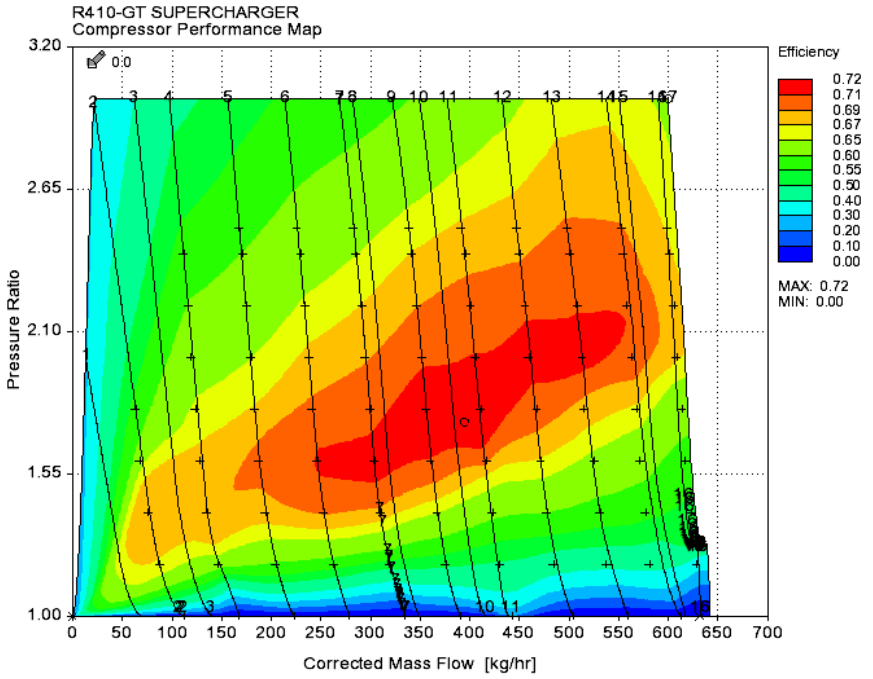

Figure 5.8 Eaton R410GT performance map

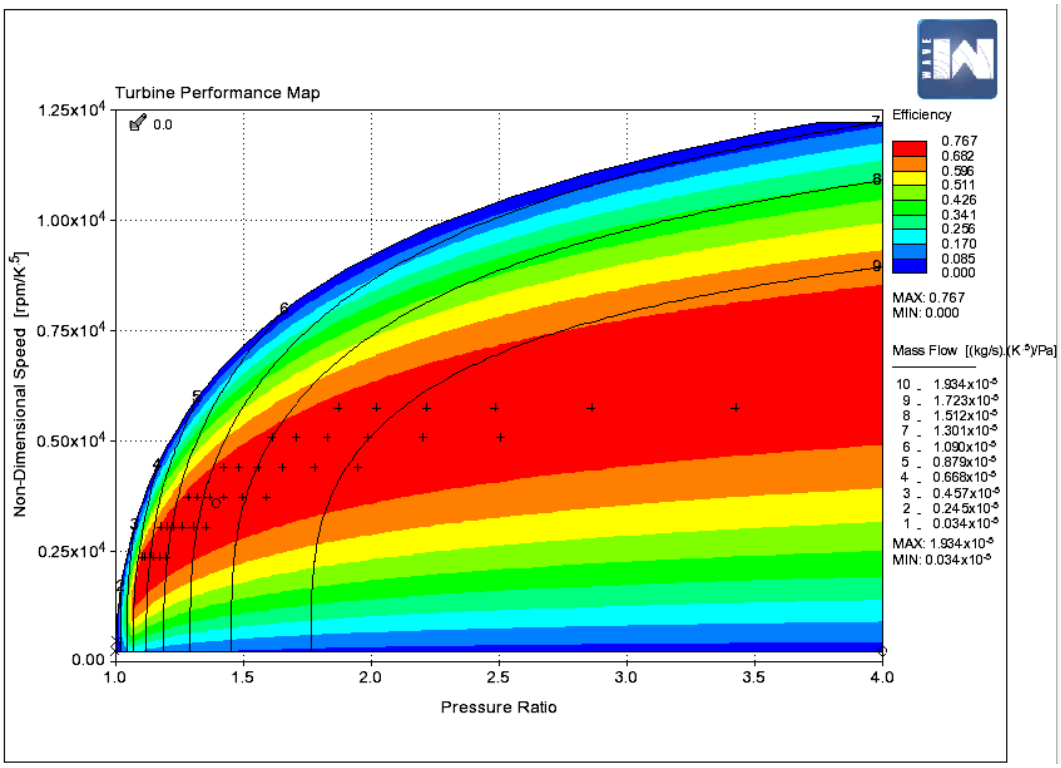

Figure 5.9 Rescaled turbine performance map

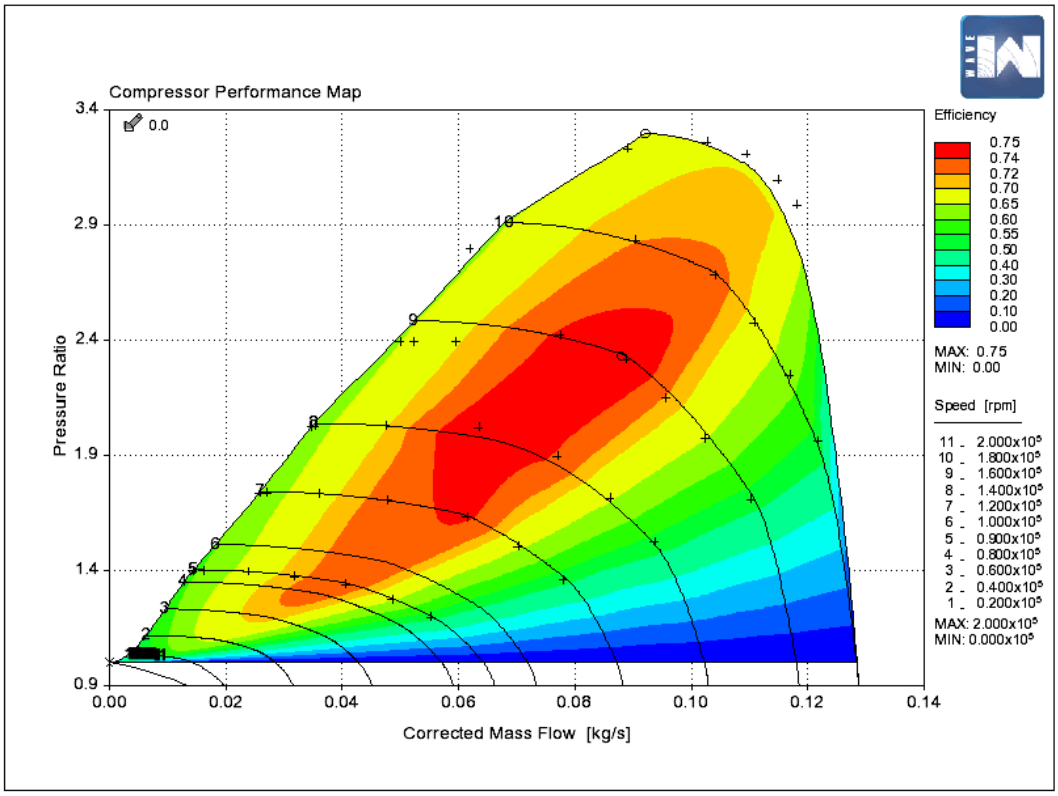

Figure 5.10 Rescaled compressor performance map

5.3.2 Prediction of Boosted uniflow 2-stroke engine full-load performance

In the case of supercharged engine operations, the supercharger is driven by the crankshaft directly under a specified gear ratio. Figure 5.11 shows the maximum brake power predicted of the 2-stroke engine boosted by R200GT with various gear ratios. The results reveal that as the gear ratio is increased from 4 to 7, the engine output reaches a maximum power of 56kW at 4000rpm. Further increase in the gear ratio leads to a drop in the brake power output. As shown in Figure 5.12, the flow rate of the supercharger R200GT reaches the high flow rate end boundary with gear ratio 7 and cannot be increased further with higher gear ratios, limiting the amount of fuel to be burned and hence the resulting mechanical work that can be produced by combustion. In the meantime, the increase in the power used to drive the supercharger at a higher gear ratio will reduce the net power output of the engine. Thus, the combination of limited engine power output and increasing power required to drive the supercharger causes the brake power output to drop beyond a gear ratio of 7.

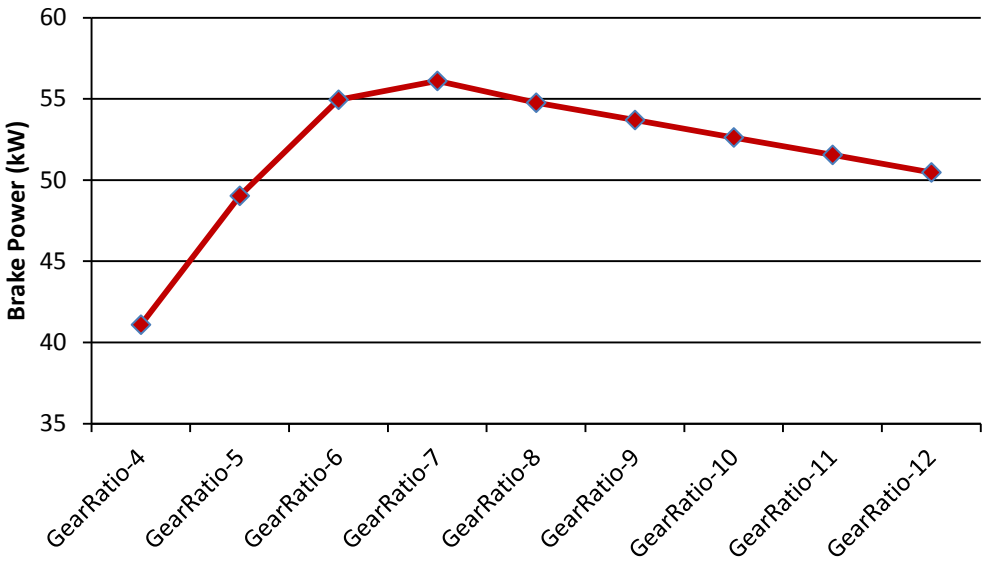

Figure 5.11 Full load brake power of engine model with R200GT supercharger at 4000rpm engine speed.

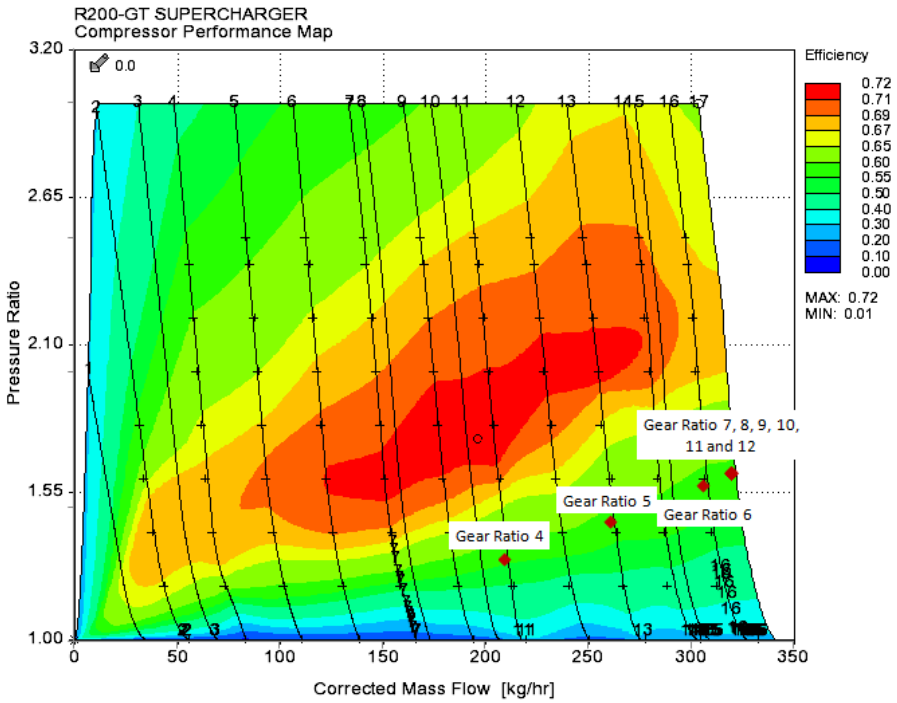

Figure 5.12 R200GT supercharger working points at engine full load at 4000 rpm engine speed

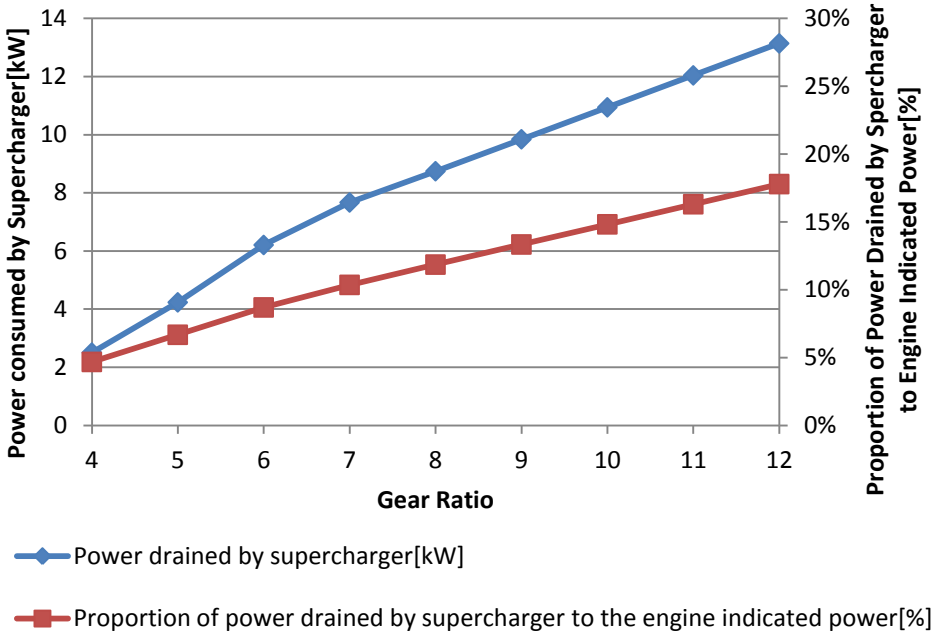

Figure 5.13 Power consumption by a R200GT supercharger and the proportion to the engine indicated power at 4000rpm full load operation

In order to increase the target output engine power, R410GT is then used. The maximum mass flow rate of R410GT is 650kg/hr, nearly 300kg/hr higher than R200GT.

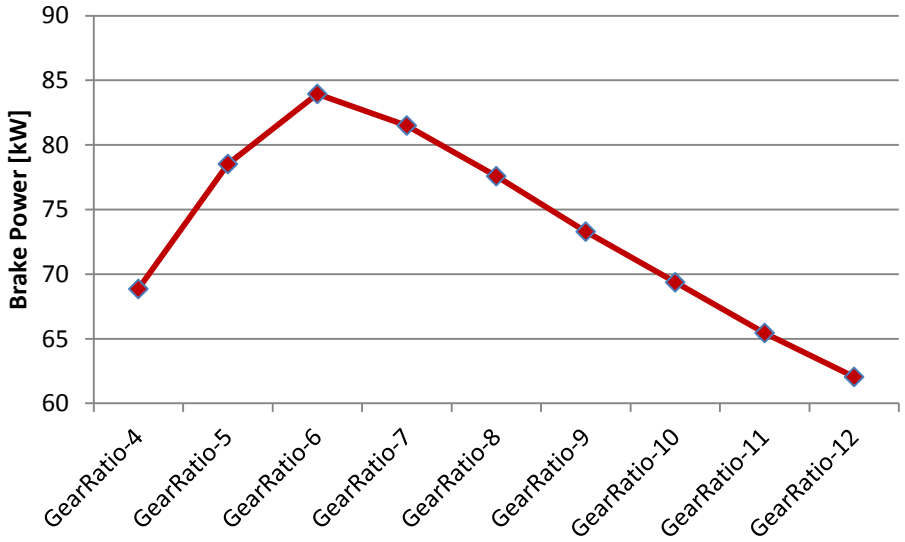

Figure 5.14 Full load brake power of engine model with a R410GT supercharger at 4000rpm engine speed.

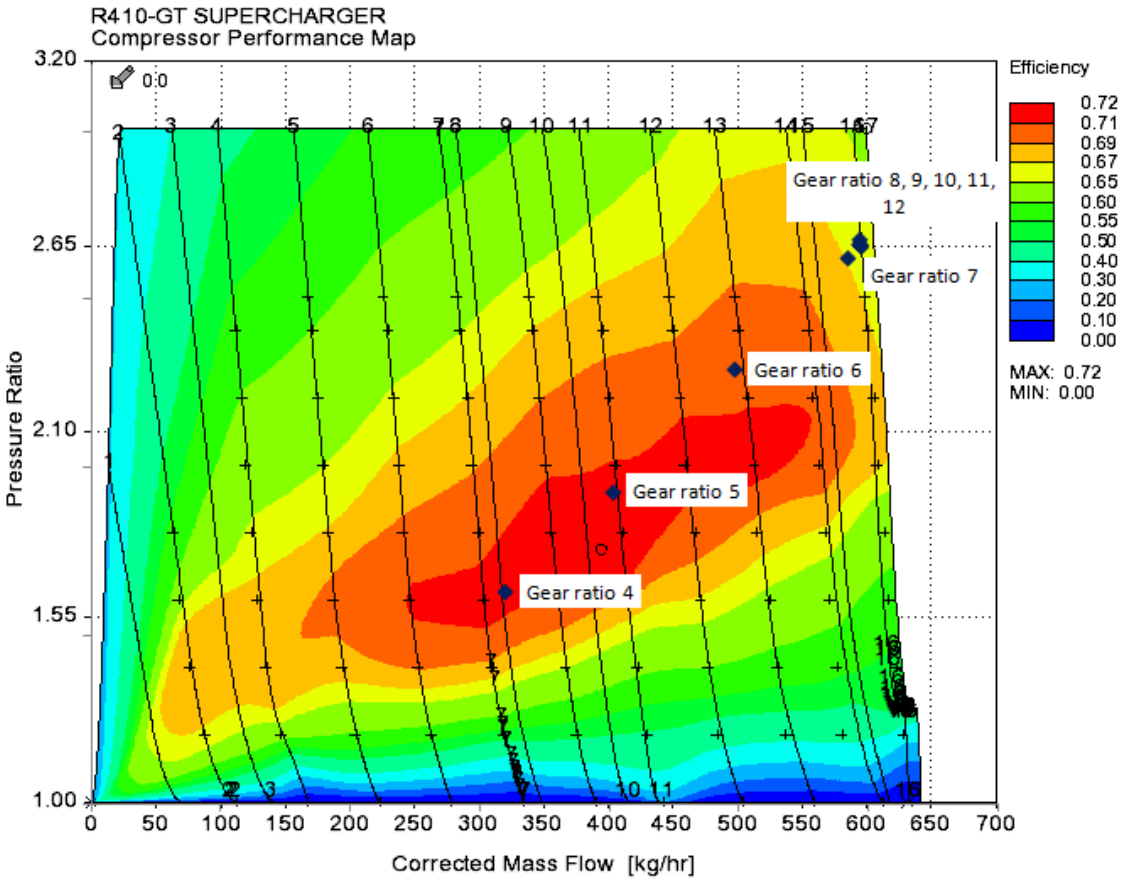

Figure 5.15 R410GT supercharger working points at engine full load at 4000 rpm engine speed

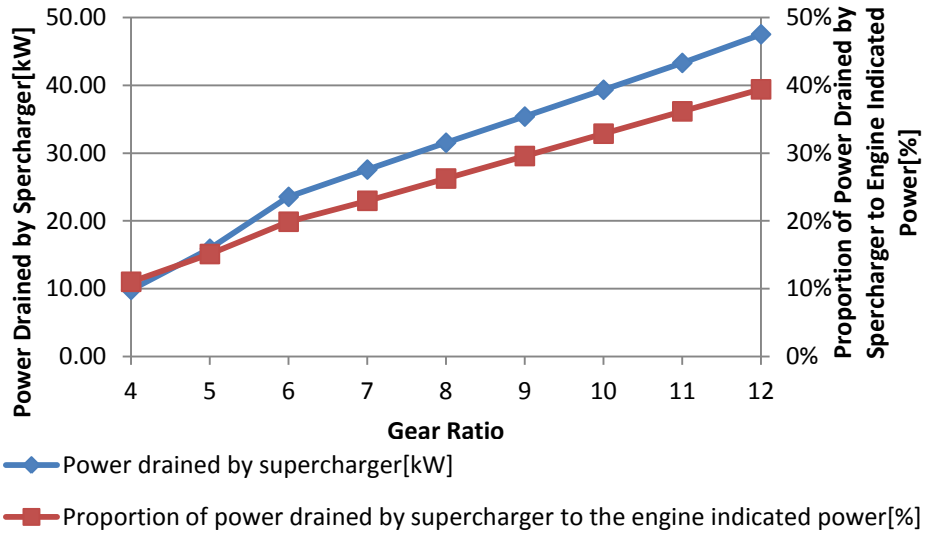

Figure 5.16 Power consumption by R410GT supercharger and the proportion to the engine indicated power at 4000rpm full load condition

As shown in Figure 5.14, the brake power reaches a maximum value of 84kW with a gear ratio 6. Figure 5.15 shows the working points of R410GT at 4000rpm engine speed and full engine load. Similar to the supercharger R200GT, when the gear ratio is increased higher than 7, the compressor is restricted by the maximum mass flow boundary and the power consumption by the supercharger can go up to nearly 40% of the engine indicated power, as shown in Figure 5.16. Therefore, gear ratio 6 shows the best compromise between the engine power output and the power consumption by the supercharger.

As shown above, the supercharger consumed a large proportion of indicated power, which leads to a poor engine overall efficiency. The turbocharger is driven by the exhaust gas, theoretically, no power drained directly from the engine output, thus the engine overall efficiency is higher, so is the engine brake power and torque.

Figure 5.17 shows the working point of the rescaled supercharger and turbocharger. As described previously, the performance map of the turbine used was TD04L4-F5, to fit the engine condition, the mass flow range was expanded by 125% and the mass flow range of the compressor TF035-13TK3S shrunk by 65%. With the rescaled compressor and turbocharger, the engine flow fits the elements' high efficiency range.

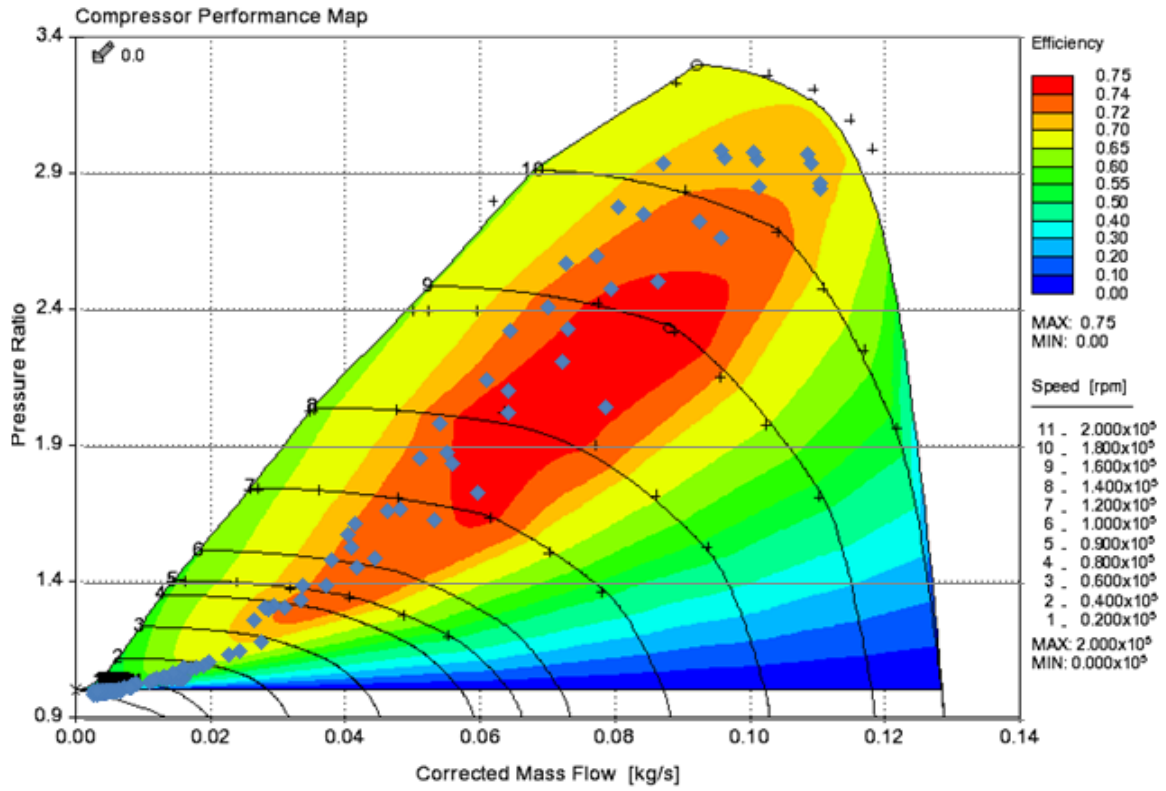

Working points of the compressor

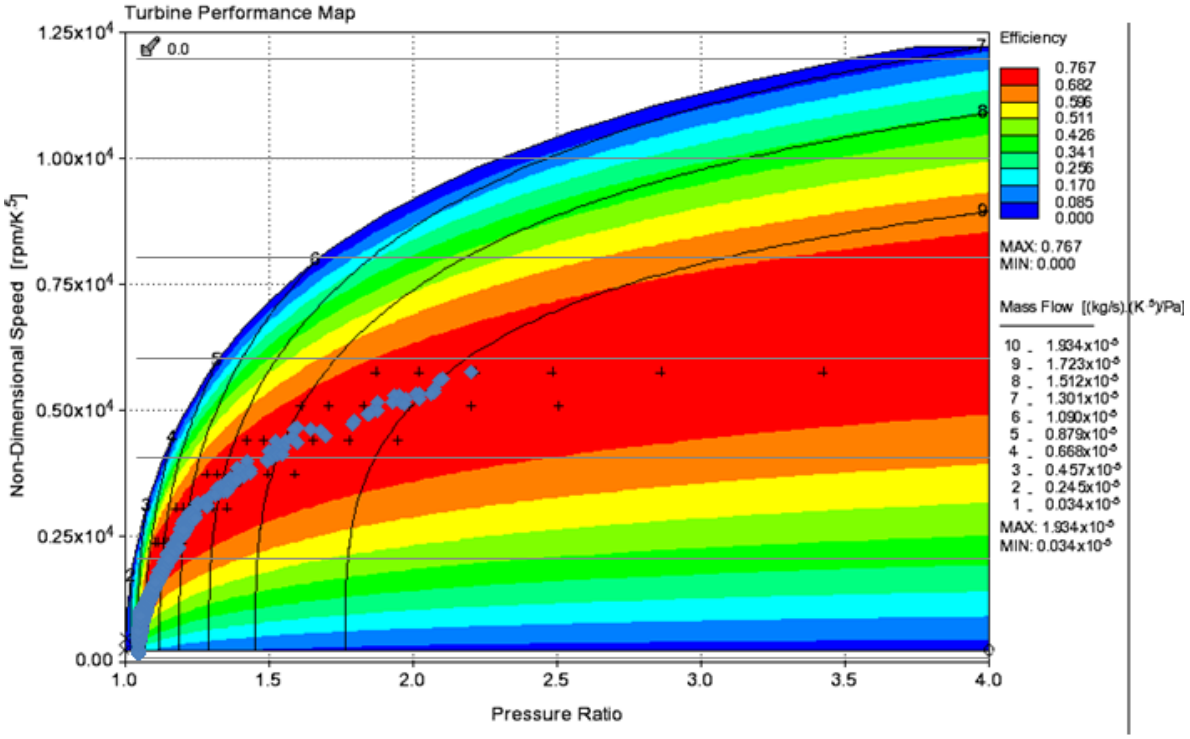

Working points of the turbine

Figure 5.17 Working points of the compressor and turbine of the model

With the rescaled turbine and compressor, the maximum boost pressure was still not higher than 3bar. The full load power and torque curves are shown in Figure 5.18. The peak power reached 105kW at 4000rpm engine speed. Meanwhile the peak torque reached 296Nm at 2000rpm, and keeps higher than 250Nm from 2000rpm to 4000 rpm.

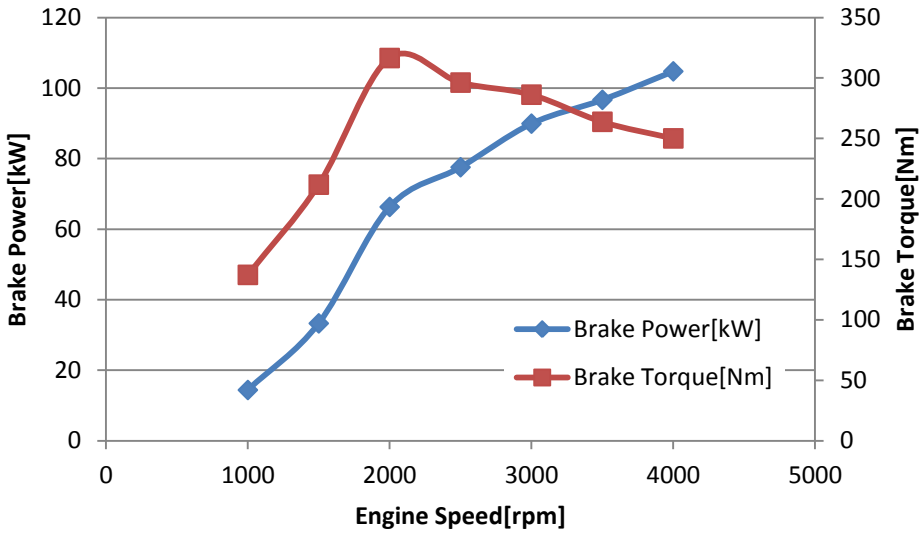

Figure 5.18 Full load power and torque curves of the turbocharged model

Figure 5.19 shows the full load brake power and torque curves of the baseline 4-stroke engine and boosted 2-stroke engine operations. The R200GT supercharged 2-stroke engine can match the torque output of the baseline 4-stroke engine up to 4000rpm but its maximum power is insufficient. With R410GT, the supercharged uniflow 2-stroke engine can produce the same maximum power at 4000rpm as the baseline 4-stroke engine at 6000rpm, and it is characterised with superior torque output across the whole speed range of the 2-stroke engine operations. With the rescaled turbocharger, both the engine power and torque target were substantially exceeded. Actually, when it is equipped with the rescaled turbocharger, the uniflow 2-stroke engine exhibits extremely high torque and the target maximum power can be reached at 2500rpm, which suggests that further downsizing of the 2-stroke engine from 3-cylinder to 2-cylinder is a viable option.

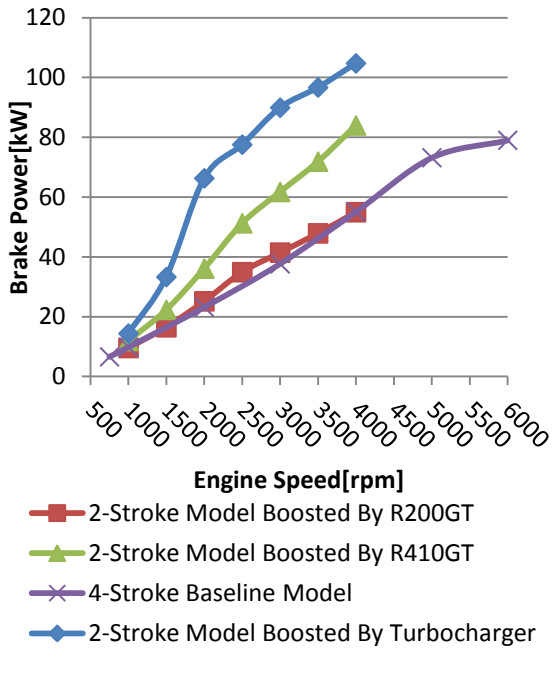

Brake Power

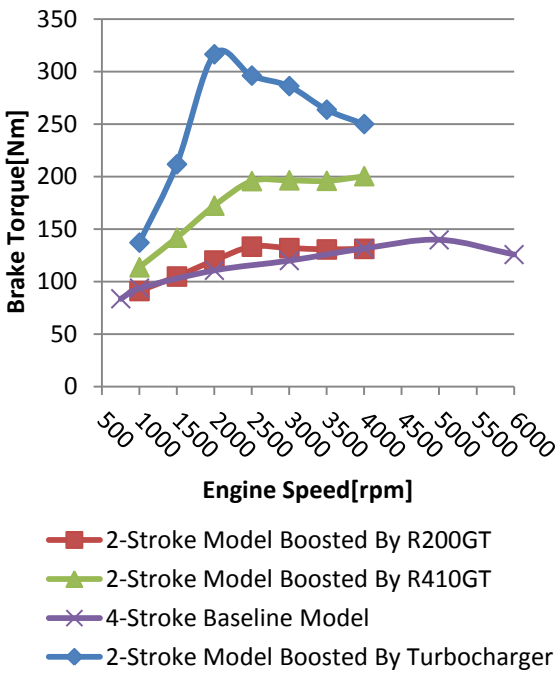

Brake Torque

Figure 5.19 Full load brake power and torque curves of all engines

5.3.3 Analysis of boosted uniflow 2-stroke engine operations

In order to compare the performance of all the engines modelled, some engine operating conditions were chosen. The first engine operation point is the high speed and high load operation of 4000rpm engine speed and 55kW brake power. As shown in Figure 5.20, the 4-stroke NA engine has the highest charging efficiency despite the boosted operation of all 2-stroke engines. Among the 2-stroke engine configurations, the turbocharged operation exhibits the lowest charging efficiency due to the higher back pressure in the exhaust manifold.

Figure 5.20 Charging efficiency of baseline 4-stroke and boosted 2-stroke engines

Figure 5.21 shows the corresponding IMEP values of the baseline 4-stroke and boosted uniflow 2-stroke engines. For a given power and torque output at the same engine speed, the IMEP value of the 2-stroke engine operation is theoretically halved. But the results in Figure 5.21 are significantly different from the theoretical values because of the lower charging and trapping efficiency of the 2-stroke scavenging process than the 4-stroke gas exchange as well as their smaller displacement volume than the baseline engine. The higher power consumption by R410GT requires more IMEP to be produced for the same brake power and torque output, and hence the highest boost pressure as shown in Figure 5.22. Since it is the pressure ratio between the intake and exhaust which determines the charging and trapping efficiencies, higher exhaust back pressure are shown by the turbocharger. As a consequence, the turbocharged operation leads to higher residual gas fraction as shown in Figure 5.23.

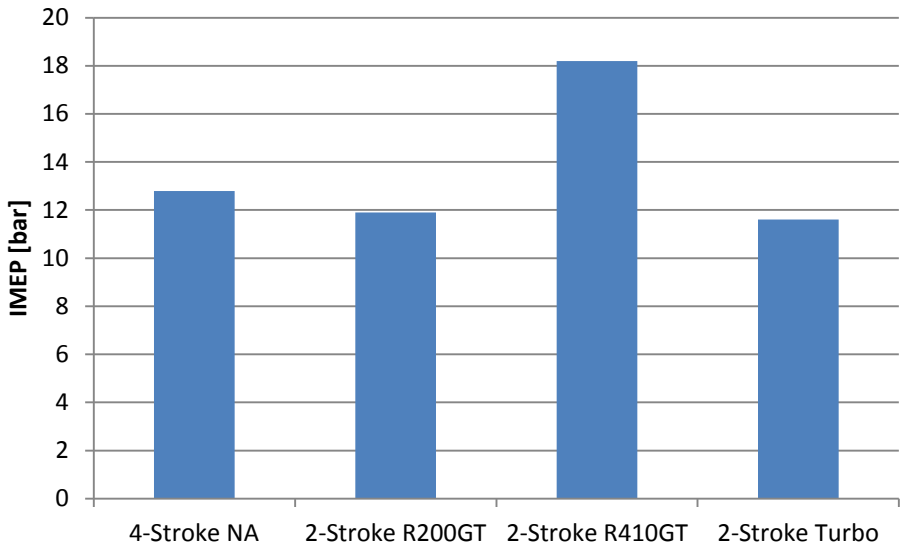

Figure 5.21 IMEP values at 4000rpm and 55kW

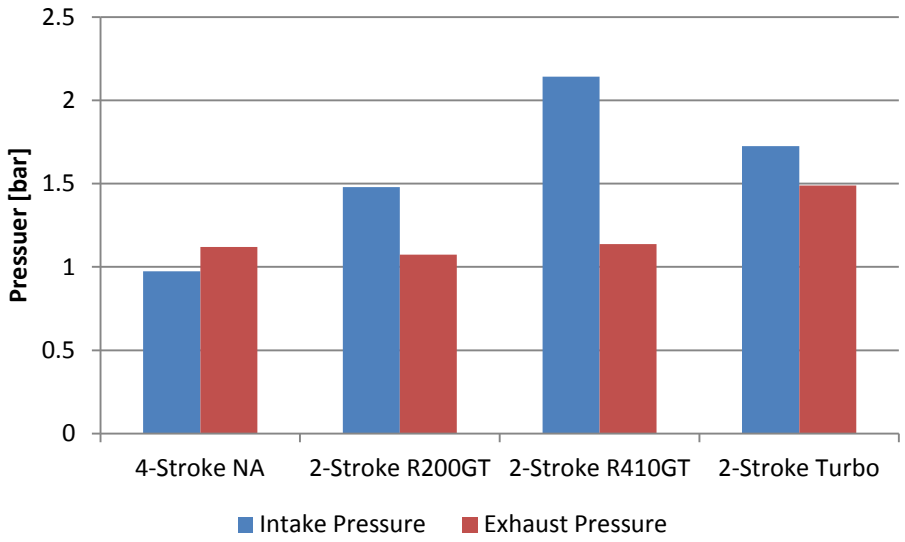

Figure 5.22 Intake and exhaust pressures at 4000rpm and 55kW

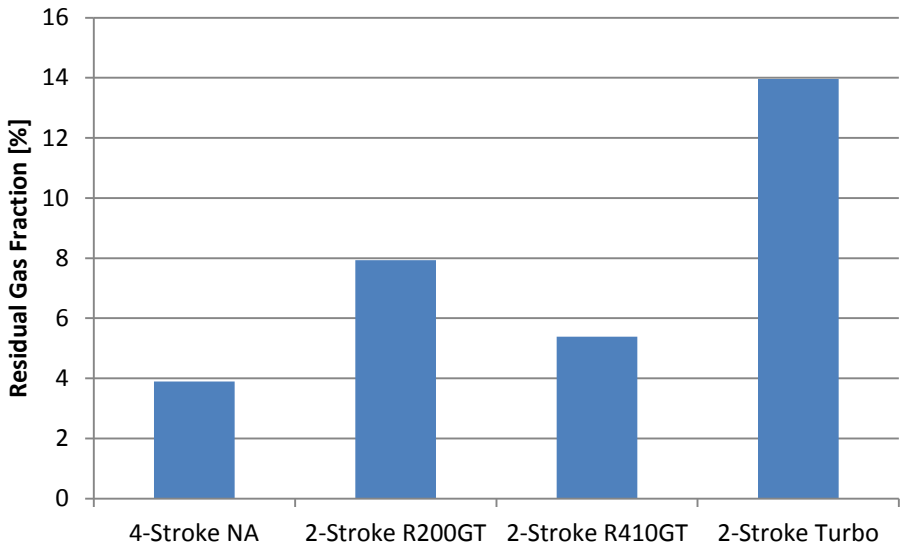

Figure 5.23 Residual Gas Fraction at 4000rpm and 55kW

Figure 5.24 shows the breakdown analysis of engine output and losses of work. For the 4-stroke baseline engine, 81.5% of indicated work is converted into the brake work at the crank shaft output. The turbocharged 2-stroke operation has the highest mechanical efficiency of 84% much higher than the supercharged 2-stroke operations, due to the absence of power consumption by a supercharger.

As shown in Figure 5.25, the turbocharged 2-stroke engine shows the same specific fuel consumption rate as the baseline 4-stroke engine. The 2-stroke engine with the larger supercharger has the highest fuel consumption.

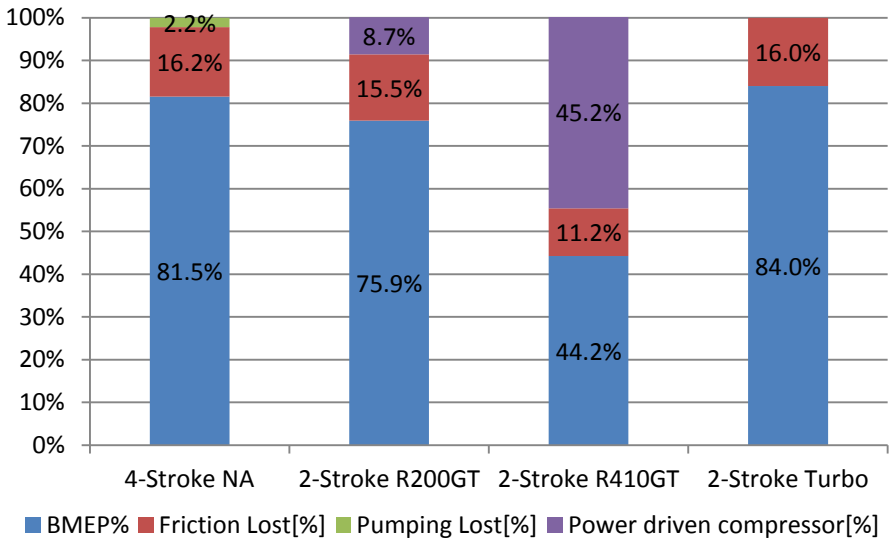

Figure 5.24 Engine output breakdown analysis at 4000rpm and 55kW

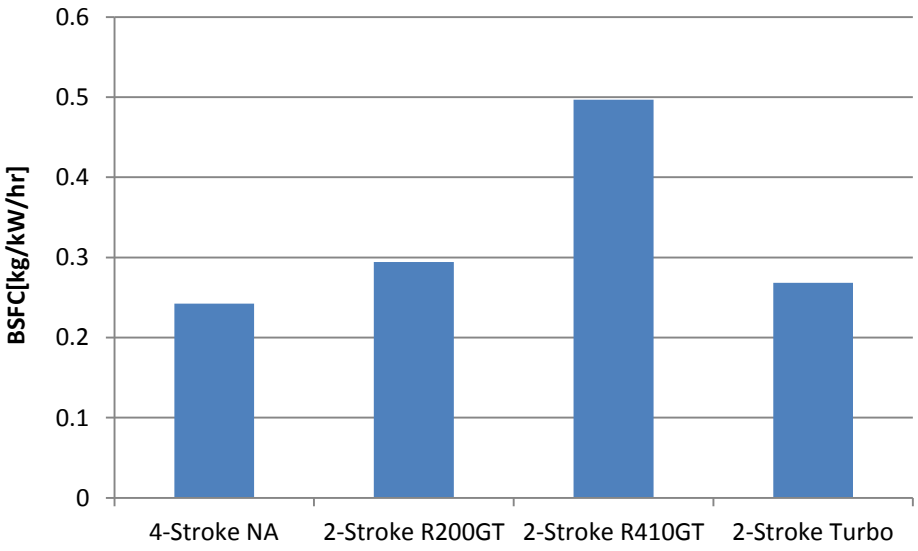

Figure 5.25 BSFC at 4000rpm and 55kW

The high speed and medium load at 4000rpm and 35kW is the second operating point chosen for comparison. As shown in Figure 5.26 to Figure 5.29, the same relative performances at this operating condition are observed for the engine charging efficiency, IMEP, intake and exhaust pressure and BSFC results as the high load operation.

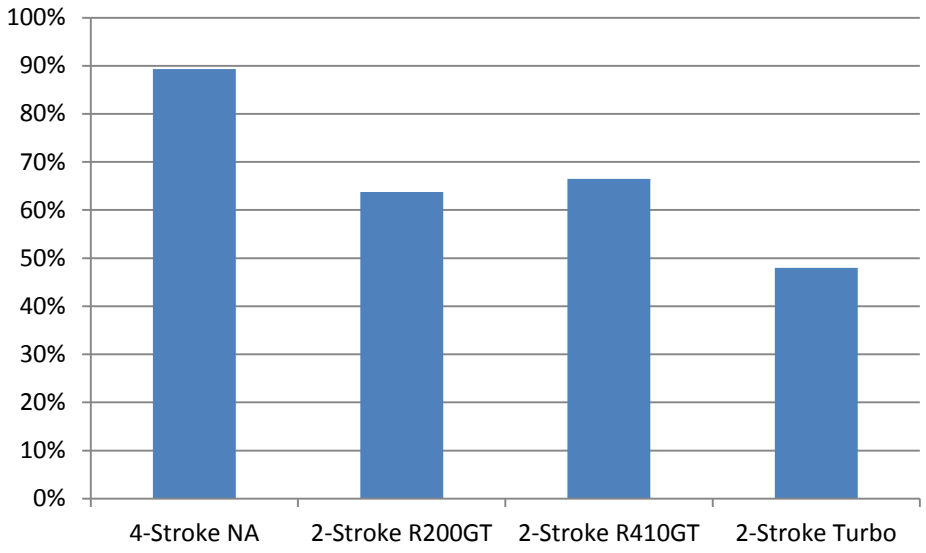

Figure 5.26 Charging efficiency at 4000rpm and 35kW

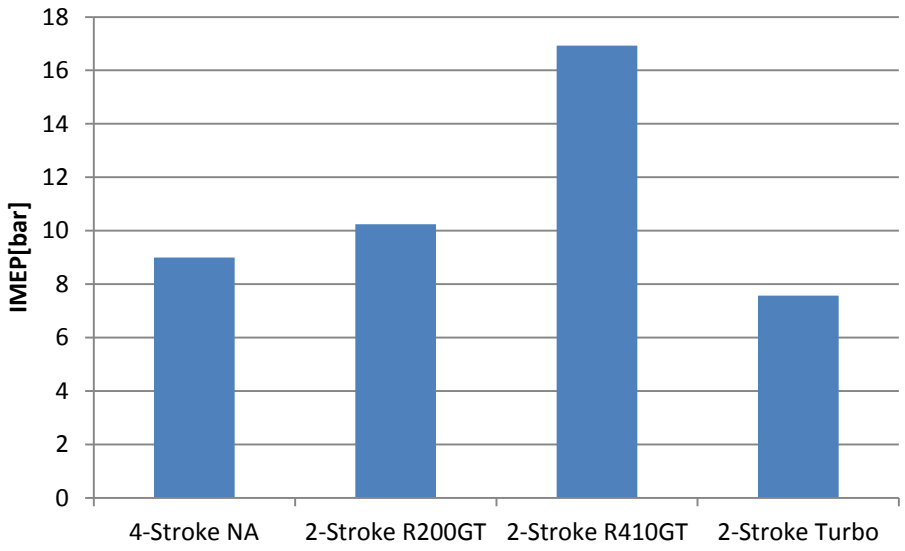

Figure 5.27 IMEP at 4000rpm and 35kW

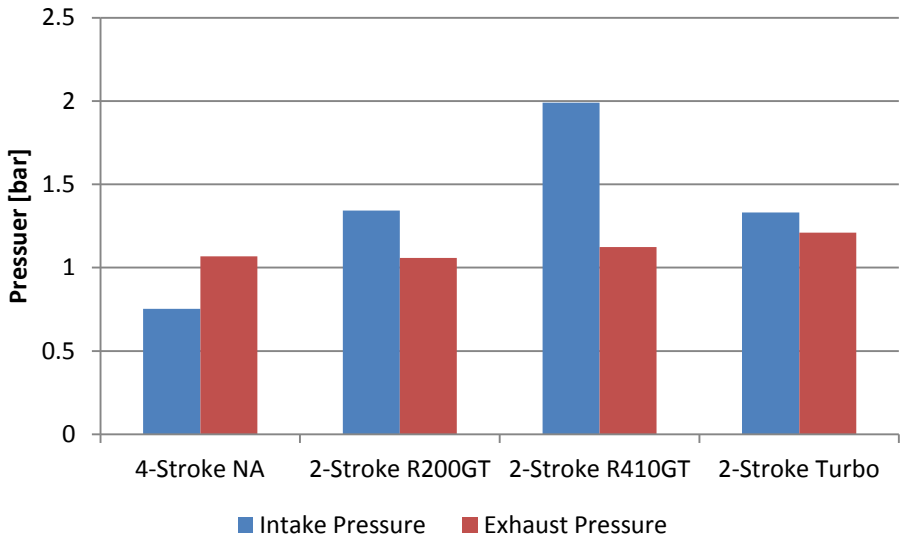

Figure 5.28 Intake and exhaust pressures at 4000rpm and 35kW

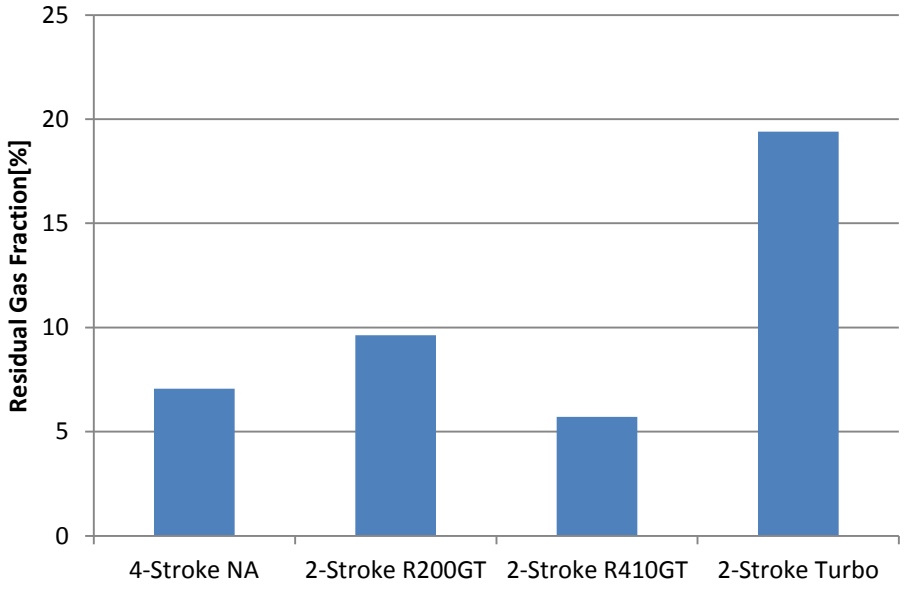

Figure 5.29 Residual Gas Fraction at 4000rpm and 35kW

However, as shown in Figure 5.30, the percentage of supercharger power increased significantly as the load was decreased. In the case of R410GT, 61.8% indicated power is used to drive the supercharger, resulting in the highest fuel consumption. According to Figure 5.31, the baseline 4-stroke engine and the turbocharged 2-stroke engine exhibit 10% increase in BSFC. In comparison, the two supercharged 2-stroke engines suffer a fuel consumption penalty of 51% and 62%, respectively.

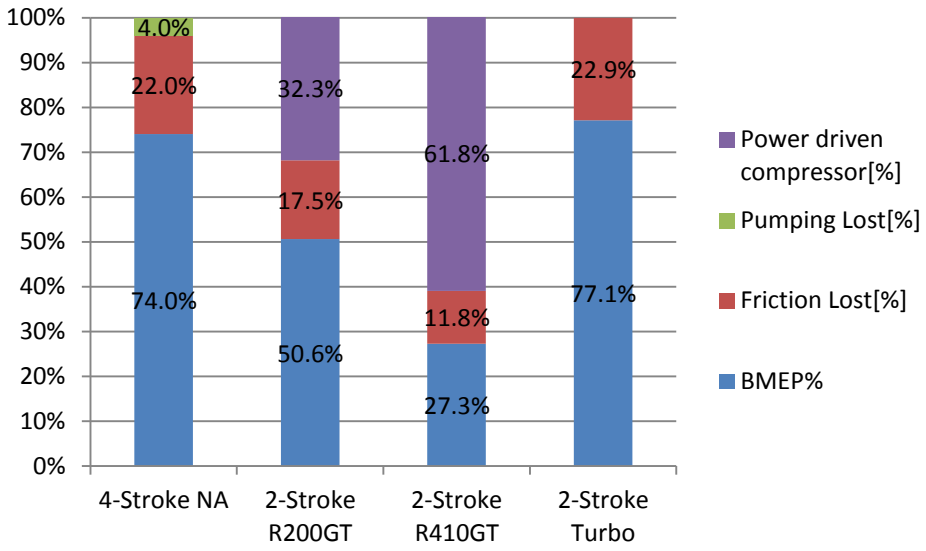

Figure 5.30 Engine output breakdown analysis at 4000rpm and 35kW

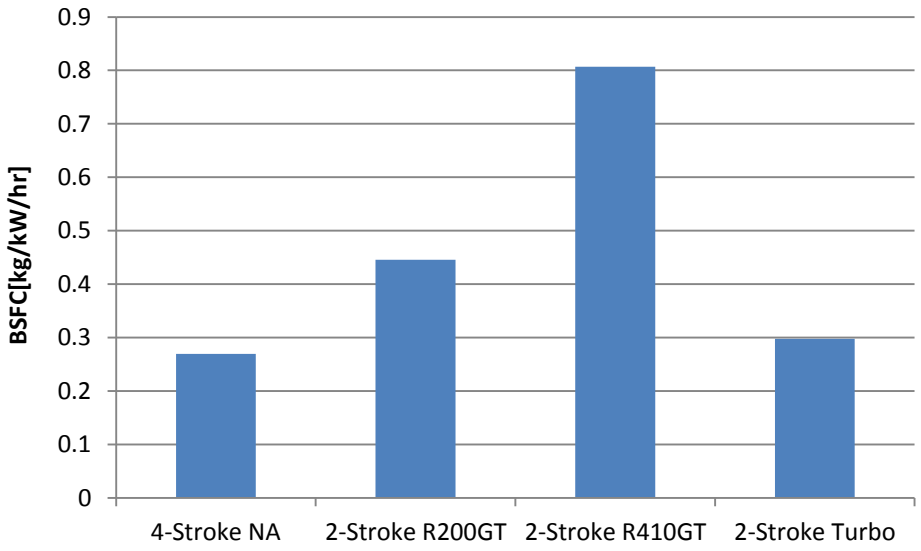

Figure 5.31 BSFC at 4000rpm and 35kW

When the load is reduced to 10kW at 4000rpm, engine efficiencies drop further. As Figure 5.32 shows, about 40% work is lost to friction in both the baseline 4-stroke engine and the turbocharged 2-stroke engine as the indicated power becomes less. In addition, the baseline 4-stroke engine incurs an additional 13.2% pumping losses. In the case of supercharged engine operations, most of the engine work is used to drive the supercharger, up to 74% with R410GT. A direct result is the fuel consumption increases to a very high level as shown in Figure 5.33.

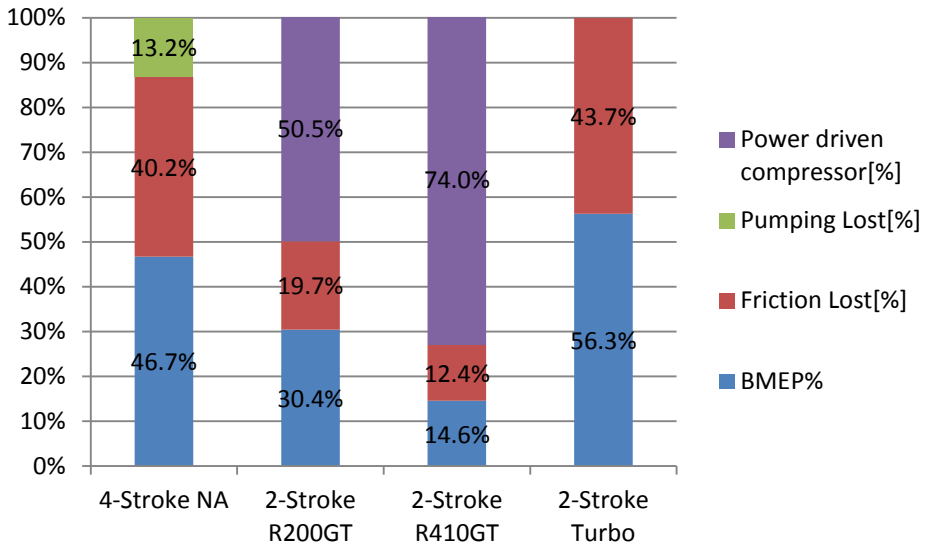

Figure 5.32 Engine output breakdown analysis at 4000rpm and 10kW

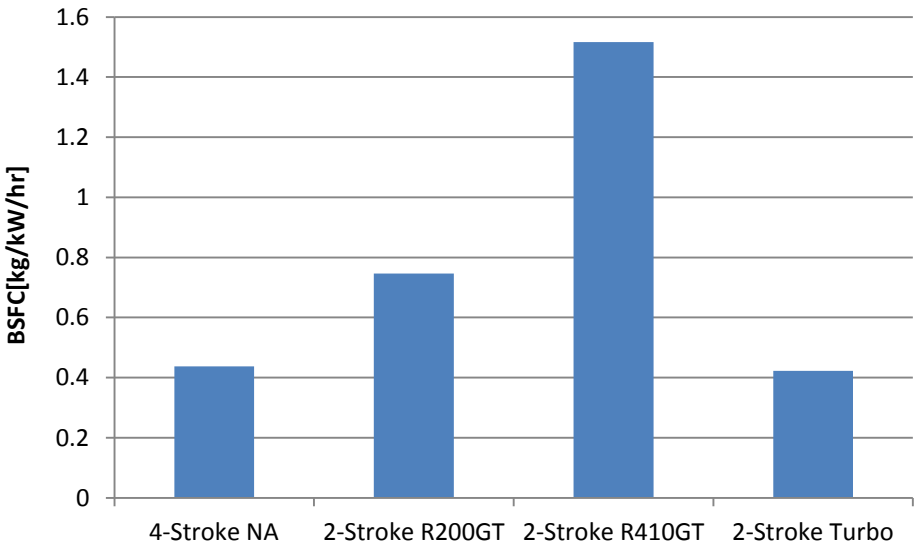

Figure 5.33 BSFC at 4000rpm and 10kW

Figure 5.34 to Figure 5.38 show the engine output breakdown analysis at 2000rpm and 1000rpm and various loads. Similar to the results at 4000rpm engine speed, the turbocharged 2-stroke engine shows similar mechanical efficiencies to the baseline 4-stroke engine, whilst the supercharged engines have to take high proportion of engine output to drive the supercharger. In addition, it is noted that the baseline 4-stroke engine is characterised with higher pumping losses at lower load than the turbocharged 2-stroke engine.

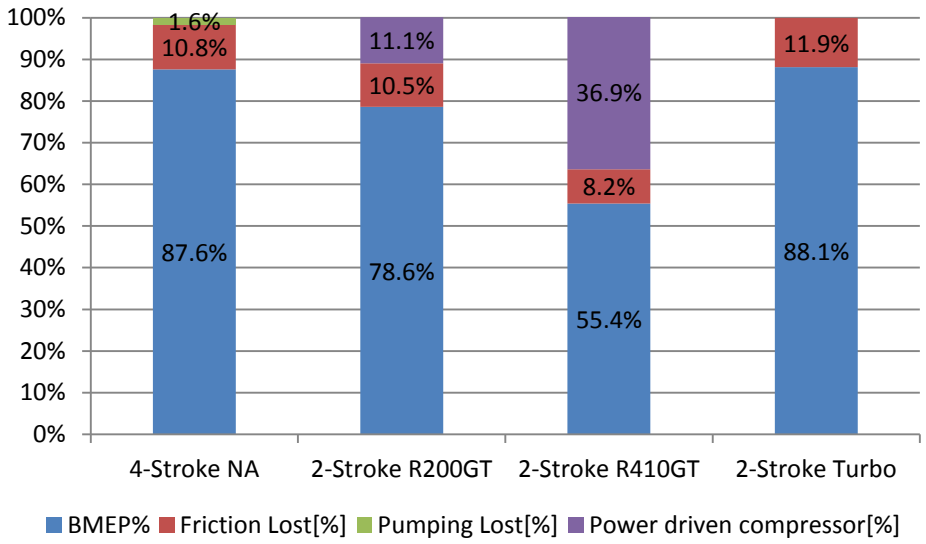

Figure 5.34 Engine output breakdown analysis at 2000rpm, 20kW

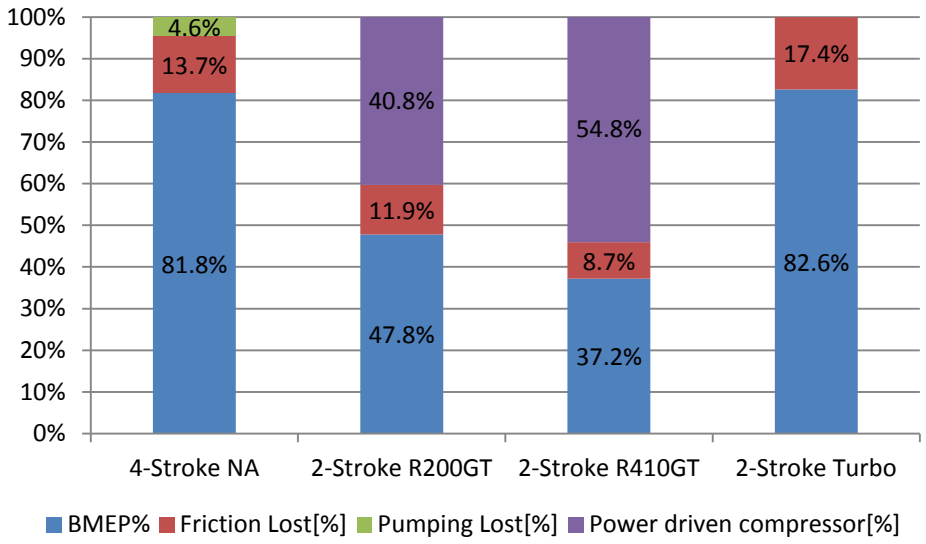

Figure 5.35 Engine output breakdown analysis at 2000rpm, 10kW

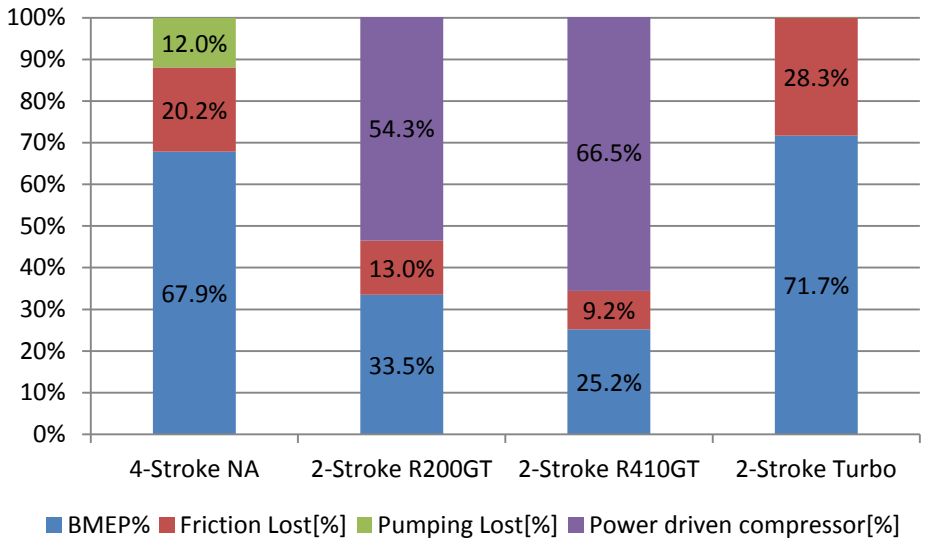

Figure 5.36 Engine output breakdown analysis at 2000rpm, 6kW

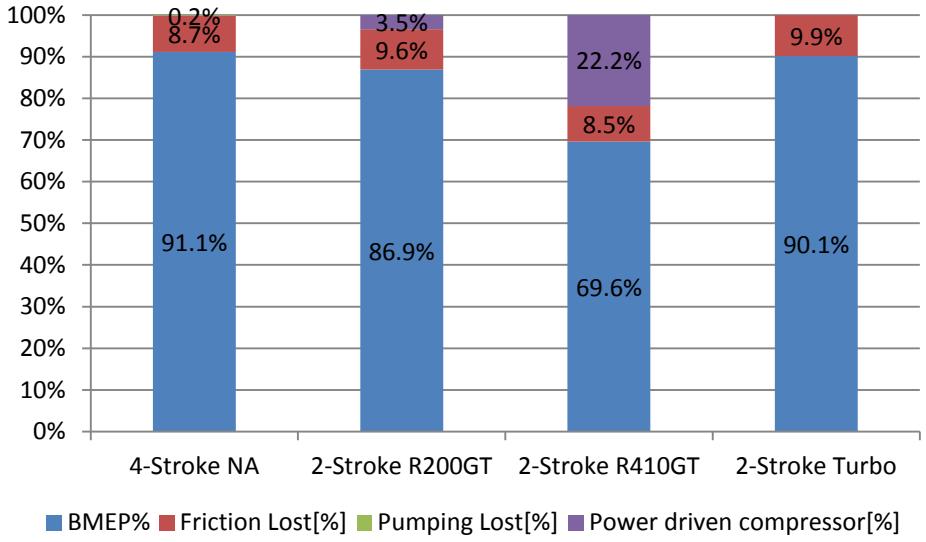

Figure 5.37 Engine output breakdown analysis at 1000rpm, 10kW

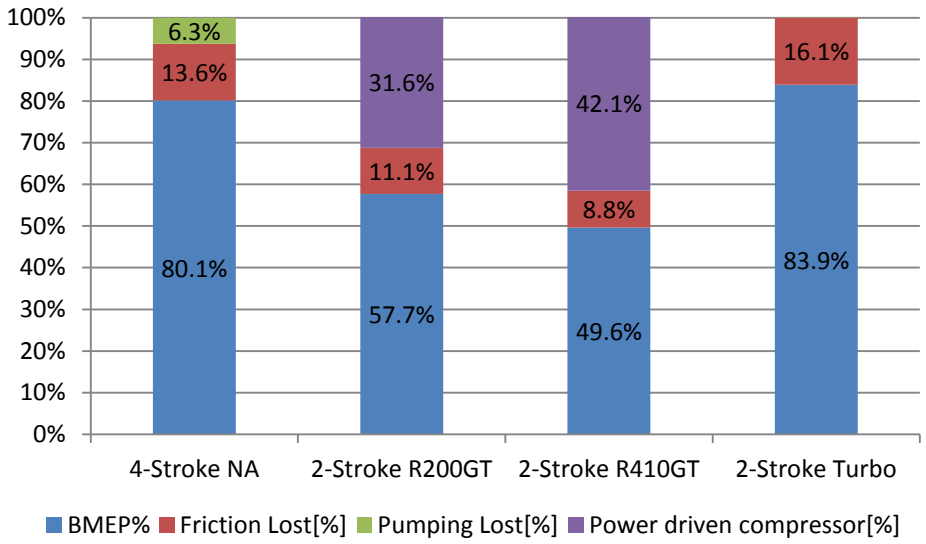

Figure 5.38 Engine output breakdown analysis at 1000rpm, 5kW

At the same engine speed and load, as shown in Figure 5.39, supercharged 2-stroke engines incur much higher fuel consumption especially at part load and low load conditions.

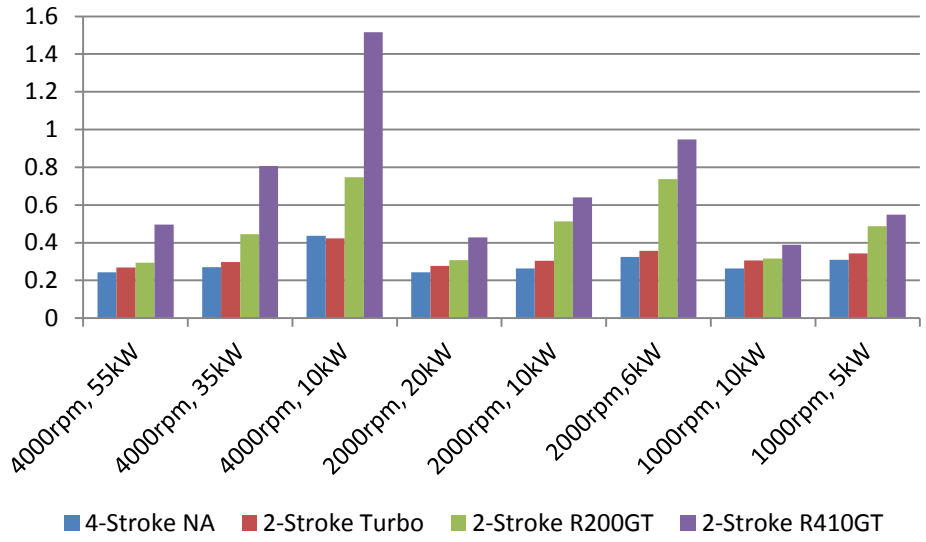

Figure 5.39 BSFC comparisons at the same speed and load conditions between 4-stroke engine and 2-stroke engines

Because 0.9 litre 3-cylinder 2-stroke engines are capable of generating higher torque outputs than the baseline 1.6 litre 4-cylinder 4-stroke engine, one possible way to improve the 2-stroke engine's fuel consumption during vehicle driving is engine

downspeeding. Equation 5.9 shows the relationship between engine speed, power and torque,

$$P = 2\pi N_s T_t \qquad \text{[E-5.9]}$$

Where

P – Engine power

N_s – Engine speed

T_t – Engine Torque

Thus, for the same engine power required to drive a vehicle, the engine operating points can be shifted to higher torque and lower engine speed when the 2-stroke engines are used.

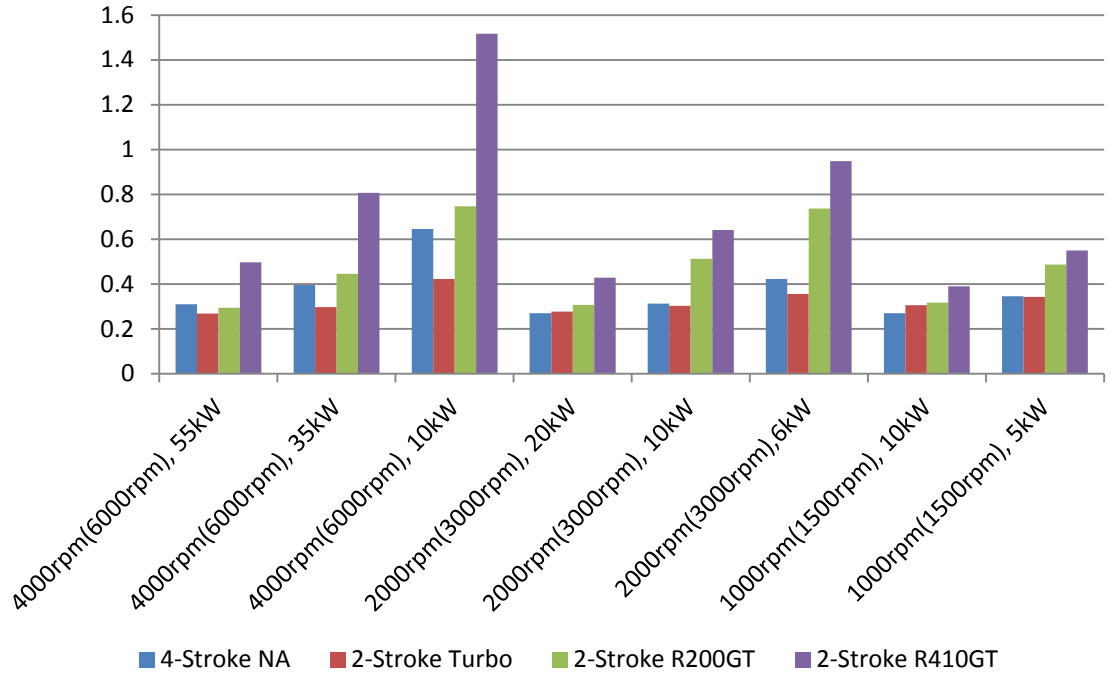

Figure 5.40 BSFC at various engine speed and load.

Figure 5.40 compares the BSFC values of the baseline 4-stroke engine operating at one and half times of the 2-stroke engines; i.e., 4-stroke 6000rpm vs. 2-stroke 4000rpm, 4-stroke 3000rpm vs. 2-stroke 2000rpm, and 4-stroke 1500rpm vs. 2-stroke 1000rpm. The results reveal that the lower fuel consumption can be obtained with the turbocharged 2-stroke engine operations than the baseline 4-stroke engine.

Furthermore, the 0.9litre turbocharged 3-cylinder 2-stroke engine model has been shown to produce excess power and torque than the targeted maximum performance of the baseline 4-stroke model. Thus, further downsizing of the turbocharged 2-stroke engine can be exploited to reduce the engine fuel consumption by reducing the engine to 0.6L capacity with two cylinders. The added benefit of the 2-cylinder vs. 3-cylinder is the removal of interference in the exhaust flows during the scavenging periods of adjacent cylinder when the exhaust duration has to be over 120ºCA.

Figure 5.41 shows the full load brake power and torque curves of the baseline 4-stroke engine, turbocharged 3-cylinder (0.9 litre) and 2-cylinder (0.6 litres) 2-stroke engines. Although the power and load delivered by the 0.6L 2-stroke engine are lower than the 0.9L 2-stroke engine, they are still higher than the baseline engine and meet the vehicle's performance requirement.

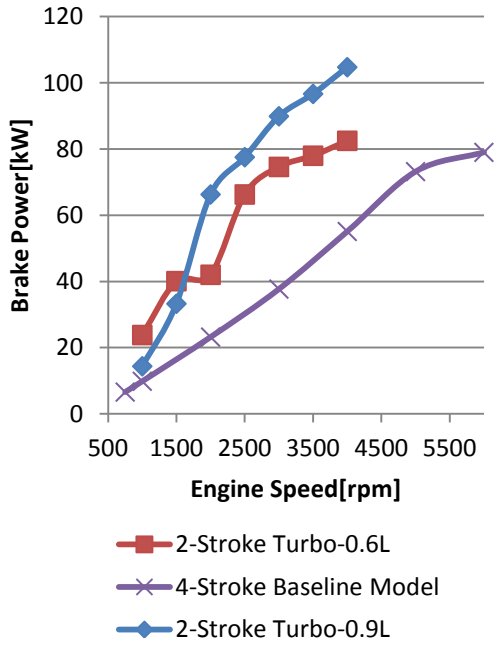

Brake Power

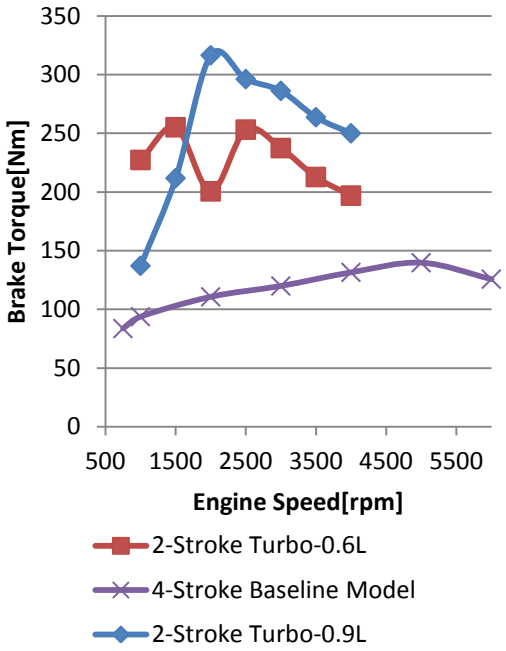

Brake Torque

Figure 5.41 Full load brake power and torque of turbocharged 2-stroke engines

Figure 5.42 shows that at the same engine speed and power, 0.6L turbocharged 2-stroke engine shows better fuel consumption than the 0.9L 2-stroke model but is still

poorer than the 4-stroke baseline engine at most of the points. However, Figure 5.43 shows that 0.6L 2-stroke engine shows the best fuel economy at most of the points when the downspeeding is employed.

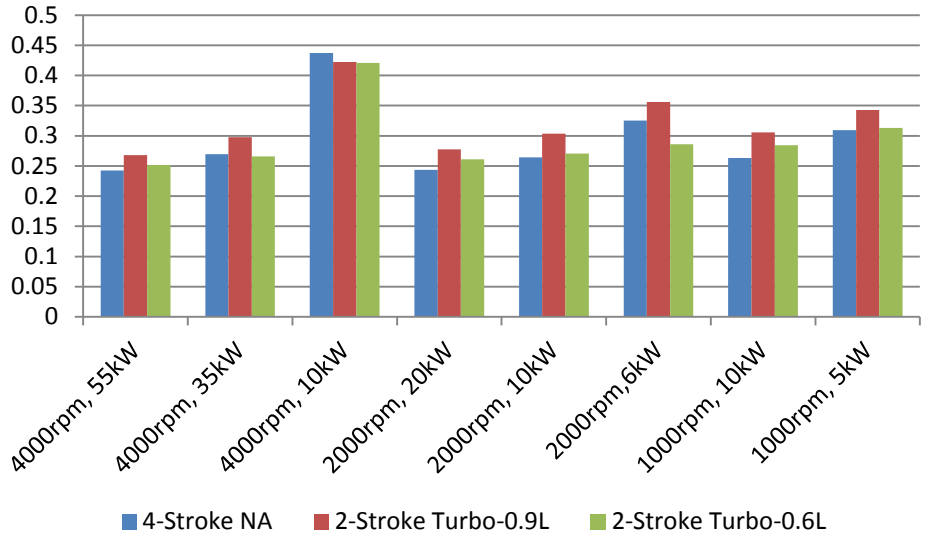

Figure 5.42 BSFC of the baseline 4-stroke and turbocharged 2-stroke engines at the same speed and power

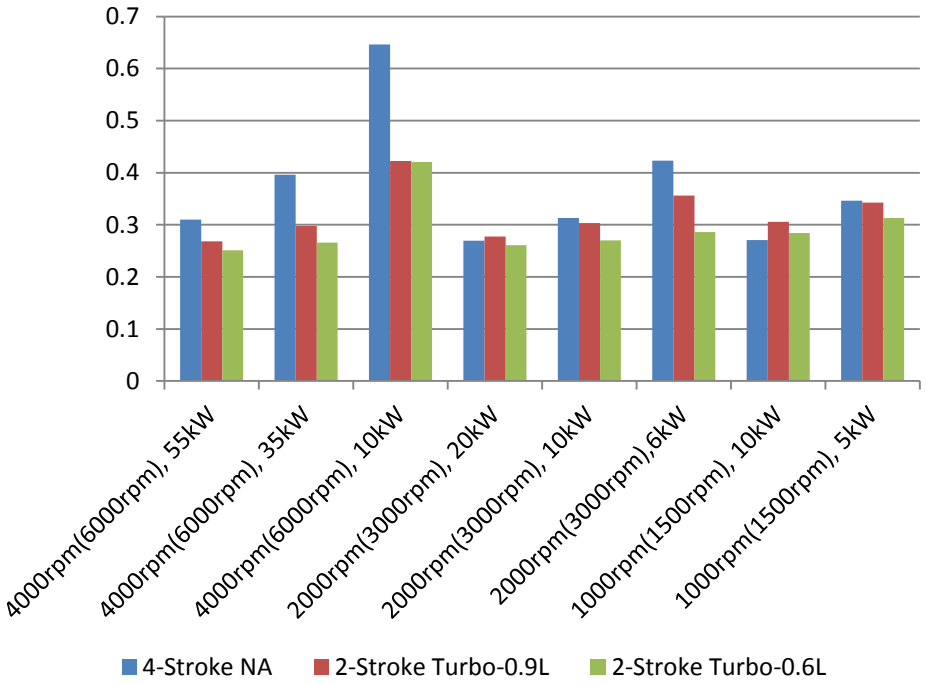

Figure 5.43 BSFC of the baseline 4-stroke and downspeeded 2-stroke engines

Figure 5.44 plots the corresponding BSFC maps of the three engines as a function of speed and load. In order to take into account of the downspeeding potential of the 2-stroke operations, Figure 5.45 includes the revised BSFC map of the 4-stroke engine which is rescaled to the speed range up to 4000rpm according to Equation 5.9. For example, the 6000rpm and 75Nm point with 47.7kW brake power of the 4-stroke model in Figure 5.44 is now shown as 4000rpm and 107.5Nm with same brake power in Figure 5.45.

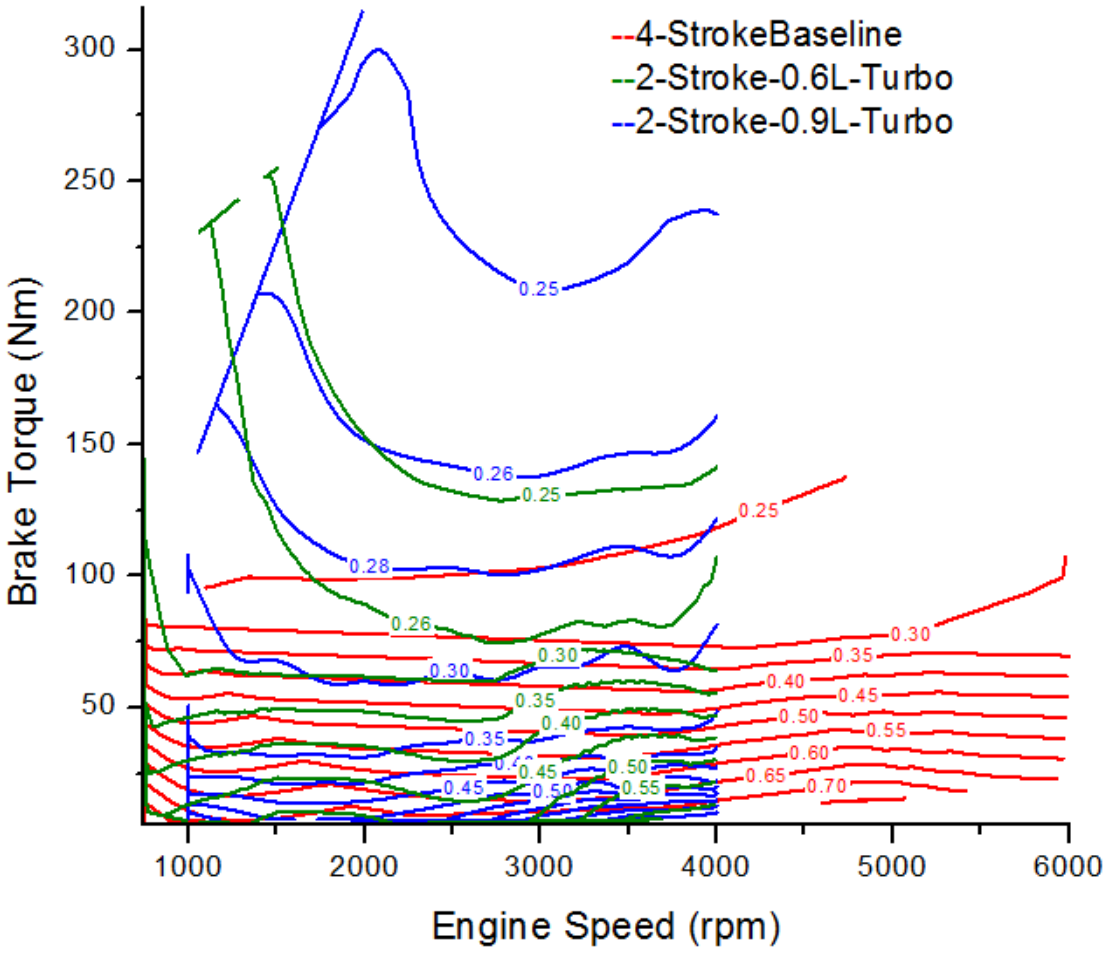

Figure 5.44 BSFC contours of the 4-stroke and turbocharged 2-stroke engines

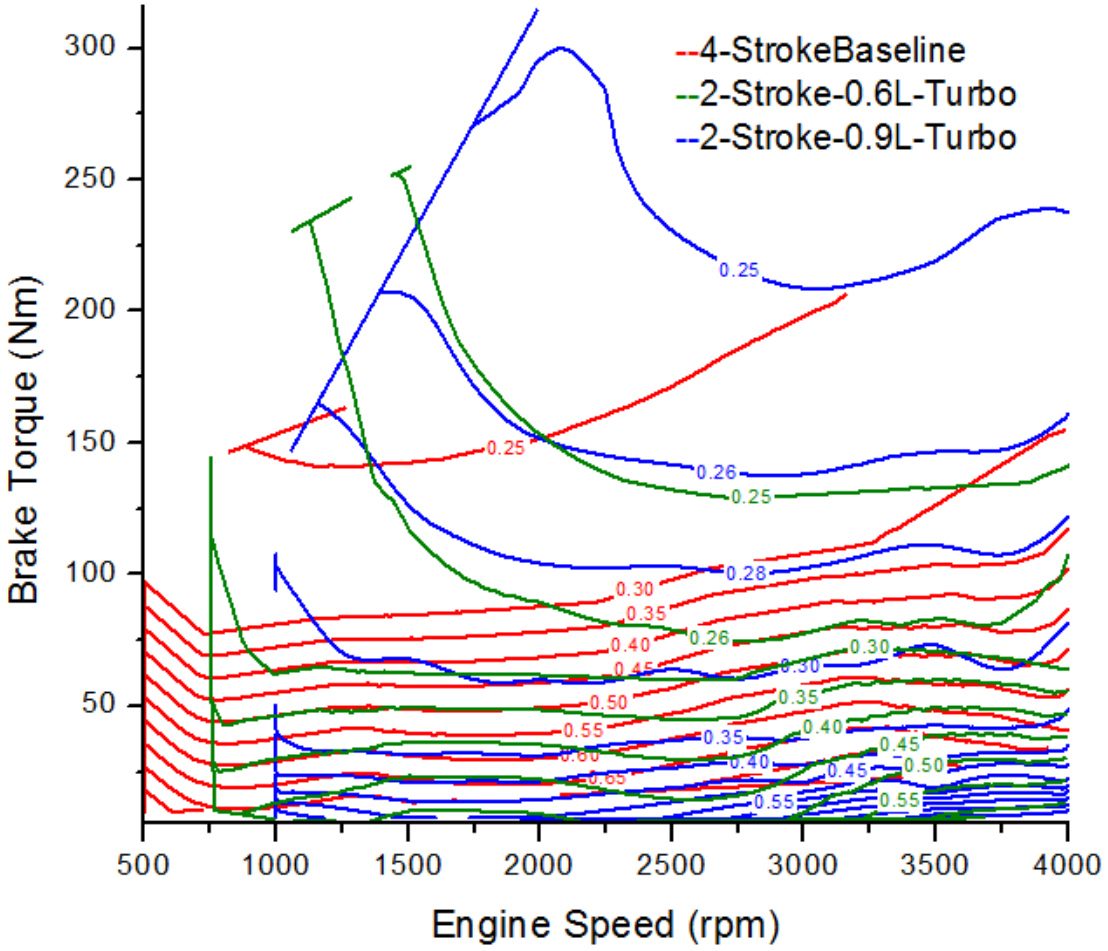

Figure 5.45 BSFC contours of the turbocharged 2-stroke engines and the rescaled BSFC map of the baseline 4-stroke engine

According to Figure 5.44, without considering the downspeeding method, both 2-stroke engines show poorer fuel economy than the baseline 4-stroke engine apart from the low load area. However, when considering the down speeding strategy, both 2-stroke engines' fuel economy surpasses the baseline engine. The 0.6L 2-cylinder turbocharged 2-stroke engine shows the lowest fuel consumption as shown in Figure 5.45.

5.3.4 2 Vehicle simulation results based on New European Driving Cycle (NEDC)

Data obtained from the engine simulation were imported to the vehicle calculation model mentioned in Section 5.2. The vehicle simulation was carried out with 3 sets of gear configurations as shown in Table 5.3. It should be mentioned that the engine weight has been assumed the same for all three engines. In practice, noticeable

weight reduction from the 4-cylinder 4-stroke engine to the 2-cylinder turbocharged 2-stroke engine will be envisaged, which could benefit the vehicle's fuel economy.

Table 5.3 Transmission gear ratio

Gear Ratio Setup	Gear Mechanical Efficiency	SET1	SET2	SET3
Number of gears		5	5	5
1st Gear ratio	0.95	5.4	3.6	2.4
2nd Gear ratio	0.96	3	2	1.33
3rd Gear ratio	0.97	2.025	1.35	0.9
4th Gear ratio	0.98	1.5	1	0.67
5th Gear ratio	0.97	1.2	0.8	0.53

Figure 5.46 shows the engine operating points during the vehicle's NEDC calculation, together with the full load torque curves of the baseline 1.6L 4-cylinder 4-stroke engine, 0.9L 3-cylinder and 0.6L 2-cylinder turbocharged 2-stroke engines. With gear set1, all engine operating points are covered for each of the three engines.

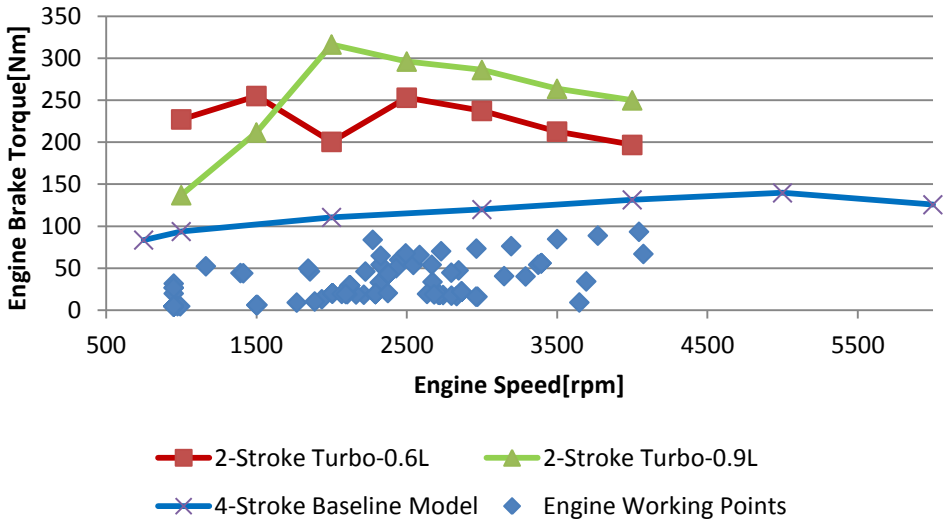

Figure 5.46 Engine operating points with gear set1 during NEDC and engine full load torque curves

Figure 5.47 and Figure 5.48 show the engine operating points and the full load curves of the engines with transmission gear set2 and set3, respectively. With down-speeded gear set2, some of the high load engine points cannot be covered by the 4-

stroke engine. This indicates that the gear set2 is beyond the down speeding boundary of the 4-stroke engine. With gear set3, the engine operating points are approaching the torque limit of the large 2-stroke engine whilst a significant proportion of engine working points is out of the area covered by the baseline 4-stroke engine.

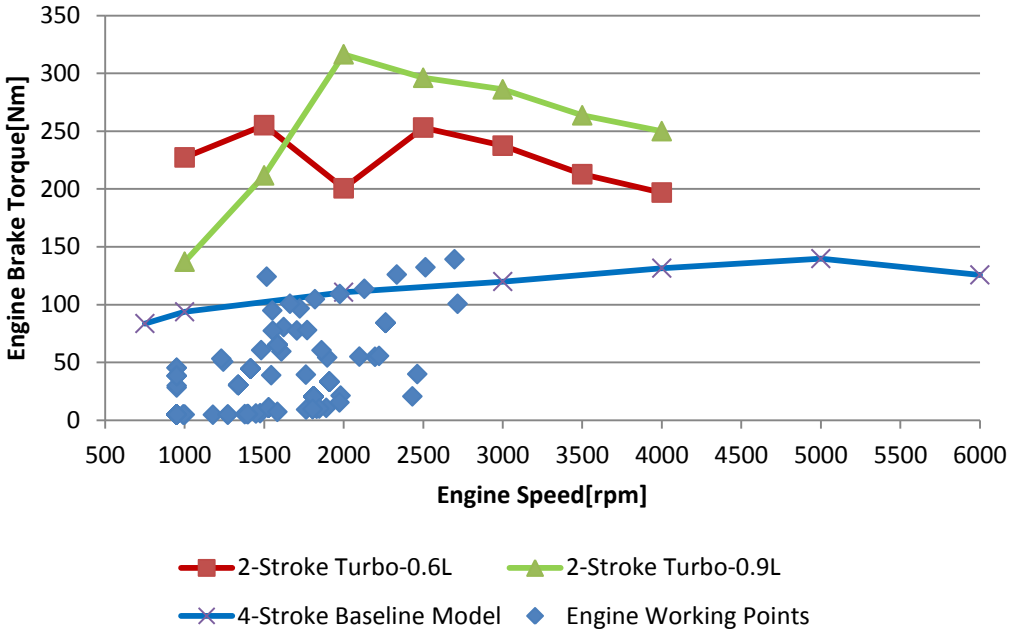

Figure 5.47 Engine operating points with gear set2 during NEDC and engine full load torque curves

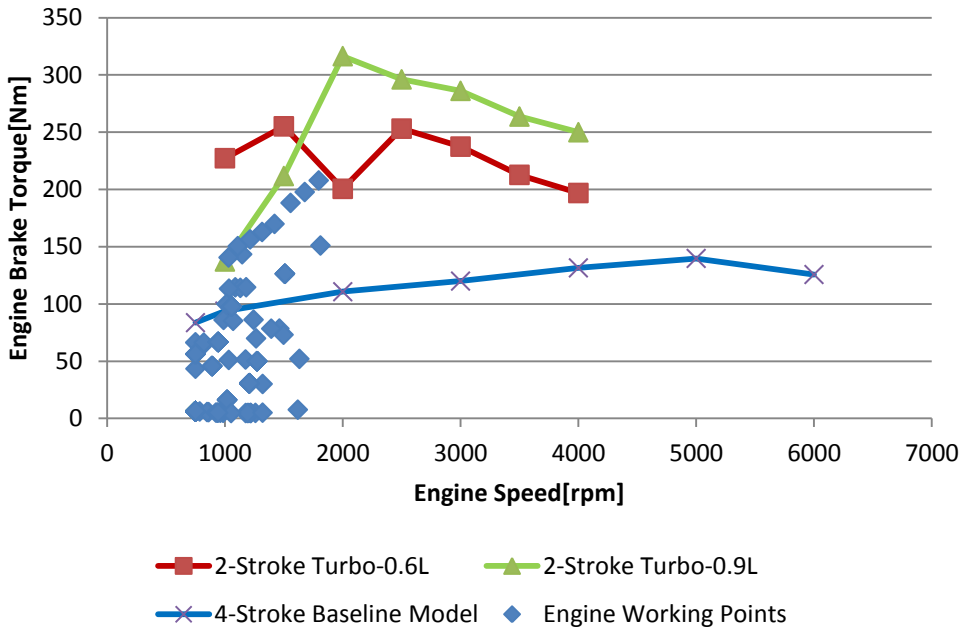

Figure 5.48 Engine operating points with gear set3 during NEDC and engine full load torque curves

Figure 5.49 shows the average fuel consumptions of all three engines with the 3 gear sets during NEDC. The downspeeding strategy improves the fuel consumption performance on all engines. However, because of their superior low speed torque, the turbocharged 2-stroke engines have wider torque margin than the 4-stroke engine and hence they can be down-speeded for better vehicle fuel economy. It can be seen that the 0.6L 2-cylinder turbocharged 2-stroke engine with gear set3 delivers 6.91L/Km fuel consumption during NEDC, which improves the fuel consumption by 23.6% over the baseline 4-stroke engine.

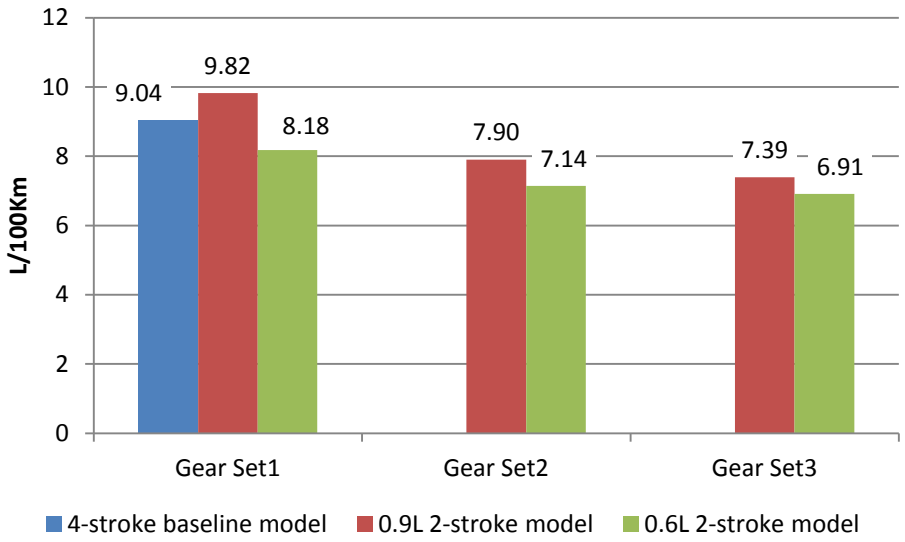

Figure 5.49 Average fuel consumption over NEDC

5.4 Summary

This chapter focuses on the 1D simulation of the engine performance and vehicle fuel consumption simulations of three engines. They are the 1.6L 4-cylinder 4-stroke NA engine as the baseline, a 0.9L 3-cylinder 2-stroke engine and a 0.6L 2-cylinder 2-stroke engine with a supercharger or a turbocharger.

All simulations are focused upon engine steady state, the transient performance has not been investigated. Because a high proportion of the engine output is used to drive the supercharger, supercharged engines cannot meet the output target without fuel economy penalties. Compare to a supercharger, a turbocharger is driven by the exhaust energy that would otherwise be lost. The turbocharged 2-stroke engines outperform the supercharged operations in both torque output and fuel consumptions, though it increases the exhaust back pressure and the residual gas fraction in the cylinder.

Because of its superior low speed torque, the turbocharged 2-stroke engine can be operated at lower speeds with a lower gear ratio to maximize the downspeeding potential. Combining downsizing and downspeeding, the 0.6L 2-cylinder turbocharged 2-stroke engine delivers 23.6% less fuel consumption compared to the baseline model without penalizing the engine power and torque output.

Chapter 6 Single Cylinder Uniflow 2-stroke Engine and Experimental Facility

6.1 Introduction

In order to verify the simulation results and carry out preliminary experimental investigation of the newly proposed Boosted Uniflow Scavenged Direct Injection Gasoline (BUSDIG) engine concept, a single cylinder engine was modified to operate as a uniflow 2-stroke direct injection gasoline engine. In this chapter, the design and implementation of the modified engine is described in detail.

6.2 Uniflow 2-stroke engine setup

Figure 6.1 shows the layout of the newly designed engine assembly for the uniflow 2-stroke operation. A single cylinder Ricardo Hydra optical engine with a bespoke four-valve DI gasoline cylinder head is used as the base engine. The engine is mounted on a dedicated single cylinder engine test bed with integrated coolant and oil cooling modules. The engine is driven by a McClure DC dynamometer with a maximum speed of 6000rpm. The dynamometer is controlled by a separate control console with a < ±5 rpm accuracy.

The original cylinder head is mounted above a glass ring. Beneath the glass ring, there is a newly designed intake block assembly consisting of an intake channel block (in Green) with embedded intake channels, an intake port block (in Blue) with embedded intake ports on a specified orientation, and a new cylinder liner with holes cut and aligned to the intake ports. The original engine extension block (in Brown) and elongated piston with a crown window is designed to accommodate a 45º mirror for in-cylinder optical access. A new longer timing belt is installed to drive both camshafts with 2 tensioners. Details of the engine geometry are given in Table 6.1. Further CAD drawings can be found in Appendix.

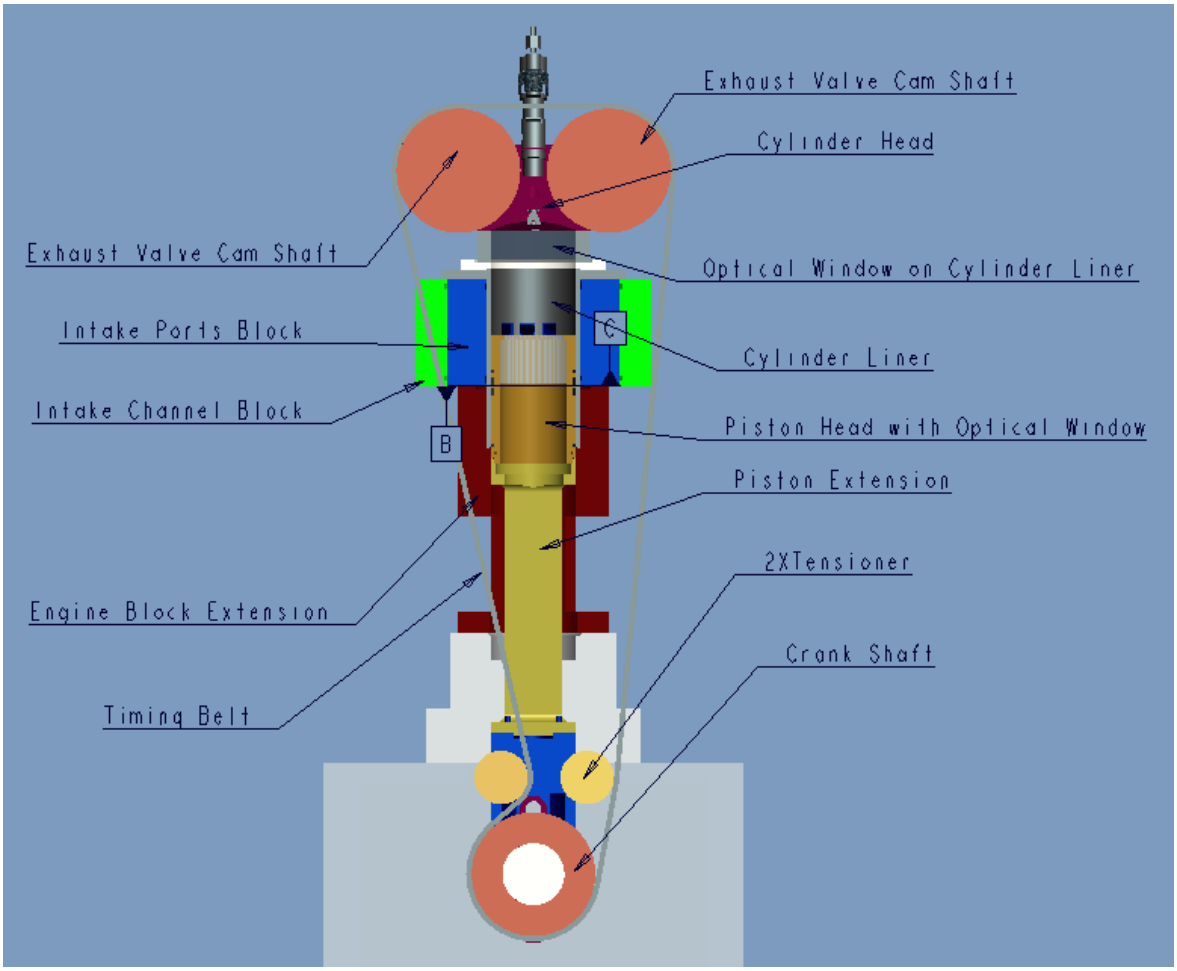

Figure 6.1 Uniflow 2-Stroke Single Cylinder Engine assembly layout

Table 6.1 Engine configuration

Combustion chamber	Pent-roof
Displaced volume	450 cc
Bore	80 mm
Stroke	89 mm
Compression Ratio	8:1 to 12:1
Inlet valves diameters	29.5mm
Exhaust valves diameters	21mm
Valve lift	9mm
Valve opening duration	110ºCA

6.2.1 Cylinder Head

The cylinder head used for the experimental engine is a bespoke single cylinder head machined from a single aluminium block by Orbital Engine Corporation Ltd. It features a pentroof combustion chamber, a centrally located injector fitting hole and a spark plug, as shown in Figure 6.2. Two independent camshafts actuate the two intake valves and two exhaust valves. For the uniflow 2-stroke operation, all 4-valves are used as exhaust valves. Since each camshaft is designed to produce a valve opening period of 110ºCA, the exhaust period can be varied between 110ºCA to 220ºCA by adjusting the relative cam phasing. A pressure transducer is installed on the cylinder head. In order to replace the air assisted injector with the piezo DI injector, an adaptor was designed for the injector to fit the injector mounting slot. This adaptor was designed for multiple injector usage. When another injector is required, no more modification was required in the cylinder head, but only fitting the adaptor to the injector.

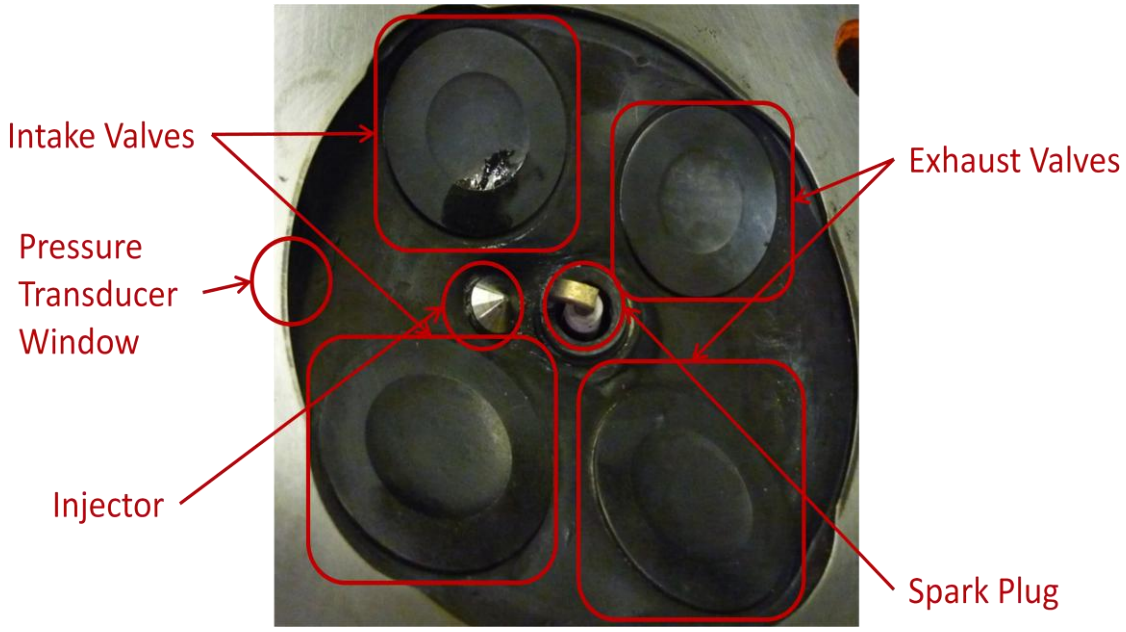

Figure 6.2 Cylinder head layout

6.2.2 Optical window ring

The optical window ring is shown in Figure 6.3. The window ring is made of fused silica and can withstand up to 50bar pressure. The ring sits into a seat with 3mm depth grove. High temperature gaskets of 1.5mm are placed on both sides of the glass ring to protect it from direct contact with the metal surfaces and provide the sealing. The glass ring is mounted between the cylinder head and cylinder block by means of 4 ring spacers positioned by the long cylinder head bolts and matched in their height to that of the glass window plus the thickness of the gaskets below and above the glass ring.

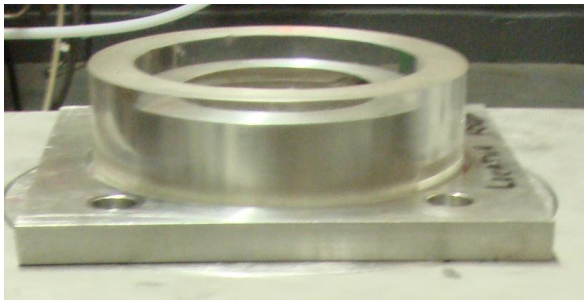

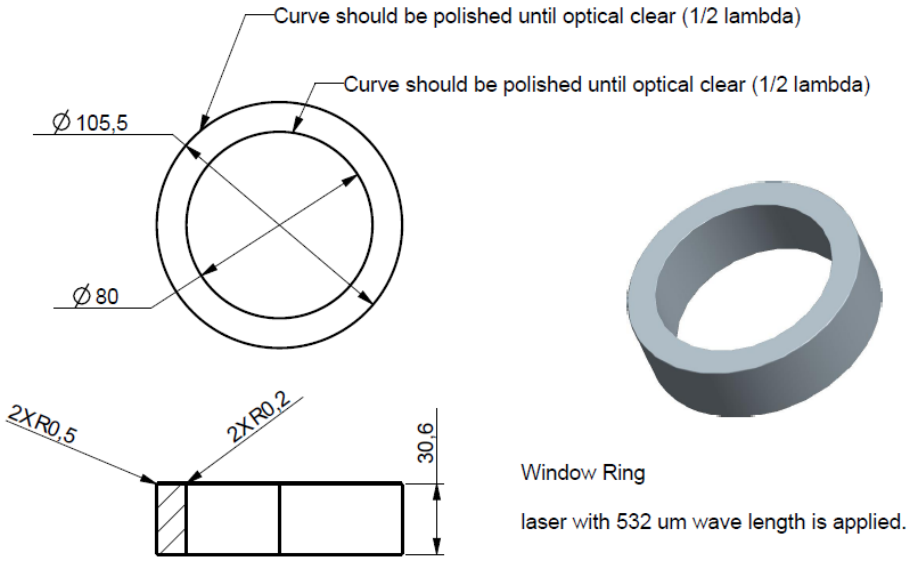

Figure 6.3 Optical window ring

6.2.3 Cylinder liner

The baseline 4-stroke Ricardo Hydra optical engine was designed with an extension block to accommodate the elongated hollow piston for in-cylinder optical access through the piston crown window via a 45 degree mirror mounted in the block. This extension block was machined with an integrated cylinder liner. As shown in Figure 6.1, a new intake block is to be mounted above this original extension block and the piston will need to travel inside both the new intake block and the original extension block. In order to prevent piston rings from damage when moving across the interface of these two blocks, a new longer liner was sourced from Mahler and installed through both blocks.

As shown in Figure 6.4, the new one-piece cylinder liner was machined with six windows in the top part, with three on opposite sides, which are aligned to the intake ports in the intake port block.

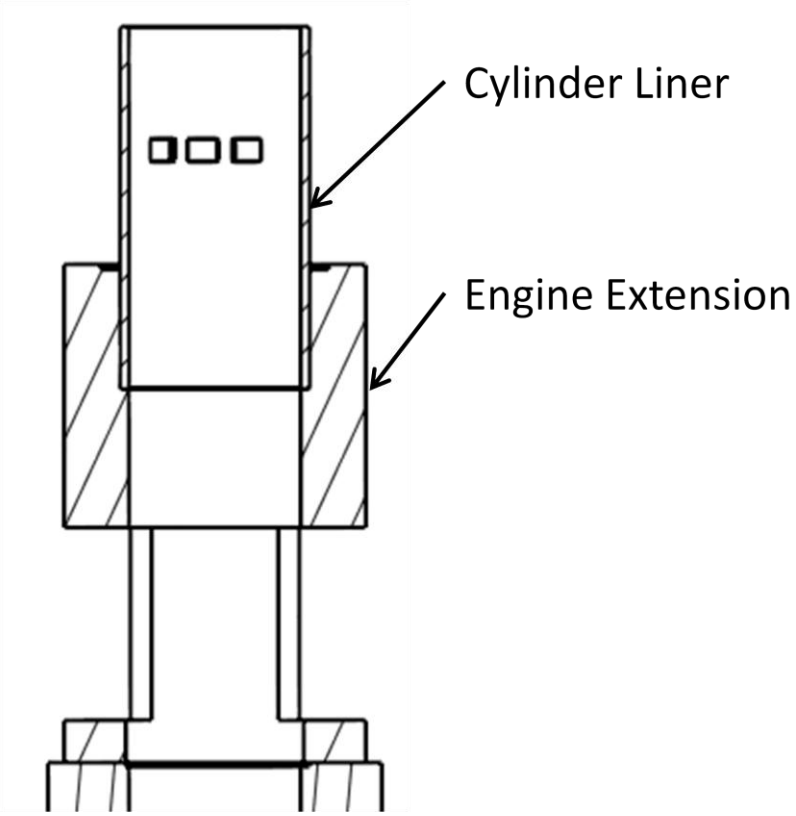

Figure 6.4 New Cylinder Liner

6.2.4 Intake port block and intake channel block

The intake port block and intake channel block are required to allow the boosted air into the combustion chamber. By having separate blocks, the geometry of the intake ports can be altered with different intake port blocks in order to study the effect of intake port design on in-cylinder flow and scavenging process. The intake port block and intake channel block layout is shown in Figure 6.5. Along the interface between the cylinder liner and intake port block, and also along the interface between the intake channel block and intake port block, two O-ring groves are machined for high temperature O-rings on both top and bottom sides to seal the intake path.

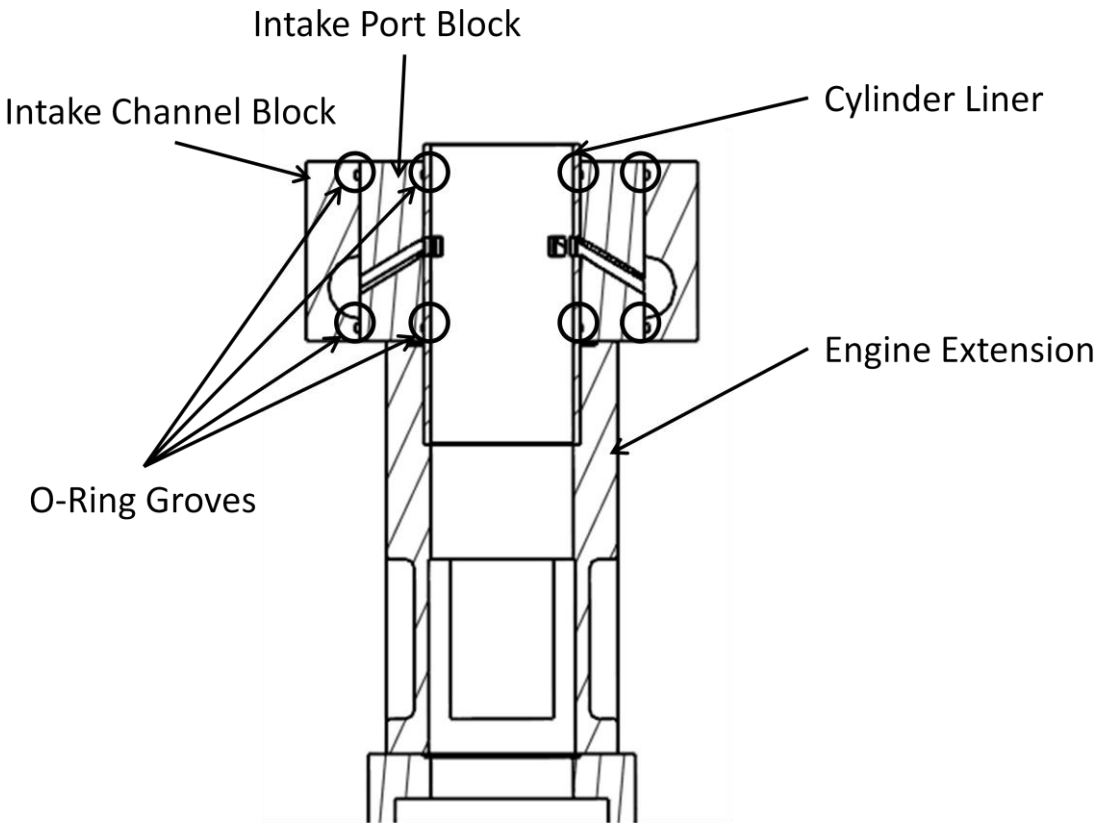

Figure 6.5 Intake port block and intake channel block layout

As shown in Figure 6.6, the intake port block is designed to provide the intake ports of appropriate geometry according to the 3D CFD simulation studies. As discussed in Chapter3, the intake ports affect the engine breathing performance directly, and the orientation of intake ports also affect the in-cylinder flow swirl generating ability. The 3D CFD simulation results suggested that the intake ports with 60º axis inclination angle and 20º swirl orientation angle gave the best performance. The exit of intake ports in the intake port block is aligned to the ports in the cylinder liner.

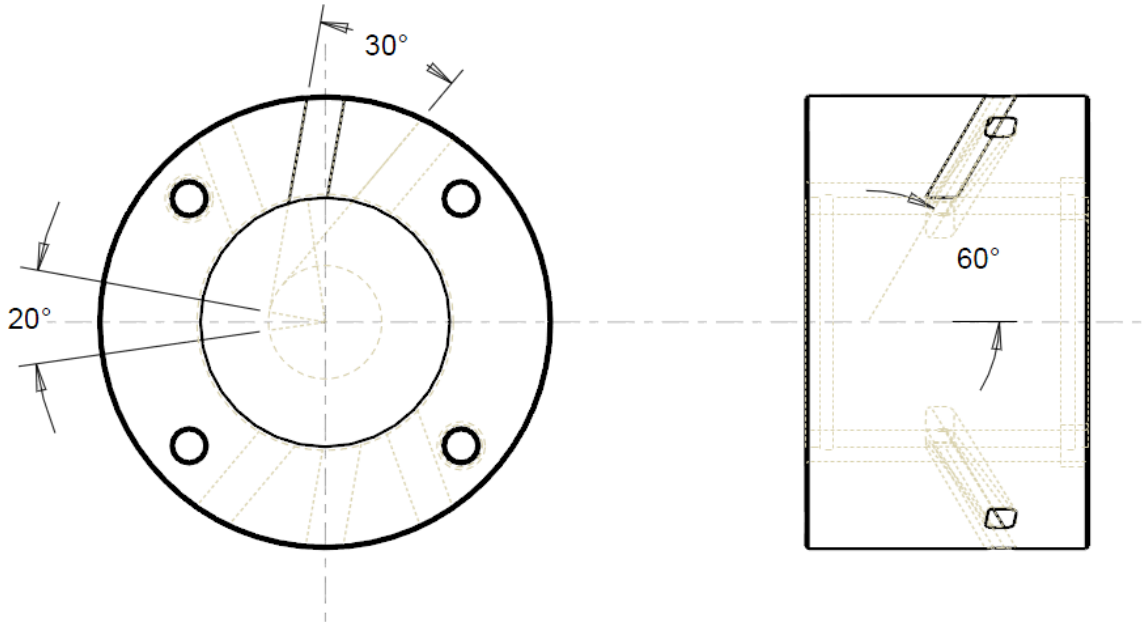

Figure 6.6 Intake port block configuration

Figure 6.7 shows the design of the intake channel block which connects the boosted intake air to the intake ports. The block features two channels on each side of the block and each channel is aligned to the 3 ports on one side of the intake port block.

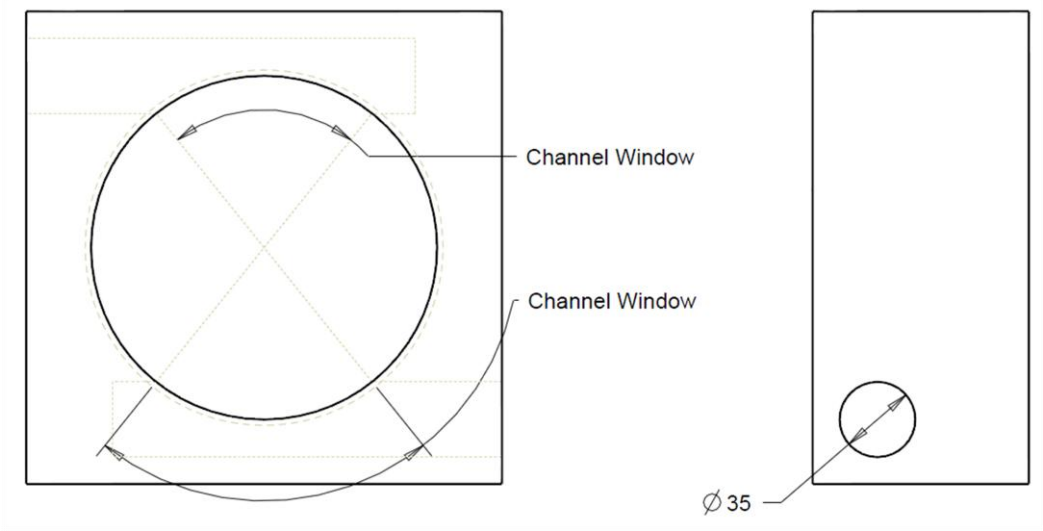

Figure 6.7 Intake channel block configuration

6.2.5 Piston assembly

As shown in Figure 6.8, the piston assembly consists of a top piston part with a flat optical window, a piston spacer and a piston extension part.

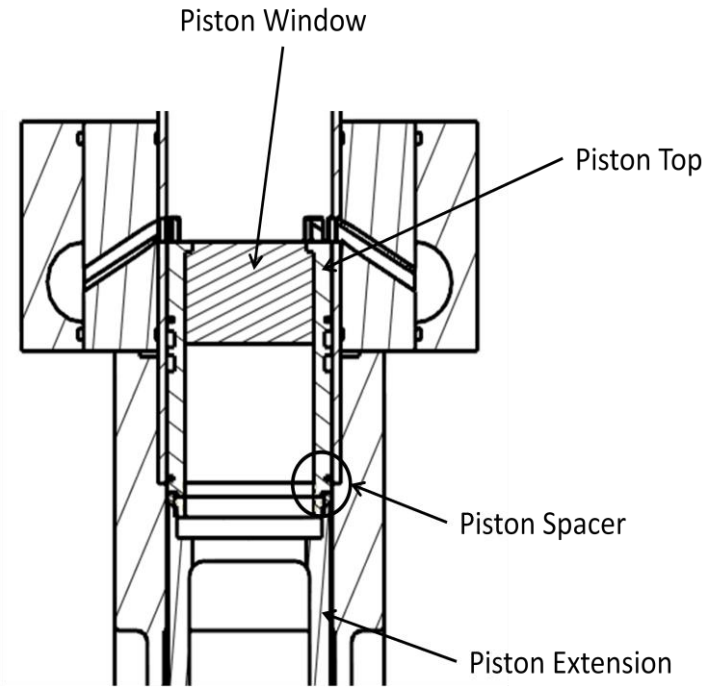

Figure 6.8 Piston assembly

The piston window is made of fused silica, same as the window ring. Along the side surface of the piston window, high temperature silicon paste was applied to fill the gap between the window and piston inner surface for sealing. High temperature gaskets were placed below and above the window. The top piston part was mounted onto the piston extension part, which is fixed to a standard piston in the engine block. Between the top piston and piston extension parts, a spacer is installed to adjust the compression ratio and intake port opening timing. For the current experiments, the engine compression ratio was set to 8:1 and the intake port opening timing period was set between 120ºATDC and 240ºATDC according to the simulation results.

6.2.6 Timing belt mounting

The base engine was designed to operate in the 4-stroke mode. The original crankshaft pulley and the camshaft gear had a ratio 1:2 in diameter. To achieve 2-stroke operation, a larger crankshaft pulley was installed to give a 1:1 ratio to the camshaft pulley, as shown in Figure 6.9, so that the camshaft will rotate as the same speed as the crankshaft.

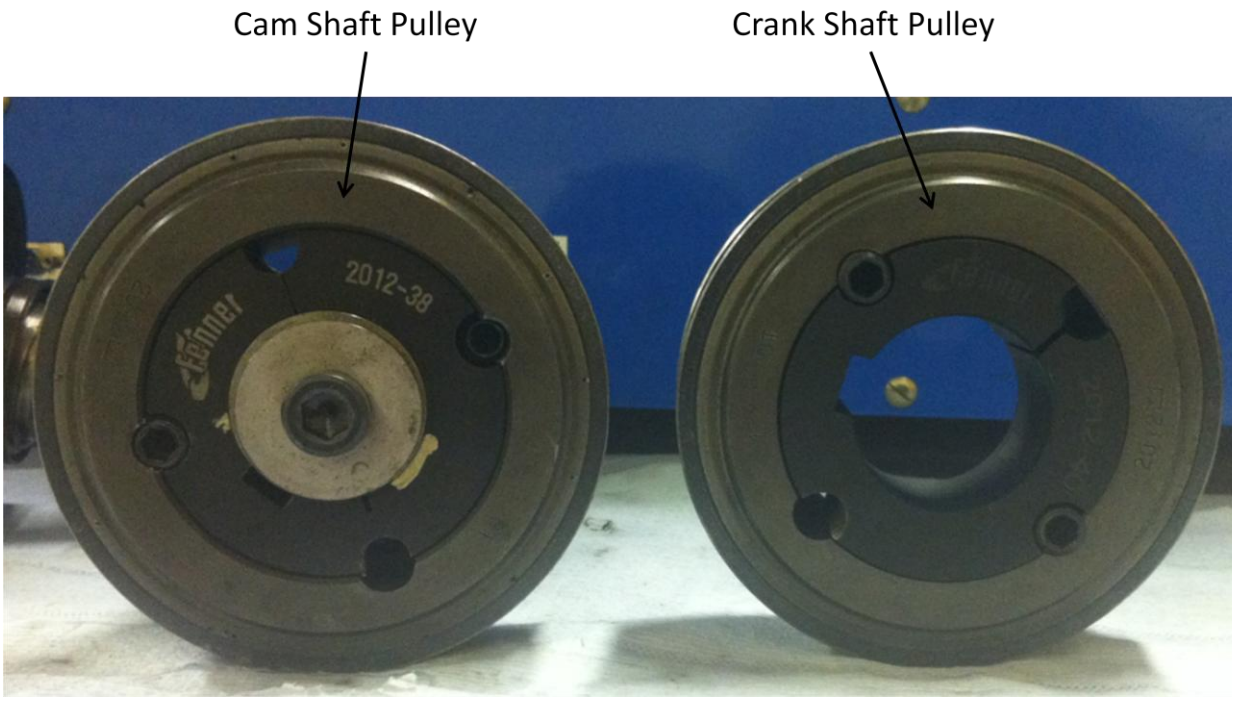

Figure 6.9 Camshaft pulley and crankshaft pulley for 2-stroke operation

The two original exhaust valves opening were set to 80ºATDC and the original intake valves opening time were set to 130ºATDC. As the opening duration was 110ºCA for all valves, so a combined exhaust period was between 80ºATDC to 240ºATDC.

6.3 Boosted air intake system

During the uniflow 2-stroke engine operation, the intake air has to be boosted to scavenge the in-cylinder burned gas from the previous cycle. Figure 6.10 presents the intake air system of the experimental engine. The 2-stage air compressor pressurizes air in the compressed air tank of about 3000L located outside the building. The pressure in the air tank can go up to 200psi. In between of the air compressor and the air tank, a shut-off valve is installed to stop charging the air tank during the engine operation. On the downstream side of the air tank, another shut-off valve and a pressure regulator are installed to open and regulate the compressed air supply and its pressure. The intake system to the single cylinder engine consists of an intake air heater, a throttle, a pressure gauge, and a particle seeding connector used to induce the flow seeding material for the Particle Image Velocimetry (PIV) measurements. A pressure relief valve along the intake airline is used to release the airline pressure.

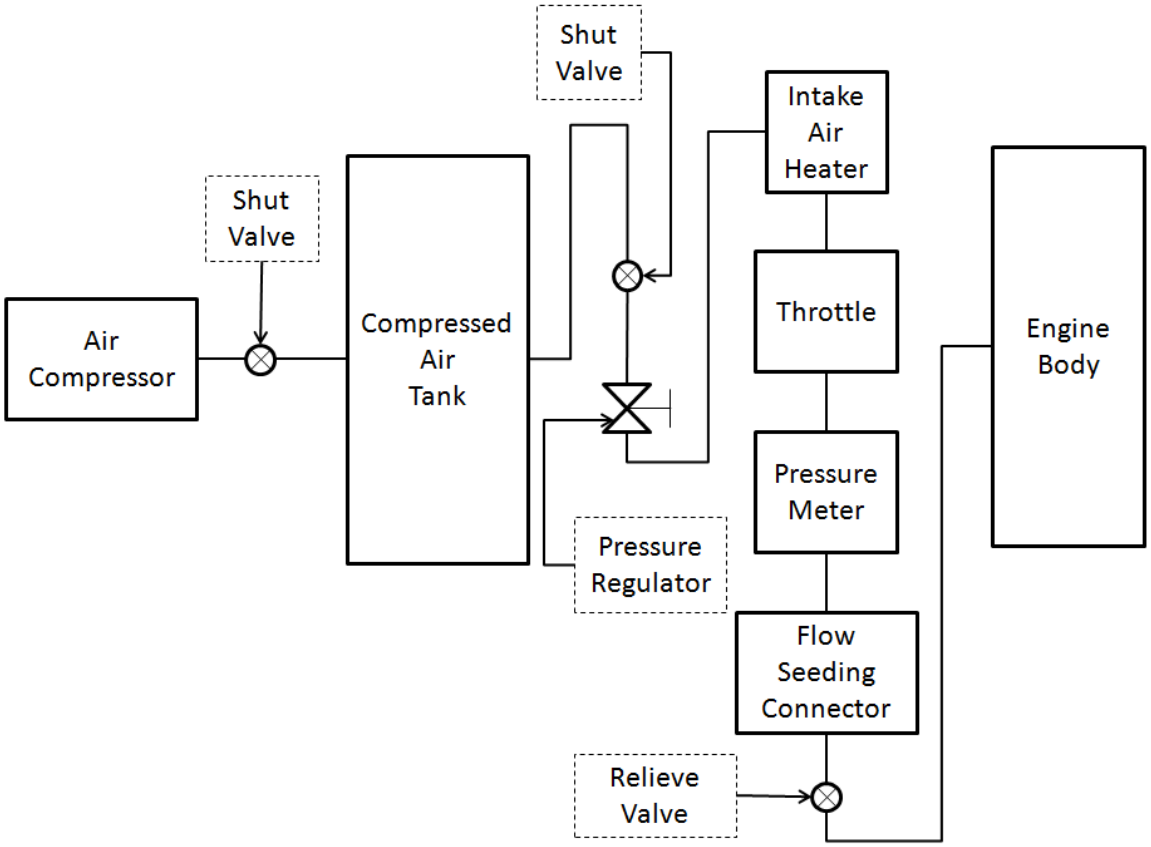

Figure 6.10 The intake system layout

Figure 6.11 shows pictures of the intake and exhaust airline layouts. Before the compressed air reach the engine, the intake airline splits into two ways in order to provide evenly distributed intake pressure on both sides of the cylinder intake block. The two exhaust pipes emerging from each side of the engine cylinder head are merged into one before the exhaust system. The reason of split exhaust lines is the cylinder head was designed for 4-stroke operation with two intake valves on one side and two exhaust valves on the other side. However, for the uniflow 2-stroke operation, both intake and exhaust valves are used as exhaust valves and hence the original intake port and exhaust port are connected together through a U-shaped tube to the exhaust system.

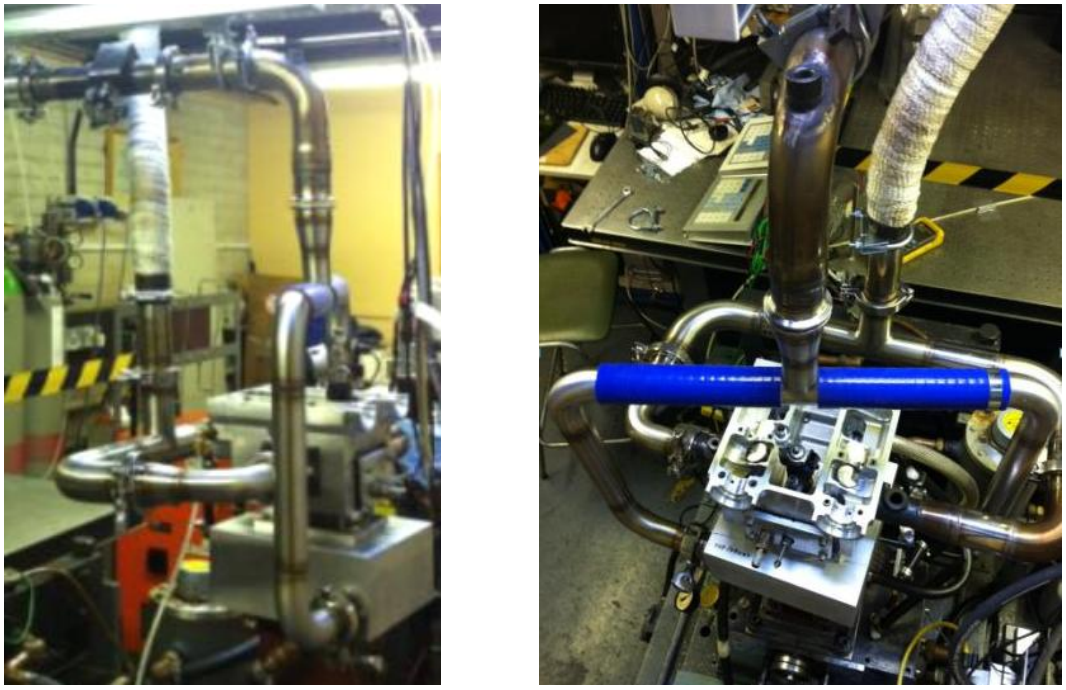

Figure 6.11 The intake(with blue pipes) and exhaust(wrapped by thermal isolation) layout in the single cylinder engine

6.4 Fuel supply system

The fuel supply system layout is shown schematically in Figure 6.12. The fuel from a fuel tank is pressurized by a pump driven by the compressed air. The outlet fuel pressure can be adjusted by the air pressure. The pressurised fuel is supplied to a common rail before the high pressure direct injection injector. A pressure gauge is installed to monitor and set the rail pressure.

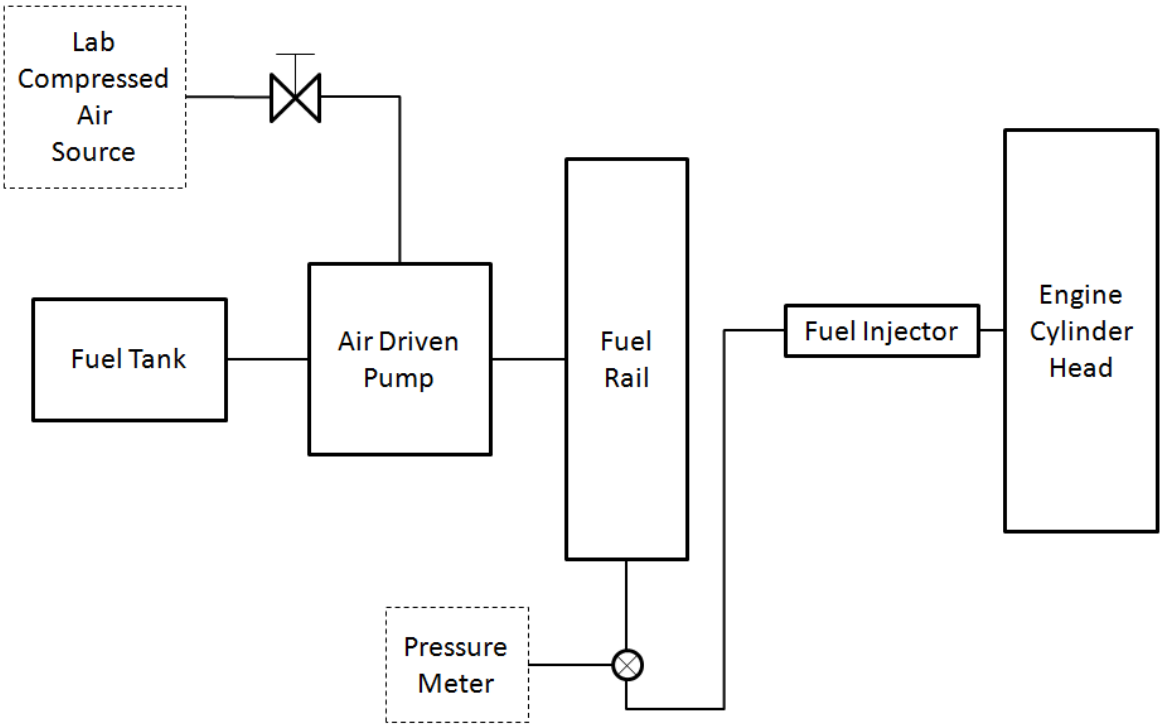

Figure 6.12 Fuel supply system layout

Figure 6.13 shows a picture of the fuel tank, fuel pump and the fuel rail. The pump is an air driven plunger pump (Powerstar 4 S64P4S64). The fuel output pressure is determined by the ratio between the area of the air drive piston, the area of the liquid drive piston and the applied driving air pressure. The relationship of the driven air pressure and the outlet fuel pressure, and the corresponding flow rate is shown in Figure 6.14.

The compressed air used to drive the pump is delivered by the pressurized airline in the laboratory; the air pressure can go up to 8bar. The pressure of air was then regulated down to the required value to control the fuel outlet pressure.

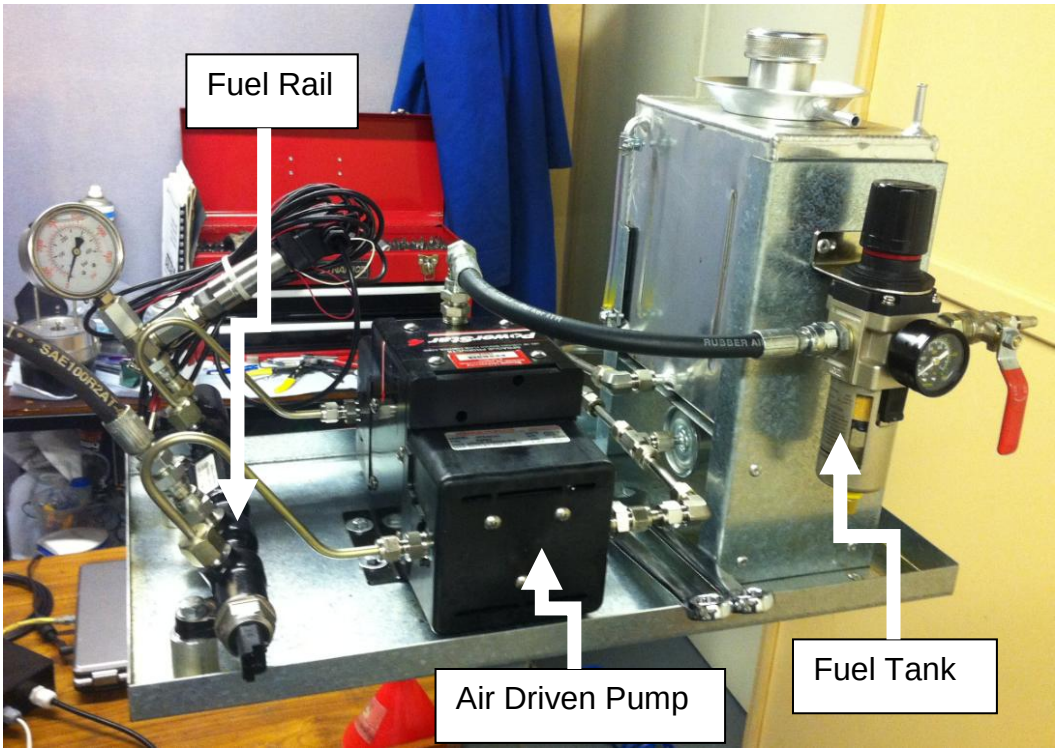

Figure 6.13 Fuel tank, air driven pump and fuel rail

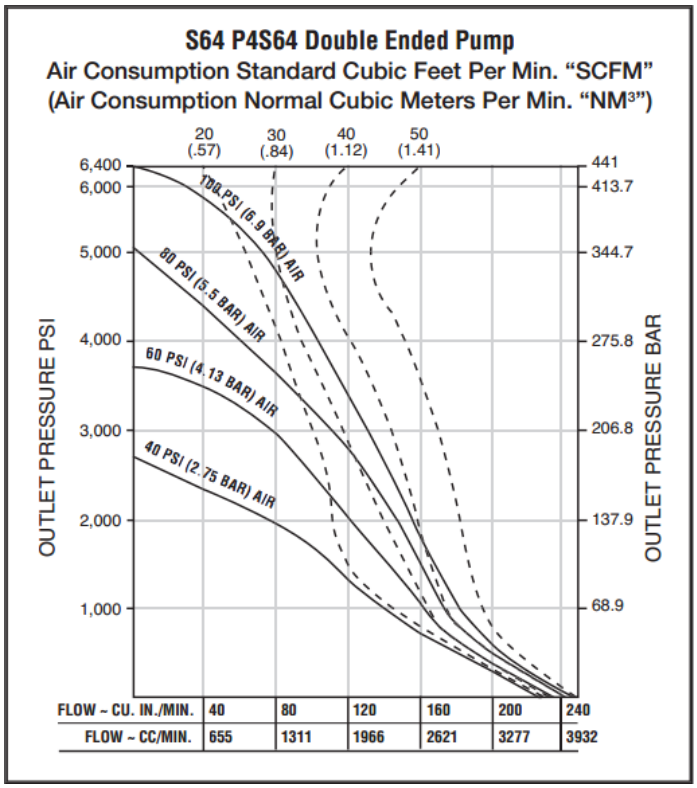

Figure 6.14 Air Pump performance curve

The fuel injector for experimental test engine is a Mahle gasoline piezo injector NGM 00084766. The injector was designed for high fuel injection pressure. The injection fuel spray is a 94º cone shape continuous surface.

6.5 Spark ignition system and Timing Unit

A separate spark ignition control system is built and used to control the spark ignition as shown in Figure 6.15.

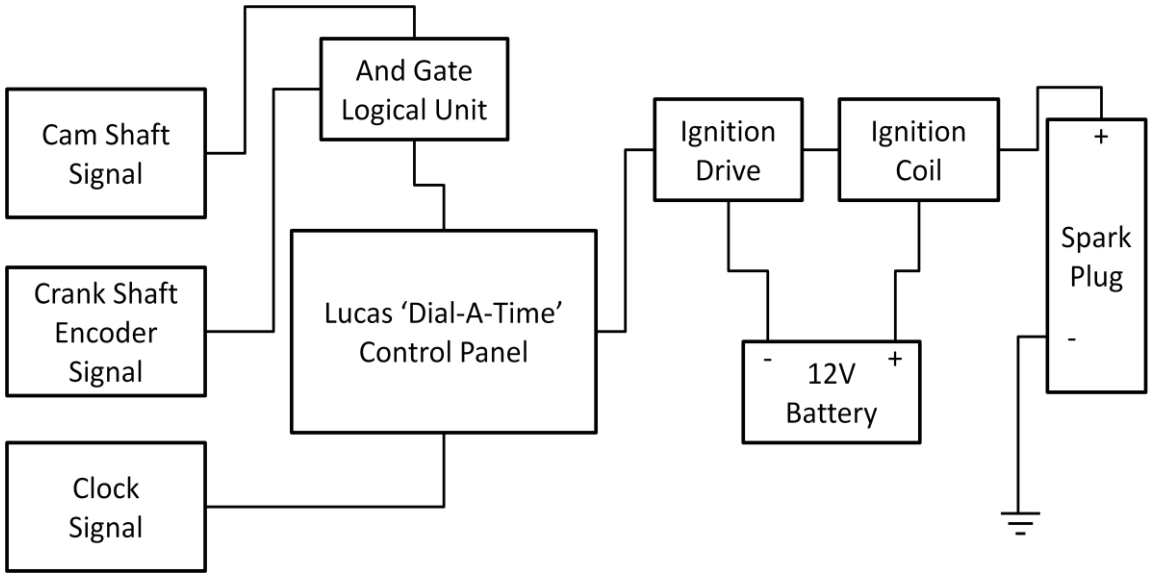

Figure 6.15 Spark ignition control system

The function of Lucas 'Dial-A-Time' unit is to pick up a reference signal and generates a spark ignition trigger with adjustable time offset and signal width. To achieve the function, Lucas 'Dial-A-Time' unit requires a reference signal and a clock signal to set the timing and width of the spark ignition, which are provided by a shaft encoder mounted onto the end of the crank shaft. This encoder generates a TTL signal for each revolution of the crankshaft as well as crank angle based clock signals of a resolution of 1ºCA.

The clock signal from the shaft encoder allows the spark timing to be set in crank angles rather than absolute time. The reference signal is generated by an "AND" gate logical unit which picks up signals from the crank shaft encoder and a signal generated by a cam sensor on the exhaust valve cam shaft pulley wheel. This original spark ignition system was designed for the 4-stroke operation which takes two revolutions per engine cycle. For the 2-stroke operation, the cam shaft signal is

set to high at all time so that a spark ignition signal is generated at each engine revolution by the Lucas ‘Dial-A-Time’ unit to initiate the spark ignition.

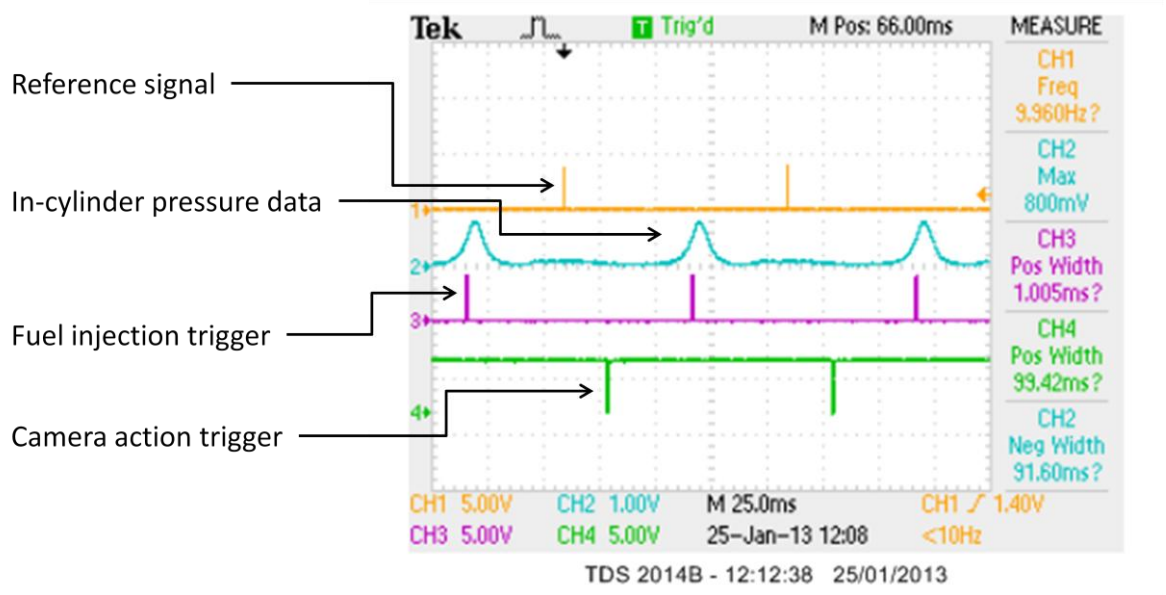

Figure 6.16 Timing sequence for fuel injection and image acquisition

As shown in Figure 6.16, in addition to the spark timing, the reference signal generated at 80ºBTDC is also used via a multi-channel signal generator to initiate the fuel injection and the image acquisition process, as to be detailed in the next chapter.

6.6 In-cylinder pressure and heat release analysis

The in-cylinder pressure measurement is obtained by a Kistler type 6055B80 piezo-electric pressure transducer, which is capable of measuring pressure up to 250bar with a sensitivity of 19.4 pC/bar and uncertainty of ± 0.1%. The transducer output signal is then send to a charge amplifier Kistler type model 568 via a high impedance cable. The charge amplifier converts the charge signal from the transducer into a voltage signal. This voltage signal was calibrated using a dead weight test bed to assign the output voltage to correct pressure. This analogue pressure signal is sent to a National Instrument board type NI USB-6251 Data Acquisition (DAQ) card, the DAQ card is a multifunction data acquisition card with 16-bits resolution and a sampling rate of 1.25 MS/s. The DAQ card then converts the analogue signal into digital signal using the shaft encoder output as the clock with a resolution of 1ºCA

and can be displayed in real time. The heat release results can then be calculated using a bespoke LabView programme based on the first law thermodynamics.

6.7 Summary

This chapter describes the design and implementation of the modifications to a single cylinder optical engine in order to achieve uniflow 2-stroke engine operations and allow in-cylinder flow and mixture measurements by laser techniques. By configuring the piston location relative to the intake ports and camshaft phase to the crankshaft, the engine breathing was set to intake ports opening duration from 120ºATDC to 240ºATDC, and the exhaust valve opening duration was set to 80ºATDC to 240ºATDC. The intake air boosting system and high pressure fuel supply system was also described. For the experiments, the intake pressure can go up to 3bar absolute pressure and the fuel pressure can go up to 250bar.

Chapter 7 In-Cylinder Flow Measurements with PIV

7.1 Introduction

This chapter presents the investigation of in-cylinder flow structure by means of the Particle Image Velocimetry (PIV) method. PIV is a non-intrusive optical technique for two-dimensional velocity measurements based on the displacement of particle images over a known time interval, the displacement is calculated as follows,

$$\vec{V} = \frac{\Delta\vec{x}}{\Delta t} \qquad \text{[E-7.1]}$$

$\vec{V}$ – Velocity vector

$\Delta\vec{x}$ – Element displacement

Δt – Time interval

In order to obtain particle images, a laser light sheet is used to illuminate the particles in the flow and the scattered light is captured by a camera, as shown in Figure 7.1. In order to calculate the flow velocity vectors, the laser unit and the camera are synchronized so that two images with a known time delay can be recorded onto two separate frames by employing the so-called frame straddling technique as shown in Figure 7.2. The pair of images is divided into a matrix of interrogation areas (IA) of $(M \times N)$ pixels, in which the cross-correlation analysis is performed to determine the average particle displacement vector and then the velocity vector.

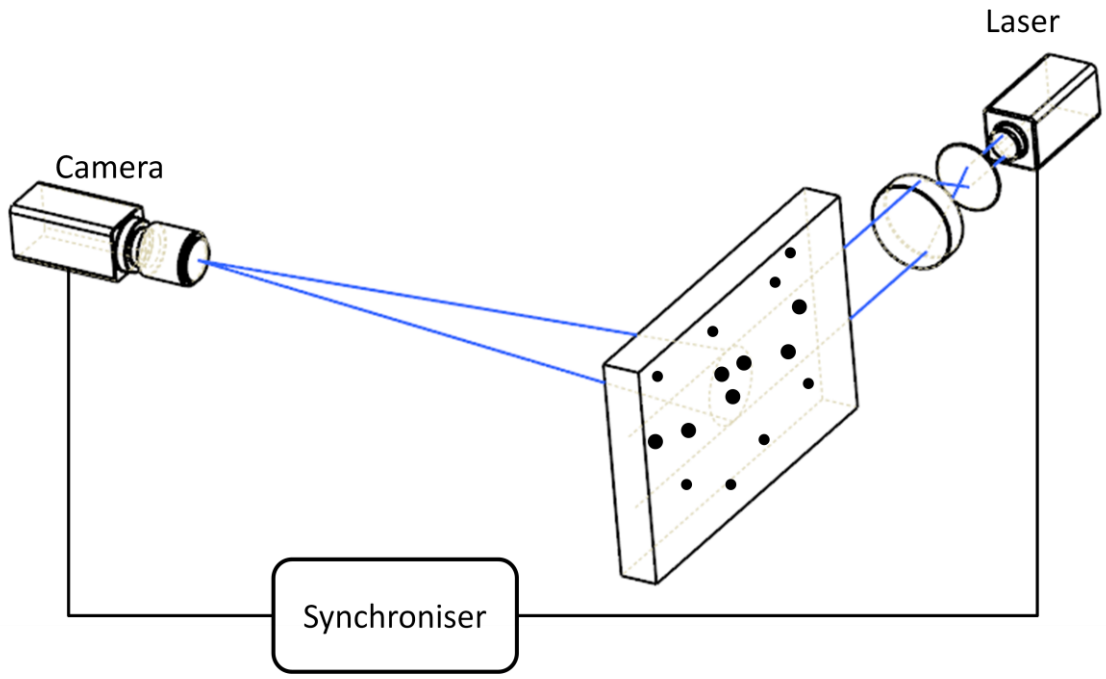

Figure 7.1 Typical PIV experimental setup

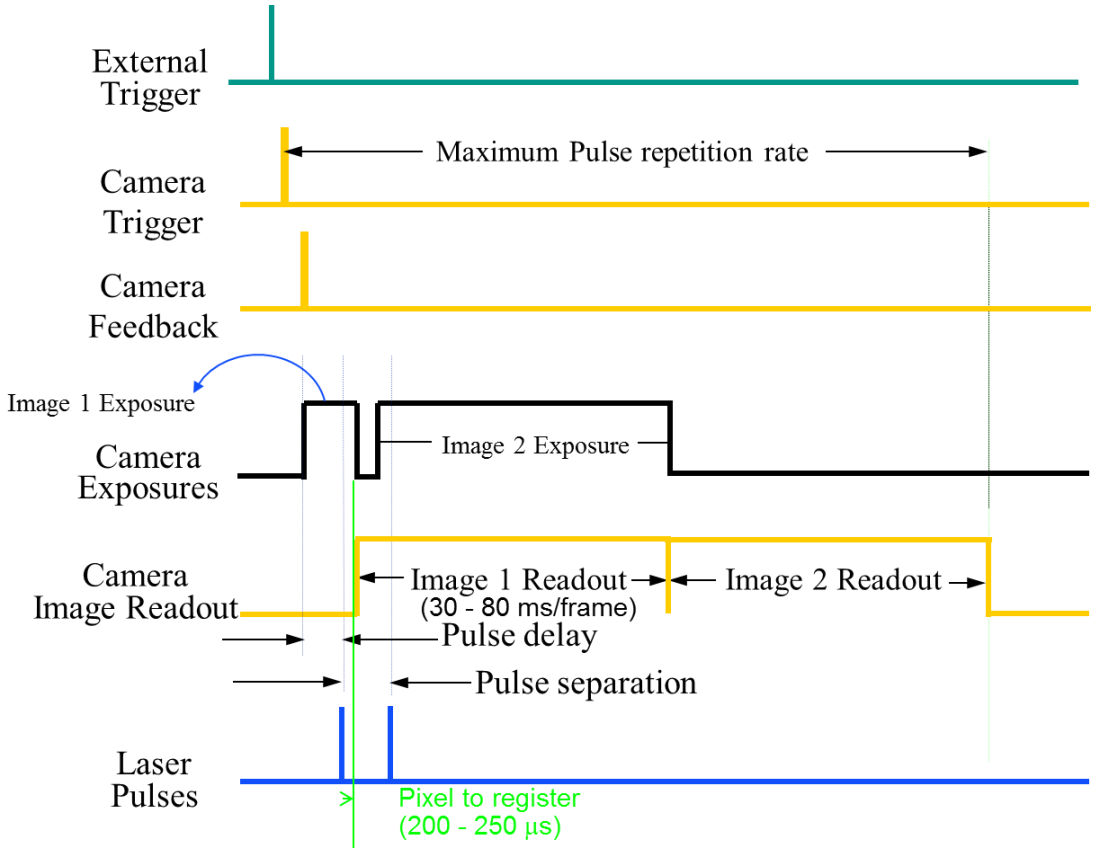

Figure 7.2 Straddling technique

7.2 Experimental setup of PIV

7.2.1 Flow seeding

The seeding particles should be non-toxic, non-corrosive, non-abrasive, non-volatile and chemically inert, as well as being small enough to faithfully follow the flow changes [72]. The seeding material used in this experiment is vegetable oil. The seeding generator is a 10F03 seeding generator supplied by Dantec Dynamics. Figure 7.3 shows the diagram of the 10F03 seeding generator.

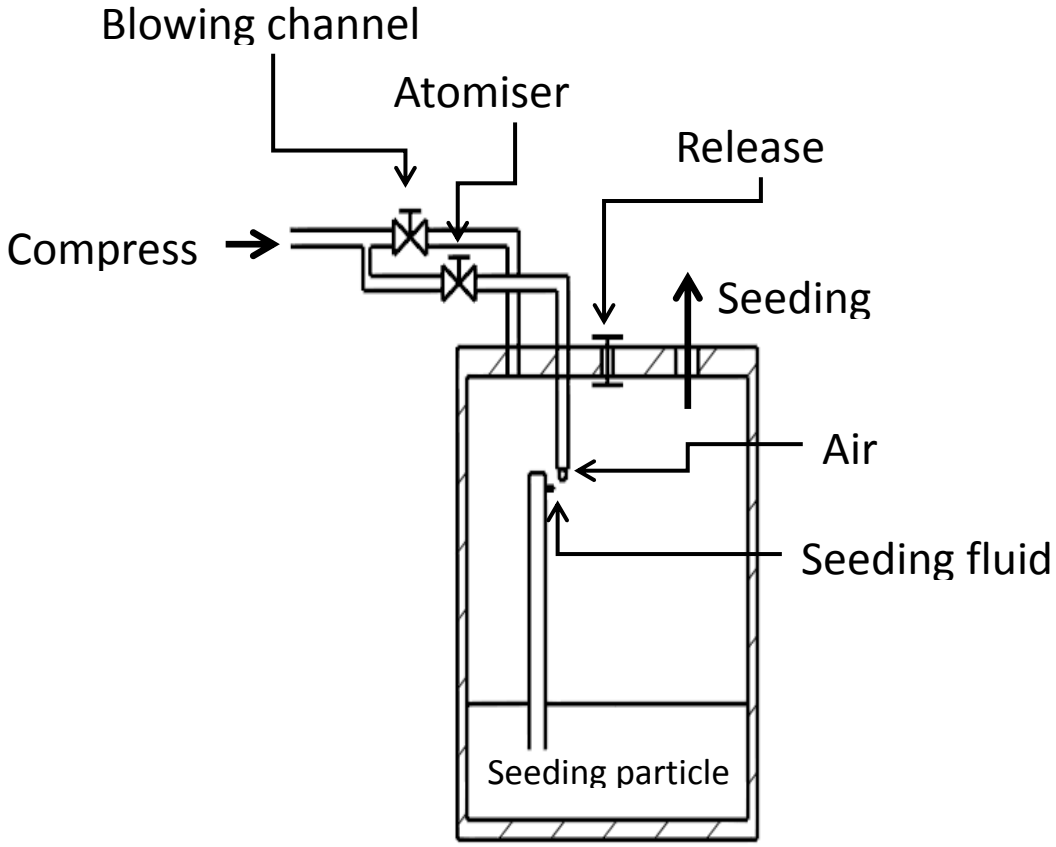

Figure 7.3 Flow seeding generator

Atomization of the seeding particles takes place according to Bernoulli's principle as shown below,

$$p + \frac{1}{2}\rho v^2 + \rho g h_e = constant \qquad \text{[E-7.2]}$$

p – Pressure

ρ – Density

v – Velocity

g – Gravity

h_e – The elevation of the point above a reference plane

The compressed air passes into the atomiser via the atomiser regulator to the air tube. The high flow velocity flow field at the exit of the compressed air tube causes a pressure drop near the tip of the other tube partially immersed in the liquid according to Bernoulli's principle. This vacuum sucks out the liquid which is dispersed into small droplets by the high speed air flow. The liquid droplets are then blown to the outlet of the seeding generator by the air flow in the chamber. The seeding generator 10F03 can continuously supply seeding flow with an average droplet size of Sauter Mean Diameter (SMD) 2μm to 5μm up to a pressure of 3bar.

7.2.2 PIV Laser

The Nd: YAG laser is the most commonly used laser for PIV measurements due to its high pulse energy. To achieve PIV measurements, two laser pulses within a short time interval are required. Two methods with Nd: YAG laser can satisfy the requirement, a single cavity Nd: YAG laser with double pulse option or a twin-oscillator, twin-amplifier frequency doubled Nd: YAG laser [73]. The illumination of PIV with the single cavity Nd: YAG laser is achieved by gating a single flash lamp discharge from the single cavity laser to provide two laser shots. This method limits the time interval between the two laser pulses to a range of 20μs to 200μs, which will greatly reduce the laser light intensity and laser pulse width. In this study, a twin-oscillator, twin-amplifier frequency doubled Nd: YAG laser has been used, which allows an infinite and independent control over the time interval, width and intensity of the laser pulses.

The laser unit used for the PIV experiments is NANO L 135-15 PIV laser by Liton Lasers. The laser unit is powered by the LPU 450 power station configured to drive 2 laser units with a 450W combined throughput. The laser head consists of two 1064μm laser units, half wave plates, mixing and steering polarisers and a harmonic

generator. The laser head supplies 532μm laser beams with up to 136mJ laser pulse energy under a 160μs optimised Q-switch delay.

7.2.2 Camera and Optics

The images of flow with seeding particles are captured with a Dantec Dynamic FLOWSENSE 4M Camera system with a CCD camera of 2048x2048 pixels, which has a minimum inter-frame time of 200ns.

The lens used for the PIV test is an UV-Nikkor 105 mm lens. A 532nm narrow band filter is also used to remove background light. The configuration of the lens is shown in Table 7.1.

Table 7.1 UV-Nikkor 105mm lens configuration

Focal Length	105mm
Aperture	f/32 to f/4
Reproduction Ratio	1:10 to 1:2
Lens Elements	6
Lens Groups	6
Maximum Angle of View	23º12’

7.2.3 PIV test setup

The PIV test experimental setup is shown in Figure 7.4. The Nd: YAG laser sheet was guided to the cylinder window ring by a high power long mirror arm for 532nm light wavelength, as shown in Figure 7.5. A 45º mirror directs the scattering light of in-cylinder flow seeding particles to the camera, and the camera set at the horizontal level was used to capture the in-cylinder images. Both the laser unit and camera was triggered by a set of signals synchronised with the reference signal.

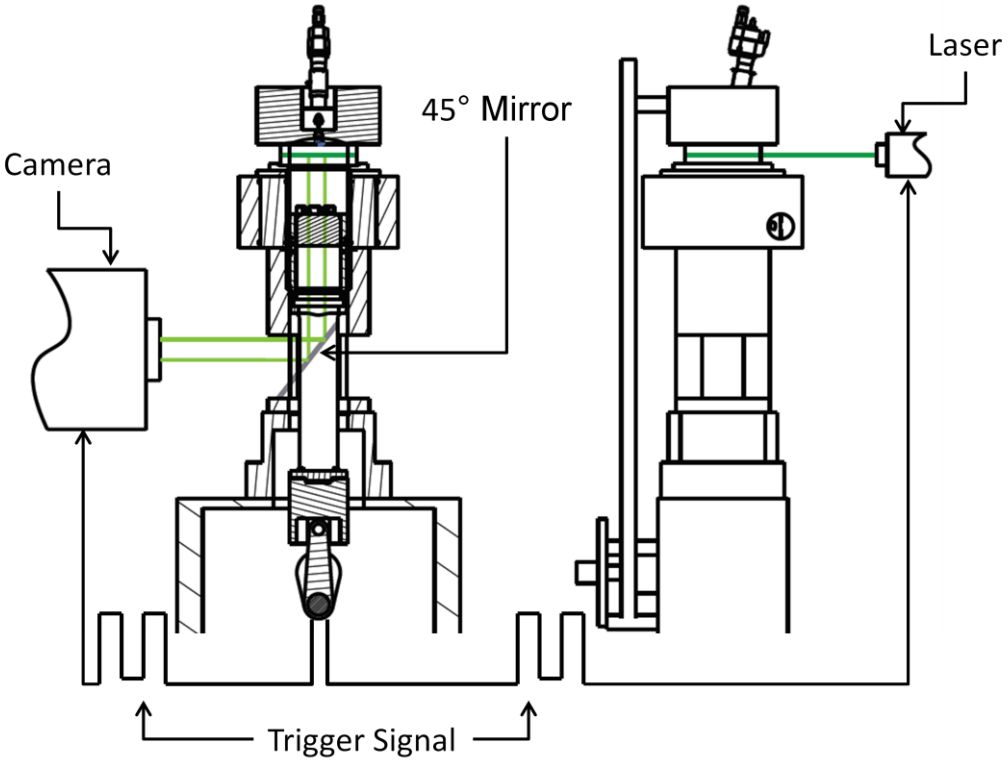

Figure 7.4 PIV test layout

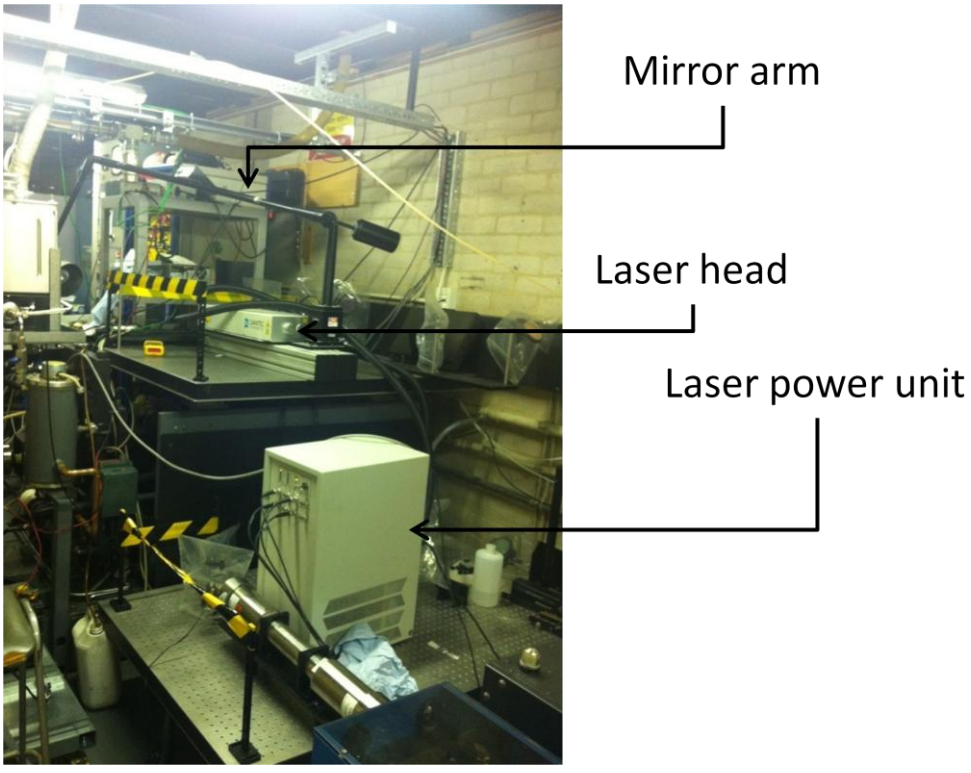

Figure 7.5 Laser lining setup

The laser sheet level is set to a horizontal level about 6mm to 8.5mm from the top edge of the cylinder window ring, which corresponds to the piston top surface location at 10ºATDC to 20 ºATDC with compression ratio of 8:1, as shown in Figure 7.6. The highest position of the laser sheet was limited by the increased scattering from the cylinder head surface.

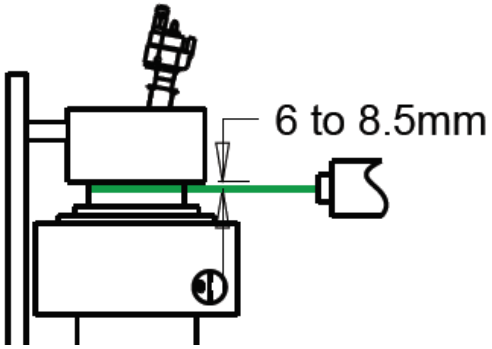

Figure 7.6 Illumination laser level position

The camera's focus was set to the laser sheet by imaging a graph paper stuck to a ruler, which was placed to intersect with the laser sheet with the cylinder head removed, as illustrated in Figure 7.7. The camera was positioned to have its field of view filled with the flow field to be measured in order to use as many as pixels as possible to increase the resolution of the region of interest. In order to protect the camera, the laser energy level was reduced when it was being focused.

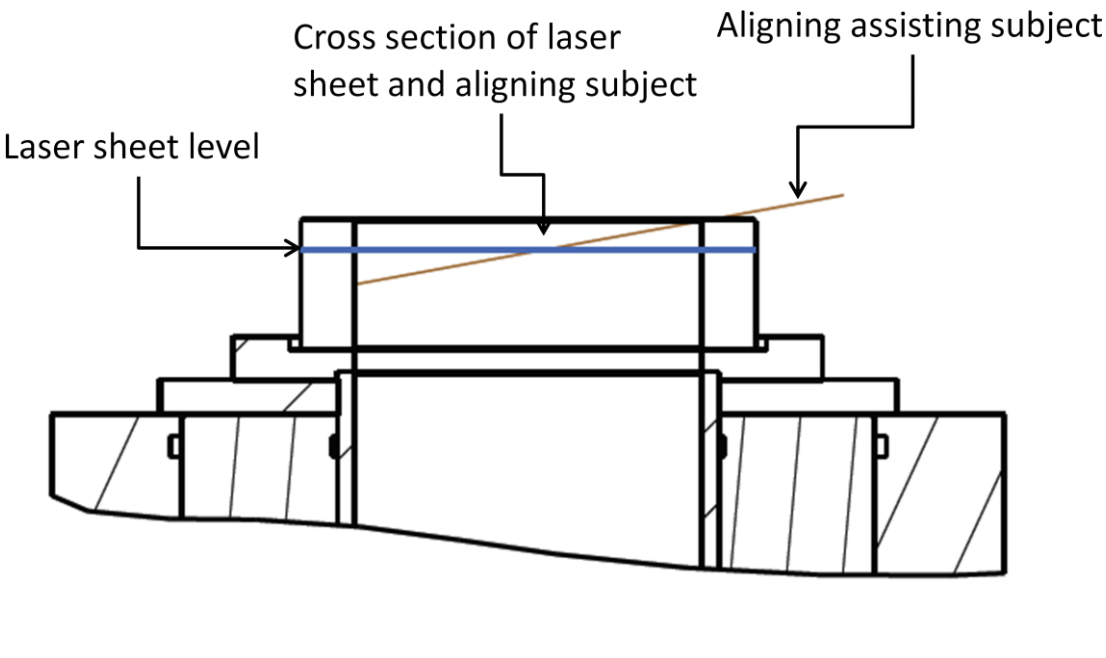

Figure 7.7 Adjusting camera focus with an assisting subject

In the current experiments, the best particle images were obtained with a low f-number of 4 due to its shorter depth of view. It was found that the maximum laser output of 136mJ was required to produce sufficient scattering light from the small oil droplets. The time interval of two laser pulses and camera actions were adjusted from 30μs to 200μs, depending on the measurement time, in order to minimize the dropout rate of the velocity vectors.

7.3 Evaluation of the particle displacement vector

The calculation of particle displacement vector evaluation was carried out by Dantec Dynamics software Dynamicstudio based on the cross-correlation method. With this method, the images recording the flow seeding particle position information is divided into a number of square interrogation areas. The velocity vector evaluation of each interrogation area is calculated by cross-correlation method. For this PIV experimental setup, a 32x32 pixels interrogation area was used combined with the Gaussian algorithm, which corresponds to a spatial resolution of 1.8mm x 1.8mm.

The cross-correlation method can be explained as follows. There is a random distribution of particles in each interrogation area, which corresponds to certain pattern of N particles in the flow,

$$\Psi = \begin{Bmatrix} x_1 \\ x_2 \\ \vdots \\ x_N \end{Bmatrix} \qquad \text{[E-7.3]}$$

$$\text{with } \boldsymbol{x}_i = \begin{Bmatrix} x_i \\ y_i \\ z_i \end{Bmatrix}$$

Ψ – The state of the particle ensemble at a given time t

$\boldsymbol{x}_i$ – The position vector of the particle i at time t, in the interrogation area of the laser sheet

For following analysis, capital letters refer to the coordinates in the image plane, so that

$$\mathrm{X} = \begin{pmatrix} X \\ Y \end{pmatrix}$$

Lower case letters are used to represent the coordinates in the object plane, so that

$$x = {}^{X}/_{M} \text{ and } y = {}^{Y}/_{M}$$

where M is the magnification factor of the imaging system.

The image intensity of a single exposure can therefore be written as [69]

$$\mathrm{I}(\mathrm{X}, \Psi) = \sum_{\mathrm{i}=1}^{\mathrm{N}} \mathrm{P}(x_{\mathrm{i}}) \cdot \tau(\mathrm{X} - \mathrm{X}_{\mathrm{i}}) \qquad \text{[E-7.4]}$$

Where $\tau(\mathrm{X} - \mathrm{X}_{\mathrm{i}})$ is the point spread function of the imaging lens and describes the impulse response of the imaging lens and $\mathrm{P}(x_{\mathrm{i}})$ represents the system transfer function, giving the light energy of the image of an individual particle inside the interrogation area IV and its conversion into an electric signal.

The next stage is to calculate the cross correlation of the interrogation areas for the pair of exposures. At this point it is advantageous to offset the two interrogation areas according to an estimated mean particle displacement [75]. This increases the fraction of matched to unmatched particle images, thereby increasing the signal to noise ratio at the correlation peak. The cross correlation function for each pair of interrogation areas is then calculated and the peak displacement vector is determined, which corresponds to the particle image displacement vector.

Assuming there is a constant displacement of all particles inside the interrogation area within the region of interest, the particle positions recorded in the second frame are given by:

$$x_{\mathrm{i}}' = x_{\mathrm{i}} + d = \begin{pmatrix} x_i + d_x \\ y_i + d_y \\ z_i + d_z \end{pmatrix} \quad \text{[E-7.5]}$$

d – The constant displacement of particles in the interrogation area

The corresponding particle image displacement can be given by:

$$D = \begin{pmatrix} M \cdot d_x \\ M \cdot d_y \end{pmatrix} \quad \text{[E-7.6]}$$

The intensity distribution of the interrogation area for the second exposure can therefore be described as:

$$\mathrm{I}'(\mathrm{X}, \Gamma) = \sum_{\mathrm{j}=1}^{\mathrm{N}} \mathrm{P}'(x_{\mathrm{j}} + d) \cdot \tau(\mathrm{X} - \mathrm{X}_{\mathrm{j}} - \mathrm{D}) \quad \text{[E-7.7]}$$

For the first capture, it can be described as:

$$\mathrm{I}(\mathrm{X}, \Gamma) = \sum_{\mathrm{j}=1}^{\mathrm{N}} \mathrm{P}(x_{\mathrm{i}}) \cdot \tau(\mathrm{X} - \mathrm{X}_{\mathrm{i}}) \quad \text{[E-7.8]}$$

The cross-correlation function of the two interrogation areas can then be written as:

$$\mathrm{R}_{II}(s, \Psi, d) = \langle \mathrm{I}(\mathrm{X}, \Gamma) \cdot \mathrm{I}'(\mathrm{X} + s, \Gamma) \rangle = \frac{1}{\mathrm{A}_I} \sum_{i,j}^{\mathrm{N}} \mathrm{P}(x_{\mathrm{i}}) \cdot \mathrm{P}\left(x_j + d\right) \int_{\mathrm{A}_I} \tau(\mathrm{X} - \mathrm{X}_{\mathrm{i}}) \cdot \tau\left(\mathrm{X} - \mathrm{X}_{\mathrm{j}} + s - D\right) \cdot d\mathrm{X} \quad \text{[E-7.9]}$$

where s is the separation plane in the correlation plane.

By distinguishing the $i \neq j$ terms, which represent the correlation of different particle images and therefore randomly distributed noise in the correlation plane, and the $i = j$ terms which contain the desired displacement data, following expression can be derived:

$$\mathrm{R}_{II}(s, \Psi, d) = \frac{1}{\mathrm{A}_I} \sum_{i \neq j} \mathrm{P}(x_{\mathrm{i}}) \cdot \mathrm{P}\left(x_j + d\right) \int_{\mathrm{A}_I} \tau(\mathrm{X} - \mathrm{X}_{\mathrm{i}}) \cdot \tau\left(\mathrm{X} - \mathrm{X}_{\mathrm{j}} + s - D\right) \cdot d\mathrm{X} +$$

$$\frac{1}{\mathrm{A}_I} \sum_{i=j} \mathrm{P}(x_{\mathrm{i}}) \cdot \mathrm{P}(x_i + d) \int_{\mathrm{A}_I} \tau(\mathrm{X} - \mathrm{X}_i) \cdot \tau(\mathrm{X} - \mathrm{X}_i + s - D) \cdot d\mathrm{X}$$

or

$$\mathrm{R}_{II}(s,\Psi,d) = \sum_{i\neq j}\mathrm{P}(x_{\mathrm{i}})\cdot\mathrm{P}\left(x_j+d\right)\cdot\mathrm{R}_{\tau}\left(\mathrm{X}_{\mathrm{i}}-\mathrm{X}_{\mathrm{j}}+s-D\right)+\mathrm{R}_{\tau}(s-D)+\sum_{i=j}\mathrm{P}(x_{\mathrm{i}})\cdot \mathrm{P}(x_i+d) \quad \text{[E-7.10]}$$

which can be divided into three parts:

$$\mathrm{R}_{II}(s,\Psi,d) = \mathrm{R}_{C}(s,\Psi,d)+\mathrm{R}_{F}(s,\Psi,d)+\mathrm{R}_{D}(s,\Psi,d) \quad \text{[E-7.11]}$$

where the first two terms R_C and R_F contribute to the background noise in the correlation plane, both resulting from the $i \neq j$ terms. $\mathrm{R}_D(s,\Psi,d)$ represents the component of the cross correlation function that corresponds to the correlation of images of particles obtained from the first exposure with images of identical particles obtained from the second exposure ($i = j$ terms) i.e.

$$\mathrm{R}_{D}(s,\Psi,d) = \mathrm{R}_{\tau}(s-D)\sum_{i=j}\mathrm{P}(x_{\mathrm{i}})\cdot\mathrm{P}(x_i+d) \quad \text{[E-7.12]}$$

Hence, this displacement correlation reached its peak at s=D, which means that the average particle image displacement vector D can be determined from the maximum of the displacement correlation distribution in the correlation plane, with the sign of D defining the direction of flow.

Although correlation can be calculated by Equation 7.9, the most efficient way of calculating correlation in practice is carried out by fast Fourier transform (FFT) algorithms, which is used in this case and processed by the Dynamicstudio analyse software.

The correlation theorem states that the cross-correlation of two functions is equivalent to a complex conjugate multiplication of their Fourier transforms:

$$\mathrm{R}_{II} \Leftrightarrow \hat{\mathrm{I}}\cdot\hat{\mathrm{I}}'^{*} \quad \text{[E-7.13]}$$

where $\hat{I}$ and $\hat{I}'$ are the Fourier transforms of the functions I and I' respectively. The cross correlation function can therefore be calculated by computing two two-dimensional FFT's on equal sized samples of the image, followed by a complex-conjugate multiplication of the resulting Fourier coefficients.

7.4 Results of PIV test

The PIV measurements were carried out at 90ºCA BTDC, 60ºCA BTDC and 30ºCA BTDC, which corresponds to 30ºCA, 60ºCA and 90ºCA after the intake ports were closed by the piston. Each measurement was repeated at three different intake pressures of 1.2bar, 1.4bar and 1.6bar. The engine speed was set to 600rpm, which equals to 1200 rpm engine speed for 4-stroke operation. PIV images of velocity vectors were recorded for each measurement point and then ensemble-averaged.

7.4.1 In-cylinder flow structure on the horizontal plane @ 600rpm engine speed

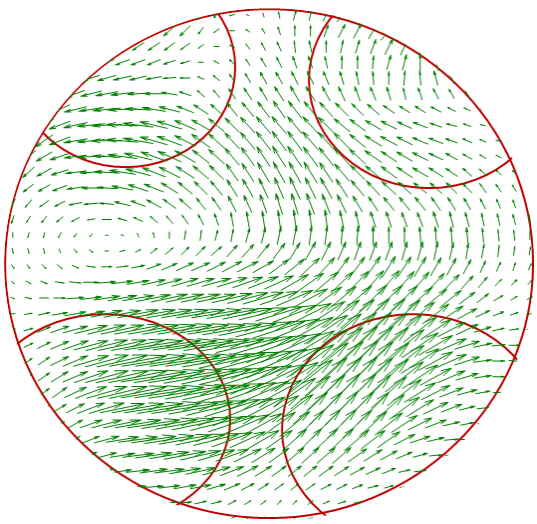

a) Boost pressure 1.2bar

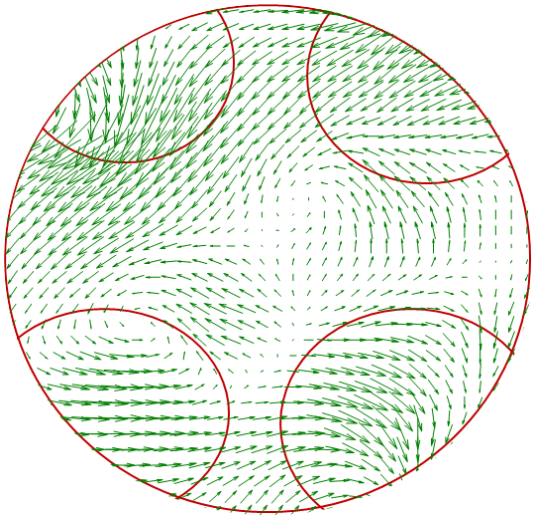

b) Boost pressure 1.4bar

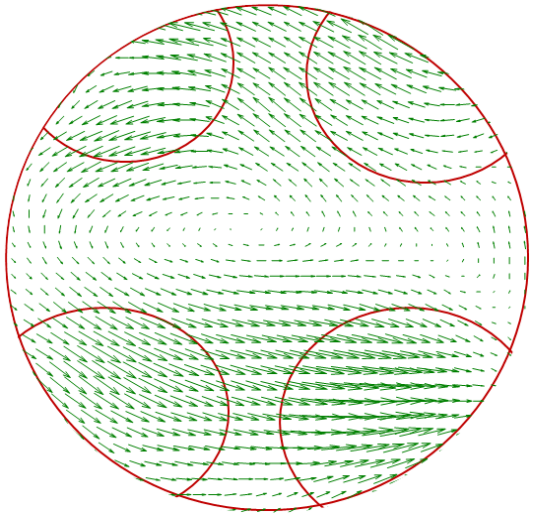

C) Boost pressure 1.6bar

Figure 7.8 Averaged flow structure @90ºCABTDC

As shown in Figure 7.8, swirl flows are detected in the measurement plane. However, the swirl flow structure is relatively unstable, high flow speed occurs along the area adjacent to either top side or bottom side of the image, corresponding to the regions next to the two opposite intake ports banks. More than one vortex centres are present at higher boost pressures of 1.4bar and 1.6bar.This suggests that while intake pressure increases, the intake flow kinetic energy is higher, this higher flow kinetic energy creates small vortex in the swirl flow structure, especially at the stage right after the intake process.

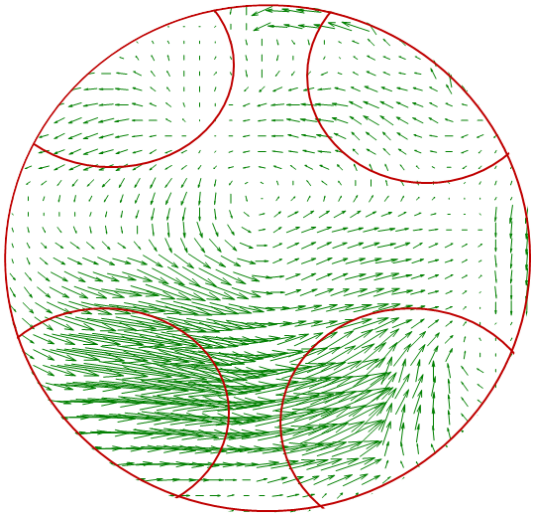

a) Boost pressure 1.2bar

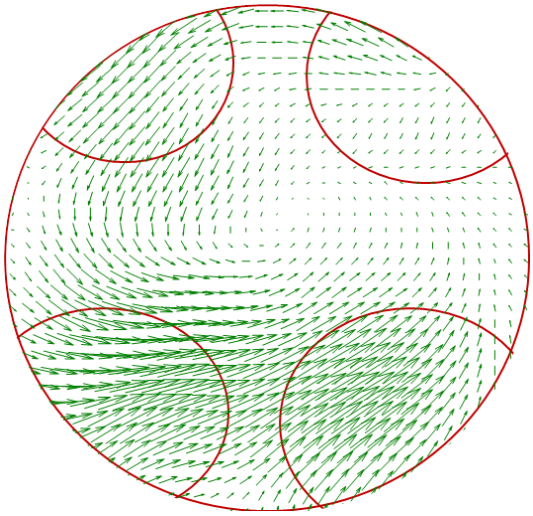

b) Boost pressure 1.4bar

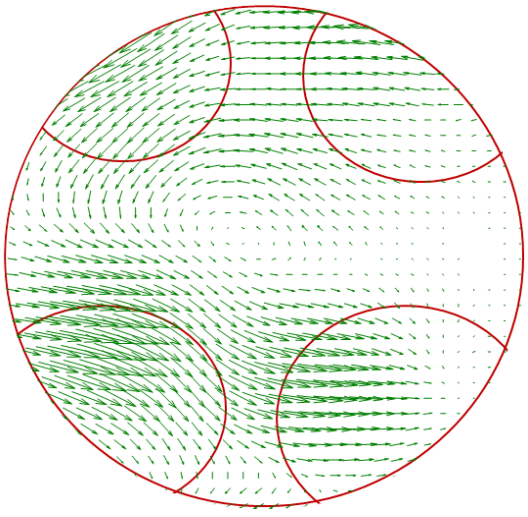

c) Boost pressure 1.6bar

Figure 7.9 Averaged flow structure @60ºCABTDC

Figure 7.9 shows the in-cylinder flow structure at 60ºCA BTDC. Compared with the flow field at the earlier crank angle, a more dominant swirl flow structure can be observed with one swirl flow centre as the other smaller vortices are merged into the

dominant one near the centre. In addition to the dominant swirl flow structure, there are many areas of low velocities, such as the right side and top side of the image in Figure 7.9 (a), both left and right side of the image in Figure 7.9 (b) and the right side of the image shown in Figure 7.9 (c). In these areas, the vertical flow dominates the air flow during the scavenging process, the CFD simulation results showed this vertical flow structure as in Figure 7.10. As the piston moves up, the vertical flow movements are enhanced with little change in the flow field in the horizontal plane.

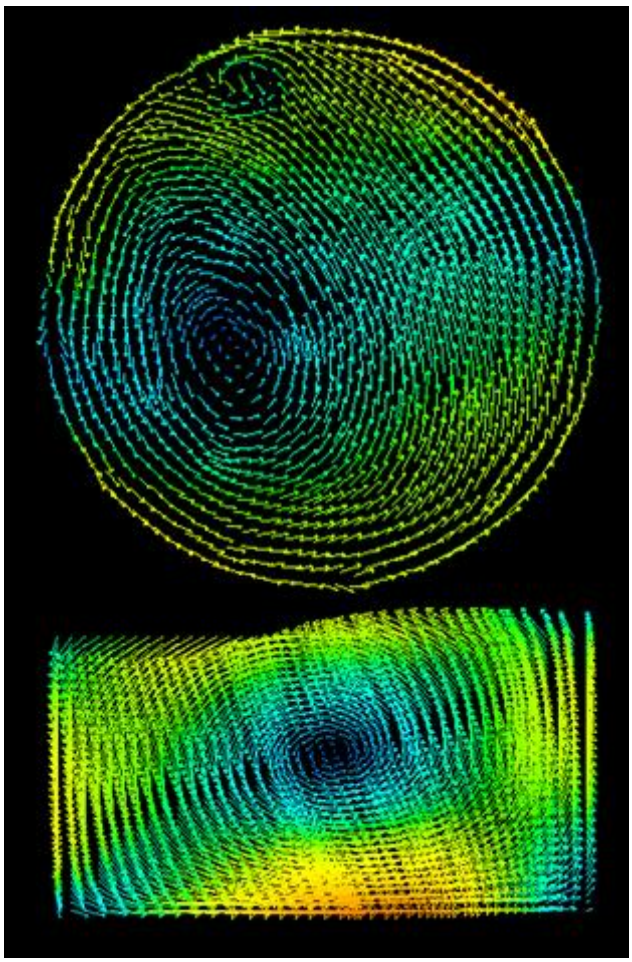

Figure 7.10 CFD simulation results of in-cylinder flow structure on the horizontal (top) and vertical plane (bottom) @60ºCABTDC

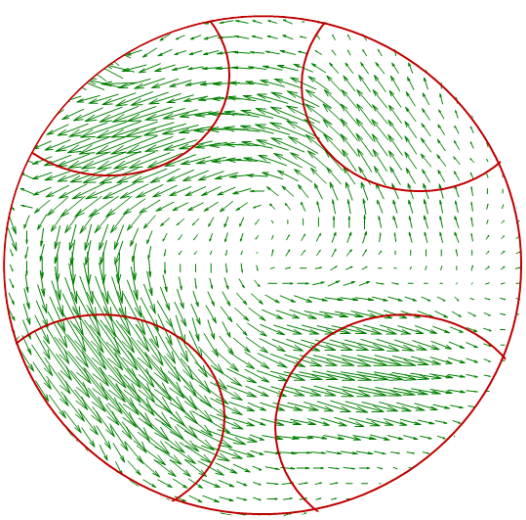

a) Boost pressure 1.2bar

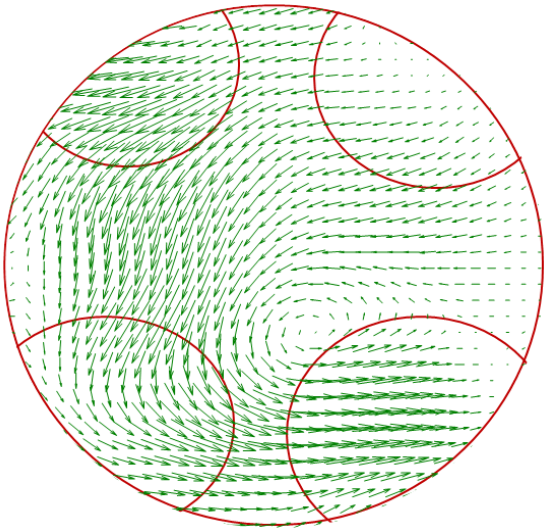

b) Boost pressure 1.4bar

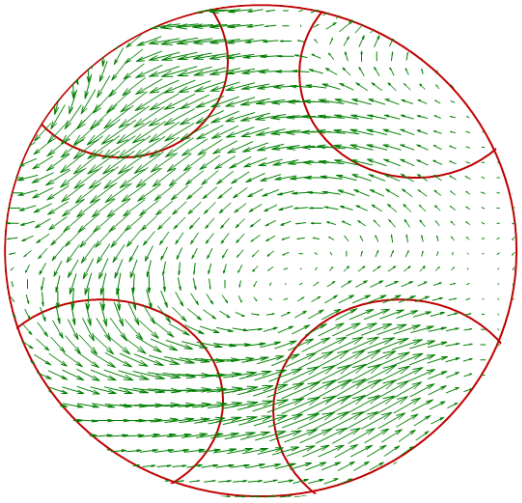

c) Boost pressure 1.6bar

Figure 7.11 Averaged flow structure @30ºCABTDC

As Figure 7.11 shows, the swirl flow structure becomes much clearer than the two previous cases at 30ºCA BTDC when the vertical tumble flow collapses and horizontal swirling flow is enhanced by the ascending piston. And while piston moves close to TDC, the flow kinetic energy is dispersed and reduced so that the small vortexes cannot survive.

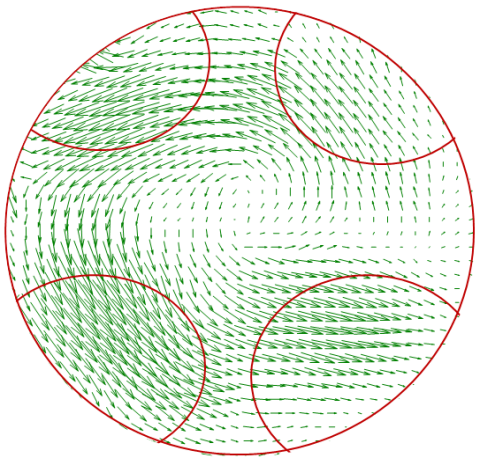

(a1) PIV results at 30ºCABTDC

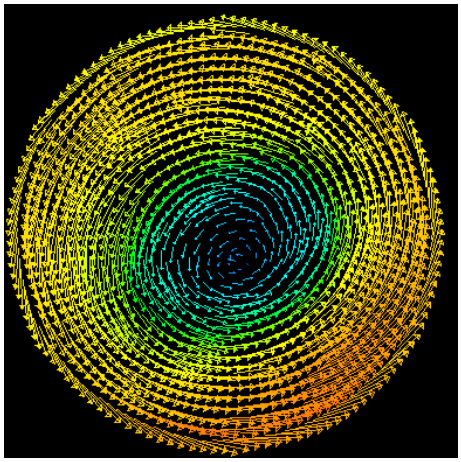

(a2) CFD results at 30ºCABTDC

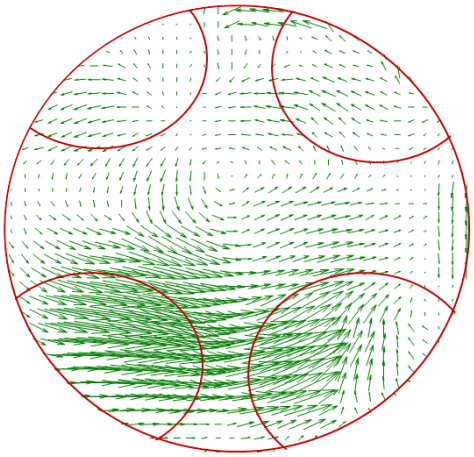

(b1) PIV results at 60ºCABTDC

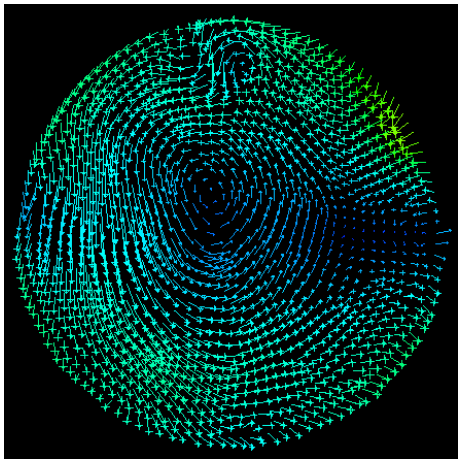

(b2) CFD results at 60ºCABTDC

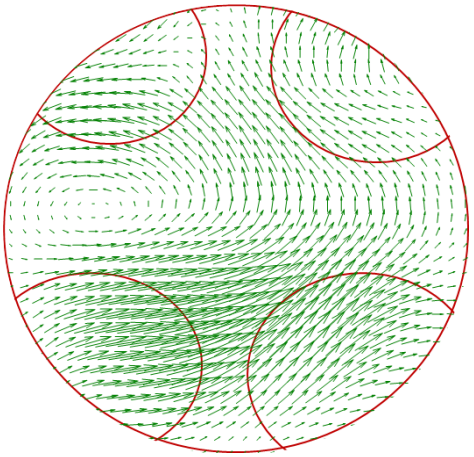

(c1) PIV results at 90ºCABTDC

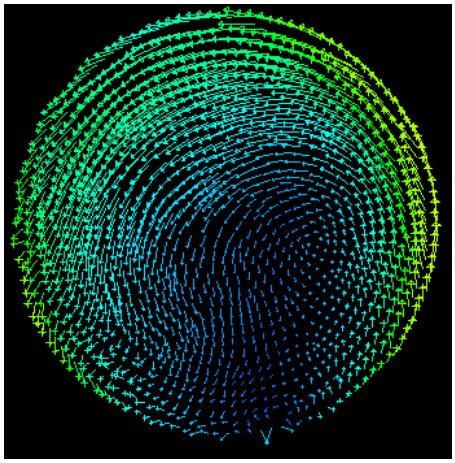

(c2) CFD results at 90ºCABTDC

Figure 7.12 Measured and flow fields with 1.2bar pressure

As shown in Figure 7.12, the CFD results are very similar to the PIV results at the three crank angles in terms of both the global flow structures and their evolution during the compression process.

Figure 7.13 shows the spatially averaged velocity values in the measurement plane. Both CFD and PIV results show that higher boost pressure leads to higher in-cylinder flow velocity and the average velocity decrease as the piston moves to TDC. In general, the CFD results show higher velocities than the PIV measurements. However, as the piston moves up towards TDC, the difference becomes smaller.

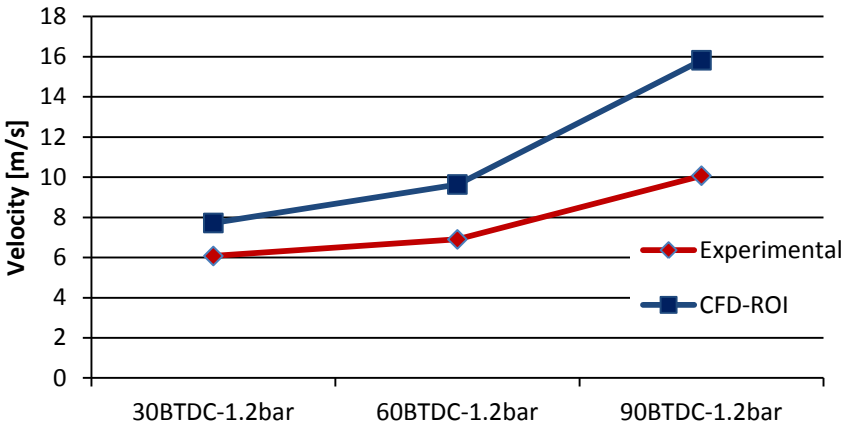

a) Boost pressure 1.2bar

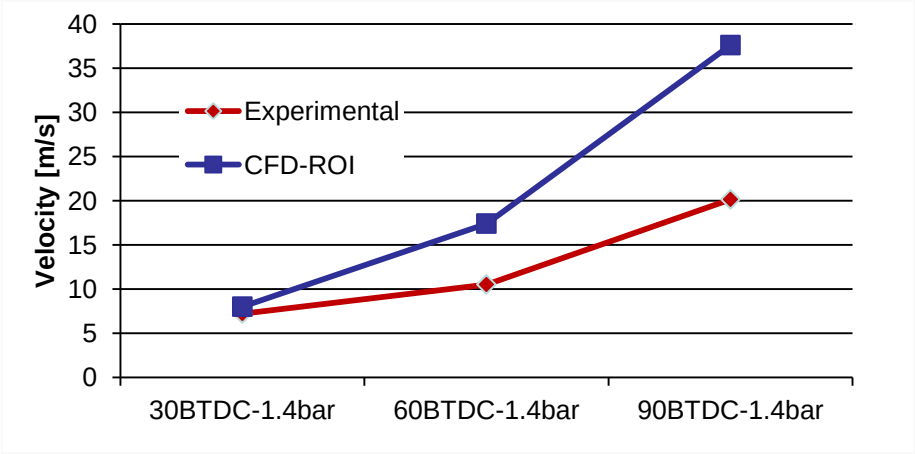

b) Boost pressure 1.4bar

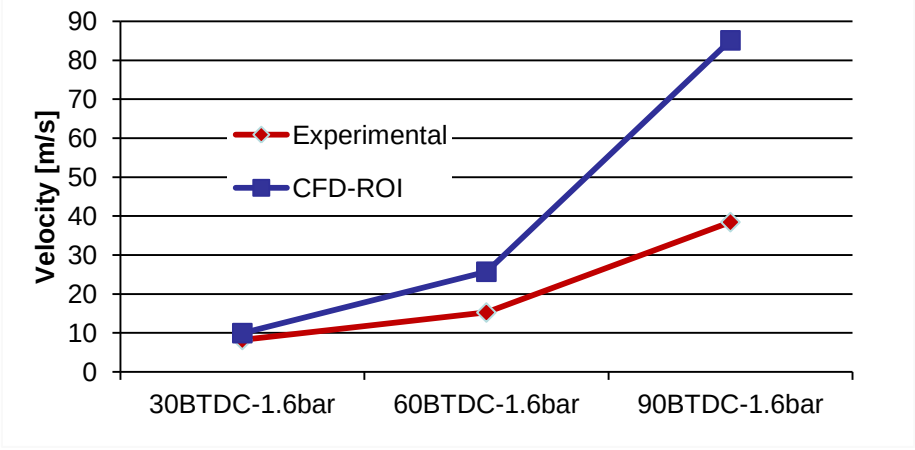

c) Boost pressure 1.6bar

Figure 7.13 Average velocity of the region of interest

7.4.2 In-cylinder flow structure on the horizontal plane @ 900rpm engine speed

In order to investigate the effect of engine speed on in-cylinder flows , the engine speed was increased to 900rpm, beyond which the timing belt drive may not be sufficient robust.

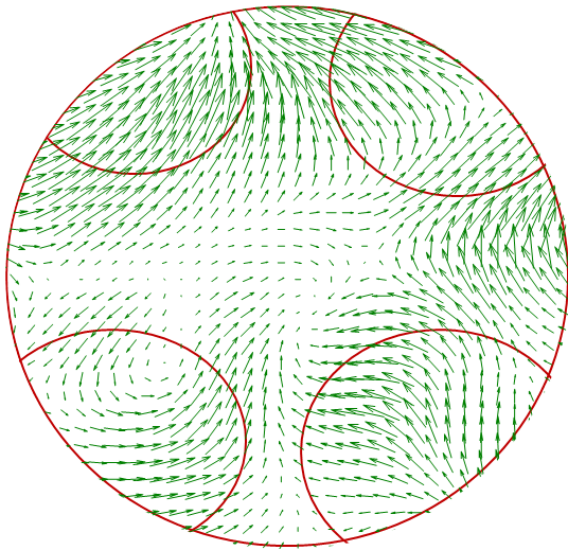

a) Boost pressure 1.2bar

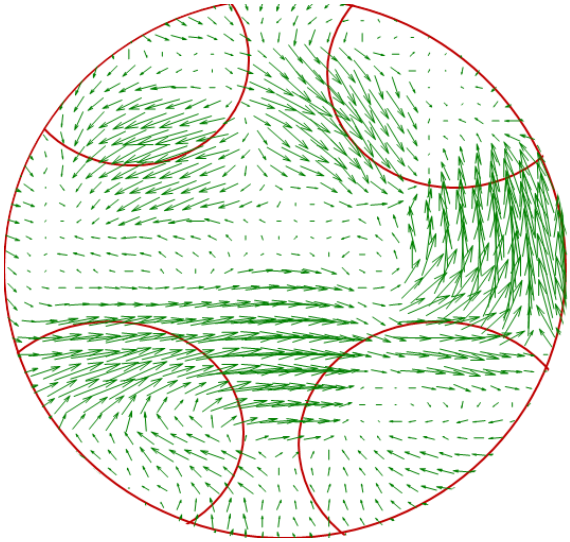

b) Boost pressure 1.4bar

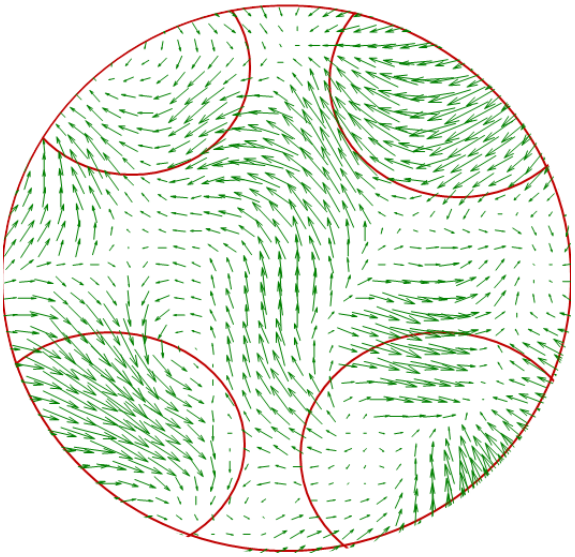

c) Boost pressure 1.6bar

Figure 7.14 Averaged flow structure @90ºCABTDC

Figure 7.14 shows the in-cylinder flow structure at 900rpm engine speed with 1.2bar, 1.4bar and 1.6bar boost pressures. Compared with the 600rpm, the swirl flow pattern can be hardly observed because of the stronger upward flow with higher piston speed. While the piston speed increases, the piston movement input extra kinetic

energy to the flow vertical movement, which interrupting the horizontal swirl flow structure.

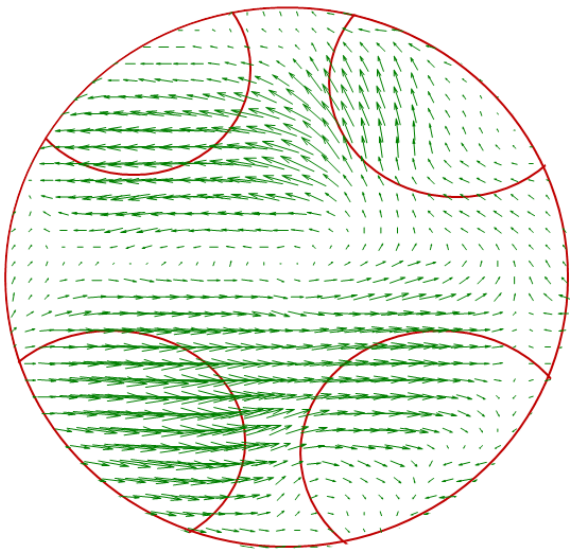

a) Boost pressure 1.2bar

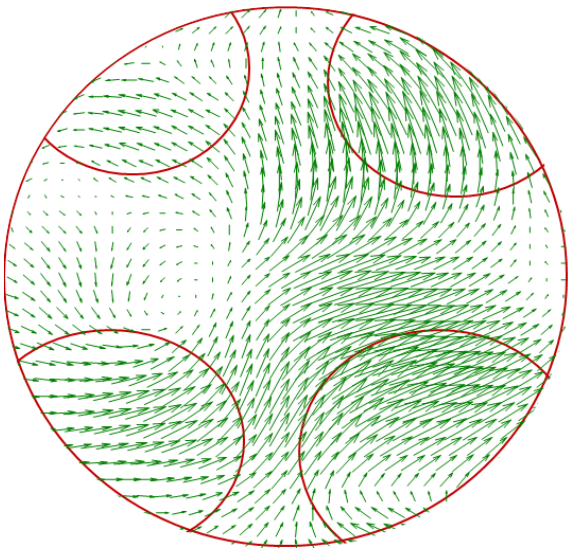

b) Boost pressure 1.4bar

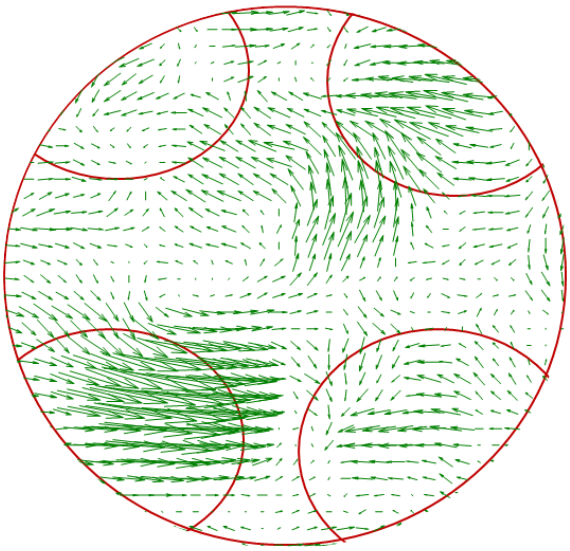

c) Boost pressure 1.6bar

Figure 7.15 Averaged flow structure @60ºCABTDC

As the piston moves up to 60ºCA BTDC, as shown in Figure 7.15, the swirl flow structure pattern begins to appear. However, because higher boost pressure delivers higher flow kinetic energy, the swirl pattern is less clear at higher boost pressure for the same reason as 600rpm engine speed

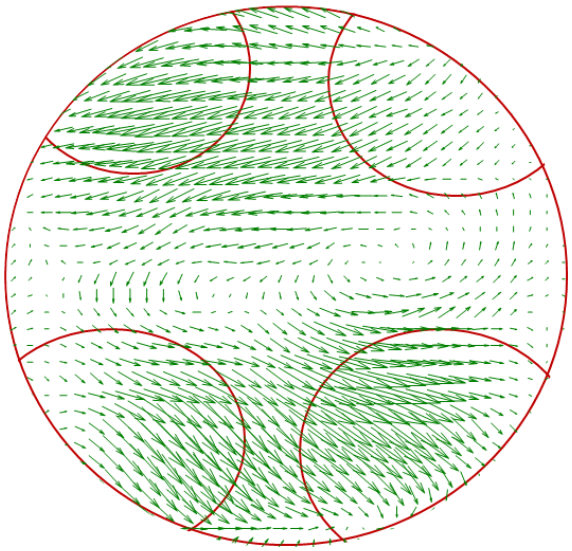

a) **Boost pressure 1.2bar**

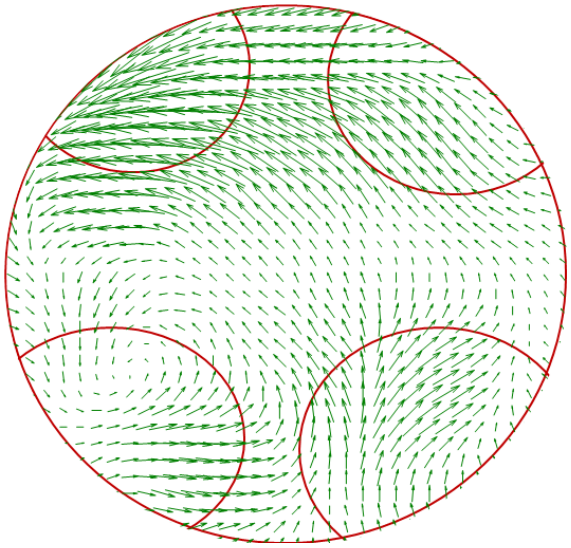

b) **Boost pressure 1.4bar**

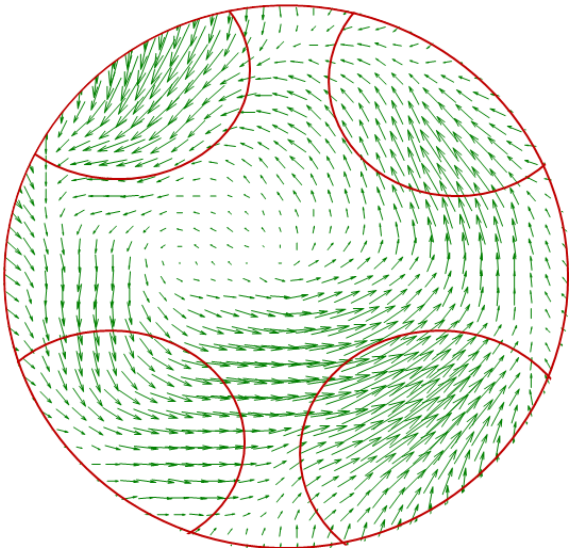

c) **Boost pressure 1.6bar**

Figure 7.16 Averaged flow structure @30ºCABTDC

As shown in Figure 7.16, the piston moves to 30ºCA BTDC, the swirl flow structure is much clearer than the cases at 90ºCA BTDC and 60ºCA BTDC, following a similar trend to the results at 600rpm.

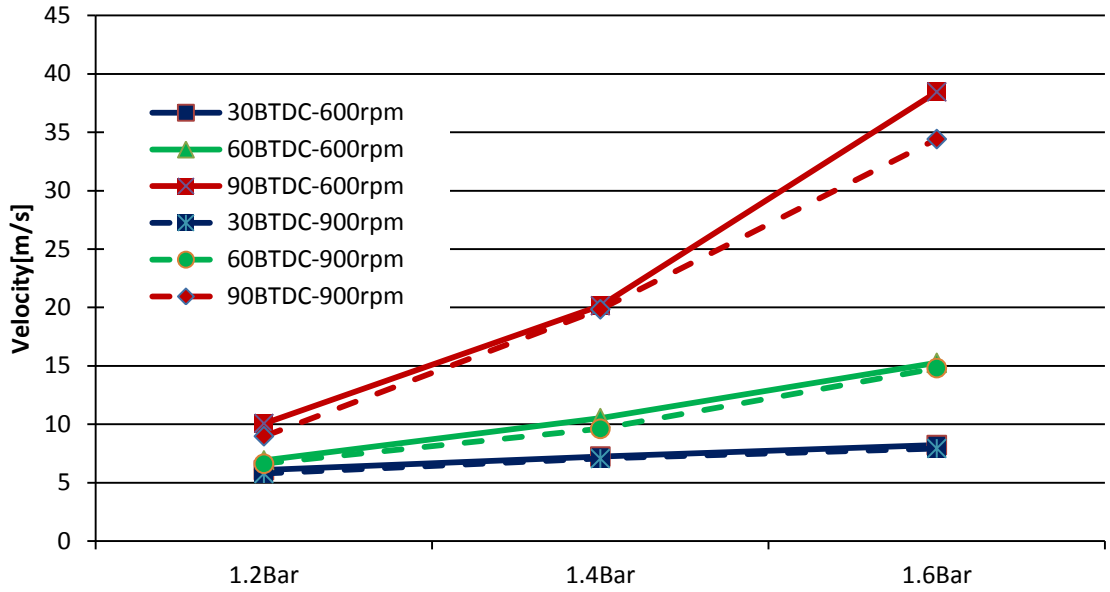

Figure 7.17 Average velocity across the region of interest on the horizontal plane

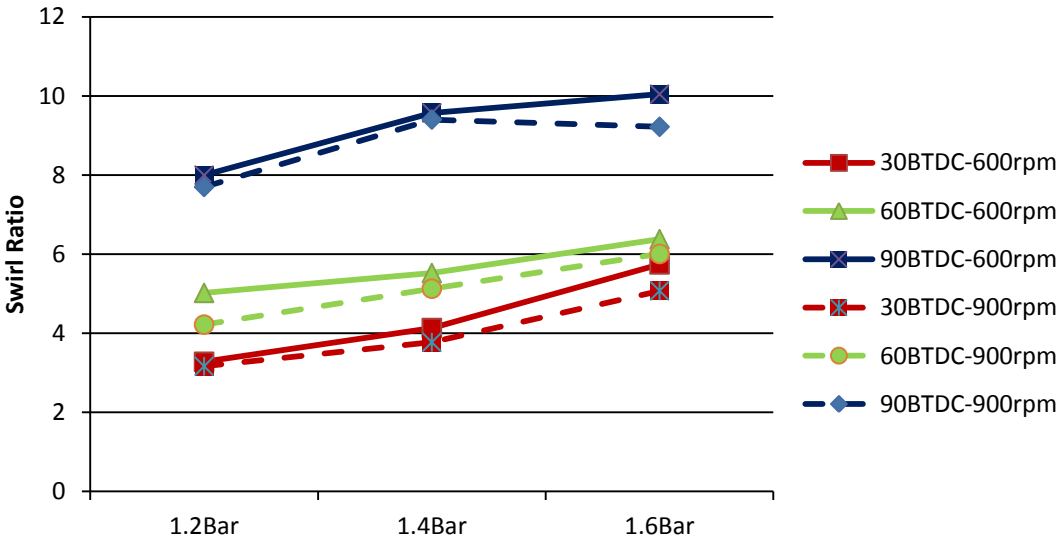

Figure 7.18 Swirl ratio across the region of interest on the horizontal plane

Figure 7.17 shows the average velocity across the region of interest on the horizontal plane. The results suggest that the increase in the engine speed from 600rpm to 900rpm has fairly small effect on the averaged horizontal flow, which is dominated by the intake port orientation instead.

Figure 7.18 shows the swirl ratios of the flows in the measurement plane calculated according to Equation 3.10. As the boost pressure becomes higher, the swirl ratio is increased by stronger radial flow because of the swirl intake port design. When the

engine speed is increased from 600rpm to 900rpm, the swirl ratios dropped because of the enhanced vertical tumble flow and shorter time at the higher engine speed.

In conclusion, at early stage of the flow structure creating process, the swirl flow structure is not stable and sensitive to the piston moving speed and intake boost pressure. However, as the piston moves towards TDC, as the flow kinetic energy disperses and reduces the small vortexes disappear and only the swirl flow structure can be obtained.

7.5 Summary

This chapter has discussed the experimental setup of a PIV system and its application to in-cylinder flow field measurements in the single cylinder 2-stroke uniflow engine with optical access. The in-cylinder flow fields and their evolution during the compression stroke were presented and the effects of intake pressure and engine speed were investigated. In addition, the PIV results were compared with the CFD calculations. It has been shown that strong swirl flows are formed just before TDC in all the cases and their swirl ratios increase with boost pressure and drops slightly at higher engine speeds.

Chapter 8 In-Cylinder Measurements of Fuel Distribution and Flame Propagation in the Uniflow 2-stroke Engine

8.1 Introduction

The fuel injection and distribution directly affect the air/fuel mixture quality and the subsequent combustion and pollutant formation process. This chapter focuses on the fuel distribution by the Planar Laser-Induced Fluorescence (PLIF) method and flame propagation imaging in the experimental uniflow 2-stroke engine. The principle of PLIF and the experimental setup are described. The experimental results of engine fuel distribution and flame propagation are discussed.

8.2 Principle of the PLIF Technique

Planar Laser Induced Fluorescence (PLIF) is a very popular optical measuring technique for the instantaneous measurement of whole-field concentration of a species. The process of laser induced fluorescence is depicted in Figure 8.1. Upon radiation by a laser beam, a molecule or atom is excited from its ground electronic state to a higher energy level. This is followed by the loss of energy to an intermediate energy state and then emission of photons to the ground electronic state.

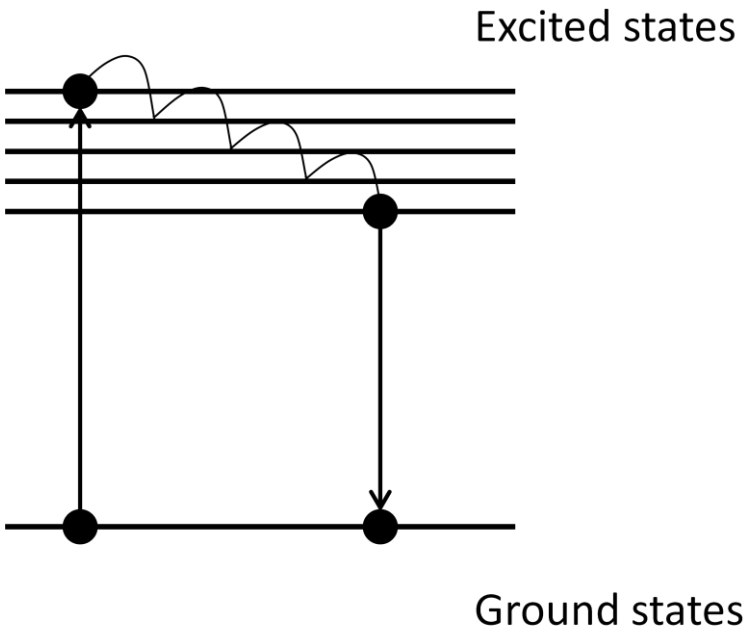

Figure 8.1 Energy level diagram of LIF

A two-energy level model is used for the LIF analysis. The rate equations for the lower and upper energy levels are described as follows:

$$dN_1/dt = -N_1(Q_{12} + B_{12}I_v) + N_2(Q_{21} + A_{21} + B_{21}I_v) \quad \text{[E-8.1]}$$

$$dN_2/dt = N_1(Q_{12} + B_{12}I_v) - N_2(Q_{21} + B_{21}I_v + A_{21} + Q_{ion} + Q_{pre}) \quad \text{[E-8.2]}$$

where

B_{12} – Einstein coefficient for stimulated absorption

B_{21} – Einstein coefficient for stimulated emission

A_{21} – Einstein coefficient for spontaneous emission

I_v – Laser spectral intensity

Q_{12} – Coefficient for collisional excitation energy

Q_{21} – Coefficient for collisional energy loss

Q_{ion} – Coefficient for Photo ionization energy

Q_{pre} – Coefficient for Predissociative energy

N_1, N_2 – Population of state 1 and 2

The collisional excitation energy coefficient Q_{12} can be omitted in most cases, most excited states are not predissociative and the photo ionization coefficient Q_{ion} can be ignored also. Thus, the Equation 8.1 and 8.2 can be simplified as follows:

$$dN_1/dt = -N_1 B_{12} I_v + N_2 (Q_{21} + A_{21} + B_{21} I_v) \quad \text{[E-8.3]}$$

$$dN_2/dt = N_1 B_{12} I_v - N_2 (Q_{21} + B_{21} I_v + A_{21}) \quad \text{[E-8.4]}$$

The upper energy level population can be negligible prior to the laser excitation, for the initial condition, $N_2|_{t=0} = 0$. In addition, the total population of molecules should be conserved because no chemical reaction occurs. So,

$$N_1 = N_1 + N_2 = constant = N_1^0 \quad \text{[E-8.5]}$$

where

N_1^0 – Total population of tracer atom prior to laser excitation

The solution of two-energy-level system is given by

$$N_2 = N_1^0 B_{12} I_v \tau (1 - e^{-t/\tau}) \quad \text{[E-8.6]}$$

$$\tau = (Q_{21} + B_{21} I_v + B_{12} I_v + A_{21})^{-1} \quad \text{[E-8.7]}$$

For laser pulse longer than to τ, the system reaches its steady value, presented as follows,

$$N_2 = B_{12} I_v \frac{A_{21}}{A_{21}+Q_{21}} \frac{1}{1+I_v/I_v{}^{sat}} \quad \text{[E-8.8]}$$

$$I_v{}^{sat} = \frac{A_{21}+Q_{21}}{B_{21}+B_{12}} \quad \text{[E-8.9]}$$

where

$I_v{}^{sat}$ – The saturation intensity

Assuming the fluorescence is emitted onto a full sphere evenly, the total number of photons N_p captured by the image sensor from a collection volume is given by

$$N_p = \eta \frac{\Omega}{4\pi} N_1^0 V_c B_{12} E_v \frac{A_{21}}{A_{21}+Q_{21}} \frac{1}{1+{I_v}/{I_v{}^{sat}}} \quad \text{[E-8.10]}$$

where

η – Transmission efficiency of the collection optics

Ω – The collection solid angle

E_v – The spectral fluence of the laser

V_c – The sampling volume

8.3 PLIF experimental setup

The engine configuration for the experimental setup of the PLIF test is the same as that used for the PIV tests described in Chapter 7. The major differences are the laser, the transmitting optics and imaging system.

A Xenon Chloride (XeCl) Excimer laser with 308nm wavelength was used for the PLIF measurement, the laser specifications are shown in Table 8.1.

Table 8.1 XeCl laser specifications

Type	**XeCl**
Model	COMPexPro 102
Max Output Power	4 W
Wavelength	308 nm
Pulse Energy	200 mJ
Pulse Length	20 ns
Pulse Repetition Rate	Max 20 Hz
Beam Size (V×H)	24mm×10 mm
Beam Divergence (FWHM)	3 mrad Vertical 1 mrad Horizontal

In order to illuminate a measurement plane in the cylinder, the laser sheet needs to be delivered through the optical window in the cylinder liner. Considering the relative locations of the engine and the laser unit, optical components are used to steer the laser beam to the precise position and focus on the measurement plane.

The required optical elements include mirrors, cylindrical lens and their mechanical holders. All elements are set on two anti-vibration platforms. The laser beam delivery system is shown in Figure 8.2.

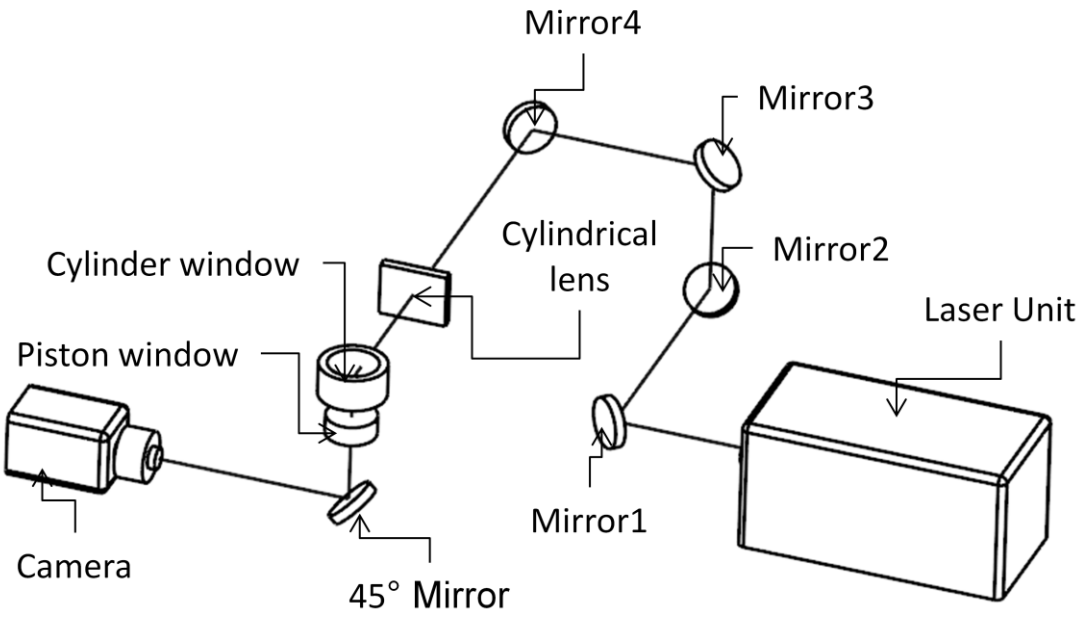

Figure 8.2 Laser beam delivery system

Mirror 1 and 2, which mounted on the lower platform, were set to the same horizontal level as the outlet of the laser unit, and steers the laser beam out of the laser unit to mirror 3. Mirror 3, mirror 4, the cylindrical lens were mounted on the higher platform and steers the laser beam to the cylinder window to illuminate the measurement plane. While lifting the laser beam level, the beam axis is flipped by mirror 4 so that a thinner laser sheet can be produced after the cylindrical lens because of the larger beam divergence on the vertical axis than on the horizontal axis

In order to expand the laser beam into a sheet, a cylindrical lens of 76.2 mm by 38.1 mm was used. The focal length of 1500mm was determined by the distance from the lens to the cylinder vertical axis, according to Equation 8.11.

$$\frac{1}{f} = (n-1)\left(\frac{1}{R_1} + \frac{1}{R_2}\right) - \frac{(n-1)^2 d}{nR_1R_2} \qquad \text{[E-8.11]}$$

where

f – Lens focal length

n – The refractive index of the lens material

R_1, R_2 – The curvature radii on the two lens surfaces

d – Required distance from lens to the subject to be focused on

The lens used in this case is anti-reflection coated by CVI Melles Griot BBAR4 248-355 coating, which provides both a very low reflection of 0.5% over a broad UV range from 248 nm to 355 nm and very high damage threshold. The resulting laser sheet thickness was about 1mm.

The fluorescence images via the 45^o mirror in the cylinder block were recorded by a Princeton Instrument PI-MAX III intensified CCD camera with the Nikon 105mm UV lens. A ST-133 controller with the Programmable Timing Generator (PTG) used to control the camera timing. A PC with an interface card and Princeton Instrument WinView/32 software was used to setup configurations and carry out data analysis.

3-pentanone was used as the fluorescence tracer for the PLIF measurements due to its high fluorescence yield and its similar boiling point (102 °C) to the iso-octane (99 °C) which was used due to its absence of deposit formation on the optical window. In this study, a mixture of 90% of iso-octane and 10% of 3-pentanone was used. The properties of iso-octane and 3-pentanone was as described in table 2.1.

8.4 Results of PLIF measurements

The PLIF measurement was carried out at 900rpm with all other engine operating parameters kept the same as the PIV experiment in Chapter 7. The direct fuel injection timing was set to 60ºCA BTDC. The injector used in this test was a Siemens gasoline piezo injector (NGM 00084766) with a cone shaped spray structure.

8.4.1 Fuel Injection characteristics

Figure 8.3 shows the first appearance of fuel spray at 110μs after the start of the fuel injection trigger sent to the injector. The injection duration was set to 200 μs. This

110μs delay corresponds to the electro mechanical lag of the injector needle opening, which was found to be constant at different injection timings and durations.

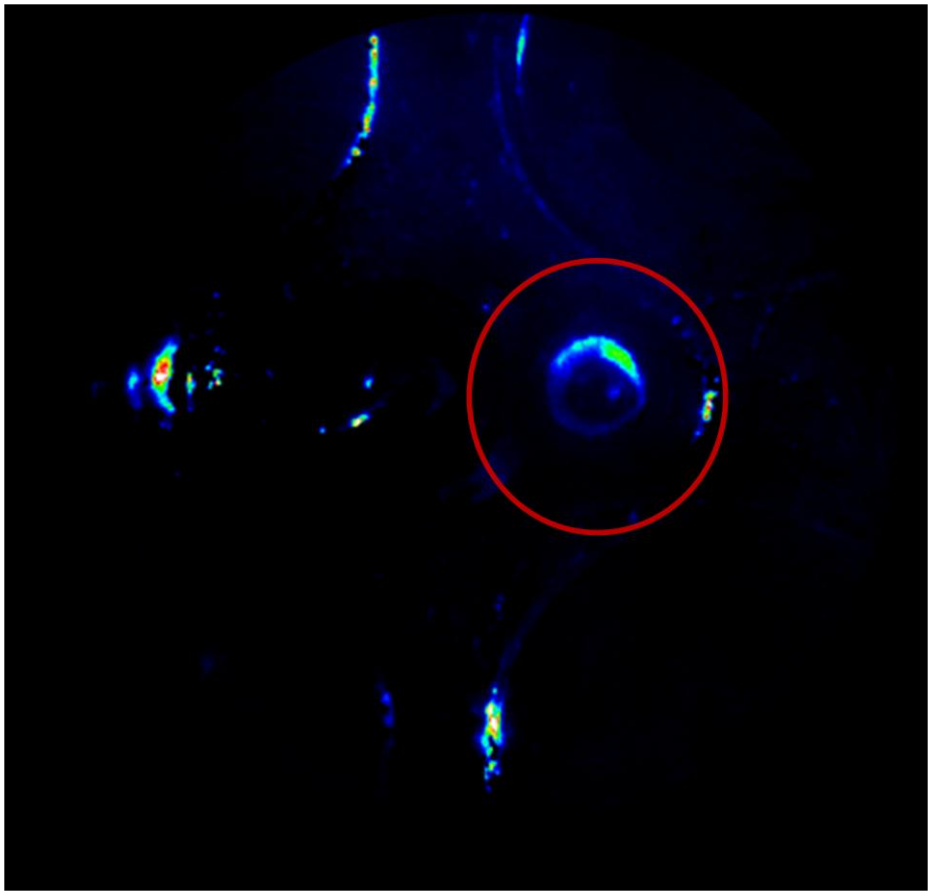

Figure 8.3 First spray image at 110μs after injector trigger signal (200μs duration)

As shown in Figure 8.4, the last image of fuel spray leaving the injector was found at 470μs after the start of the injection trigger. Taking into account of the injection duration (200 μs) and the injector opening delay (110 μs), there was a delay of 160 μs for the injector needle to be fully seated after the end of the injection trigger. In addition, it is noted that there is an area of strong fluorescence emission on the injector side (right side of the image), indicating the occurrence of fuel spray impingement on the piston.

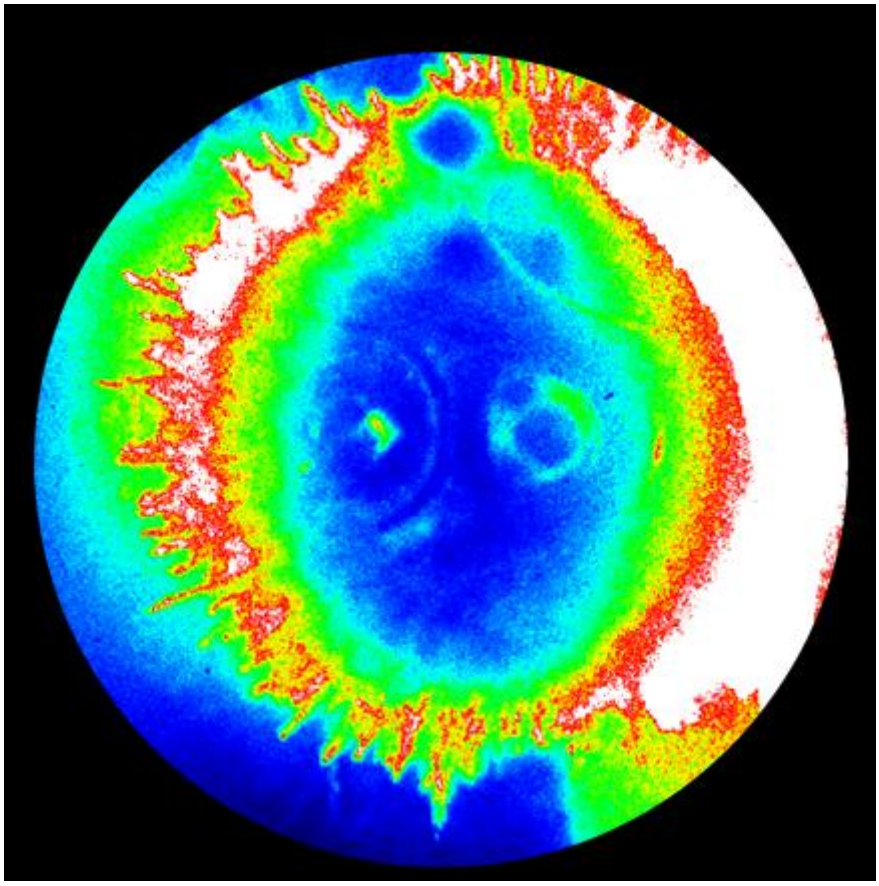

Figure 8.4 The end of Injection image at 470μs after injector trigger signal (200μs duration)

Figure 8.5 shows the fuel spray structure at 500μs after the start of injection trigger (30 μs after the closure of the injector needle). At this stage, a second fuel spray cloud was present around the injector although only one injection trigger was applied. This could be a result of the bounce of the needle valve when it was closed due to excessive force, which could be eliminated by optimising the injector drive signal.

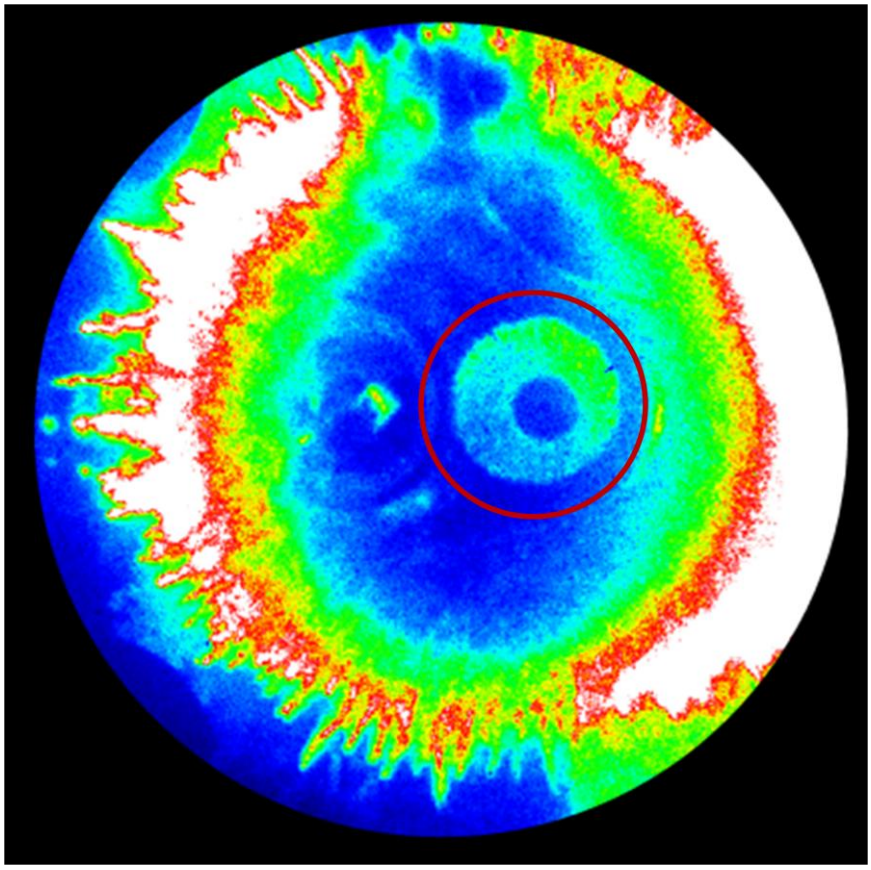

Figure 8.5 In-cylinder image at 500μs after injector trigger signal (200μs duration)

Figure 8.6 shows the fuel spray patterns at 600μs, 700μs, 1000μs and 2000μs after the start of injection trigger. At 600μs the second fuel injection was finished. At 700μs, two fuel sprays mixed together and higher fuel concentration was present on the far side to the injector, due to the pent roof combustion chamber shape and the angle of injector. Because of its much higher velocity and momentum, the early fuel spray development was hardly affected by the strong in-cylinder swirl flow.

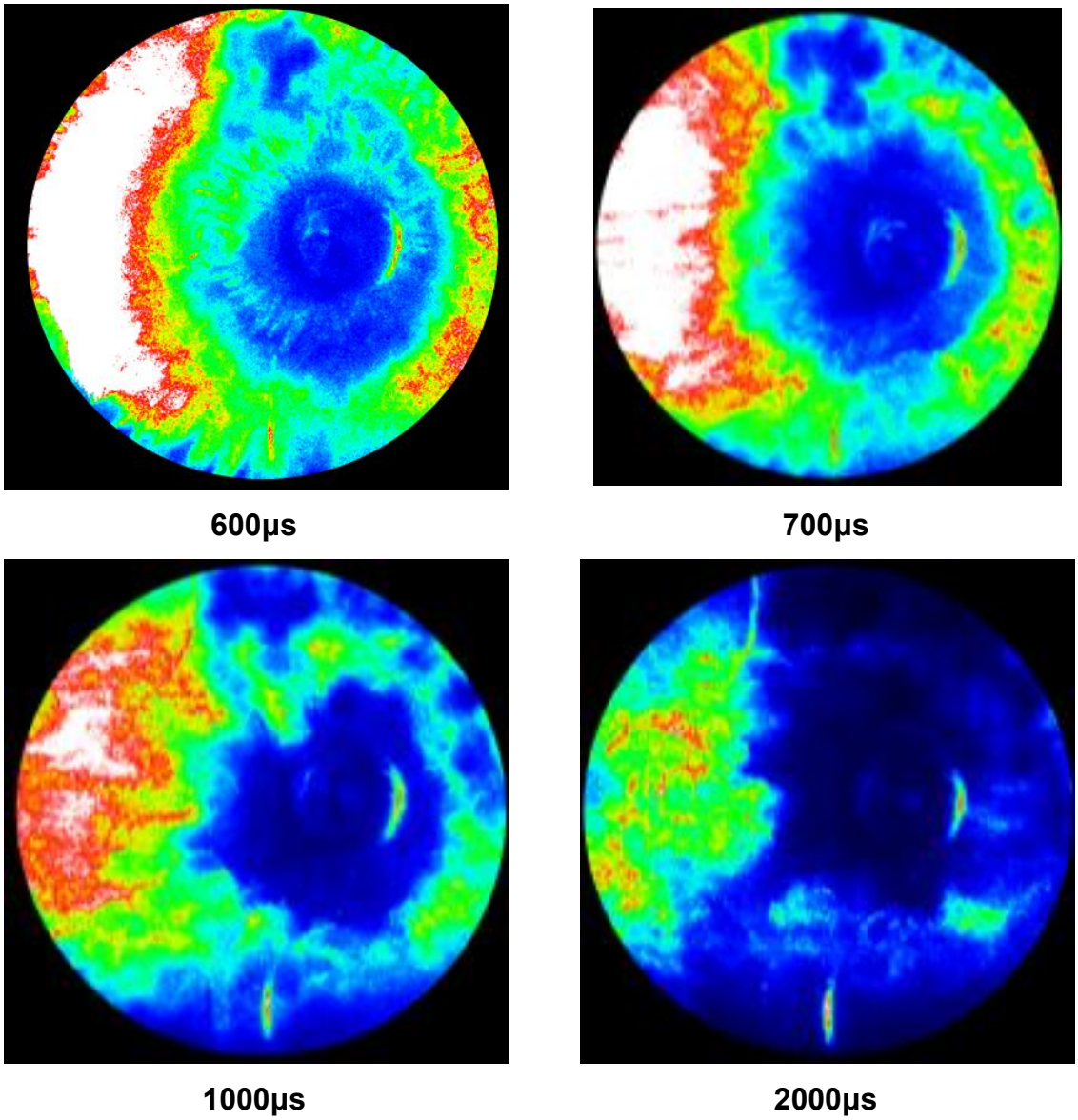

Figure 8.6 In-cylinder images of the fuel distribution

8.4.2 Fuel distribution at 15°CA BTDC

For the fuel distribution study, PLIF images of different conditions were taken at 15ºCA BTDC when the spark ignition was to take place with the Start Of Injection (SOI) timing set to 60ºCA BTDC. The boost pressure was set to 1.2bar, 1.4bar and 1.6bar. The fuel injection pressure was set to 100bar, 150bar and 200bar for each intake boost pressure and the injection duration set at 200µs, 300µs and 400µs. For each condition, twenty images were taken from consecutive engine cycles and the same process was repeated 5 times, so that an ensemble averaged image of 100 frames was obtained and analysed. One background image was taken without fuel injection prior to the PLIF fuel images and used to remove the ambient light from the reflection and other light sources.

For the post-processing of the fuel distribution data, a mean light intensity of all pixels in the region of interest (I_{mean}) was calculated. The region of interest was a round shape area with 50mm diameter, which is the visible in-cylinder area. This value can be used for the comparison of the in-cylinder fuel quantity. Then the deviation of the light intensity at each pixel from the mean light intensity was calculated as the CoV of each ensemble averaged frame (CoV_f), this value can be used to indicate the homogeneity of fuel distributions. For all images taken at the same engine operating condition, an average value of the mean light intensity of each frame was calculated, and then the deviation of the mean light intensity to the ensemble average value was used to calculate the CoV of the images taken at same engine condition (CoV_{cyc}). This value was used to present the cyclic variation. The calculations are shown as follows,

$$I_{mean} = \sum_{i=1}^{N_p} I_i \Big/ N_p \qquad \text{[E-8.12]}$$

$$\mathrm{CoV_f} = \left(\sum_{i=1}^{N_p} (I_i - I_{mean})^2 \Big/ N_p\right)^{1/2} \qquad \text{[E-8.13]}$$

$$I_{mean,cyc} = \sum_{1}^{M_p} I_{mean,i} \Big/ M_p \qquad \text{[E-8.14]}$$

$$\mathrm{CoV_{cyc}} = \left(\sum_{i=1}^{M_p} (I_{mean,i} - I_{mean,cyc})^2 \Big/ M_p\right)^{1/2} \qquad \text{[E-8.15]}$$

where

N_p – The pixel number in the region of interest

M_p – The frame number of each image batch taken at same condition

I_i – The light intensity of each pixel

I_{mean} – The mean light intensity of all pixels in the region of interest of each frame

$I_{mean,cyc}$ – The mean light intensity of all frames taken at same condition

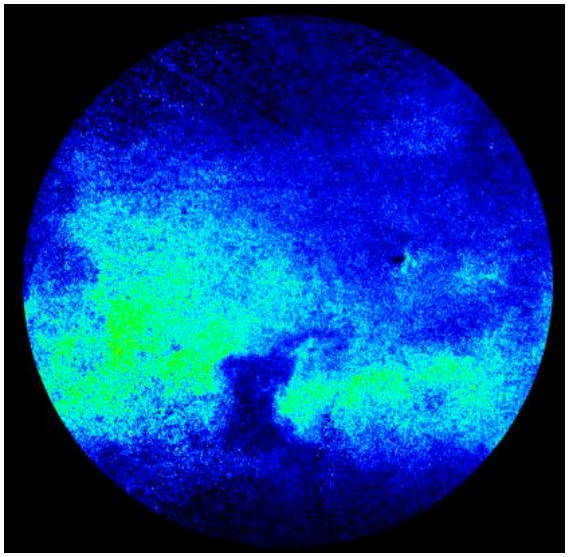

a) Injection duration 200μs

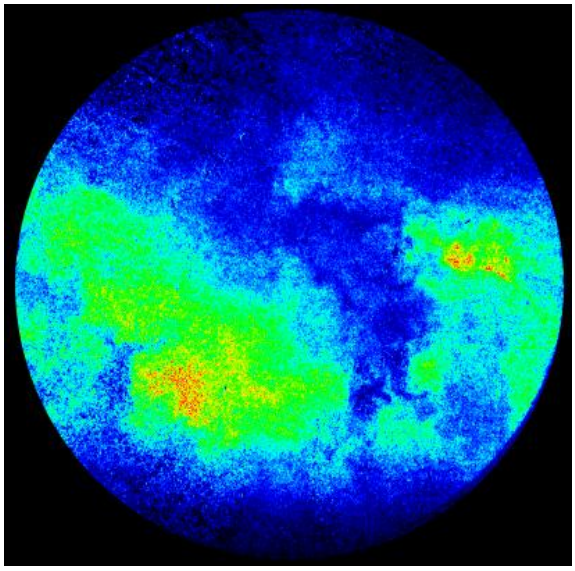

b) Injection duration 300μs

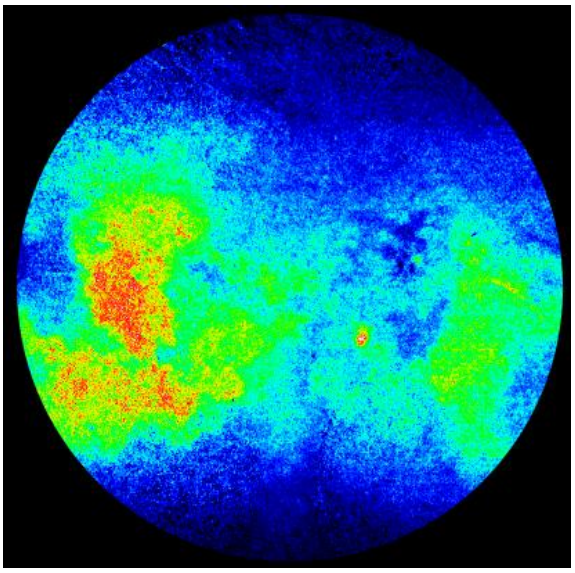

c) Injection duration 400μs

Figure 8.7 In-cylinder images of the fuel distribution with 1.2bar boost pressure and 100bar fuel injection pressure

Figure 8.7 shows the in-cylinder fuel distribution images taken under 1.2bar intake boost pressure and 100bar fuel injection pressure, the fuel injection trigger pulse width was set to 200μs, 300μs and 400μs.

As expected, the PLIF image is characterized with stronger light intensity and larger areas of the higher intensity as more fuel is injected. In addition, the fuel distribution appears more homogenous with more fuel injected.

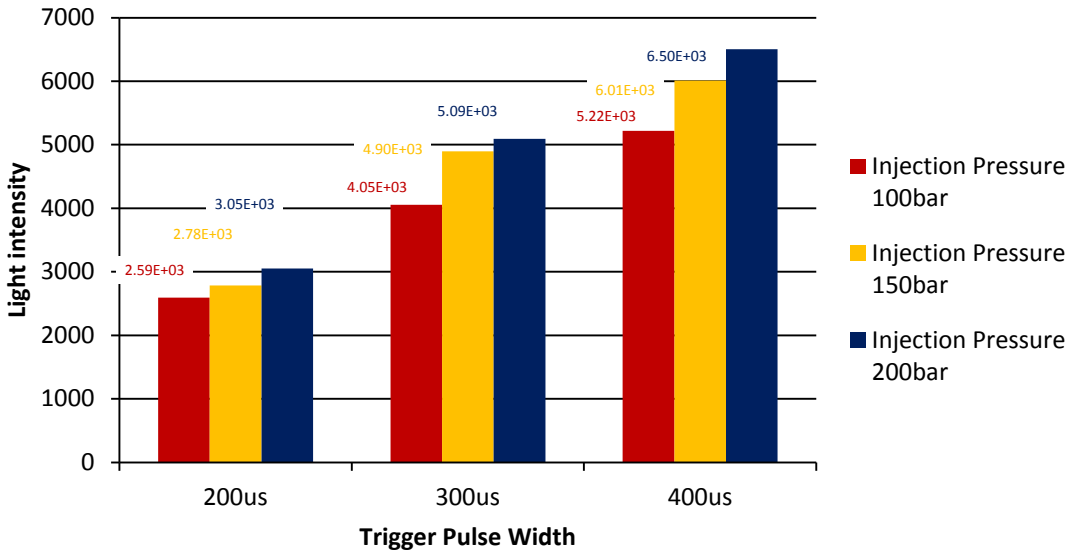

a) Boost pressure 1.2bar

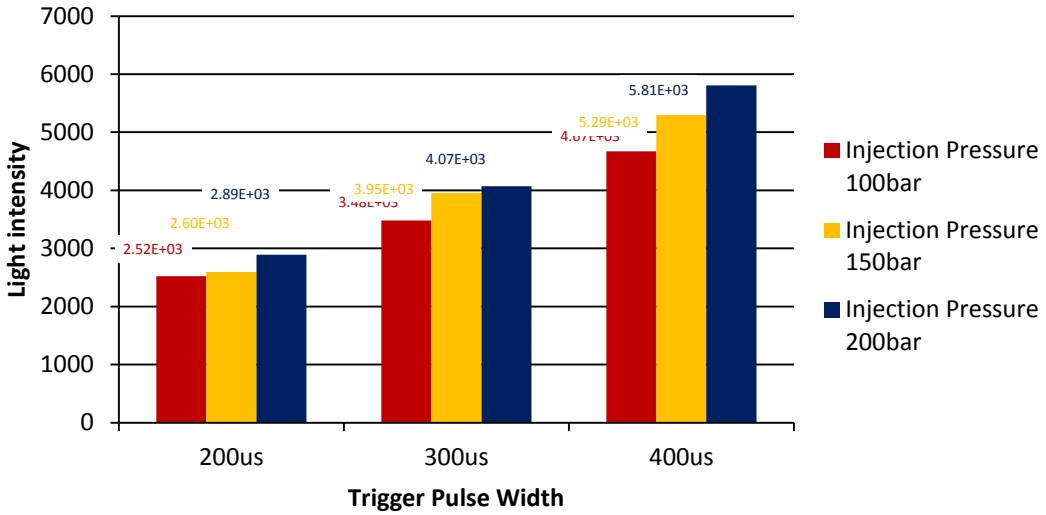

b) Boost pressure 1.4bar

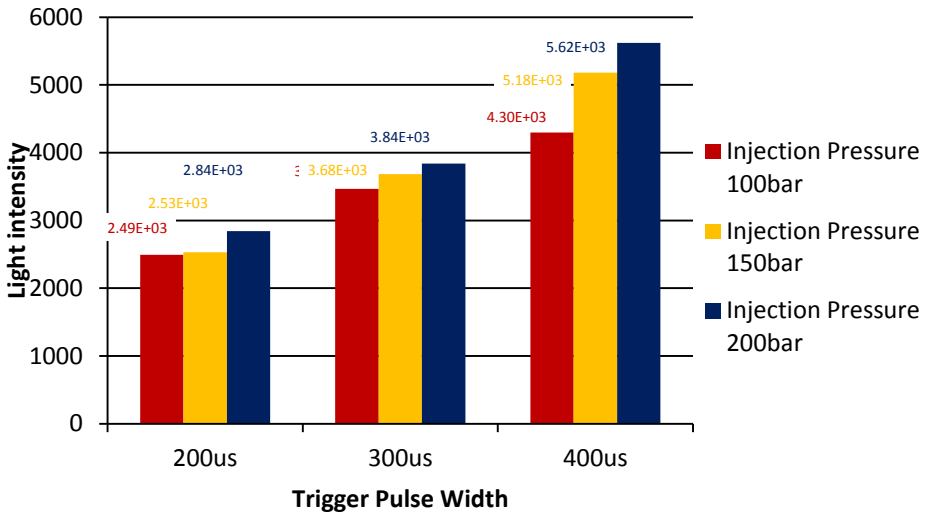

c) Boost pressure 1.6bar

Figure 8.8 Averaged light intensity of the ensemble averaged image

Figure 8.8 shows the mean light intensity of the ensemble averaged PLIF image taken at the same engine operating condition. The results indicate that the fluorescence intensity (quantity of fuel) increased with the injection duration at a faster rate than the injection pressure. When the intake boost was increased, the fuel delivery quantity dropped slightly due to the increase of fuel injection back pressure.

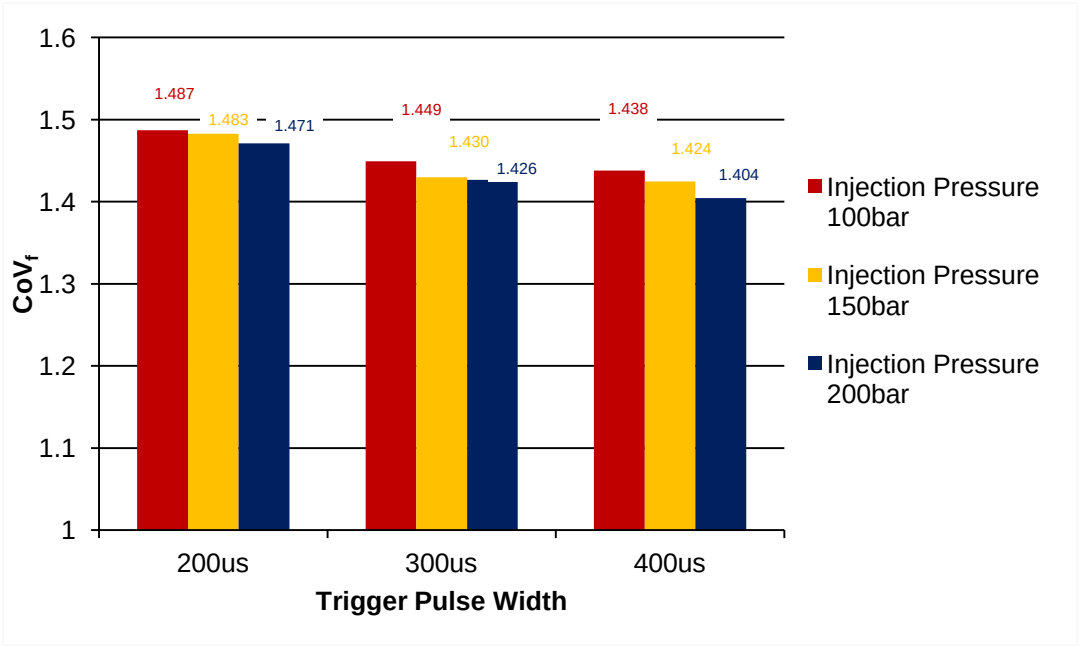

a) Boost pressure 1.2bar

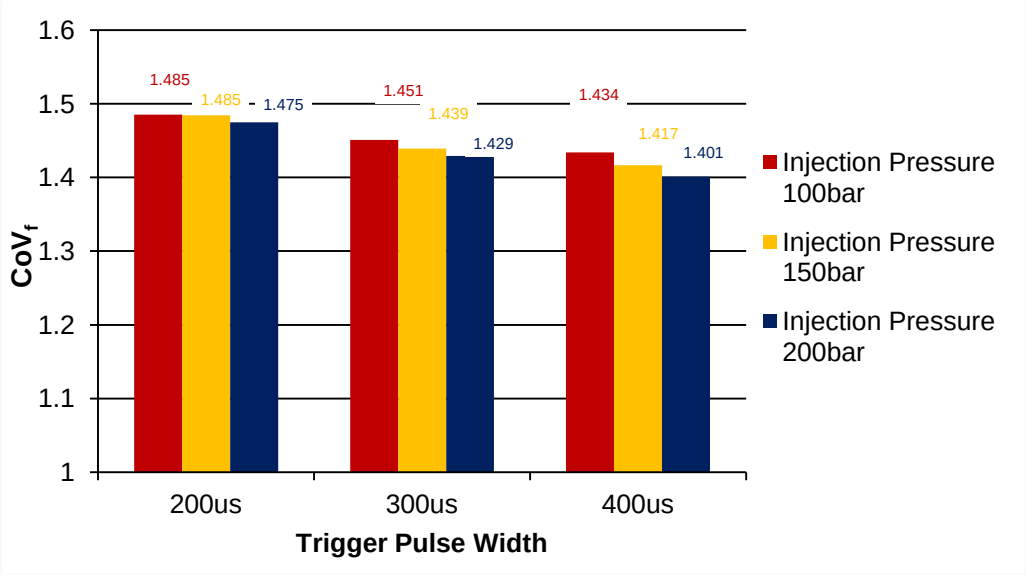

b) Boost pressure 1.4bar

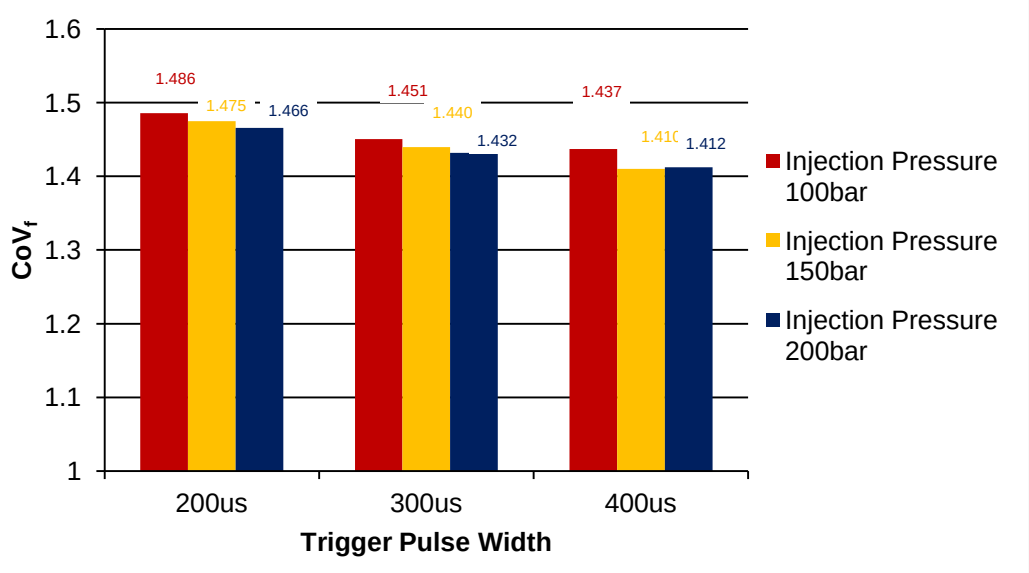

c) Boost pressure 1.6bar

Figure 8.9 CoV_f of the light intensity in the ensemble averaged image

Figure 8.9 shows the spatial variation of light intensity, CoV_f, in each ensemble averaged image. With either longer fuel injection duration or higher fuel injection pressure, the spatial variation of fluorescence light intensity became smaller, indicating a more uniform fuel distribution. The intake boost pressure barely showed any effect on fuel distribution uniformity. Related research work has suggested that the introduction of swirl creates a velocity drop near the cylinder centre in the radial profiles of axial velocity, and as the swirl strength is increased, the drop gets wider and the centreline velocity decreases [76]. The reduction in flow is undesirable as it can result in not only a poorly scavenged central region but also a poor air/fuel

mixture area. With the swirl scale generated by the intake ports orientation and the intake boost pressure used, the results indicate that the fuel distribution was dominated by the fuel injection process due to much higher spray kinetic energy than the swirl flow.

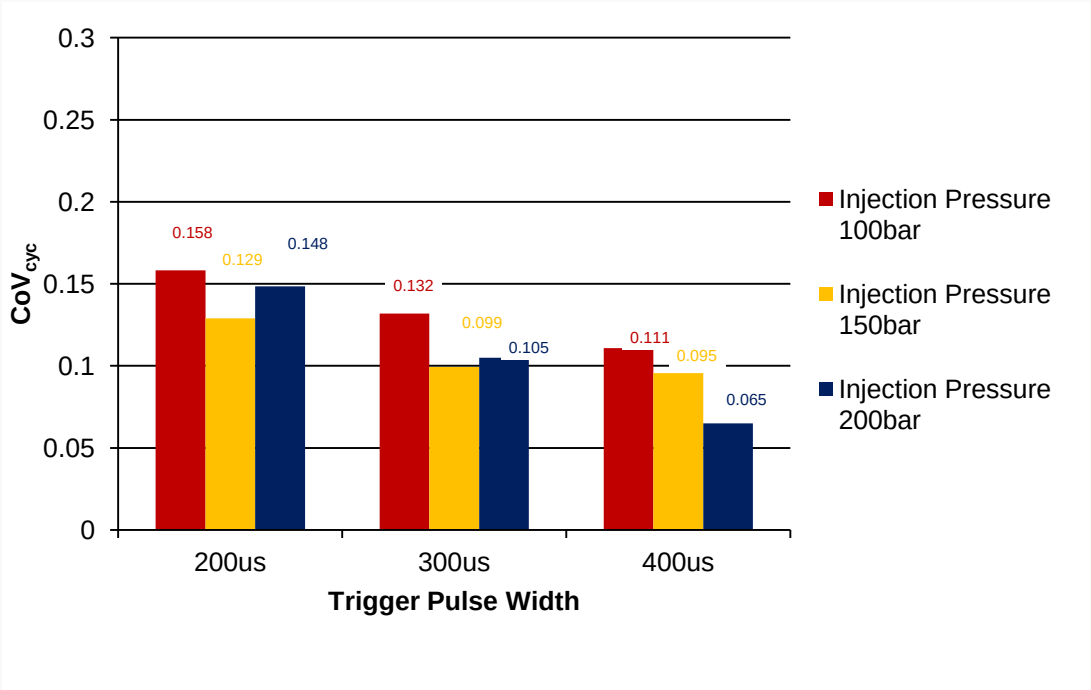

a) Boost pressure 1.2bar

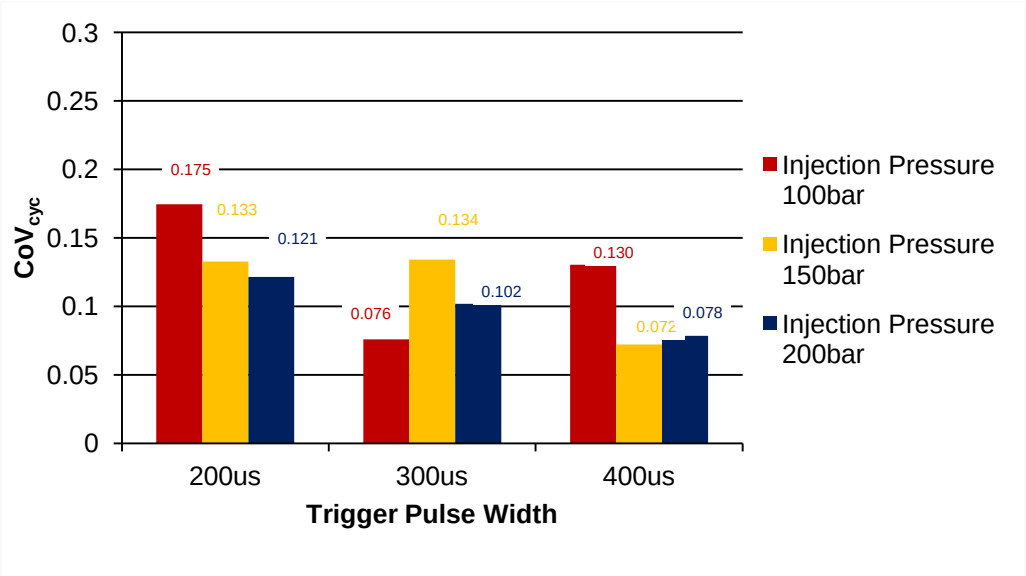

b) Boost pressure 1.4bar

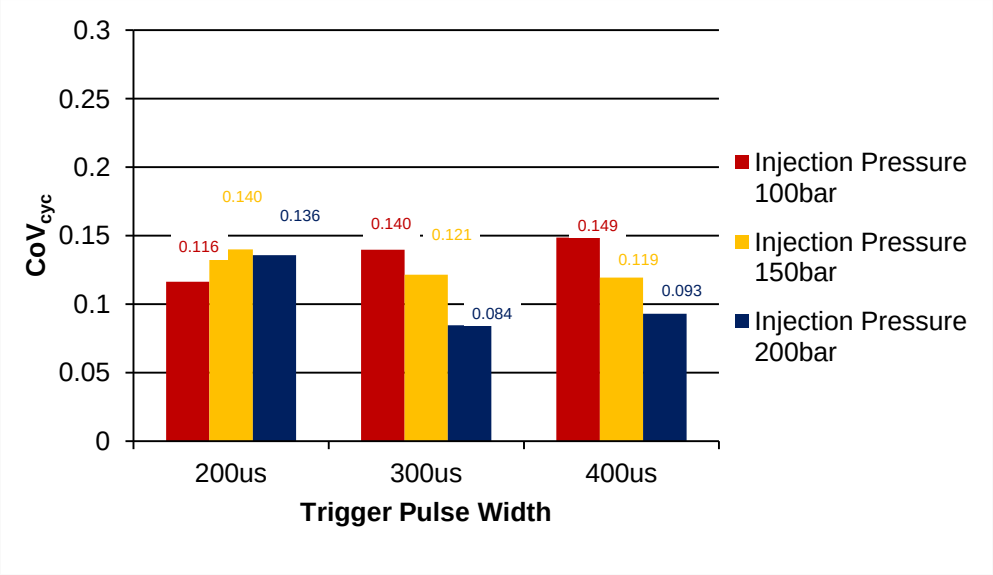

c) Boost pressure 1.6bar

Figure 8.10 CoV_{cyc} of image batch at same condition

As shown in Figure 8.10, the cyclic variation of the averaged light intensity, CoV_{cyc} was low in all cases, an indication of excellent repeatability of the DI. In most of the cases, higher fuel delivery quantity resulted in the lowest cyclic variation. Figure 8.11 shows individual images taken with 200μs fuel injection duration, 100bar fuel injection pressure and 1.2bar boost pressure. Although variation in terms of fuel distribution can be observed, in terms of overall light intensity, the variation is very small.

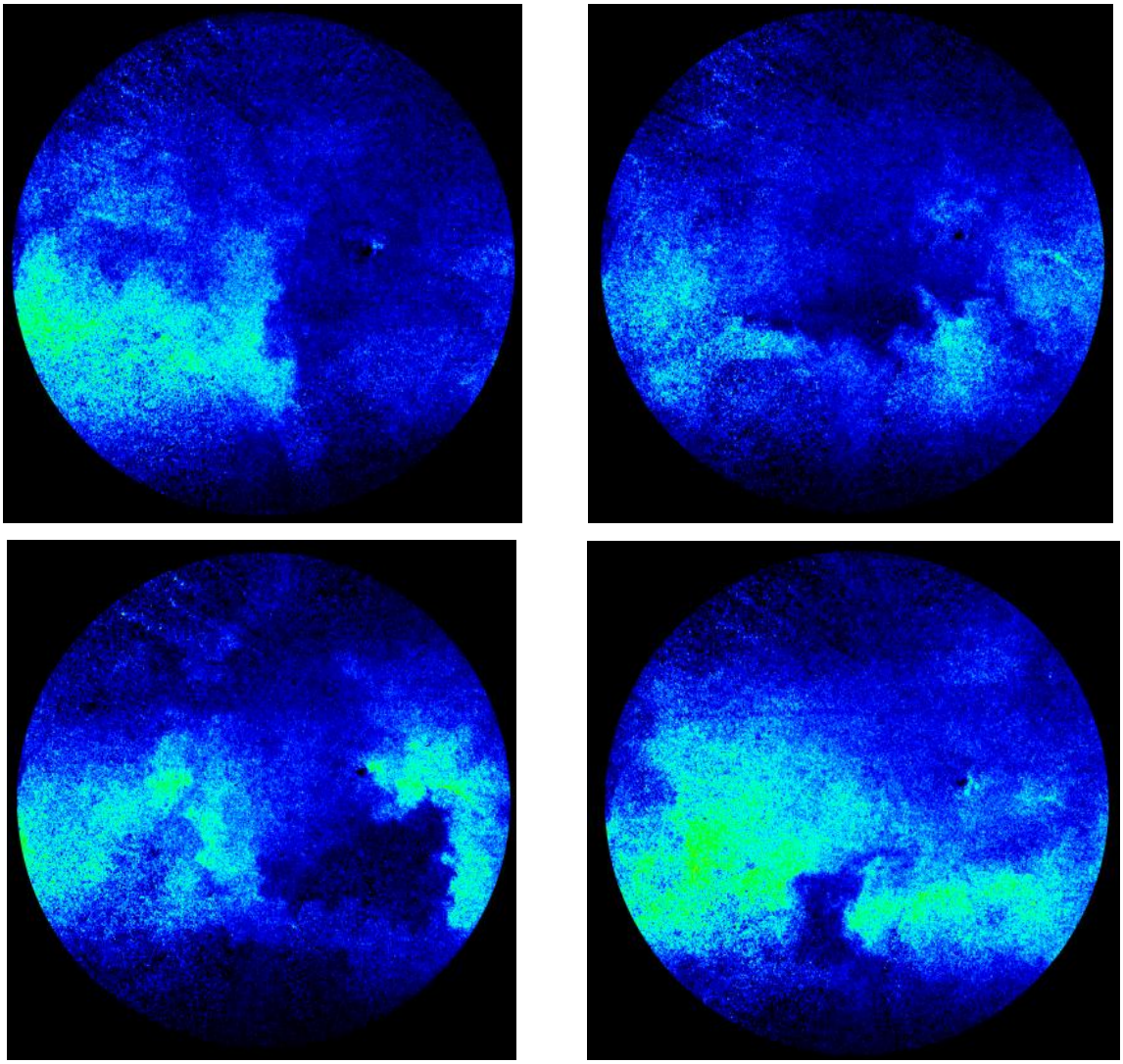

Figure 8.11 Fuel distribution - 200μs fuel injection trigger, 100bar fuel injection pressure and 1.2bar boost pressure

8.4.3 Fuel distribution at 15°CA BTDC and SOI 120°CA BTDC

Further PLIF measurements at 15ºCA BTDC were carried out with an earlier fuel injection timing of 120ºCA BTDC at the same engine operating condition. As shown in Figure 8.12, for all engine operating conditions, the advanced fuel injection timing reduced the CoV_f of the fuel distribution and produced a more homogeneous charge. This suggests that for this particular case, advanced fuel injection timing is preferred considering the in-cylinder charge homogeneity.

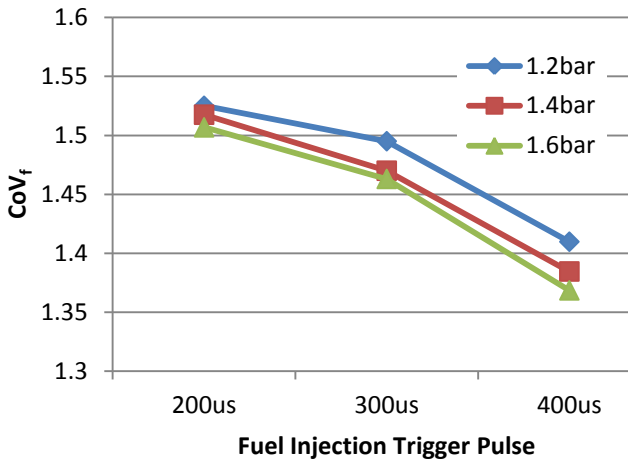

100bar fuel injection pressure and SOI @ 60ºCA BTDC

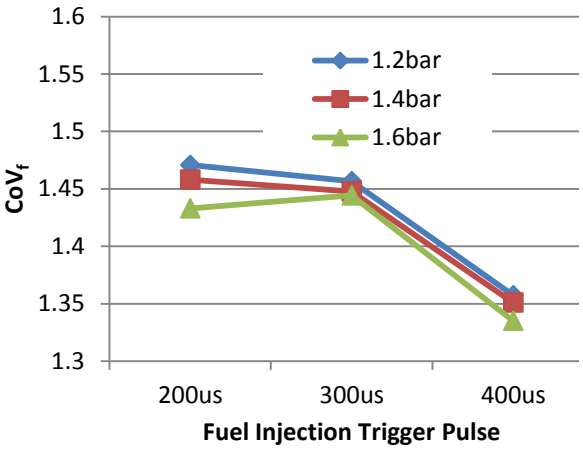

100bar fuel injection pressure and SOI @ 120ºCA BTDC

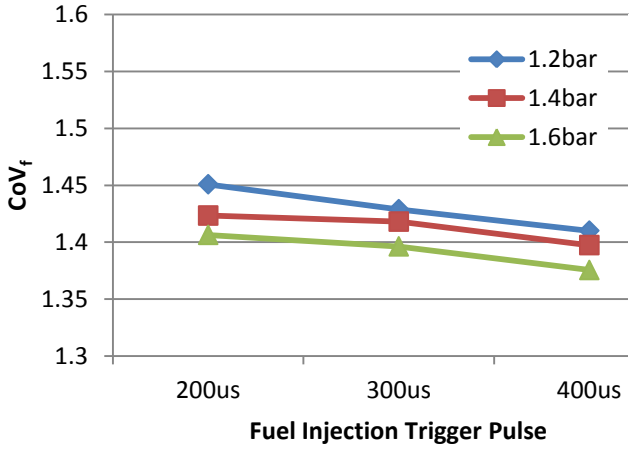

150bar fuel injection pressure and SOI @ 60ºCA BTDC

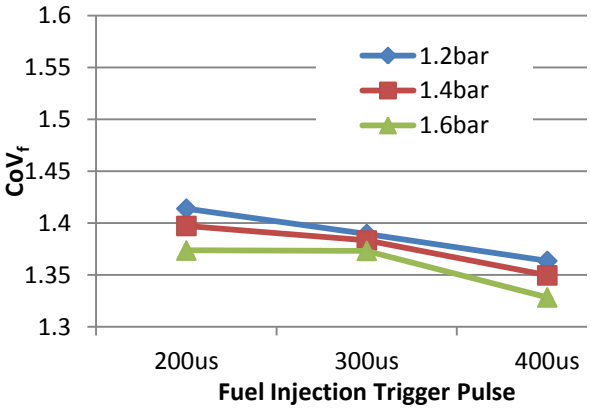

150bar fuel injection pressure and SOI @ 120ºCA BTDC

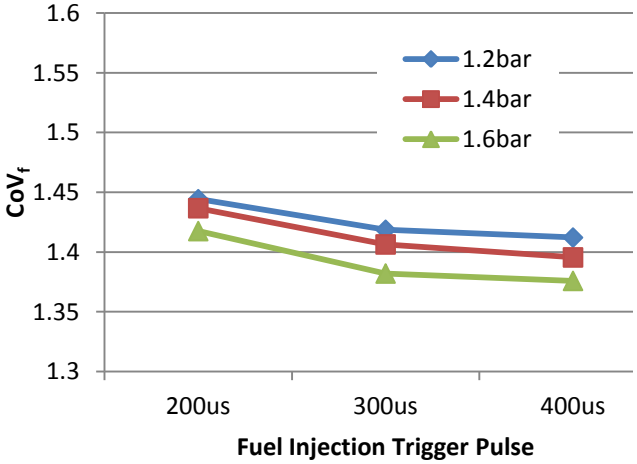

200bar fuel injection pressure and SOI @ 60ºCA BTDC

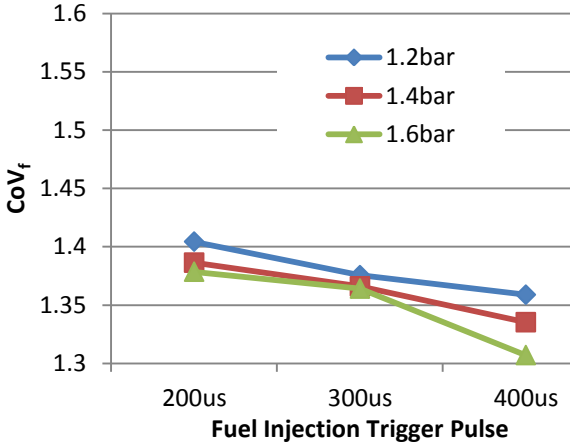

200bar fuel injection pressure and SOI @ 120ºCA BTDC

Figure 8.12 CoV_f of the fuel distribution

For the cyclic variation, although the injection timing was advanced, the improvement of cyclic variation was not realized. As discussed for the cases under 600rpm engine speed, the cyclic variation is actually very low, furthermore, the in-cylinder flow structure creating process was random to a certain extent which would affect the cyclic variation results. Advancing the fuel injection timing in this case would not improve the cyclic variation further.

The results of in-cylinder fuel distribution measurements suggests that while considering the in-cylinder mixture quality, richer mixture is preferred, in this case, the lambda value of 1 is preferred. However, no direct results indicating the relationship between lean mixture and the combustion performance. Furthermore, for SI combustion, due to the narrow time window between the end of engine breathing process and the suitable combustion timing, the fuel injection timing is suggested to be as early as possible after all ports and valves are closed.

8.5 Combustion Studies

In order to obtain images of in-cylinder combustion, the window ring in cylinder liner was replaced by a metal ring with the same dimensions. The engine speed was 600rpm and spark timing at 15ºCA BTDC. The fuel injection timing was set to 60ºCA BTDC. The boost pressure was 1.2bar and air/fuel ratio was 14.7. The intake port opening duration is from 120ºCA ATDC to 240ºCA ATDC and exhaust valve opening duration is 90ºCA ATDC to 240ºCA ATDC. The direct chemiluminescence of flame was recorded without laser illumination.

The engine in-cylinder pressure and heat release rate data are shown in Figure 8.13 and 8.14. The heat release calculation was shown below,

$$dQ/_{d\theta} = \frac{\gamma}{\gamma-1} p \frac{dV}{d\theta} + \frac{1}{\gamma-1} V \frac{dp}{d\theta} \qquad \text{[E-8.16]}$$

where

$dQ/_{d\theta}$ – Heat release rate

γ – Specific heat ratio

p – In-cylinder pressure

V – In-cylinder volume

The engine IMEP was 2bar. The CA10, CA50 and CA90 were at 9ºCA BTDC, 2ºCA ATDC and 31ºCA ATDC, respectively. The heat release result illustrated a relatively long and low heat release process at the late stage of the combustion. This heat release process can also be observed in the images taken at late flame propagation stage, a small flame core lasted about 5 ºCA to 10ºCA after the rapid burning process. This is probably because of the effect of the in-cylinder swirl flow structure, the flow structure kept mixing the unburned fuel and other in-cylinder components, diluting the unburned air/fuel mixture, thus the combustion speed was reduced.

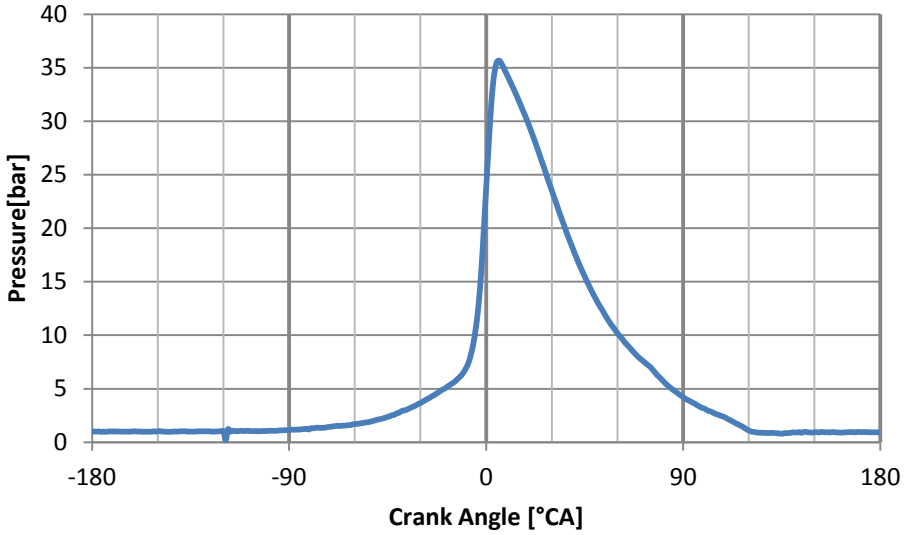

Figure 8.13 In-cylinder pressure curve

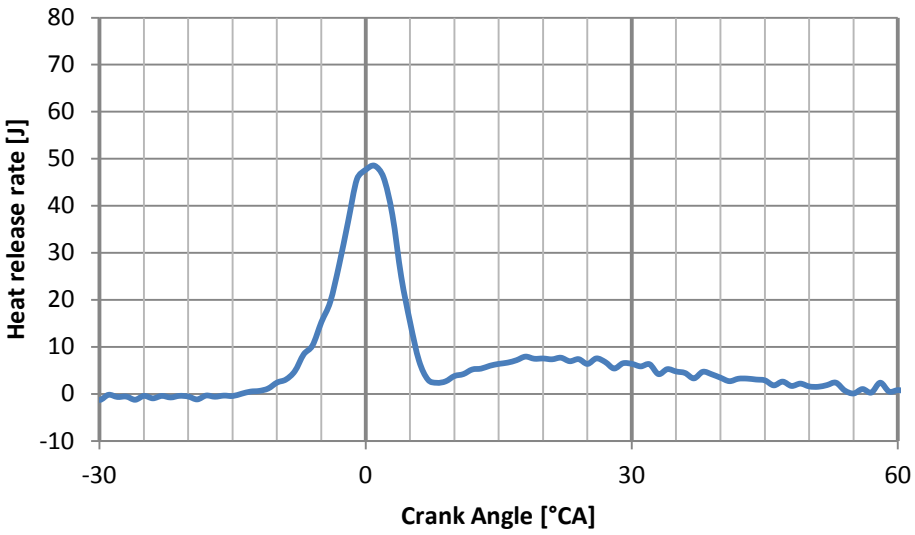

Figure 8.14 Heat release curve

Two image acquisition systems were used for the flame propagation study on the uniflow 2-stroke engine. A NAC Memrecam fx 6000 high speed video camera coupled with a DRS Hadland Model ILS3-11 intensifier was used to record the high speed frame sequence continuously with 512x384 pixel resolution at 6000fps. Higher resolution snapshot images from different cycles were obtained by the Princeton ICCD camera.

15ºCA BTDC

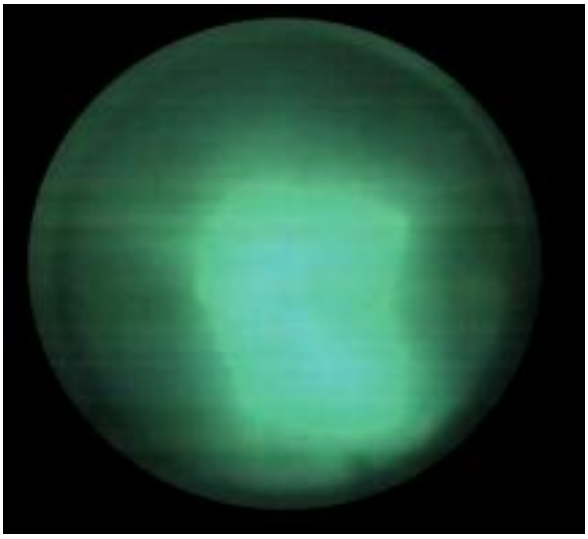

9ºCA BTDC)

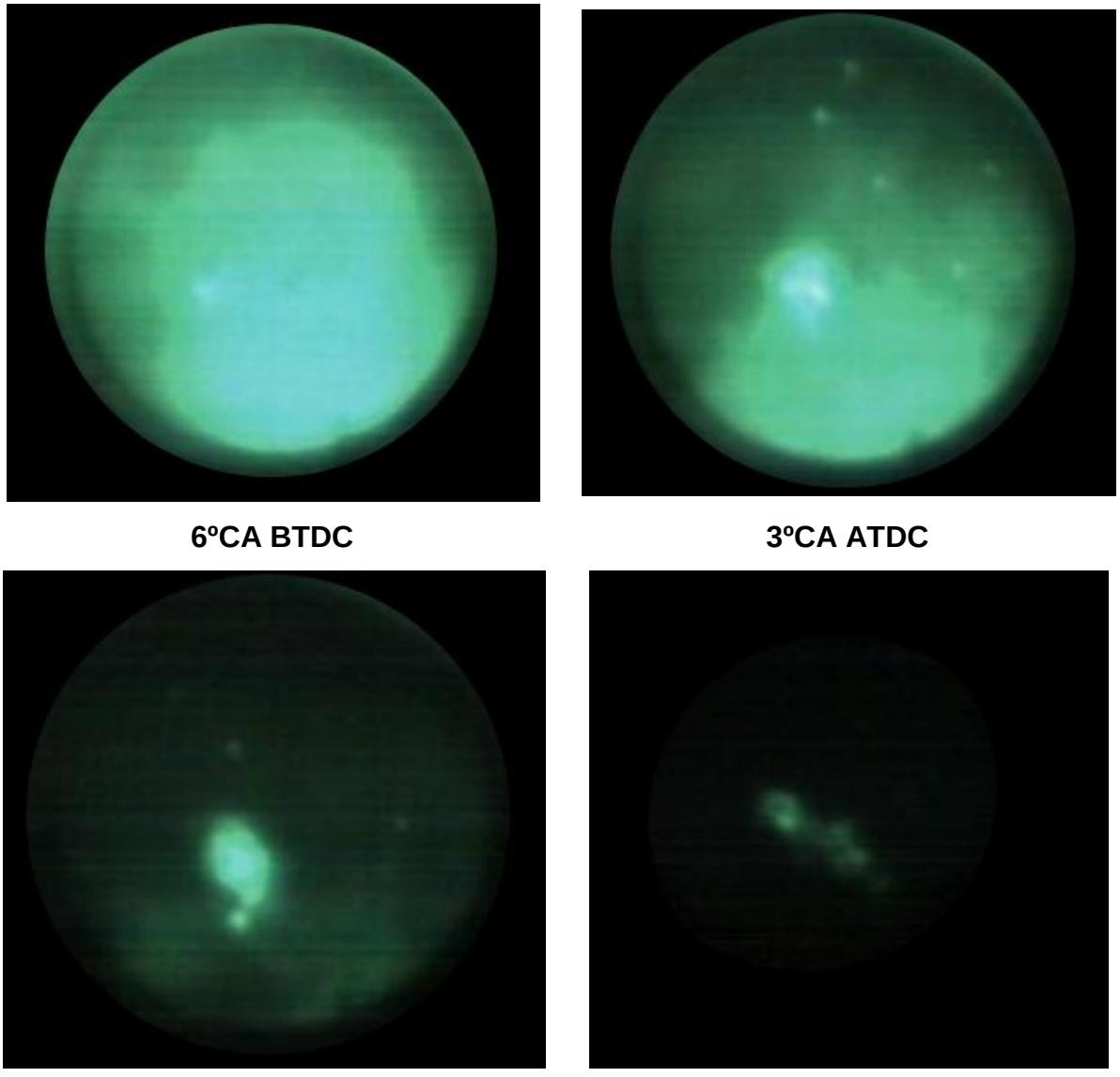

6ºCA BTDC **3ºCA ATDC**

15ºCA ATDC **18ºCA ATDC**

Figure 8.15 Flame Propagation images sequence

Figure 8.15 shows the high speed sequence of images of combustion taken by the high speed video camera. After the ignition, the flame kernel was forced to the bottom side of the image. Both the flame centre and the flame front moved in the clockwise direction due to the effect of in-cylinder swirl flow. As it approached the cylinder wall, the flame front was quenched around TDC. The flame region seen at 15ºCA ATDC and afterwards was most likely caused by the combustion of locally fuel rich mixture and after-burn of CO to CO_2 in the burned gas region.

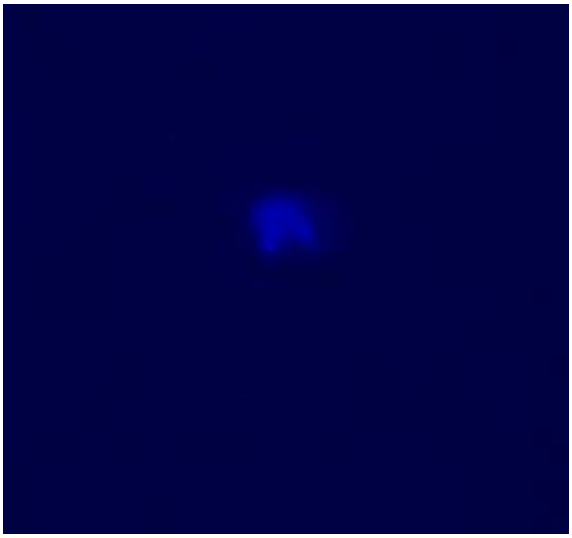

15ºCA BTDC

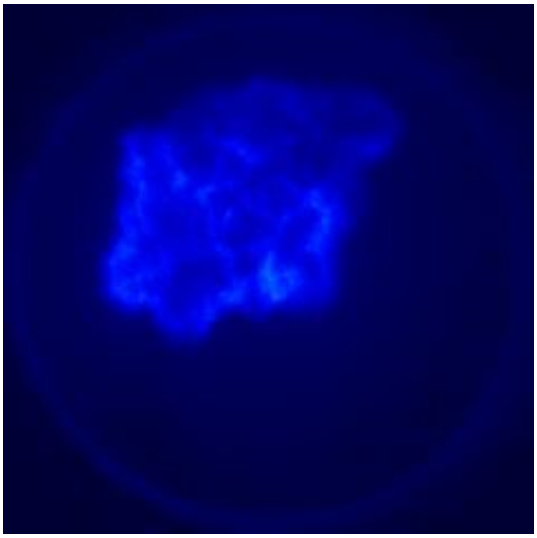

10ºCA BTDC (CA10)

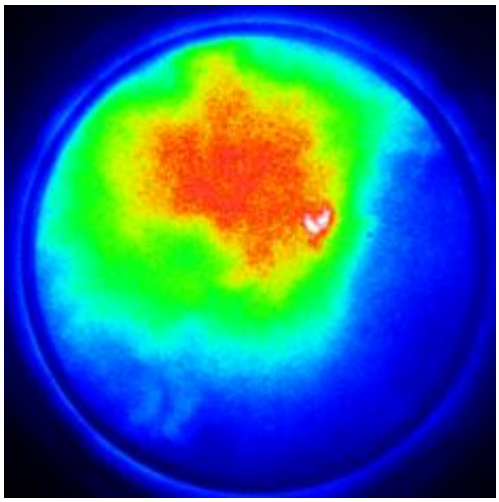

5ºCA BTDC

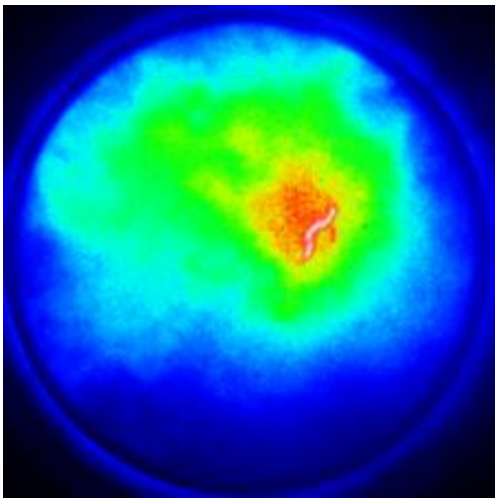

TDC (CA50)

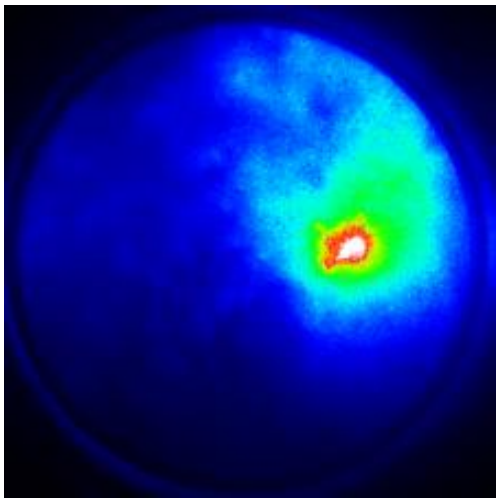

5ºCA ATDC

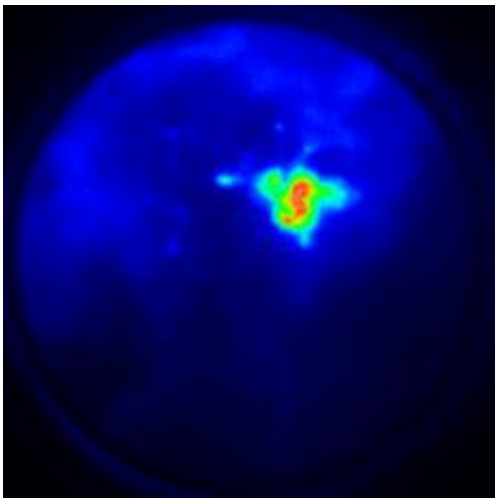

10ºCA ATDC

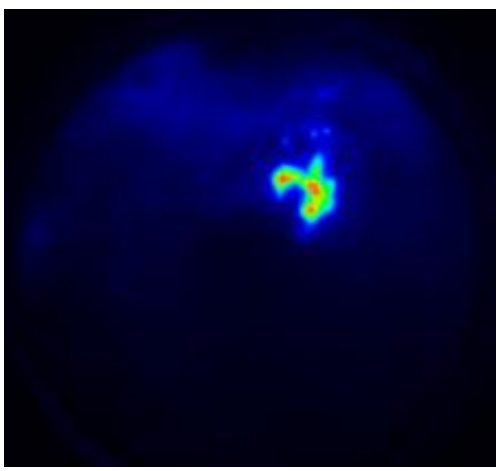

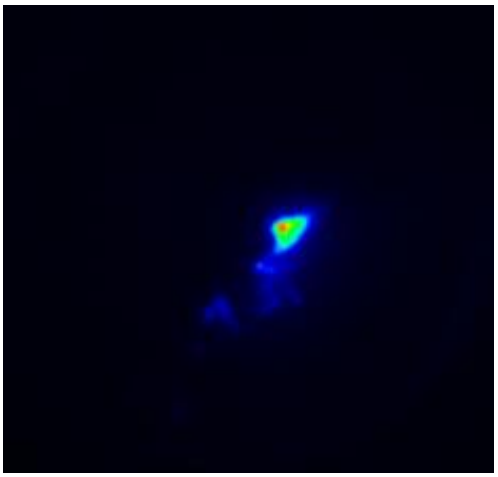

15ºCA ATDC **20ºCA BTDC**

Figure 8.16 Flame Propagation images

Figure 8.16 shows the higher resolution individual images from different cycles taken by the ICCD camera PI-MAX III. Although all images were taken from different cycles, the results still suggest that the flame was blown toward one side of the cylinder wall and then shrunk back to the flame core around the centre of the combustion chamber. The higher temperature core and after-burn near the spark plug are particularly visible.

With the in-cylinder flow structure and strength organized by current engine configuration, the flow is not too strong to breach the flow propagation sequence, but also not too weak that will be broken by the expansion of the combustion. The flame propagation was dominated by the combustion expansion at early stage and dominated by the in-cylinder swirl flow when the kinetic energy of the combustion explosion getting lower. This feature could be helpful for improving the combustion efficiency especially at the late stage of the combustion and could be helpful for reducing engine emissions.

8.6 Summary

This chapter explained the engine configuration and experimental facilities for PLIF measurements on fuel distribution study and the flame propagation study in the uniflow 2-stroke engine.

For the fuel distribution study, various intake boost pressures, fuel injection pressures, injection durations and fuel injection timings were used. The results were

compared in terms of the fuel delivery quantity indicated by the fluorescence intensity; the fuel distribution uniformity presented by the CoV_f and the cyclic variation measured by CoV_{cyc}.

For the flame propagation study, two camera systems has been used in order to take continuous frame sequence and high resolution images taken cycle by cycle. The results from two systems were consistent.

Chapter 9 Conclusions and Recommendations for Future Work

9.1 Introduction

Research has been carried out on the feasibility and potential of a boosted uniflow 2-stroke direct injection gasoline engine as a highly downsized powerplant for automotive applications. Both numerical calculations and engine experiments were carried out in the study.

3D CFD calculation was used for in-cylinder flow structure and fuel distribution studies. In addition, the results of the 3D CFD calculations were used to set up the initial and boundary conditions for the 1D engine simulation, which significantly reduced the complexity and time spent in the engine simulation and predictions. The geometry of the boosted uniflow engine was then optimised for maximum performance.

Following the simulation study, a uniflow 2-stroke single cylinder engine was commissioned with a newly designed intake engine block. The block features uniflow intake ports and incorporates optical access for in-cylinder measurements. The PIV technique was used for in-cylinder flow structure measurements and the PLIF technique for the in-cylinder fuel distribution measurements. Stable combustion was achieved and the combustion process was studied by means of high speed imaging.

9.2 Design of intake ports

Different intake port designs were analysed using CFD in order to evaluate their effects on in-cylinder flow characteristics. The main findings of the 3D CFD calculations are as follows:

(i) As the axis inclination angle is changed from 30º to 90º with an increment of 15º, the delivery ratio increased due to enlarged effective area of the intake ports. Because of the air short circuiting effect, the trapping efficiency falls as the axis inclination angle increases. The charging and scavenging

performance of 60º and 75º axis inclination angle are slightly less than those of the 90º axis inclination angle ports. In light of the negative effect of air short circuiting of larger angles, 60º axis inclination angle was chosen in the subsequent analysis.

(ii) For a given engine bore diameter and fixed value of the port width ratio, intake ports can be arranged with wider port width and less number of ports or narrower port width and more number of ports. The calculations has shown that with the same swirl orientation angle and port width ratio, air mass flow rate through intake ports is independent of the number of intake ports when the port width ratio is kept constant. For a given swirl orientation angle, the swirl ratio decreases slightly as the number of ports is reduced. That is, a higher swirl ratio can be obtained with a larger number of narrower ports due to higher flow velocity and more organised swirl flow.

(iii) When the swirl orientation angle is increased from 43º to 51º, the delivery ratio falls gradually from 2.4 to 1.9, which requires a reduced port width ratio. In addition, a larger swirl orientation angle produces a greater swirl ratio. The best scavenging performance is obtained with a swirl orientation angle of 20°. When the swirl orientation angle is less than 20°, the scavenging performance and the trapping efficiency decrease because of the air short circuiting effect, although the delivery ratio increases. When the swirl orientation angle becomes greater than 20°, the scavenging performance also declines because of the reduction in the delivery ratio. Therefore, the 60° axis inclination angle and 20° swirl orientation angle has been adopted in the uniflow 2-stroke engine design.

9.3 In-cylinder fuel distribution

The Discrete Phase Model is used to simulate the direct fuel injection process of an outward open piezo DI gasoline injector with a 90º cone spray angle. The injected fuel is treated as particles and droplet breakup calculation is included to model the atomisation process. The results of the CFD calculations can be summarised as follows:

(i) The fuel evaporation rate increases during the high pressure fuel injection process and then slows down after the end of injection. Faster fuel

evaporation takes place at retarded injection timings due to higher charge temperature. The main cause for the less total fuel vapour from the early injection cases is the liquid fuel impingement because of the in-cylinder swirl flow and lower charge density during the earlier injection.

(ii) Split injections were found to improve the fuel atomisation and mixture formation. Because of the reduced momentum of each injection of shorter duration, the split injection reduces the liquid impingement of early injection. In addition, it is shown that the total fuel evaporation is improved as the percentage of the first injection is reduced from 50% to 20%.

9.4 Uniflow engine geometry and scavenging timings

The uniflow 2-stroke engine design has been analysed by the 1D engine model with calibrated Frictional Mean Effective Pressures (FMEP). The effect of bore and stroke ratio on the engine performance was studied to determine the appropriate bore and stroke of the 2-stroke engine. The impact of timings of the intake ports and exhaust valves on engine performance was investigated. The main conclusions include:

(i) The bore to stroke ratio for maximum engine performance is 1.13. In order to accommodate the vehicle packaging, the stroke was fixed to 67mm. Therefore, for the targeted 0.3 litre displacement volume per cylinder, a bore of 76mm and stroke of 67mm were chosen

(ii) The intake port/exhaust valve timing optimisation has been carried out for maximum performance. The intake port opening time is set to 120ºATDC, and closure at 240ºATDC. The exhaust valve opening duration was set to 80ºATDC to 240ºATDC.

9.5 The boosted uniflow 2-stroke powertrain and its application to a vehicle

The full load performance of the boosted uniflow 2-stroke engine dictates the number of cylinders of such engines, which can ultimately help in selection of a suitable

boosting system according to its compressed air flow rate. In turn, the potential benefits from engine downsizing and downspeeding will depend on the performance of the boosted uniflow 2-stroke engine. The 1D engine simulation has been used to assess the maximum torque and power which can be obtained from different configurations of turbocharger and supercharger with the peak cylinder pressure below 120bar. A vehicle driving simulation program was developed and applied to analyse the fuel economy benefits over the NEDC. The main conclusions are as follows:

(i) Among all the boost system configurations with various modes of supercharger and turbocharger considered, the turbocharger shows the best efficiency from a thermodynamic point of view. The low efficiency of the supercharger is mainly due to the mechanical losses especially at low load.

(ii) Both the 3-cylinder 0.9 litre and the 2-cylinder 0.6 litre uniflow 2-stroke engine are capable of matching the performance of the NA 1.6 litre 4-stroke engine output with an optimised turbocharger.

(iii) With the same transmission ratio, the 3-cylinder 0.9 litre 2-strok engine showed 8.6% increase in fuel consumption and the 2-cylinder 0.6 litre 2-stroke engine improved the fuel economy by 8.2%. However, with 33.3% downspeeding, the fuel economy can be improved by 12.6% by the 3-cylinder engine and 18.1% respectively by the 2-cylinder engine, respectively. With 44.4% downspeeding strategy, the fuel economy went up to 18.3% and 23.6%.

9.6 Single cylinder uniflow 2-stroke engine and its in-cylinder flow and fuel distributions

A single cylinder DI gasoline engine was converted to operate as an uniflow 2-stroke engine by incorporating a new intake block, modified cylinder liner, a new timing belt and crank sprocket, as well as customised intake and exhaust systems. The intake block was designed with swirl intake ports based on the CFD calculations and provided the optical access for the in-cylinder flow and fuel measurements. The single cylinder engine was operated successfully up to 900rpm.

The in-cylinder flow measurements by PIV showed similar trend with the CFD calculation. It was found that the swirl flow structure was less well defined at the end of the intake process. The swirl flow structure became more apparent and the swirl ratio was significantly enhanced at the end of the compression stroke due to the piston movement and conservation of momentum.

During the in-cylinder fuel injection measurements, a delay between the injection electrical drive signal and the start of injection was noted and it was measured as 110μs. A similar delay was also detected between the electrical drive signal and the closure of the injector at the end of injection process. When the quantity of fuel injected was small, the in-cylinder fuel distribution exhibited high cycle to cycle variations. As the fuel injection was increased, the in-cylinder fuel distribution became more uniformly distributed and showed less cyclic variations.

The uniflow 2-stroke engine was fired successfully by setting the intake port opening duration to 120ºATDC and exhaust valves opening from 80º to 240ºATDC. Both high resolution single shot images and crank angle resolved high speed flame propagation images were recorded and analysed. Following its formation around the spark plug, the flame was found to move towards one side of the combustion chamber due to the in-cylinder swirling flow. The after-burn of locally fuel rich mixtures was found after the flame front was extinguished.

9.7 Recommendations for future work

9.7.1 Engine simulations

In the current research, the 3D CFD simulation was used to model the effect of intake port design and was able to show the general flow structure in the cylinder as measured via the PIV technique. In order to use the 3D CFD to guide the design and optimisation of the direct injection uniflow 2-stroke engine, further evaluation and calibration of the fuel injection and spray models will be required. In addition, the combustion model needs to be developed to predict the heat release process and engine performance. Both spark ignition flame propagation and autoignition models should be included in the combustion modelling so that the autoignition combustion at part-load operation can be analysed as a function of engine parameters.

9.7.2 In-cylinder flow and fuel distribution measurements

The intake block in the single cylinder uniflow 2-stroke engine has the flexibility of varying the intake port orientation. Due to the time constraint, only one intake port design was implemented. It is recommended that additional experiments can be carried out with different intake port designs in order to optimise the in-cylinder flow and scavenging process. In addition to the in-cylinder flow and fuel distribution on a horizontal plane, the PIV and PLIF techniques can be used to obtain the flow and fuel distributions in a vertical plane through the optical liner. Although the in-cylinder flame propagation investigation has been carried out, the test was only in initial state. Further experimental tests and analysis work would be very helpful on understanding the combustion characteristic of a uniflow 2-stroke engine.

9.7.3 Engine thermal and emission performance

Although fired engine operation was realised in the single cylinder uniflow 2-stroke engine, it was difficult to carry out systematic thermodynamic engine experiments. In order to evaluate the full potential of the uniflow 2-stroke direct injection gasoline engine, it would be desirable to design and build such an engine that has the capability to operate at speeds up to 3500rpm and withstand cylinder pressure up to 120bar. The engine should be equipped with variable cam timing devices on the exhaust valves so that the scavenging process can be adjusted according to the speed and load. The combustion system should include centrally mounted injector and spark plug for optimum mixture formation. In addition, variable boost pressure and exhaust back pressure should be provided to simulate the interactions between the engine and a turbocharger.

References

[1] I. C. O. C. TRANSPORTATION, “EU CO2 EMISSION STANDARDS FOR PASSENGER CARS AND LIGHT-COMMERCIAL VEHICLES,” January 2014.

[2] “New Car CO2 Report 2013,” *The 12th report,* 14 March 2013.

[3] F. Zhao, M.-C. Lai and D. Harrington (1999), “Automotive spark-ignited direct-injection gasoline engines,” *Energy and Combustion Science,* vol. 25, p. 437–562, 1999.

[4] T. Kume, Y. lwamoto, K. lida, M. Murakami, K. Akishino and H. Ando(1996), “Combustion Control Technologies for Direct Injection SI Engine,” *SAE International,* 960600.

[5] J. Harada, T. Tomita, H. Mizuno, Z. Mashiki and Y. Ito (1997), “Development of Direct Injection Gasoline Engine,” *SAE International,* 970540.

[6] M. Kano, K. Saito, M. Basaki, S. Matsushita and T. Gohno (1998), “Analysis of Mixture Formation of Direct Injection Gasoline Engine,” *SAE Technical Paper,* 980157.

[7] H. Zhao, J. Li, T. Ma and N. Ladommatos (2002), “Performance and Analysis of a 4-Stroke Multi-Cylinder Gasoline Engine with CAI Combustion,” *SAE International,* 2002-01-0420.

[8] L. Cao, H. Zhao, X. Jiang and N. Kalian (2005), “Numerical Study of Effects of Fuel Injection Timings on CAI/HCCI Combustion in a Four-Stroke GDI Engine,” *SAE International,* 2005-01-0144.

[9] A. Oakley, H. Zhao and N. Ladommatos (2001), “Experimental Studies on Controlled Auto-ignition (CAI) Combustion of Gasoline in a 4-Stroke Engine,” *SAE International,* 2001-01-1030.

[10] M. Christensen, B. Johansson, P. Amnéus and F. Mauss (1998), “Supercharged Homogeneous Charge Compression Ignition,” *SAE International,* 980787.

[11] N. Ito, T. Ohta, R. Kono, S. Arikawa and T. Matsumoto (2007), “Development of a 4-Cylinder Gasoline Engine with a Variable Flow Turbo-charger,” *SAE International,* 2007-01-0263.

[12] D. Han, S.-K. Han, B.-H. Han and W.-T. Kim (2007), “Development of 2.0L Turbocharged DISI Engine for Downsizing Application,” *SAE International,* 2007-01-0259.

[13] T. Noyori, T. Ohira, T. Nakamura and Y. Akamatsu (2003), “Development of a 660cc Turbo-Charged Spark-Ignition Direct-Injection Engine,” *SAE International and Society of Automotive Engineers of Japan, Inc,* 2003-32-0013 / 20034313.

[14] S. Keppeler, H. Schulte and H. J. Ecker (1998), “The Technical Ramifications of Downsizing HSDI Diesel Technology to the 300 cc Displacement Class,” *SAE International,* 981916.

[15] H. J. Ecker, M. Schwaderlapp and D. K. Gill (2000), “Downsizing of Diesel Engines: 3-Cylinder / 4-Cylinder,” *SAE International,* 2000-01-0990.

[16] J. Turner, A. Popplewell, R. Patel, T. Johnson, N. Darnton, S. Richardson, S. Bredda, R. Tudor, C. Bithell, R. Jackson, S. Remmert, R. Cracknell, J. Fernandes, A. Lewis, S. Akehurst, C. Brace, C. Copeland, R. Martinez-Botas, A. Romagnoli and A. Burluka (2014), “Ultra Boost for Economy: Extending the Limits of Extreme Engine Downsizing,” *SAE International,* 2014-01-1185.

[17] T. Lake, J. Stokes, R. Murphy, R. Osborne and A. Schamel (2004), “Turbocharging Concepts for Downsized DI Gasoline Engines,” *SAE international,* 2004-01-0036.

[18] W. P. Attard, S. Konidaris, E. Toulson and H. C. Watson (2007), “The Feasibility of Downsizing a 1.25 Liter Normally Aspirated Engine to a 0.43 Liter Highly Turbocharged Engine,” *SAE International,* 2007-24-0083.

[19] M. Thirouard and P. Pacaud (2010), “Increasing Power Density in HSDI Engines as an Approach for Engine Downsizing,” *SAE International,* 2010-01-1472.

[20] W. Attard, H. C. Watson, S. Konidaris and M. A. Khan (2006), “Comparing the Performance and Limitations of a Downsized Formula SAE Engine in Normally Aspirated, Supercharged and Turbocharged Modes,” *SAE International,* 2006-32-0072.

[21] N. Fraser, H. Blaxill, G. Lumsden and M. Bassett (2009), “Challenges for Increased Efficiency through Gasoline Engine Downsizing,” *SAE International,* 2009-01-1053.

[22] G. P. Blair (1990), “The basic design of two-stroke engines,” no. ISBN 1-56091-008-9, 1990.

[23] “Daihasu press release, 58th Frankfurt Motor show.,” 14th September, 1999.

[24] R. Knoll (1998), “AVL Two-Stroke Diesel Engine,” *SAE Technical Paper,* 981038.

[25] J. Abthoff, F. Duvinage, T. Hardt, M. Krämer and M. Paule (1998), “The 2-Stroke DI-Diesel Engine with Common Rail Injection for Passenger Car Application,” *SAE Paper,* 981032.

[26] Y. Moriyoshi, K. Kikuchi, K. Morikawa and H. Takimoto (2001), “Numerical Analysis of Mixture Preparation in a Reverse Uniflow-Type Two-Stroke Gasoline DI Engine,” *SAE Paper,* 2001-01-1815/4235.

[27] E. C. O. Pereira, E. F. A. Rodrigues and J. J. G. Martins (1997), “Design of a Fuel Efficient Uniflow Two Stroke Semi-Direct Injection Engine,” *SAE Paper,* 970367.

[28] E. Mattarelli, C. A. Rinaldini, G. Cantore and P. Baldini (2012), “2-Stroke Externally Scavenged Engines for Range Extender Applications,” *SAE International,* 2012-01-1022.

[29] Y. Li, H. Zhao, Z. Peng and N. Ladommatos (2001), “Analysis of Tumble and Swirl Motions in a Four-Valve SI Engine,” *SAE International,* 2001-01-3555.

[30] M. Lorenz and K. Prescher (1990), “Cycle Resolved LDV Measurements on a Fired SI-Engine at High Data Rates Using a Conventional Modular LDV-System,” *SAE International,* 900054.

[31] A. E. Catania, C. Dongiovanni, A. Mittica, G. Molina and E. Spessa (1995), “A New Test Bench for HWA Fluid-Dynamic Characterization of a Two-Valved In-Piston-Bowl Production Engine,” *SAE International,* 952467.

[32] F. E. Corcione and G. Valentino (1990), “Turbulence Length Scale Measurements by Two-Probe-Volume LDA Technique in a Diesel Engine,” *SAE Technical Paper Series,* 902080.

[33] M. Auriemma, F. E. Corcione, R. Macchioni, G. Seccia and G. Valentino (1996), “LDV Measurements of Integral Length Scales in an IC Engine,” *SAE TECHNICAL PAPER SERIES,* 961161.

[34] S.-C. Yoo, K. Lee, M. Novak, H. Schock and P. Keller (1995), “3-D LDV Measurement of In-Cylinder Air Flow in a 3.5L Four-Valve SI Engine,” *SAE TECHNICAL PAPER SERIES,* 950648.

[35] T. Obokata, T. Hashimoto, S.-i. Gojuki, T. Karasawa, S. Shiga and T. Kurabayashi (1992), “LDA Characterization of Gas Flow in a Combustion Chamber of a Four-Stroke S.I. Engine,” *SAE International,* 920519.

[36] D. W. LEE (1938), “A STUDY OF AIR FLOW IN AN ENGINE CYLINDER,” LANGLEY llLIEMORIAL AERONAUTICAL LABORATORY, NTATIONAL ADVISORY COMMITEE FOR AERONAUTICS, LANGLEY FIELD, REPORT No. 653 September 16, 1938.

[37] M. Rönnbäck and W. X. Le (1991), “Study of Induction Tumble by Particle tracking Velocimetry in a 4-Valve Engine,” *SAE International,* 912376.

[38] H.-J. Neußer, L. Spiegel and J. Ganser (1995), “Particle Tracking Velocimetry -

A Powerful Tool to Shape the In-Cylinder Flow of Modern Multi-Valve Engine Concepts," *SAE TECHNICAL PAPER SERIES,* 950102.

[39] L. Fan, R. D. Reitz and N. Trigui (1999), "Intake Flow Simulation and Comparison with PTV Measurements," *SAE TECHNICAL PAPER SERIES,* 1999-01-0176.

[40] G. Valentino, L. Allocca and L. Marchitto (2011), "PIV Investigation of High Swirl Flow on Spray Structure and its Effect on Emissions in a Diesel-Like Environment," *SAE International,* 2011-01-1286.

[41] M. Ekenberg, R. Reinmann, E. Olofsson, B. Gillet and B. Johansson (2001), "The Influence of a Late In-Cylinder Air Injection on In-Cylinder Flow Measured with Particle Image Velocimetry (PIV)," *SAE International,* 2001-01-3492.

[42] W. Zeng, M. Sjöberg and D. Reuss (2014), "Using PIV Measurements to Determine the Role of the In-Cylinder Flow Field for Stratified DISI Engine Combustion," *SAE International,* 2014-01-1237.

[43] B. Khaligh (1990), "Intake-Generated Swirl and Tumble Motions in a 4-Valve Engine with Various Intake Configurations- Flow Visualization and Particle Tracking Velocimetry," *SAE International,* 900059.

[44] D. H. Shack and W. C. Reynolds (1991), "Application of Particle Tracking Velocimetry to the Cyclic Variability of the Pre-Combustion Flow Field in a Motored Axisymmetric Engine," *SAE TECHNICAL PAPER SERIES,* 910475.

[45] W. Church and P. V. Farrell (1998), "Effects of Intake Port Geometry on Large Scale In-Cylinder Flows," *SAE International,* 980484.

[46] D. L. Reuss, T.-W. Kuo, B. Khalighi, D. Haworth and M. Rosalik (1995), "Particle Image Velocimetry Measurements in a High-Swirl Engine Used for Evaluation of Computational Fluid Dynamics Calculations," *SAE International,* 952381.

[47] D. L. Reuss (2000), "Cyclic Variability of Large-Scale Turbulent Structures in Directed and Undirected IC Engine Flows," *SAE International,* 2000-01-0246.

[48] S. Haider, T. Schnipper, A. Obeidat, K. E. Meyer, V. L. Okulov, S. Mayer and J. H. Walther (2013), “PIV study of the effect of piston position on the in-cylinder swirling flow during the scavenging process in large two-stroke marine diesel engines,” *Journal of Marine Science and Technology,* vol. 18, no. 1, pp. 133-143 , 2013.

[49] C. Arcoumanis, H. G. Green and J. H. Whitelaw (1985), “Velocity and concentration measurements in a model diesel engine,” *Experiments in Fluids,* vol. 3, pp. 270-276, 1985.

[50] T. Ksdota, F.-Q. Zhao and K. Miyosh (1990), “Rayleigh Scattering Measurements of Transient Fuel Vapor Concentration in a Motored Spark Ignition Engine,” *SAE Technical Paper,* 900481.

[51] C. Espey, J. E. Dec, T. A. Litzinger and D. A. Santavicca (1994), “Quantitative 2-D Fuel Vapor Concentration Imaging in a Firing D.I. Diesel Engine Using Planar Laser-Induced Rayleigh Scattering,” *SAE Technical Paper,* 940682.

[52] P. Miles and M. Dilligan (1996), “Quantitative In-Cylinder Fluid Composition Measurements Using Broadband Spontaneous Raman Scattering,” *SAE Technical Paper,* 960828.

[53] C. Schulz and V. Sick (2005), “Tracer-LIF diagnostics: quantitative measurement of fuel concentration, temperature and fuel/air ratio in practical combustion systems,” *Energy and Combustion Science,* vol. 31, p. 75–121, 2005.

[54] W. Hwang, J. E. Dec and M. Sjöberg (2007), “Fuel Stratification for Low-Load HCCI Combustion: Performance & Fuel-PLIF Measurements,” *SAE International,* 2007-01-4130.

[55] S. Shen and I. Nagata (1995), “Prediction of excess enthalpies of ketone-alkane systems from infinite dilution activity coefficients,” *Thermochimica Acta,* vol. 258, pp. 19-31, 1995.

[56] X. Wang, Z. Zhan, X. Yu, T. Hu, Y. Qiao, Y. Zhu and S. Jiang (2014), “Experimental Study on Injector Spray Pattern Optimization for a Turbocharged

GDI Engine Combustion System," *SAE International,* 2014-01-1439.

[57] V. S. Movva (2004), "SIMULATION OF FLUID FLOW IN INTERNAL COMBUSTION ENGINES USING WAVE ACTION SIMULATION," *MASTER OF SCIENCE. Thesis,* 2004. Texas Tech University.

[58] S. A. Orszag and I. Staroselsky (2000), "CFD: Progress and problems," *Computer Physics Communications,* 127 (2000) 165–171.

[59] P. Sagaut (1998), Large Eddy Simulation for Incompressible Flows, An Introduction, Springer, 1998.

[60] G. Alfonsi (2009), "Reynolds-Averaged Navier–Stokes Equations for Turbulence Modeling," *Transactions of the ASME,* vol. 62, no. 040802-20, JULY 2009.

[61] U. G. Riegler and M. Bargende (2002), "Direct Coupled 1D/3D-CFD-Computation (GT-Power/Star-CD) of the Flow in the Switch-Over Intake System of an 8-Cylinder SI Engine with External Exhaust Gas Recirculation," *SAE International,* 2002-01-0901.

[62] C. Forte, E. Corti, G. M. Bianchi, S. Falfari and S. Fantoni (2014), "A RANS CFD 3D Methodology for the Evaluation of the Effects of Cycle By Cycle Variation on Knock Tendency of a High Performance Spark Ignition Engine," *SAE Technical Paper,* 2014-01-1223.

[63] L. Cornolti, A. Onorati, T. Cerri, G. Montenegro and F. Piscaglia (2013), "1D simulation of a turbocharged Diesel engine with comparison of short and long EGR route solutions," *Elsevier Applied Energy,* 111 (2013) 1–15.

[64] "ANSYS FLUENT 12.0/12.1 Documentation," 2009-01-29 .

[65] J. B. Heywood (1988), Internal Combustion Engine Fundamentals, 1988.

[66] K. Jaffri, H. G. Hascher, M. Novak, K. Lee, H. Schock, M. Bonne and P. Keller (1997), "Tumble and Swirl Quantification within a Motored Four-Valve SI Engine Cylinder Based on 3-D LDV Measurements," *SAE International,* 970792.

[67] G. D'Errico, A. Onorati and S. Ellgas (2008), "1D thermo-fluid dynamic modelling of an S.I. single-cylinder H2 engine with cryogenic port injection," *Elsevier International Association for Hydrogen Energy,* 3 3 (2 0 0 8) 5 8 2 9 – 5 8 4 1.

[68] "WAVE help system 8.3," 2010.

[69] S. K. Chen and P. F. Flynn (1965), "Development of Single Cylinder Compression Ignition Research Engine," *SAE Paper,* 650733.

[70] Z. J. Sroka (2012), "Some aspects of thermal load and operating indexes after downsizing for internal combustion engine," *J Therm Anal Calorim,* vol. 110, p. 51–58, 2012.

[71] A. Melling (1997), "Tracer particles and seeding for particle image velocimetry," *Meas. Sci. Technol.,* vol. 8, p. 1406–1416, 1997.

[72] H. Zhao (2012), Laser Diagnostics and Optical Measurement Techniques, ISBN 978-0-7680-5782-9, 2012.

[73] R. J. Adrian (1991), "PARTICLE-IMAGING TECHNIQUES FOR EXPERIMENTAL FLUID MECHANICS," *Annual Reviews. Fluid Mech.,* vol. 23, pp. 261-304, 1991.

[74] J. Westerweel (1997), D. Dabiri and M. Gharib, "The effect of a discrete window offset on the accuracy of cross-correlation analysis of digital PIV recordings," *Experiments in Fluids,* vol. 23, pp. 20-28, 1997.

[75] K. M. Ingvorsen, K. E. Meyer, J. H. Walther and S. Mayer (2013), "Turbulent swirling flow in a model of a uniflow-scavenged two-stroke engine," *Experiment Fluids,* no. 54:1494, 2013.

[76] C. J. Rutland (2011), "Large-eddy simulations for internal combustion engines - a review," *International Journal of Engine Research,* p. 12: 421, 2011.

Appendix

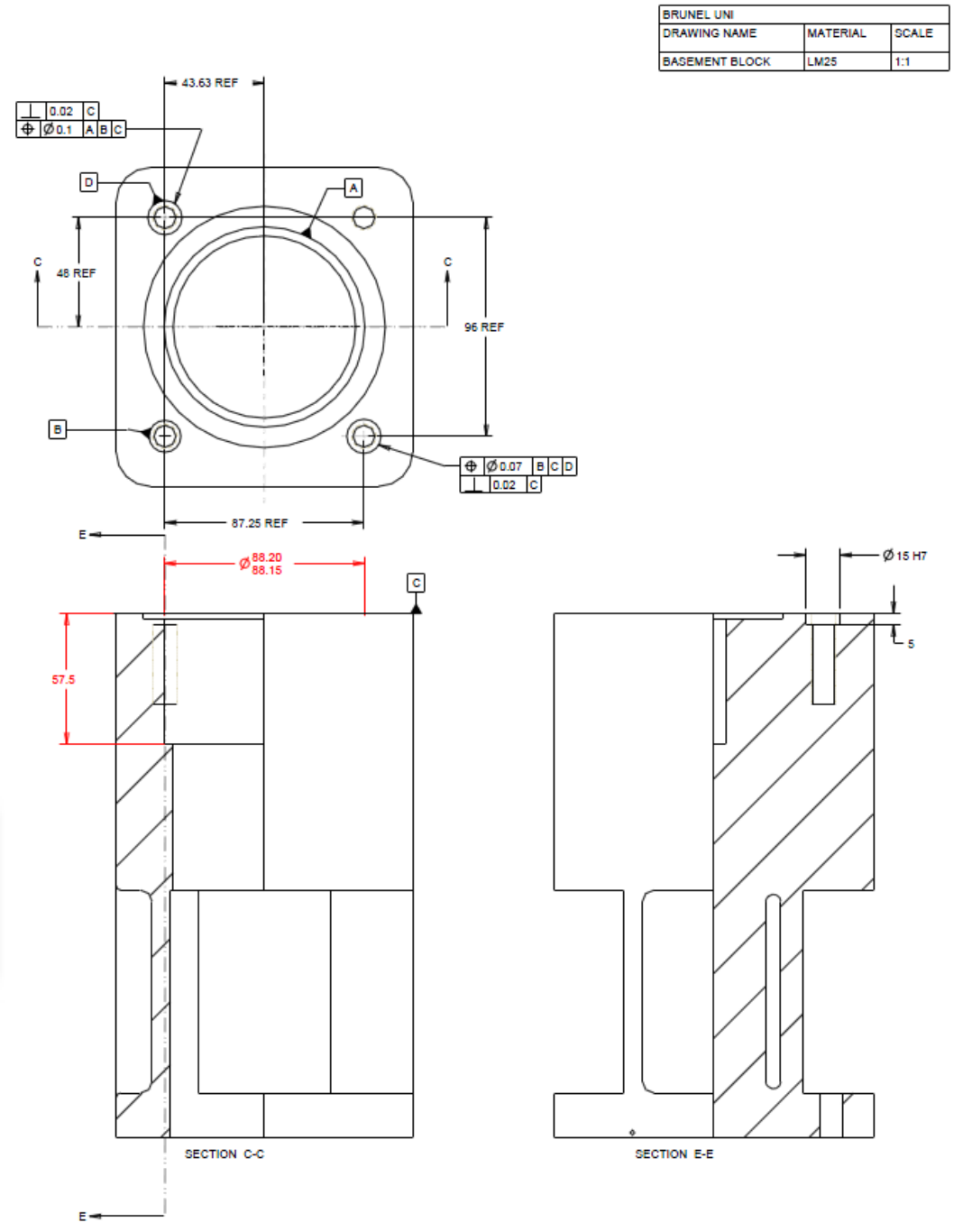

Figure. A1 Engine block extension modification

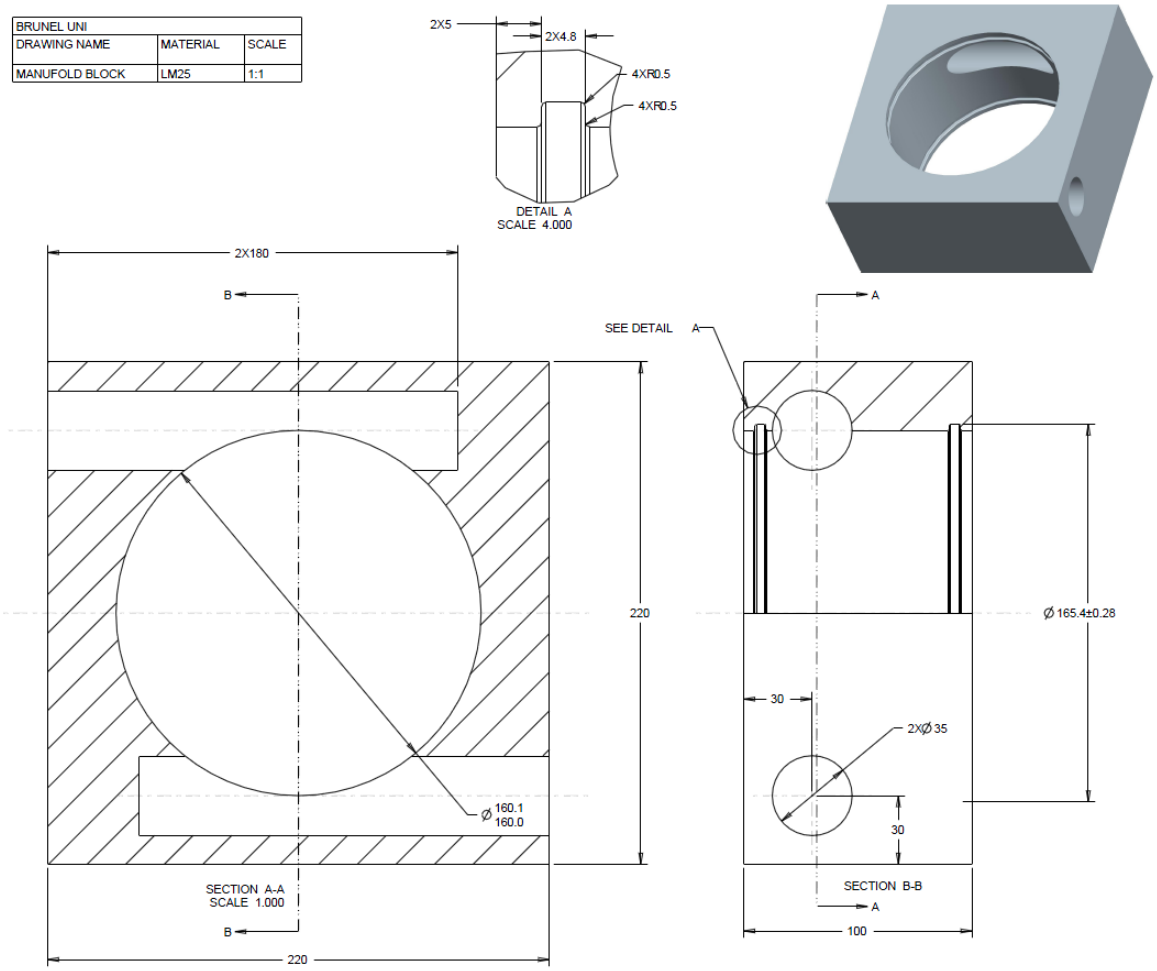

Figure. A2 Intake block

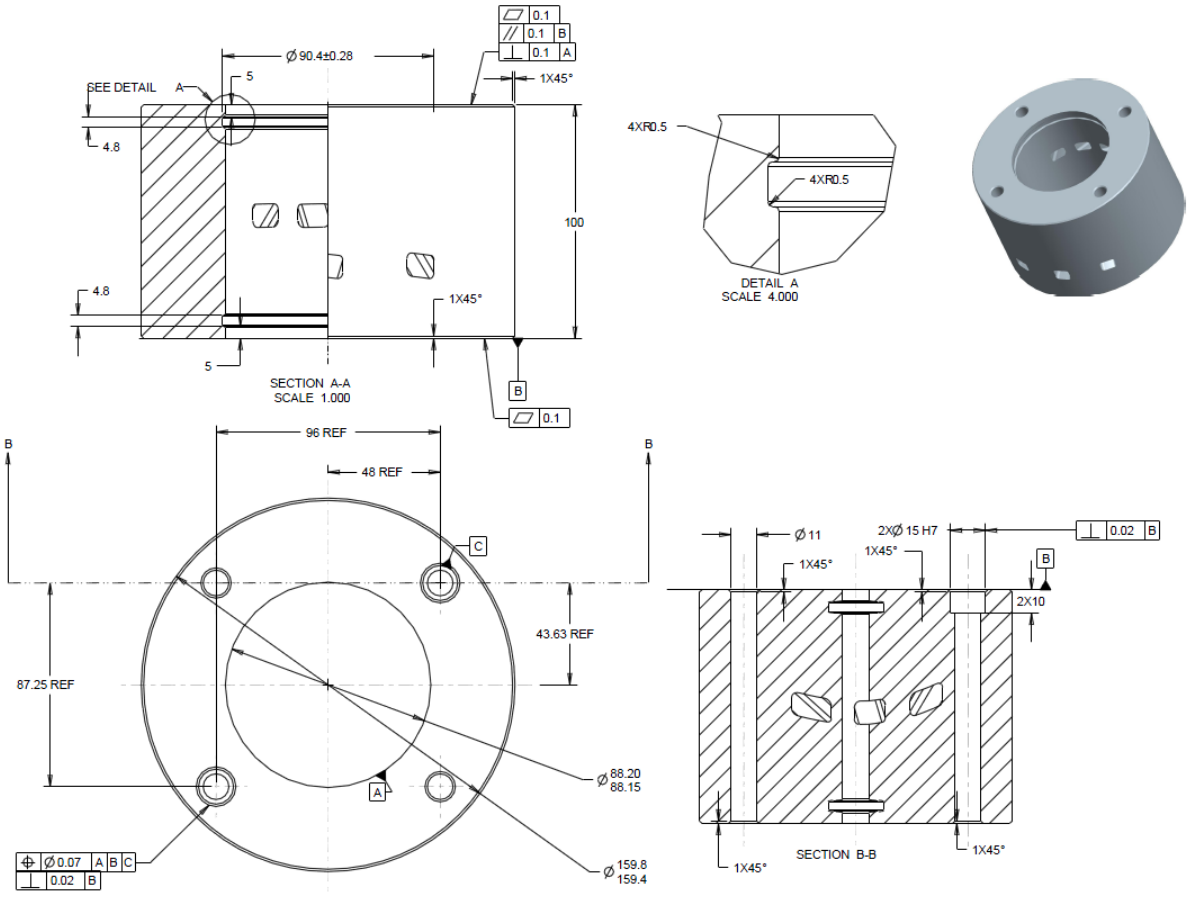

Figure. A3 Port block

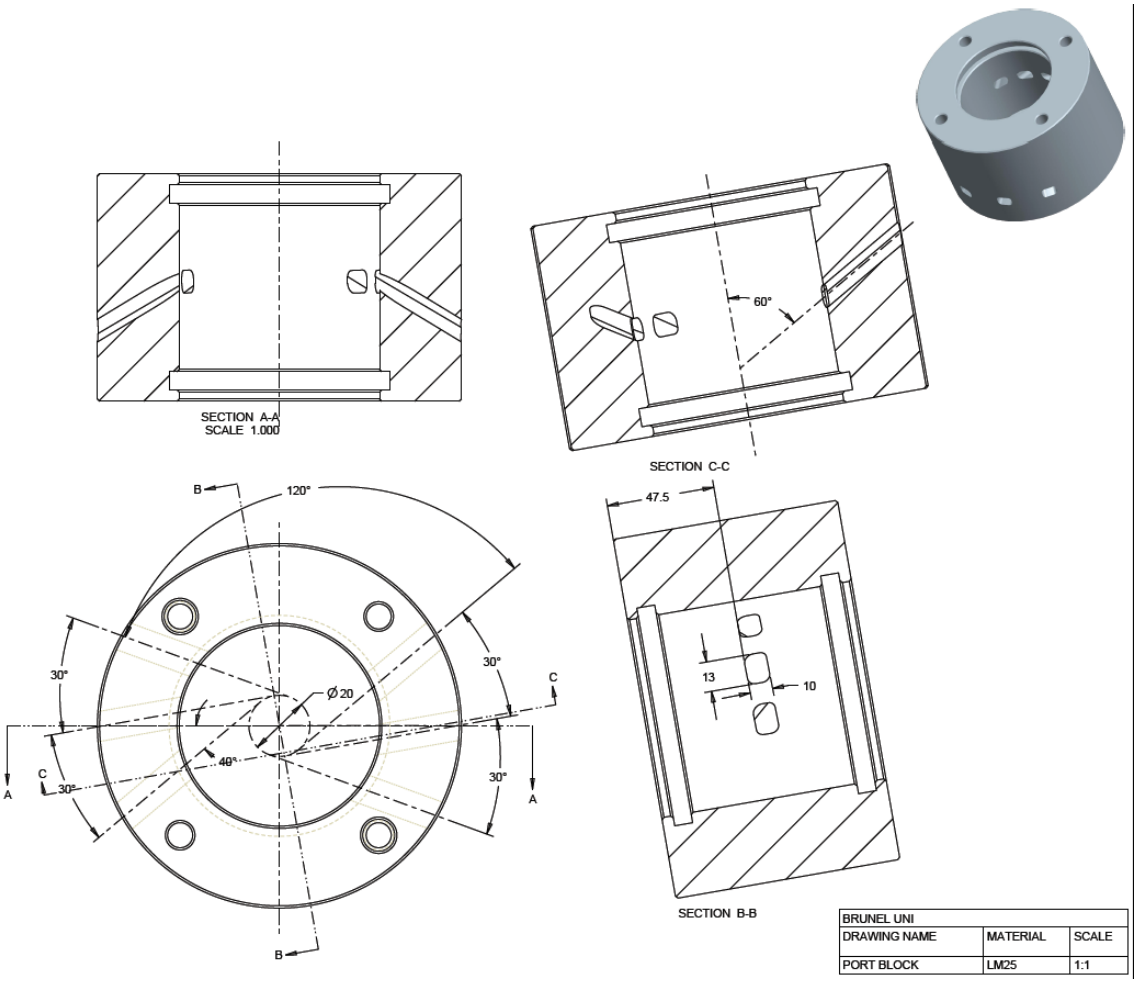

Figure. A4 Ports structure in the port block

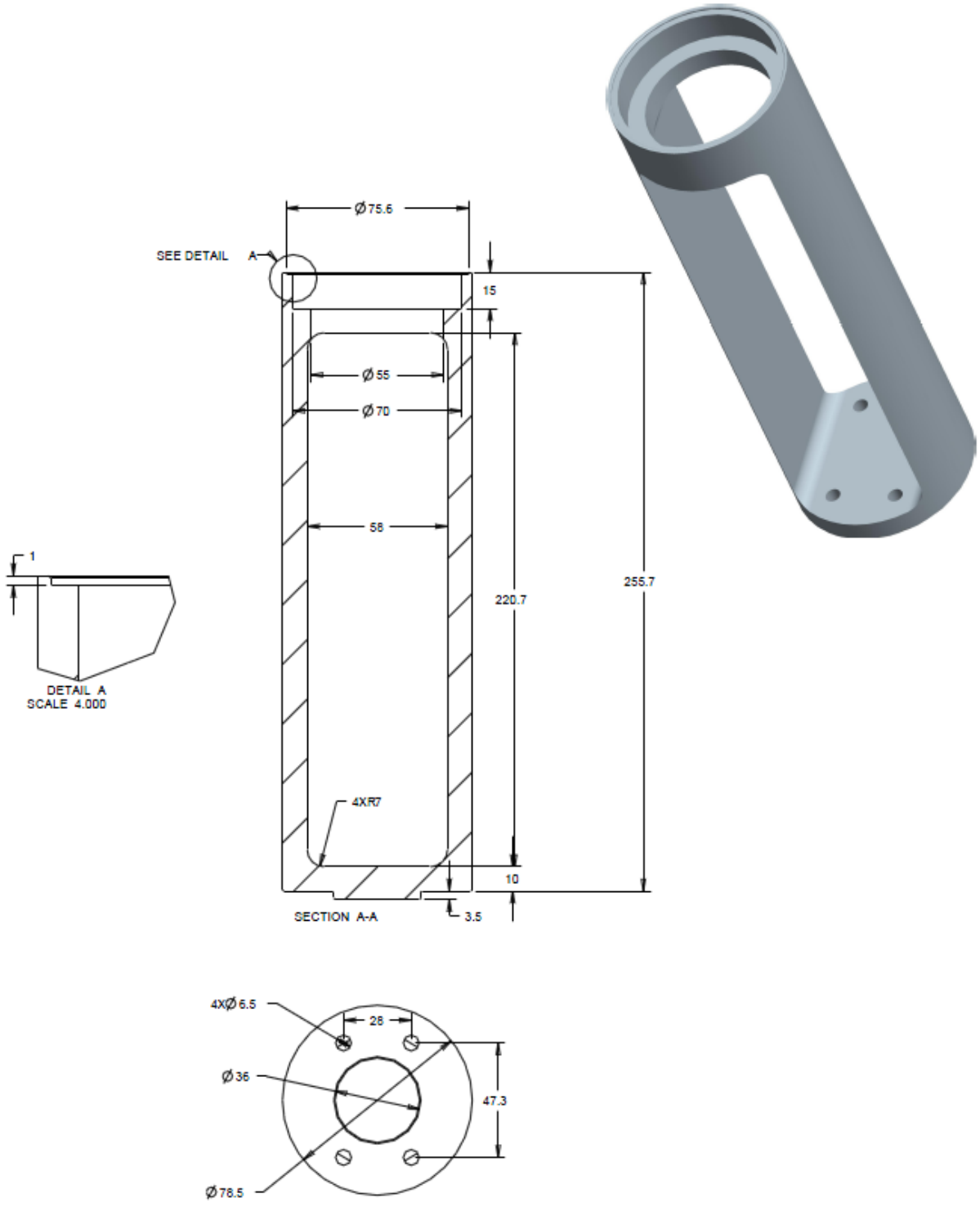

Figure. A5 Piston extension

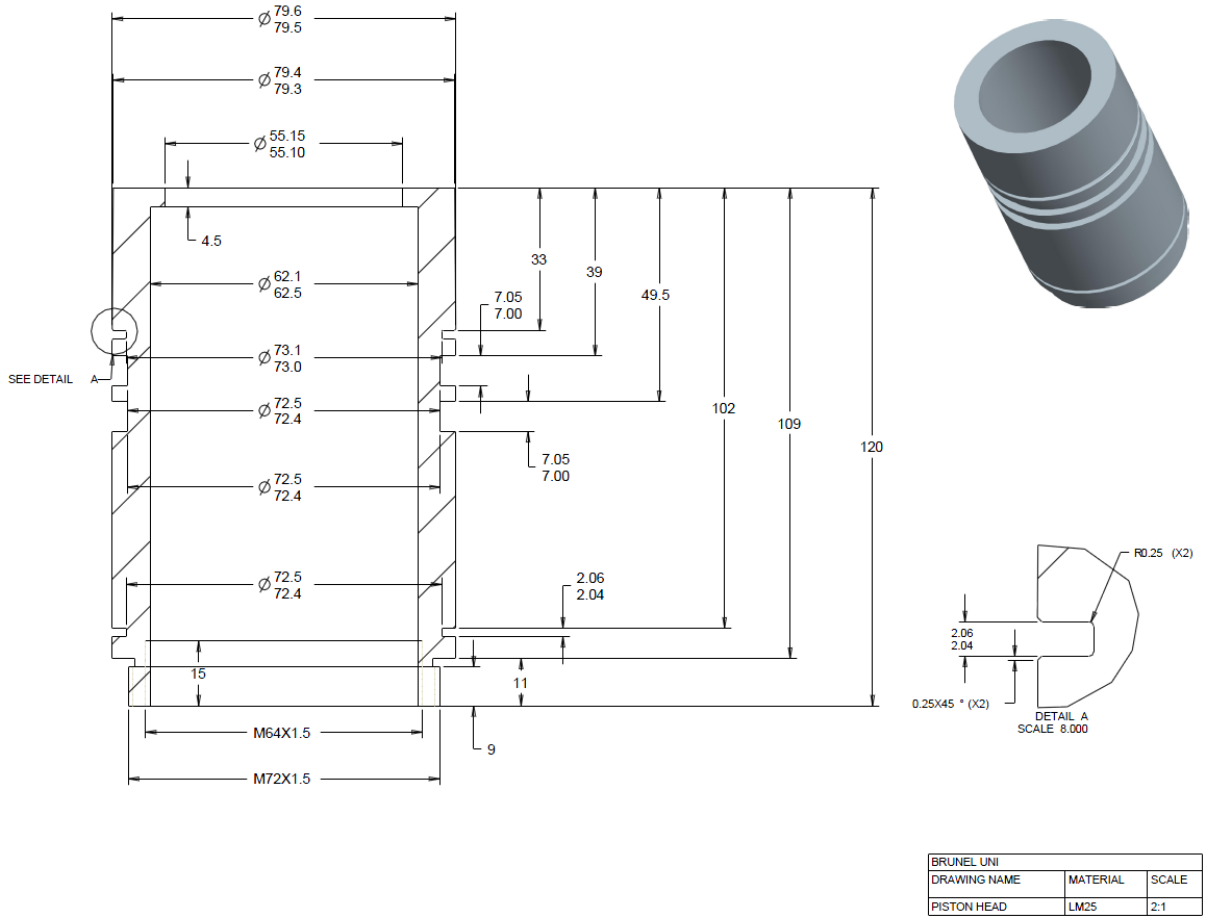

Figure. A6 Piston head